WITAM-2016

2nd INTERNATIONAL CONGRESS ON THE WORLD OF TECHNOLOGY AND ADVANCED MATERIALS

Book of Proceedings 2016

28 SEPTEMBER - 02 OCTOBER 2016
KIRŞEHİR/TURKEY

Dear Participants,

Welcome to the 2nd International Congress on the World of Technology and Advanced Materials-WITAM 2016. The first one was held at the University of Batna in Algeria on the 17th-18th of November 2015.

The congress will bring together academics, physicists, chemists, engineers and material scientists from all over the world, and we hope that you will take this opportunity to promote academic collaboration and friendship and to explore the city of Kirsehir.
WITAM 2016 covers these topics listed below in five days via two parallel sessions;

- *Materials*
- *Metamaterials, Applications*
- *Synthesis*
- *Functional Materials*
- *Polymer Materials*
- *Composite and Ceramic Materials*
- *Nanomaterials and Nanotechnology*
- *Biomaterials and Healthcare Applications*
- *Optical, Electronic, Magnetic and Spintronic Materials*
- *Spectroscopy*
- *Condensed Matter and Statistical Physics*
- *Energy*
- *Theoretical and Computational Science*
- *Free Topics*

This abstract book includes all the submitted abstracts to the WITAM 2016 Congress on technologies and advanced materials. In total, there are 151 oral presentations including five invited talks and 161 poster presentations. More than 200 presenters are coming to the congress from different countries as well as different cities of Turkey.

I would like to thank all the participants, the members of the organising and scientific committee. I would also like to express my gratitude to Ahi Evran University Rectorship for making this event a success.

Again, a warm welcome to Kırşehir City.

Prof. Dr. Mustafa Kurt
The President of the WITAM 2016

SCIENTIFIC COMMITTEE

President:

M. Kurt	Ahi Evran Univ. (Turkey)

Members:

A. Belgacem-Bouzida U.	Batna (Algeria)
G. Uğur	Gazi Univ. (Turkey)
Z. Boumerzoug	Biskra Univ. (Algeria)
H. Ünver	Ankara Univ. (Turkey)
H. M. Tütüncü	Sakarya Univ. (Turkey)
B. Legendre	Paris 11 Univ. (France)
F. El Haj Hassan	Libanaise Univ. (Liban)
S. Uğur	Gazi Univ. (Turkey)
D. Bradai	USTHB (Algeria)
A. Taşkıran	Team Man., Elec. Drive Sys. (Germany)
D. Rached	S.Belabes Univ. (Algeria)
M. Ozduran	Ahi Evran Univ. (Turkey)
N. Bouaouadja	Sétif Univ. (Algeria)
H. Yaşar Ocak	Dumlupınar Univ. (Turkey)
F. Göktaş	Yıldırım Beyazıt Univ. (Turkey)
H. Baaziz	U. Msila (Algeria)
N. Sundaraganesan	Annamalai University (India)
Y. Karataş	Ahi Evran Univ. (Turkey)
G. Koza	Ahi Evran Univ. (Turkey)
J. Paulsdorf	PSS (Germany)
N. Arikan	Ahi Evran Univ. (Turkey)
Y. Djaballah	U. Batna (Algeria)
M. Burjanadze	Jülich (Germany)
R. Karapınar	Mehmet Akif Ersoy Univ. (Turkey)
Z. Charifi	U. Msila (Algeria)
S. Nezir	Kırıkkale Univ. (Turkey)
S. Goumri-Said	Alfaisal Univ. (Saudi Arabia)

ORGANIZING COMMITTEE

Chairman

Prof. Dr. Mustafa KURT
Vice-chancellor of Ahi Evran University, Kırşehir, Turkey

Co-Chairs

Prof. Dr. Gökay UĞUR	Gazi University, Turkey
Assoc. Prof. Dr. Şule UĞUR	Gazi University, Turkey
Assoc. Prof. Dr. Yunus KARATAŞ	Ahi Evran University, Turkey

Organizing Committee

Prof. Dr. Mustafa KURT (Turkey)
Prof. Dr. Gökay UĞUR (Turkey)
Assoc. Prof. Dr. Şule UĞUR (Turkey)
Assoc. Prof. Dr. Yunus KARATAŞ (Turkey)
Assoc. Prof. Dr. Nihat ARIKAN (Turkey)
Assoc. Prof. Dr. Harun ÇİFTÇİ (Turkey)
Assoc. Prof. Dr. Hülya ÖZTÜRK (Turkey)
Assoc. Prof. Dr. Yusuf ERDOĞDU (Turkey)
Assist. Prof. Dr. Mustafa ÖZDURAN (Turkey)
Assist. Prof. Dr. Osman ÖRNEK (Turkey)
Assist. Prof. Dr. Gökhan SÜRÜCÜ (Turkey)
Assist. Prof. Dr. Ganimet MÜLAZIMOĞLU KIZILIRMAK (Turkey)
Assist. Prof. Dr. Tevfik Raci SERTBAKAN (Turkey)
Assist. Prof. Dr. Emine TANIŞ (Turkey)
Dr. Abdullah CANDAN (Turkey)
Dr. Ahmet İYİGÖR (Turkey)
Dr. Cihan KÜRKÇÜ (Turkey)
Dr. Bekir SATILMIŞ (Turkey)
Dr. Zuhal ALIM (Turkey)
Dr. Selgin AL (Turkey)
Res. Assist. Zühre ÇALIŞIR (Turkey)
Lect. Emrah AYDEMİR (Turkey)

ETHICAL DECLARATION

Papers have been placed here by the authors and did not undergo any refereeing process. Authors are responsible for the content of the work and the copyright.

CONTENT

On the structural and electronic properties of Neodymium chalcogenides NdX (X= S, Se, Te): an ab initio study of the B2 phase **Abdullah Candan**	1
Fabrication of Inverted Type Organic Solar Cells with Metal Doped TiO_2 Thin Films as an Electron Selective Layer **Arif Kösemen, Zühal Alpaslan Kösemen, Betül Canimkubey, Sadullah Öztürk, Osman Örnek, Şaban Fındık, Mustafa Erkovan**	6
Applications of Geometric Morphometrics to Systematic Biology **Aslı Doğan Sarıkaya**	9
Solar Power Potential of Kırşehir City **Dilek Ferudun**	13
Comparison of Mobile Application, Mobile Site and Responsive Web Site in Web Site Design **Emrah Aydemir**	17
Examination of Internet Usage of Vocational School Students for Obtaining Information **Emrah Aydemir, Salih Ermiş**	21
The Mechanical Properties of ZrSbTe and HfSbTe Compounds **Engin Deligöz, Hacı Özışık, Havva Boğaz Özışık**	26
The Investigation of Some Probiotics Proporties of Lactic Acid Bacteria Izolated from Traditionally Produced Shalgam Juice in Mersin Region **Esin Kiray**	29
All Solution-Based Fabrication of CuO Thin Film/Si Nanowires Heterojunction Devices for Optoelectronic Applications **Funda Aksoy Akgul, Guvenc Akgul**	33
Preparation of CuO Thin Films by Chemical Bath Deposition Method and Their Solar Cell Application with Si Nanowires **Funda Aksoy Akgul, Guvenc Akgul**	37
Synthesis and Structural Characterization of ZnO and TiO_2 Nanoparticles **Funda Aksoy Akgul, Guvenc Akgul**	42
Phenotypic and Genotypic Characterization for Grain Yield in Wheat (*Triticum vulgare* L.) **Mehmet Emin Yazici, Ufuk Karadavut, Çetin Palta, Galip Şimşek, Kübra Soğanci**	46
Fabrication of CdTe-Si Nanowire Heterojunctions for Photodetector Applications **Guvenc Akgul, Funda Aksoy Akgul**	50
Ga-doped ZnO/Si Heterojunction Nanodiodes: Fabrication and Characterization **Guvenc Akgul, Funda Aksoy Akgul**	54
Structural Characterization of Zinc Titanates Nanocomposites by X-Ray Absorption Spectroscopy **Guvenc Akgul, Funda Aksoy Akgul**	58
Cytogenetic Effects of different concentrations and different time periods of Strontium onto *Lens culinaris* Medik **Hakan Sepet, Murat Çanlı**	62
Comparison of Cytogenetic Effects of Barium and Strontium in different concentrations onto *Lens culinaris* Medik **Hakan Sepet, Murat Çanlı**	66
Electronic Properties and Reactivity Descriptors of 5-chloro-2-amino benzophenone **Hamit Alyar**	70
The Magnetic and Electronic Properties of $Ce_{1-x}Pr_xIn_3$ Compounds **Havva Bogaz Ozisik, Haci Ozisik, Engin Deligoz**	74
Hysteresis Behavior of GaAs Semiconductor in an IR Image Converter **Hilal Kurt**	78
Low Pressure Argon Discharges in a Microdischarge Cell with Gap Cathode **Hilal Kurt**	80
Comparison of the Electronic Properties of the II-VI ZnS and ZnSe Cathodes in Plasma-Semiconductor Structure **Hilal Kurt**	83

Parameter Estimation of Weibull Growth Model in Maize **Mehmet Emin Yazıcı, Ufuk Karadavut, Kübra Soğancı, Galip Şimşek**	86
Ceramic Filter Simulation Manufacturing by Powder Injection Molding Method **Levent Urtekin**	91
Species of Microfungi Isolated From *Buxus sempervirens* L. in Küre Mountains National Park Forest Ecosystems **Makbule Erdoğdu**	94
Temperature Dependent Electrical Characteristics of Au/p-CuO/n-Si/Ag Structures **Muhammmet Kaya, Funda Aksoy Akgul, Guvenc Akgul**	98
Electrical Characterization of p-type CuO Thin Film/n-type Si Nanowire Heterojunction Diodes **Muhammmet Kaya, Funda Aksoy Akgul, Guvenc Akgul**	102
Comparison of Cytogenetic Effects of Titanium and Strontium in different time periods onto Fabaceae **Murat Çanlı, Hakan Sepet**	106
Cytogenetic Effects of different concentrations of Barium onto Monocotyledon (*Triticum aestivum* L.) and Dicotyledon (*Lens culinaris* Medik) **Murat Çanlı, Hakan Sepet**	110
Applying Ishihara Pseudoisochromatic Plates on a Computer **Murat Işık, Mustafa Yağcı**	113
Realise and Design of Application Development Kit for PIC **Murat Işık, Mustafa Yağcı**	116
Absorption Coefficient of Hydrothermally Synthesized Barium Titanate Reacted at Different Temperatures and Varying Reaction Times in a Highly Alkaline Solution **Songül Akbulut, Murat Özen, Saynur Kurtuluş, Mehmet Şahin**	120
Friction Stir Spot Welding of Aluminium 6061 T6 **Mustafa Sudağ, Adnan Akkurt**	124
Experimental and Theoretical Studies on Theobromine Dimers and Theobromine-DMSO Complexes **Mustafa Tuğfan Bilkan**	128
Frequency and gate voltage effects on the dielectric properties and electrical conductivity of Al/Co-PVC/p-Si structures **İlbilge DÖKME**	133
Current-Voltage characteristics of Al/Co-PVC/p-Si structures **İlbilge DÖKME**	138
The first principle study of mechanical properties of Rh_3Sc compound **Osman Örnek, Mustafa Özduran and Nihat Arıkan**	142
Interpreting Out-of-Control Signals in Multivariate Processes Using Artificial Neural Network **Özkan Sarıkaya and M. Akif Bakır**	145
Diagnosing the Source of Variance Shifts in Multivariate Processes: An Artificial Neural Network Approach **Özkan Sarıkaya and M. Akif Bakır**	149
Mathematical analysis of controlled slow release of poly-Ɛ-caprolactone microspheres encapsulated with doxycycline hyclate **Özlem Aydın**	153
Producing fibers containing dipyridine complexes via electrospinning for use in antibacterial textile industry **Ruken Esra Demirdöğen, Fatih Mehmet Emen, Zehra Gülten Altın**	156
Producing Boron Nitride containing fibers via electrospinning for use in cleaning waste water polluted with oil **Ruken Esra Demiröğen, Zehra Gülten Altın, Fatih Mehmet Emen**	159
Phase transformation of HgSe at high pressure: An ab initio constant pressure study **Sebahaddin Alptekin**	162
Quality and Earthquake Risk of the Building in Urban Areas: A Case Study for Kırşehir, Turkey **Seda Çellek, M. Mustafa Önal**	166

The current-voltage and interface States Properties of Ag/GO-PVA/p-Si structure **Şükrü Karataş**	170
Ab initio calculation of $AgXO_3$ (X: Nb, Ta) under pressure **Şevket Şimşek**	175
Preparation of a New Metal-Metal Oxide Electrolyte Diode **Zehra Gülten Altin, Ruken Esra Demiröğen, Fatih Mehmet Emen, Derya Kilic**	179
Pasta ın a manufacturing plant L-tpye matrix and risk assessment study **Zehra Gülten Altın, Esra Ruken Demirdöğen, Fatih Mehmet Emen**	182
Application of a New Catalyst in Synthesis of Biolubricant via Modification of Canola Oil **Zehra Gülten Altın, Mustafa Dağ, Ruken Esra Demirdöğen, Fatih Mehmet Emen, Derya Kılıç**	185
Synthesis of two new metal halogen complexes; $Cd((2A1MB)_2)Cl_2$ and $Hg((2A1MB)_2)Cl_2$: Spectroscopic properties and antimicrobial activity **Zuhre Calisir, Fahriye Ercan, Elif Sevim, Nuri Ercan, Ali Sevim, Gozde Ciplak, Mustafa Kurt**	188
Microfungal diversity of Ihlara valley **Faruk Selçuk**	192
Investigation of structural and electronic properties of Yttrium (III) Hydride under high hydrostatic pressure **Cihan Kürkçü, Ziya MERDAN, Hülya ÖZTÜRK**	197
Restoration of motility to *Escherichia coli* YK4104 *fliA* mutant by the alternative sigma factor σ^{28} of *Geobacillus kaustophilus* and *Anoxybacillus flavithermus* **Ali Sevim, Elif Sevim**	201

On the structural and electronic properties of Neodymium chalcogenides NdX (X= S, Se, Te): an ab initio study of the B2 phase

Abdullah Candan

Central Research and Practice Laboratory (AHİLAB), Ahi Evran University, TR-40100 Kırşehir, Turkey

**e-mail corresponding author: acandan@ahievran.edu.tr*

Keywords: Neodymium chalcogenides, electronic structure, elastic constants, phonon frequencies.

ABSTRACT

Using an ab initio pseudopotential method within a generalized gradient approximation of the density functional theory, the structural and electronic properties of neodymium chalcogenides in the B2 (CsCl) structure have been studied. The ground-state properties, including, lattice constant and bulk modulus are in good agreement with the available theoretical data. Electronic band structures, partial and total densities of states have been derived for NdX (X= S, Se, Te).

1. INTRODUCTION

Rare-earth chalcogenides have been widely investigated due to spintronic applications in recent years [1, 2]. Thus, several theoretical and experimental studies have been performed to investigate some properties of neodymium chalcogenides NdX (X= S, Se, Te) [3-6, 9, 10]. Fumer et al [3] measured the energies and widths of the crystal field by neutron inelastic scattering experiments of NdS and NdSe chalcogenides. Papamantallos et al [4] have studied the magnetic structures and ordered moments of these chalcogenides at 4.2 K with the help of neutron diffraction. In addition to theoretically, the electronic, magnetic and optical properties of neodymium chalcogenides by performing LSDA+U and full potential linearized augmented plane wave (FP-LAPW) method by Shankar et al [5]. On the other hand Singh [6] investigated the acoustic attenuation due to phonon–phonon interaction and thermoelastic relaxation mechanisms in B1 structured NdS, NdSe and NdTe along ⟨100⟩, ⟨110⟩ and ⟨111⟩ crystallographic directions at room temperature. First principles study of the structural, elastic and electronic properties of NaCl-type neodymium chalcogenides NdX (X= S, Se, Te) have been performed using full-potential linearized augmented plane-wave plus local orbital method (FP-LAPW+lo), within Generalized Gradient Approximation based on Perdew-Burke-Ernzerhof (PBE-GGA) [7, 8] functional by Singh et al [9]. Mogulkoc et al [10] have conducted the electronic and thermodynamic properties in cubic crystal structures (B1, B2 and B3) of NdTe by means of the Vienna ab initio simulation package (VASP) based on the DFT. The aim of this study is to give structural and electronic properties of NdX (X= S, Se, Te) in CsCl (B2) phase are investigated by the plane-wave pseudopotential method. We focus especially on the investigation of the stability of NdX (X= S, Se, Te) in the B2 phase.

Neodymium chalcogenides belong to the class of binary rare-earth chalcogenides with space group Pm3m (number 221) having (B2) CsCl-type structure. These are typical members of rare earth chalcogenides having Wyckoff's position Nd (0, 0, 0) and X (1/2, 1/2, 1/2), where X= S, Se and Te. Crystal structure of neodymium chalcogenides NdX (X= S, Se, Te) are shown in figure 1.

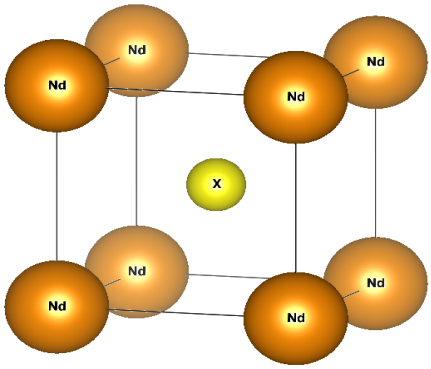

Figure 1. Crystal structure of Neodymium chalcogenides NdX (X= S, Se, Te).

All the calculations have been performed using the plane-wave pseudo-potential DFT method implemented in the Quantum-ESPRESSO code [11]. The Perdew–Burke–Ernzerhof (PBE) [7] exchange-correlation functional was treated at the generalized gradient approximation (GGA). The Nd ($4f^4 6s^2$), S ($3s^2 3p^4$), Se ($3d^{10} 4s^2 4p^4$), and Te ($4d^{10} 5s^2 5p^4$) states are treated as valence electrons. The single-particle functions were expanded in a plane-waves basis set up to the kinetic energies cut-off 60 Ry. The Fermi distribution function with a smearing parameter of 0.01 Ry was used to integrate the bands at Fermi level [12].

2. RESULTS AND DISCUSSION

The calculated values for a_0 and B of Neodymium chalcogenides NdX (X= S, Se, Te) have been summarized in Table 1. The present calculated lattice constant for NdTe is in good agreement with the available theoretical result [8]. In the available literature, there are no theoretical and experimental data reported for the lattice constant of NdS and NdSe.

The predicted equilibrium lattice parameter is about 0.71 % smaller than the theoretical data [10] for NdTe. It is noticed that the lattice parameters for the three Neodymium chalcogenides NdX (X= S, Se, Te) are comparable with slight increases from NdS to NdSe to NdTe. NdS has the highest value of the bulk modulus. It is noted that the bulk modulus *B* decrease in magnitude in the following sequence:
NdS → NdSe → NdTe, i.e. in inverse sequence to a_0.

Table 1. Calculated lattice constants (Å), and Bulk modulus(GPa) for Neodymium chalcogenides NdX (X= S, Se, Te).

Compounds	References	a_0 (Å)	B (GPa)
NdS	Present	3.513342	87.46
NdSe	Present	3.644788	77.07
NdTe	Present	3.852435	67.99
	[10]	3.88	62.26

The calculated electronic band structure of NdX (X= S, Se, Te) along the high symmetry directions in the Brillouin zone given in Fig. 1. It is seen that there is no band gap at the Fermi level, as a result, NdX (X= S, Se, Te) chalcogenides exhibit a metallic character. The overall band profile and DOS for NdTe chalcogenide is in good agreement with previous theoretical result [10].

From the total and the partial density of states of NdX (X= S, Se, Te) and shown in Fig. 2. The valence band is composed of the X (S, Se, Te)-p and Nd-d states. Conduction bands are mainly formed because of Nd-d states.

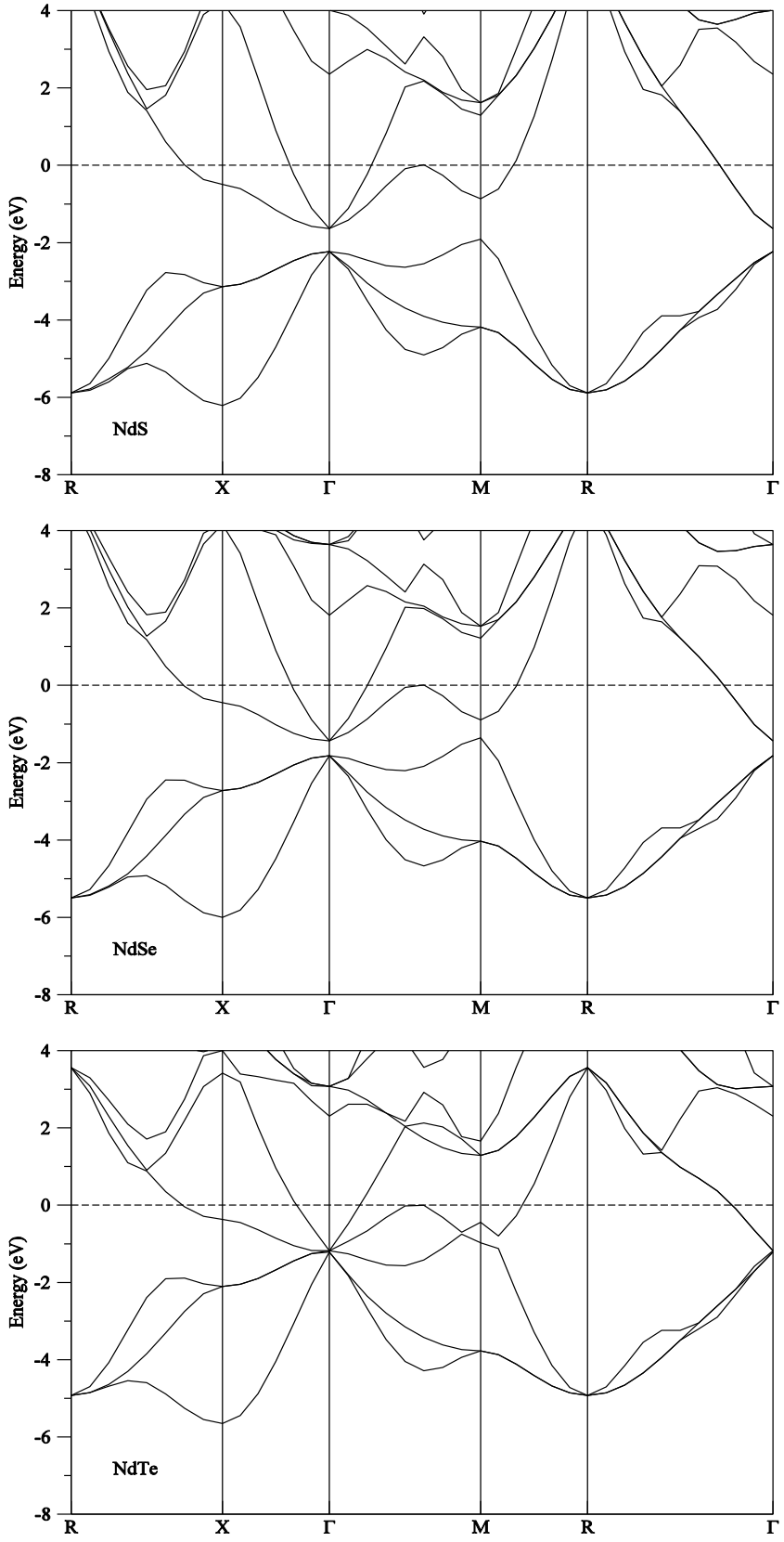

Fig. 1. Calculated electronic band structure of NdX (X= S, Se, Te) along several lines of high symmetry in the Brillouin zone.

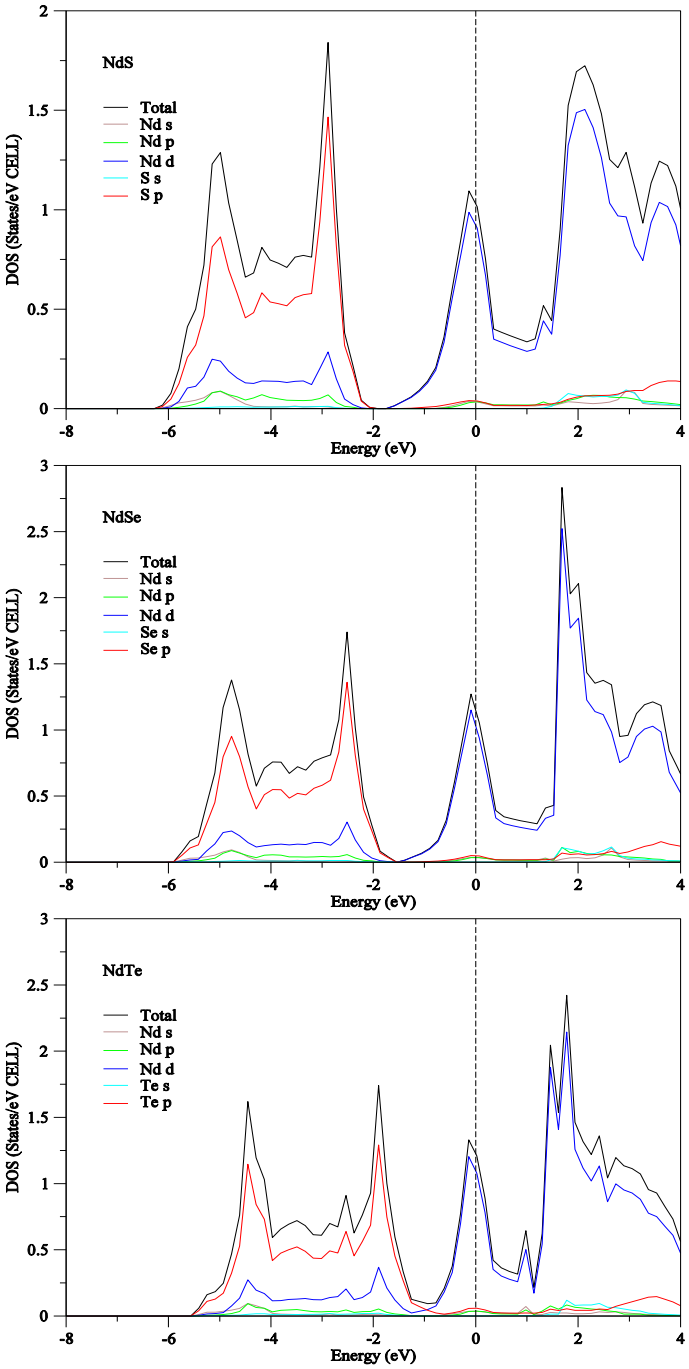

Fig. 2. Calculated partial and total DOS for Neodymium chalcogenides NdX (X= S, Se, Te), the Fermi level is set at 0 eV.

3. CONCLUSION

The structural and electronic properties of NdX (X= S, Se, Te) in CsCl (B2) phase are investigated using ab-initio method with plane-wave pseudopotential. The optimized lattice constants of Neodymium chalcogenides NdX (X= S, Se, Te) are 3.513 Å, 3.644 Å and 3.852 Å, respectively.

REFERENCES

[1] Horne, M., Strange, P., Temmerman, W. M., Szotek, Z., Svane, A., & Winter, H., Journal of Physics: Condensed Matter, (2004), 16(28), 5061.
[2] Vogt, O., & Mattenberger, K., Journal of alloys and compounds, (1995), 223(2), 226-236.
[3] Furrer, A., & Warmining, E., Journal of Physics C: Solid State Physics, (1974), 7(18), 3365.
[4] Schobinger-Papamantellos, P., Fischer, P., Vogt, O., & Kaldis, E., Journal of Physics C: Solid State Physics, (1973), 6(4), 725.
[5] Shankar, A., Rai, D. P., & Thapa, R. K. Journal of Semiconductors, (2012), 33(8), 082001.
[6] Singh, D., Materials Chemistry and physics, (2009), 115(1), 65-68.
[7] Perdew, J. P., Burke, K., & Ernzerhof, M., Phys. Rev. Lett., (1996), 77(18), 3865.
[8] Perdew, J. P., & Wang, Y., Physical Review B, (1992), 45(23), 13244.
[9] Singh, R. P., Singh, R. K., & Rajagopalan, M., Chalcogenide Letters, (2011), 8(5), 325-340.
[10] Mogulkoc, Y., Ciftci, Y. O., & Colakoglu, K., Journal of Optoelectronics and Advanced Materials, (2014), 16(5-6), 529-535.
[11] Giannozzi, P., Baroni, S., Bonini, N., Calandra, M., Car, R., Cavazzoni, C., ... & Dal Corso, A., Journal of physics: Condensed matter, (2009), 21(39), 395502.
[12] Methfessel, M. P. A. T., & Paxton, A. T., Physical Review B, (1989), 40(6), 3616.

Fabrication of Inverted Type Organic Solar Cells with Metal Doped TiO_2 Thin Films as an Electron Selective Layer

Arif Kösemen[a*], Zühal Alpaslan Kösemen[b,c], Betül Canimkubey[b], Sadullah Öztürk[d], Osman Örnek[e], Şaban Fındık[e], Mustafa Erkovan[b]

[a]Department of Physics, Muş Alparslan University, Muş, Turkey
[b]Department of Physics, Gebze Technical University, Kocaeli, Turkey
[c]TUBİTAK UME Optics Laboratory 41470 Gebze, Kocaeli,Turkey
[d]Enginnering Department, Fatih Sultan Mehmet Vakif University, 34080 Istanbul, Turkey
eDepartment of Metallurgy and Materials Engineering, Ahievran University, Kırşehir, Turkey

**a.kosemen@alparslan.edu.tr*:

Keywords: Inverted type solar cells, TiO2 thin film, doped metal oxide semiconductors

ABSTRACT

This study reports the new approach to inverted type organic solar cells with Eu doping metal ions for TiO_2 thin film used as electron transport layer. Sol-gel method was used for prepare TiO2 thin films. Optical and structural properties of the thin films were characterized by using UV-Vis spectrophotometer, XRD, XPS and SEM. Eu was doped in TiO_2 layer in order to increase electron transport from the active to cathode electrode. Eu was doped in TiO_2 with different concentrations as 0, 5 and 7 %. Solar efficiency of the fabricated device increased with 5 % Eu doping concentration from 1.1 % to 2. 45 %. P3HT:PCBM mixtures was used as active layer.

1. INTRODUCTION

Although many researches have been focused on the improvement the power conversion efficiency and life time of organic solar cells by compose new devices structures and obtained new donor-acceptor materials it has not yet been sufficient progress [1,2]. In order to overcome such problems inverted type organic solar cells having excellent device stability and low production cost have been developed in recent years. Extensively, metal oxide materials such as ZnO, TiO2 and Cs2CO3 etc. used as buffer layer to collect electrons by ITO electrode [3]. Among these metal oxides TiO2 is a very famous oxide material for using in inverted type solar cells as electron collective and hole blocking layer. Metal ion doped TiO2 thin films used and investigated very extensively as electron selective layer for inverted type organic solar cells [4,5]. Best of our knowledge Eu doped TiO_2 has not been used before as electron selective layer for inverted type organic solar cells. In this study we successfully fabricated Eu doped TiO_2 thin films and used in the inverted type solar cell structure.

2. RESULTS AND DISCUSSION

Inverted type solar cells were produced with device structure as ITO/Eu:TiO2/P3HT:PCBM/ Al. Assembled device structure were given in the figure 1. TiO_2 thin films were fabricated on ITO coated glass substrate by sol-gel method. Titanium n-butoxide, ethanol, isopropanol alcohol, and acetic acid were mixed with (1:20:20:0.15) molar ratio, respectively, for 5 nights at RT. And then final mixture coated by spin-casting on ITO substrate. In order to doped TiO_2 with Eu Eu-acetate was added into the final mixture with different concentrations.

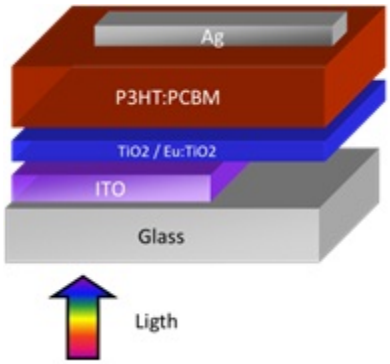

Figure 1. Schematic illustration of the assembled devices.

It is clearly seen from the SEM image of the structure that the TiO_2 thin films are coated uniformly and covers the entire ITO surface (figure 2). Figure.2 shows that fiber-like structures formed in the surface of the all samples. But surface properties of the TiO_2 thin films almost remain the same by Eu doping.

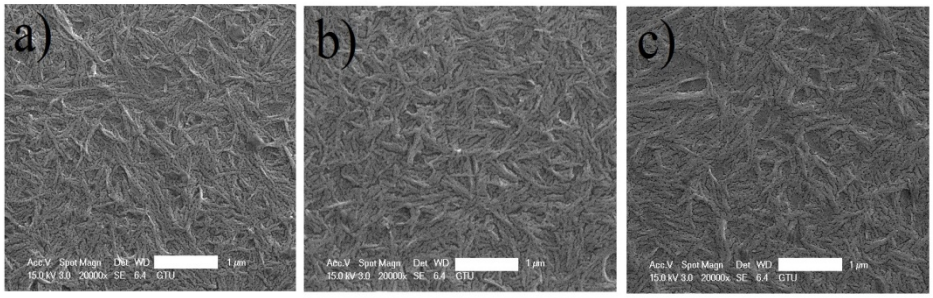

Figure 2. SEM images of TiO2 thin films with Eu doping concentration. a) 0%, b) 5 %, c) 7 %.

Crystal properties of the Eu doped and undoped TiO_2 thin films analayzed by X-Ray diffraction (XRD) spectra of thin films on the Y axis offset (Figure 3). It is clearly seen that form the figure 3, it is obtained that from the figure 3, all the diffraction peaks of doped and undoped samples indicates anatase phase and no other phase are obtained by Eu doping.

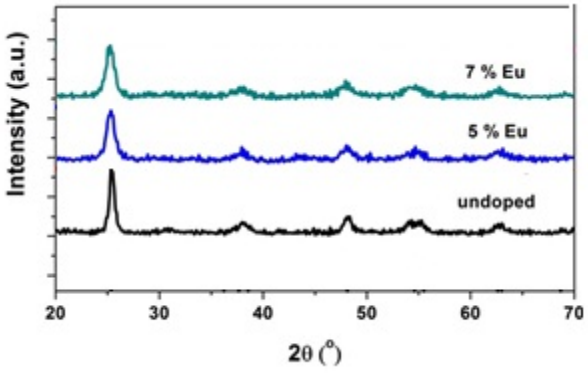

Figure 3. X-ray diffraction spectra of the Eu-doped TiO2 thin films.

Figure 4 shows that current - voltage (I-V) characteristic of the solar cells fabricated with different Eu doping concentrations (0 %, 5 % and 7 %) under illumination conditions (100 mW/cm^2). Shunt resistance (Rsh) and series resistance (Rs) were obtained from the invers slope at Voc and Jsc in the I-V graph, respectively. The open circuit voltage (Voc), short circuit current, filling factor (FF), power conversion efficiency (η), shunt resistance (Rsh) and series resistance (Rs) were estimated from the I-V curve and summarized in Table 1. Inverted type organic solar cell fabricated with undoped TiO2 electron selective

layer exhibited power conversion efficiency of 1.16 %, short circuit current of 6.01mA/cm2, filling factor of 0.36 and open circuit voltage of 0.54V. The Voc, FF and Isc increased with increasing Eu dopant concentration in TiO2 layer from 0 % to 5% concentration value. Besides, Rs becomes larger and Rsh becomes smaller with increasing Eu concentration up to 5 %, and after that concentration level, Rs begun to increase and Rsh begun to decrease again.

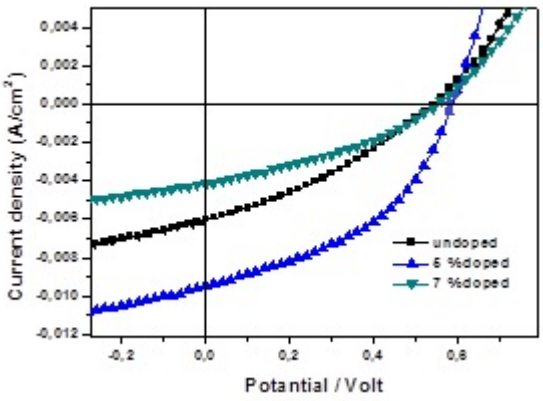

Figure 3. I-V curves of the solar cells fabricated with TiO2 and Eu doped TiO2 layers.

Table 1. Insert the table caption here

Eu	FF	V_{oc}(volt)	I_{sc}(mA/cm^2)	η (%)	R_S (Ω cm^2)	R_{Sh} (Ω cm^2)
0%	0,36	0,54	6,01	1,16	62	238
5%	0,44	0,58	9,47	2,47	25	241
7%	0,35	0,54	4,16	0,78	71	277

3. CONCLUSION

Eu doped and undoped TiO_2 thin films were fabricated on the ITO coated glass substrate successfully. P3HT:PCBM mixture was used as active layer the inverted type organic solar cell structure The goal of presented work was that a dramatic increase was achieved in the current density from 6.01 mA/cm^2 to 9.47 mA/cm^2 at 5 % Eu doping concentration. Isc and Voc showed the maximum values at 5 % Eu concentration, and solar cell efficiency of 2.47 %.

4. ACKNOWLEDGEMENTS

This research is supported by Ahi Evran University Grant no.: MMF.A3.16.009.

REFERENCES

[1] Y. Liang, Z. Xu, J. Xia, S. T. Tsai, Y. Wu, G. Li, C. Ray, L. Yu, Adv. Mater., 22 (2010) 135–138
[2] Yu-Wei Su, Shang-Che Lan, Kung-Hwa Wei, Mater. Today 15 (2012) 554.
[3] Y. J. Cheng, F. Y. Cao, W. C. Lin, C. H. Chen, C. H. Hsieh, Chem. Mater., 23 (2011) 1512–1518.
[4] C. Liu, H. Chen, D. Zhao, L. Shen, Y. He, W. Guo, W. Chen , Appl. Phys. Lett. 105 (2014) 053301
[5] M. C. Wang, H. J. Lin, T. S. Yang, Journal of Alloys and Compounds 473 (2009) 394–400

Applications of Geometric Morphometrics to Systematic Biology

Aslı Doğan Sarıkaya[a*]

[a]*Department of Anthropology, Faculty of Arts and Sciences, Ahi Evran University, TR-40100 Kırşehir, Turkey*

**e-mail corresponding author*:aslidgn@gmail.com

Keywords: Geometric Morphometrics, Landmark, Systematic Biology

ABSTRACT

Geometric Morphometrics is a new analytical approach to comparison of digitized images from species. This technique provides biologists to test the relationship between morphological and molecular data and the evolutionary forces modeling of biological forms (e.g., size, shape, ecology and the effects of genetic drift on the rate of morphological evolution). The main advantage of geometric morphometrics data contain two- or three-dimensional which obtained from homologous landmarks. The procedure of geometric morphometrics starts with the defining landmarks of shape on species and then Generalized Procrustes Analysis (GPA) should perform to superimpose landmark configurations which is important procedure because it removes variation due to differences in translation, orientation, and size. After all this steps shape variations visualize with transformation grids using thin plate spline (TPS) algorithm to figure out deformations of average shape. Though geometric morphometics started to use in many biological species since ten years it recently started to use in archeological and paleontological remains. There are numerous studies on plant species and animalia species as mammals (especially rodents), fishes and insects in literatures via geometric morphometrics. As the main advantage of geometric morhpometric data is easy to analyze with multivariate statistic techniques and comparable with phylogenetic and ecological variables thus systematic biologist often started to apply. Up to now, we studied cranium, mandible, post cranial skeleton (scapula, humerus etc.) of blind mole rats. Having a big taxonomic complexity of many species we aimed to solve such problems the comparable data of geometric morphometrics.

1. INTRODUCTION

For organisms, the shape, together with being the most remarkable characteristic of the phenotype, has been utilized for hundreds of years in scientific studies due to its being able to establish the link between the genotype and the environment. The distinction between morphometric structures that are expressed in terms of shape and size is very important in biological researches, and morphometrics can simply be described as a quantitative way to refer in shape comparisons [1], [2]. The first known method of morphometrics is defined as "traditional" morphometrics and is based on the measurement of linear lengths. In addition to these lengths which can be expressed as length, height, and angle; also the ratios depending on the lengths or areas can be calculated. Although traditional morphometrics studies are relatively easy and cost efficient, there are certain disadvantages of it. The most important problem is that the linear distances usually are proportional to the sizes of the organisms studied; they do not contain information about the shape of the organisms. These data sets contain less information than expected because of many metrics' overlapping or being at the same direction. Since the various measurements are taken from a single point, they are not so independent from the others, so that, a small error at the location of this point affects many measurements. These data sets also contain less information than the effort spent, because some of the aspects may be unnecessarily measured and some may overlap. Overlapping measurements lead to confusion in defining localized shape changes, and the same results can be obtained from measurements from organisms with two different shape structures [2]. With all of these, it is not possible to graphically describe the measurements of the shape obtained by classical methods.

Approximately 20 years ago Rohlf and Marcus [3] announced a new methodology, which can be named as "revolution in morphometry", by evaluating these problems of traditional morphometry. The first foundations of the Geometric Morphometrics, which involves the geometrical presentation of classical analyses based on the sets of linear distances, and approaches that use the anatomical coordinates, were thus taken. The "Geometric Morphometrics" which is based on a mathematical foundation, reveals the diversity and morphological transformation caused by variation and shape analysis [2]. In many geometric morphometrics approaches, the Landmark Method (Procrustes Method) is the most widely used one; and the best understood part of this method is the mathematical and statistical features [4], [5].

The geometric morphometrics based on Landmark foundation, primarily begins with obtaining 2 or 3 dimensional coordinates of the landmarks that are defined as biological. Landmarks are homologous anatomical regions that are biologically significant and that provide shape description; and are reference points in the same plane that are reliable and repeatable with no changes in their topographical positions according to the other landmarks [2]. Since the results from this method are directly linked to the quality of the landmarks, it is important that evolutionarily significant landmarks are used and that the correct landmarks are identifiable. Each landmark have to be in all of the organisms that are being worked on; and if there is no landmark used even in one single organism being worked, it must be approximated or not used in any landmark. Due to the fact that extra landmarks may contain unnecessary information, the number of landmarks should be determined in a balanced manner, and they should not exceed the number of the samples studied. Bookstein [6] has classified landmarks into three categories according to the places used: Type I, Type II and Type III. Type I landmark is placed with a criterion based on homology. The Type I landmark is placed in certain areas, such as the tendons that are attached to the bones or the veins that merge in the insect wing. Type II landmarks are placed not only by biological but also by geometrical criteria. For example, like the dots at the extreme end of the contour line in the dental crowns of the rodents. Type III landmarks are defined only geometrically and are placed at the extreme end of the curve, such as the endpoints of a diameter. These landmarks that are located along the curve on the curve are called semi-landmarks.

The data obtained from landmarks contain many variations, arising from the position, orientation and scaling that do not reflect the shape of the organism. First of all, it is necessary to remove this variation that is not related to the shape and transform the variables into shape variables. Only in this way, the statistical comparisons and graphical representations can be made. The method used to eliminate the variation that is not related to the shape on the object is called "Superimposition Method" and there are different superimposition methods [7]. The most commonly used of these methods is the Generalized Procrustes Analysis (GPA) that overlays landmark configurations using the least squares calculation for reversing and rotation parameters. First, the centroids of each configuration are turned into origins. The configurations are scaled by a common unit size and the centroids are overlaid. Finally, configurations are rotated in the way that provides the lowest sum of the Euclidean distance squares between the landmarks [8]. This process continues until the average shape is obtained. After applying the GPA to all the samples, the coordinate differences of the responsible landmarks are calculated and the shape differences are revealed. The obtained data is used in multivariate statistical analyzes allowing the comparison of the shape variations. Alternatively, deformations of the shape are visualized by the "Thin Plate Spline" method. Thin Plate Splines are the maps that locate the reference points. They allow the comparison of reference points of an object or group with the other objects or groups. According to this method, deformation disturbances from an object to another object on the deformation grids are visualized and it is possible to determine where these defects are located.

2. RESULTS AND DISCUSSION

When the geometric morphometrics in biological researches are evaluated, we see that there are studies related to many groups of animals and plants in the literature. Many studies on fish, insects, and birds have important findings in explaining the phylogenetic relationships of species. Together with this, it is notable that researches with rodent groups are of particular interest. The analyses performed by using the dorsal, ventral and lateral images of the skulls of the Africa *Mastomys'* three sibling species have revealed the cross-species differences of shapes [9]. In the study carried out using the skull images of 71 populations of *Arvicanthis'* Africa, Sudan and Egypt was focused on the phylogenetic effects of biogeographic factors [10]. In the study that was conducted using two different types of cranial and dental characters of *Mus*, the

results of the comparison of traditional morphometrics and geometric morphometrics intra-species variations have been shown [11]. Swiderski [12] has tried to explain the allometric shape variations with geometric morphometrics by using the mandibles of different age groups of two *Sciurus niger* localities. By considering the environmental variables such as altitude, the average temperature, precipitation rate, the human population and vegetation, the geographical variations of *Thrichomys apereoides* were compared with images of mandible and cranium [13]. The shape variations of the tooth structures of 17 sub-species of *Microtus californicus* have been explained with geometric morphometrics, by taking the geographical features into consideration [14]. The differences between the age groups and sexual dimorphism of two geographically separate types: *Aethomys ineptus* and *Arvicanthis niloticus* are discussed in geometric morphometrics [15]. Geometric morphometrics studies on cranium and mandible of the *Marmots,* of which there's little information on the phylogenetic and morphologic evolution, have been the subject of many research, by being supported by ecological and molecular studies [16], [17], [18].

We also have carried out a series of studies regarding the blind mole rat, which is one of the rodent groups in Turkey, by starting from geometric morphometrics approach. We have performed geometric morphometrics applications on the skull, mandible and other skeletal structures of this species, which maintain the taxonomic problem due to the diversity of the number of their chromosomes (Figure 1).

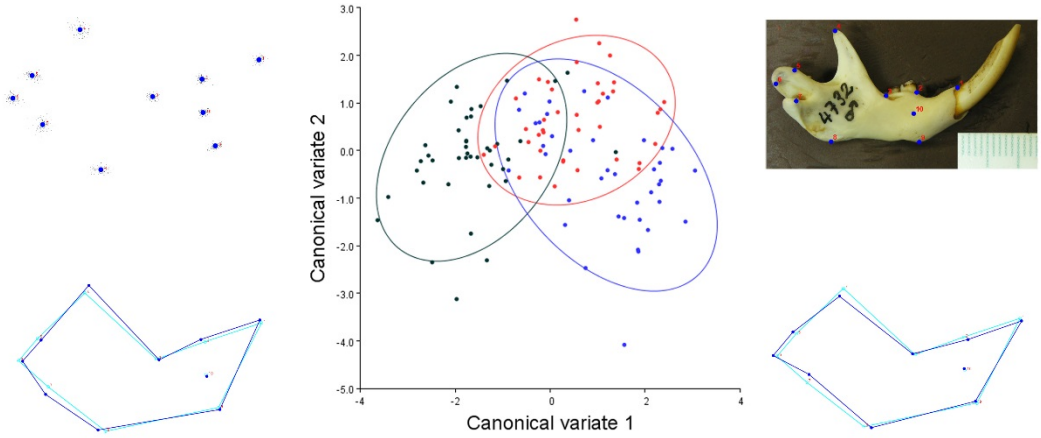

Figure 1. Graphical representation of Geometric Morphometrics protocol. Data from [19].

3. CONCLUSION

Although the geometric morphometrics is a method that can effectively identify the shape differences and has many applications and developing methods around the world, the studies in our country are very limited. The use of geometric morphometrics can be of great benefit while determining shape differences in systematic biology, rather than using expert views or traditional measurements. Although Geometrical Morphometrics is an effective method of comparing shapes, there are some limitations of it. The landmarks used may not always be sufficient to fully capture the shape of the object that is in use, thus, the outline method may need to be used. But the outline method, which only contains information about the external shape of the organism, does not provide information about the internal structure. There are especially limitations in studies of 3D data sets. With developing imaging systems and computer programming technology, it is expected that these problems will also be solved.

REFERENCES

[1] Pavlinov Y, *In: Information technologies in biodiversity research*. St.Petersburg, (2001), 41-64.
[2] Zelditch M L, Swiderski D L, Sheets H D and Fink W L, *Geometric morphometrics for biologists: a primer*, Elsevier, (2004), 1–400.
[3] Rohlf F.J., Marcus L.F., *A revolution in morphometrics*. Trends Ecol. Evol., (1993), 8, 129– 132.
[4] Bookstein F, *Combining the tools of geometric morphometrics,* Eds Marcus L., Corti M., Loy A., Slice D. Advances in morphometrics. N.Y.L. Plenum Press, (1996), 131–152.

[5] Dryden, I.L. and Mardia, K.V. *Statistical shape analysis*. John Wiley and Sons, New York, (1998), 347.
[6] Bookstein F L, *Morphometric tools for landmark data: geometry and biology.* Cambridge: Cambridge Univ. Press, (1991), 198.
[7] Adams, D.C., Rohlf, F.J. and Slice, D.E. *Geometric morphometrics: ten years of progress following the 'revolution'*. Ital. J. Zool., (2004), 71, 5-16.
[8] Rohlf, F.J. and Slice, D.E., *Extensions of the Procrustes method for the optimal superimposition of landmarks.* Syst. Zool., (1990), 39, 40-59.
[9] Lalis A, Evin A and Denys C, *Morphological identification of sibling species: the case of West African Mastomys (Rodentia: Muridae) in sympatry*. Comptes Rendus Biologies, (2009), 5, 480–488.
[10] Fadda C and Corti M, *Three-dimensional geometric morphometrics of Arvicanthis: implications for systematics and taxonomy*, J. Zool. Syst. Evol. Research, (2001), 39, 235–245.
[11] Macholan M, Mikula O and Vladimir V, *Geographic phenetic variation of two eastern-Mediterranean non-commensal mouse species, Mus macedonicus and M. cypriacus (Rodentia: Muridae) based on traditional and geometric approaches to morphometrics.* Zoologischer Anzeiger, (2007), 247, 67–80.
[12] Swiderski D L, *Morphological evolution of the scapula in tree squirrels, chipmunks, and ground squirrels (Sciuridae): an analysis using thin-plate splines*. Evolution, (1993), 47, 1854–1873
[13] Monteiro L R, Bonato V and dos Reis S F, *Evolutionary integration and morphological diversification in complex morphological structures: mandible shape divergence in spiny rats (Rodentia, Echimyidae),* Evolution and Development, (2005), 7(5), 429–439.
[14] McGuire J L, *Geometric morphometrics of vole (Microtus californicus) dentition as a new paleoclimate proxy: Shape change along geographic and climatic clines*. Quaternary International, (2010), 212, 198–205.
[15] Abdel-Rahman E H, Taylor P J, Contrafatto, G Lamb J M, Bloomer P and Chimimba C T, *Geometric craniometric analysis of sexual dimorphism and ontogeneticvariation: A case study based on two geographically disparate species, Aethomys ineptus from southern Africa and Arvicanthis niloticus from Sudan (Rodentia: Muridae).* Mamm. Biol., (2009), 74, 361-373.
[16] Cardini A, *The geometry of the marmot (Rodentia: Sciuridae) mandible: phylogeny and patterns of morphological evolution.* Syst. Biol., (2003), 2, 186-205.
[17] Cardini A and O'Higgins P, *Post-natal ontogeny of the mandible and ventral cranium in Marmota species (Rodentia, Sciuridae): allometry and phylogeny*. Zoomorphology, (2005), 124, 189–203
[18] Caumul R and Polly D, *Phylogenetic and Environmental Components of Morphological Variation: Skull, Mandible, and Molar Shape in Marmots (Marmota, Rodentia)*. Evolution, (2005), 59(11), 2460–2472
[19] Doğan, A., *Türkiye Nannospalax (Mammalia:Rodentia) Kromozomal Formlarında Scapula, Humerus ve mandibula Şekil Analizi.* Doktora Tezi. Zonguldak Karaelmas Üniv. , (2010).

Solar Power Potential of Kırşehir City

Dilek Ferudun[a]

[a]*Department of Geography, Faculty of Arts and Sciences, Ahi Evran University, TR-40100 Kırşehir, Turkey*

dilekferidun@gmail.com

Keywords: solar power, Kırşehir, potential, CORINE, GIS

ABSTRACT

Nowadays, energy sources have vital importance to support daily life due to ever growing world population and continous development in technology especially after the industrial revolution. Since energy sources such as oil, coal, lignite, etc have exhaustible properties, people have started to using renewable energy sources in other words inexhaustible energy sources one of which is solar power. Producing electricity by using solar power is becoming more common day by day in the world. As Turkey is located in between central/medium latitutes, it can be regarded as a lucky country with regard to solar power. Efficiency in solar power decreases from southern part to northern part in the country. Kırsehir is a city located in Central Anatolia, and its location is on the fourth place on account of sunshine duration. There is minor difference between its zone and three of which zones coming before it. When it comes to determine solar power potential of a region, it cannot be taken into account only sunshine duration of this region. On the contrary, a map of solar power potential is made by using all of the parameters such as topographic conditions, location, compatibility for placement of the solar panels, industry, distribution of agricultural areas. Purpose of the study to determine solar power potential and rate of sunshine of Kirsehir City. In this study, zones of Kırsehir which are convenient for the installation of solar panels are determined by using CORINE datas (2012) and Geographical Information Systems (GIS) software and by taking into account residential areas, industry, location, fertile farmland, green areas, distribution of water resources, direction of urban development.

1. INTRODUCTION

Requirement for energy have risen especially after industrial revolution (Küçükkalay M. A.,1997) and since it is noticed that energy sources exhaustible, people have started to use renewable energy sources (Dinçer F., 2011). There are lots of alternatives in terms of renewable energy sources. Solar energy is one of the most common used renewable energy types (Gevorkian P .,2011). The types of renewable energy are shown on table 1.

Table 1. Renewable Energy Sources and Sources of This Energy

Renewable Energy Sources	Source of Energy
Solar Power	Sun
Wind Power	Wind
Wave Power	Ocean and Seas
Biomass energy	Biological Wastes
Geothermal energy	Underground Waters
Hydraulic energy	Rivers
Hydrogen energy	Water and Hydroxides

Solar Power Systems are used for different purposes, and these are: producing electricity directly from sunlight (photovoltaic systems), to heat water by solar energy (solar hot water), using the sun's heat to produce electricity (solar electricity), using solar energy to heat and light buildings (passive solar heating and daylighting), industrial and commercial uses of the sun's heat (solar process space heating and cooling). According to the records, used solar energy capacity in the world has been increasing steadily from 2004 (figure 1). Turkey comes on third row in terms of the benefiting from solar energy capacity in the world (figure 1), and Kirsehir comes on forth row in terms of solar energy capacity in Turkey (figure 2).

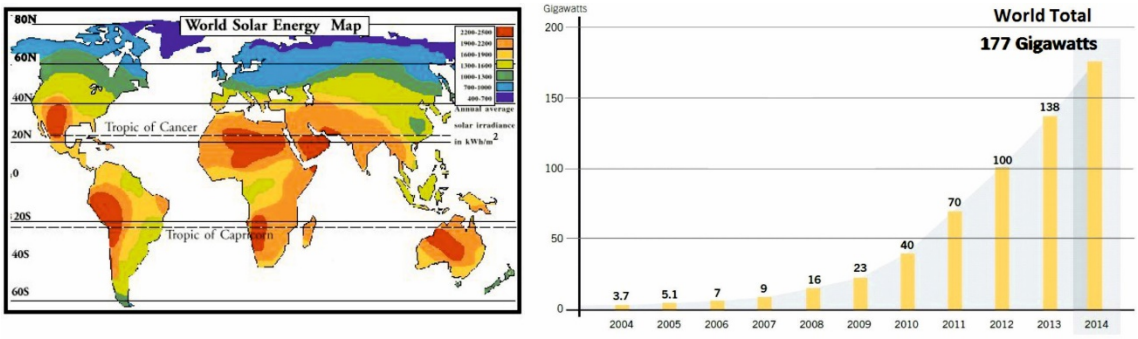

Figure 1. Solar Energy Capacity and Its Usage in the World (Source: http://sites.uci.edu/energyobserver) and changing between 2004 and 2014 (Renewables Global Status Report 2014, UNEP, France).

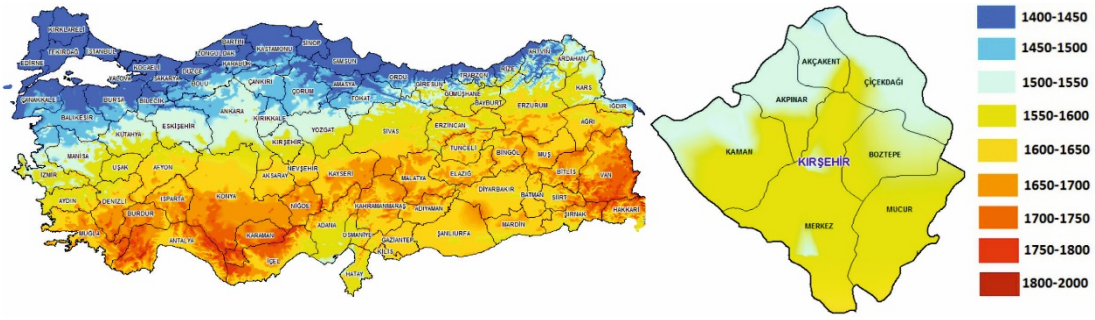

Figure 2. Annual solar radiation of Turkey and Kırşehir-Total solar radiation KWh/m^2-year Source: www.enerjiatlası.com)

Turkey is a lucky country in terms of benefiting from solar energy when compared to the northern countries. When solar radiation numbers are taken into account, two thirds of the nations are able to benefit highly from solar energy. Solar energy is used widely to heat water in Turkey. Especially in 2013, huge investments were made into heating water by using solar power. In terms of the usage of solar energy for heating water, Turkey constitutes of 3 percent of total usage in the world, and China comes first in terms of the total usage with 70 percent within this category. Countries coming after China are USA with 4.5 percent, Germany with 3.3 percent and Turkey with 2.9 percent (Renewables 2014 Global Status Report, UNEP).

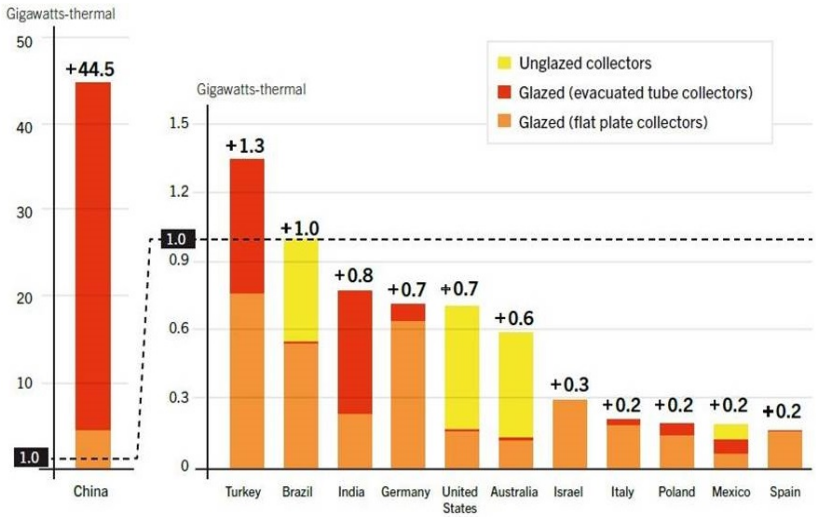

Figure 3. Solar water heating collectors additions,top 12 countries for capacity added 2013 (Source: Renewables 2014-Global Status Report, UNEP, France).

Purpose of this study is to determine solar power potential and rate of sunshine of Kirsehir City. Also, convenient areas for installation of solar energy farms and panels are determined in this study. For this purpose, CORINE (Coordination of Information on the Environment) data sets belonging to 2012 year and GIS (Geographical Information Systems 10.3.1 version) software are used. Farm lands, residential areas and industrial areas are taken into account while making determinations.

2. RESULTS AND DISCUSSION

Central district of Kirsehir has 1550-1600 KWh/m2 solar radiation value annually. To detect areas convenient for solar energy farm installation, maps of residential areas and wild life areas are produced (figure 4).

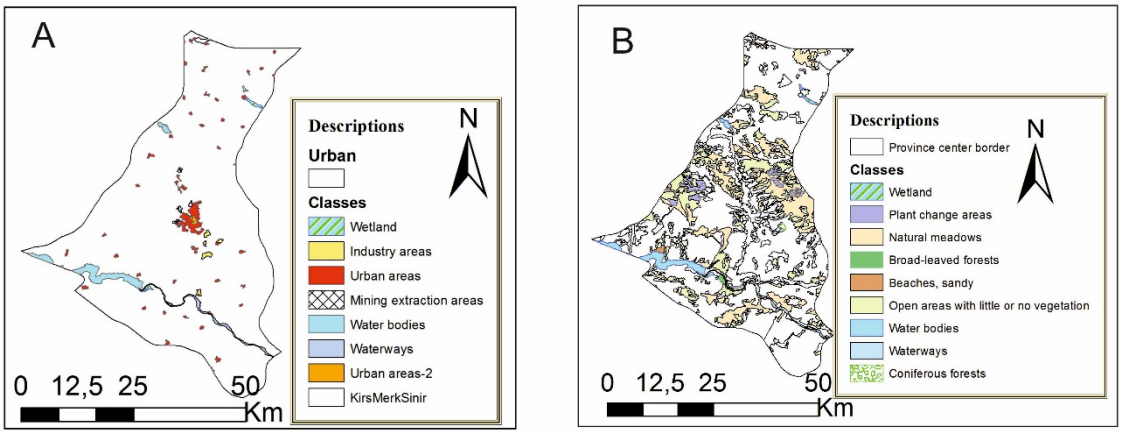

Figure 4. Maps of Central district of Kirsehir : A: Urban Areas B: Wild life Areas. It is produced by using (CORINE 2012) data sets.

Urban areas-2 shows interrupted settlements while urban areas show uninterrupted settlements in terms of residential areas (Figure 4-A). In this map, water areas are shown since they are not convenient for settlement and commercial usage. In Figure 4-B, wild life areas which are free from settlements and urban fabric are shown. This areas constitute the areas which needs to be protected by the officials. Of these areas, open areas with little or no vegetation can be used for the activities determined since they are convenient for field study and pose no harm to natural balance.

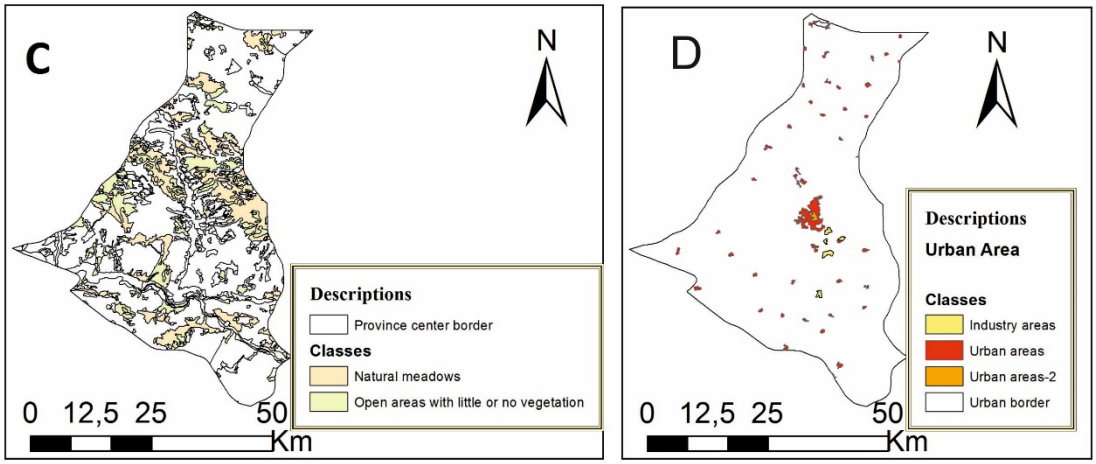

Figure 5. Areas convenient for solar panels C: Convenient areas for Solar power plants D: Convenient areas for roof solar panels

Areas convenient for solar power panels can be divided into two categories (figure 5) one of which is solar power plants which can be installed on wide areas and the other is solar panels which can be installed only

on rooftops. In Kirsehir, almost every building (if not all) has a rooftop, so there is a convenient area for each building. Additionally, areas having little or no plant cover are very convenient for the installation of solar power plants.

3. CONCLUSION

Turkey is a middle latitude country, and due to this fact that the level of utilization from solar energy decreases from south to north. Kirsehir is located on the central part of Turkey, and its location can be considered well in terms of utilization from solar energy (annually 1550-1600 KWh/m2)

Areas which are convenient for solar panel installation are determined by using CORINE 2012 data sets. During this determination, water bodies, broad-leaved forests, plant change areas and wetlands are not taken into account since they are not eligible for panel installation.

Kirsehir is a very convenient city for solar panel installation not only for industrial sector but also for residential area. While making maps of convenient areas for solar power plants, empty areas, residential areas and grasslands are taken into account. There are lots of uncultivated lands, and these lands are not suitable for agriculture since they lack of plant cover on a large scale. It is considered as one of the most convenient options to use these areas for installation of solar power plants in terms of energy politics of the city and strategic terrain usage. Solar energy can be used for heating water, lighting, heating-cooling and producing electricity.

To determine the areas which are convenient for solar power plant installation as correct as possible, it is needed to determine the direction of urban development correctly and city grow should be in harmony with the city planning.

It is believed that this study will be very useful for solar power plant installation, and set an example for similar studies.

REFERENCES

[1] Dinçer F., Türkiye'de Güneş Enerjisinden Elektrik Üretimi Potansiyeli - Ekonomik Analizi ve AB Ülkeleri ile Karşılaştırmalı Değerlendirme, KSU Mühendislik Dergisi, 14(1), (2011).
[2] Gevorkian P., Large-Scale Solar Power System Design, ISBN: 0071763279 (2011).
[3] Küçükkalay M.A., Endüstri Devrimi ve Ekonomik Sonuçlarının Analizi, Süleyman Demirel Üniversitesi İktisadi ve İdari Bilimler Fakültesi Dergisi, 51-68,(1997).
[4] Renewables Global Status Report (2014), UNEP, France.
[5] http://sites.uci.edu/energyobserver

Comparison of Mobile Application, Mobile Site and Responsive Web Site in Web Site Design

Emrah Aydemir

[a]*Department of Computer Tecnology, Technical Sciences and Vocational Schools, Ahi Evran University, TR-40100 Kırşehir, Turkey*

ABSTRACT

This research was conducted to give an idea about which systems would be preferable to mobile systems, which is an indispensable element of today when institutions and organizations want to make websites. The research has been conducted independently of the browsers, revealing the properties of mobile applications, mobile web sites and flexible sites that are now being used effectively and comparing them with each other. After the examinations and comparisons made, a situation assessment was made rather than a definite judgement, and the advantages and disadvantages of each system were presented. This study will give an idea about which systems to use to those who will build websites or will have websites built.

1. INTRODUCTION

Certainly, the devices that provide wireless communication are the most affected by the rapid development of technology. The very first of these devices are smartphones and tablets, which have started to be adopted by a large majority of the world. The fact that tablet computer sales increased to the value of 256.3 million in 2014 from 206.8 million the previous year, and mobile phone sales reached the value of 1862.8 billion in 2014, from 1807 billion the previous year supports this idea [1]. The rapid development of mobile technology in this way has made it necessary, rather than an advantage, for companies that want to compete strongly to offer mobile services. Since it is not imaginable anymore not to use internet shopping sites, news sites, banking services, air, land or sea transportation services at home, it has made us more selective in terms of these services. For this reason, such mobile services should offer maximum convenience to the users to be preferred.

Today's mobile services need to be organized according to the characteristics of the devices, rather than being a simple and small form of applications in the computer environment. Mobile services are thus assessed within their own context. These services vary with various parameters ranging from the collection of the required data to the amount and presentation of the information presented to the user. These differences require that the interface components be customized and developed specifically for mobile use during the development of mobile services [2]. For this reason, mobile applications and web sites have been examined and compared in this study.

Mobile Applications

These are programs developed for mobile devices and using the programming language required by that environment for each environment. As each environment, device and programming language have different characteristics from each other, they require different expertise and dynamics [3]. The most common ones among mobile platforms can be considered;

- Android
- iOS
- BlackBerry

- Symbian
- Windows
- webOS
- MeeGo
- and bada.

Features of mobile applications can be listed as follows. [4].

Mobile Application Features

- Phone owners with an application market can be reached.
- There is always the possibility of interaction with the users, and instant data exchange possibility.
- There is also the possibility to work without internet connection when necessary.
- There is a need to develop software specific to each operating system.
- Access to the application is implicit, and it must be downloaded from the application market, or a setup file must be provided from another location.
- It is difficult to update applications, requiring separate effort for each platform.
- Applications can be deleted from the phone by the user.
- It is very difficult to attract organic traffic to application. It does not provide a positive contribution to the main site.
- Applications are highly efficient for regular use.
- With the applications, much more user data can be obtained.
- Mobile applications are flexible, allowing for more innovative work.
- A serious mobile application budget is needed for each platform separately.

Web Sites

Web sites can be viewed from both computer browsers and mobile browsers. It is possible to group Web sites under four categories [5].

Responsive Web Sites

Such web sites have different page layouts for different resolutions. If the area where the site is viewed is reduced or enlarged by holding from the lower or upper right corner of the browser, it can be seen that the page layout gets changed. During this change, the transition between the different page layouts appears to be softer and more fluid. The media and content items within the page layout vary depending on the viewing area of the browser. Definitions of this design and software approach, which is more satisfying for users [10], can be created with adaptive design and liquid design. Responsive website design is the latest content visualization approach in the expanding range of devices and operating systems [9].

Adaptive Web Sites

Adaptive-type interfaces have different page layouts for different resolutions. If the area in which the browser is viewed is tried to be reduced or enlarged, the page layout will not change. However, if the area in which the site is viewed reaches a resolution scale defined by the team that has prepared the site, then the page layout within the viewing area changes and adapts itself to the new resolution.

Fluid / Liquid Web Sites

Content and media elements in page layouts that are prepared as liquid vary in width values depending on the viewing area of the browser, but these contents do not show variations such as crossing from left to down or from right to down. For this reason, if you view at a resolution other than the defined page scales, the page layout will disrupt.

Static Web Sites

Such websites do not vary depending on the situation. Whatever your screen resolution, they will always remain static. When you open it with any one of your smartphone, tablet or computer, you will always see the same page layout, but you will find scroll bars that you need to scroll right or left or up and down.

Mobile Site

These are the web sites prepared according to the designs by applying the features of responsive and adaptive web sites mentioned above, completely taking the mobile devices into consideration and ignoring the high resolutions of the laptop and computers. These sites must be responsive in themselves. Designs are usually based on devices with the smallest resolution. When the normal web site name is written to the browser to reach these web sites, if the resolution of the device is below the resolution defined as mobile device, it is automatically redirected to another web page. For example, when https://www.flypgs.com is opened on the computer, the normal site is opened, but when it is opened on mobile devices, it is immediately directed to another site, https://mobile.flypgs.com. These two websites are created completely independent of each other.

When comparing the systems shown here, it is thought that it is more understandable to see the advantages and disadvantages on the table below [6, 7].

Table 1. Advantages and disadvantages of mobile application, mobile site and responsive site

	Advantages	Disadvantages
Mobile Apps	• More advantageous than other options in terms of user experience • Can be used without internet connection, information is always available • Fast and fluid use • Innovative • Use after only one download • Can send an announcement with instant message to users • Can obtain detailed information about users	• Accessibility from all devices is less than others • The necessity of re-approving every update made by the market • Users not happy with frequent updates • The most expensive solution compared to others • Users being able to delete if they do not like • Difficulty in attracting organic traffic to the application • Separate operation for each operating system
Mobile Site	• Convenient and easy user experience, optimized for every mobile screen • Fast and easy access on all mobile platforms as specially designed for mobile • Not as costly as responsive but a cheaper way considering its advantages • Easier to attract organic traffic than mobile application • Opens in every operating system and does not require a separate effort.	• Can not be accessed without the Internet. • Can not reach to users unless they want to • Difficulty in obtaining detailed data about the user • Creating more costs • Two different URLs for the mobile site • In case of redirecting, slightly reduced page opening speed • Having to manage two different sites • Some difficulty in analyzing the data • Difficulty for a single website to work on every screen in the same way and existence of some deficiencies
Responsive (Mobile Compatible) Site	• Access to contacts on every device and browser • Easy to apply • With responsive design, a single site is optimized for all screens. • Managing a single site for all devices offers much more convenience as a site administrator • Not having to redirect users and rapid opening speed thanks to only on URL • Not having to create separate content, and SEO settings working as effectively on mobile as desktop computers • Marketing budget usage for a single website • Less work and less money on a single web site than two web sites	• Unable to reach users without internet • Can not reach to users unless they want to • Slightly slow loading of pages on mobile devices • Not compatible to work on old devices on which older browsers are installed because of responsive web sites being a new technology • While trying to satisfy both the mobile and the desktop user, not being able to provide full satisfaction for both

2. RESULTS AND DISCUSSION

In general, content and services will have an impact when the choice is made between mobile site, mobile application and responsive site. For more general topics, web sites can be browsed on mobile browsers while mobile applications can be preferred for more specialized works and personalization. Mobile web sites or responsive sites will continue to be indispensable because they can be developed once and used on different devices and platforms. Use of mobile sites or mobile-compatible sites can be appropriate in sites that focus on contents like news, shopping and entertainment or that serve as corporate information and blog, along with the benefits of search optimization. It has been verified that mobile applications are a powerful promotional tool for business organizations and increase the number of users. It appears that users are using applications in the roles of administrator, distributor, and other user [8]. All together, it should be taken into consideration how difficult it is to find local mobile application developers in our country, and that these experts work on large budget projects or private GSM companies with hourly wages [3]. In the light of all these discussions, hybrid solutions combining the advantages of both will reach to us [11].

Mobile-compatible responsive web sites may be preferred by people who do not want to use and manage two different websites. However, organizations which can analyze the different data, which have a professional team, and which can afford extra cost, may prefer mobile sites. If a lot of design updates are not aimed on websites, it may be preferable to choose responsive (flexible / mobile compatible) website design. This option is a good choice for small and simple websites, and it will also make web addresses easier. Choosing an independent mobile website may be a better option for web sites that are intended to update in design or add new items. While it is good choice in large and complex websites, this option can provide a more optimal user experience if some certain devices are aimed.

REFERENCES

[1] GARTNER, Gartner says worldwide traditional pc, tablet, ultramobile and mobile phone shipments to grow 4.2 percent in 2014, *Gartner*, **2016**. http://www.gartner.com/newsroom/id/2791017, Erişim tarihi: 24.09.2016.

[2] NAMLI, Çiğdem. *Mobil uygulama kullanılabilirliğinin değerlendirilmesi*. Yüksek Lisans Tezi. Fen Bilimleri Enstitüsü, **2010**.

[3] KESKİN, Nilgün ÖZDAMAR; KILINÇ, Hakan. Mobil öğrenme uygulamalarına yönelik geliştirme platformlarının karşılaştırılması ve örnek uygulamalar. *Açıköğretim Uygulamaları ve Araştırmaları Dergisi*, **2015**, 1.3.

[4] ERSOY, Fırat, Mobil Site&Mobil Uygulama Savaşının Galibi Sizce Kim?, http://www.firatersoy.com/mobil-site-mobil-uygulama-karsilastirma, **2015**, Erişim Tarihi: 24.09.2016.

[5] BAYRAK, Yakup. Responsive mi olsun yoksa Adaptive mi tartışmasına son…, http://blog.designedbysherpa.com/2014/04/responsive-mi-olsun-yoksa-adaptive-mi-tartismasina-son, **2014**, Erişim Tarihi: 24.09.2016.

[6] KONU, Selin, Responsive Web Sitesi Mi Mobil Web Sitesi Mi Mobil Aplikasyon Mu?, https://www.linkedin.com/pulse/20141124154323-203582692-responsive-web-sitesi-mi-mobil-web-sitesi-mi-mobil-aplikasyon-mu, **2014**, Erişim Tarihi: 25.09.2016.

[7] DOĞAN, Leyla, Mobil Uyumlu Site mi? Mobil Site mi? Mobil Uygulama mı?, http://www.corneadigital.com/blog/mobil-uyumlu-site-mi-mobil-site-mi-mobil-uygulama-mi, **2015**, Erişim Tarihi: 25.09.2016.

[8] PAJNİC, Goran, DAVOR Bosnjakovic, and IVAN Kelic. "The Potential Of Mobile Applicationsin Organization And Promotion." Interdisciplinary Management Research, **2014**, 10: 296-303.

[9] ALİCAN, Özgür, Esnek Web (Responsive Web) Sitesi Tasarımında Tipografi Sorunları, Yedi: Sanat, Tasarım ve Bilim Dergisi, **2014**, Yaz (12), 85-91.

[10] Gardner, Brett S. Responsive web design: Enriching the user experience. Sigma Journal: Inside the Digital Ecosystem, **2011**, 11(1), 13-19.

[11] CHARLAND, Andre; LEROUX, Brian. Mobile application development: web vs. native. Communications of the ACM, **2011**, 54.5: 49-53.

Examination of Internet Usage of Vocational School Students for Obtaining Information

Emrah Aydemir[a], Salih Ermiş[b]

[a]*Department of Computer Tecnology, Technical Sciences and Vocational Schools, Ahi Evran University, TR-40100 Kırşehir, Turkey*
[b]*Department of Electronics and Automation, Technical Sciences and Vocational Schools, Ahi Evran University, TR-40100 Kırşehir, Turkey*

Abstract:
This study was conducted to examine the pre-exam internet usage of Ahi Evran University Vocational School students while they learnt the information about in which hall they were going to take examination. In the study, in addition to examining whether the students use their own mobile internet or their friends' mobile internet while accessing the internet, which system, which browsers and which software they use while reaching the internet were also examined. The analysis of the data is done considering the age, gender and departmental differences of the students. With this study, it is thought that the systems to be made to the students will give an idea about the construction of information systems by considering these data.

Introduction

Today, the internet has entered into every field of our life, has been made easy to use by everyone and has become an integral part of life. The Internet has become a powerful reference tool that enables many information and goals to be realized. Particularly young people spend a significant part of their time with the activities done on the internet. The use of the internet among young people is very common for reasons such as having fun, communicating, entering networking sites, playing games, doing research, obtaining information, and doing homework [1-2]. With the rapid development of communication and computer technology in the last years, the internet has become indispensable in meeting all kinds of daily needs of people [4]. Computer and internet usage rates were 54.8% and 55.9% respectively in the 16-74 age group in April, 2015. These rates were 64% and 65.8% for males and 45.6% and 46.1% for females. Computer and internet usage rates were 53.5% and 53.8% in 2014 [3]. In this study, an information access interface was established on the internet for the students in Vocational School to learn exam rooms and places for mid-term, final and makeup exams. Through this system, students' internet usage habits were examined according to criteria such as age, sex, class, department.

A Model Application for Internet Use for Obtaining Information

In this study, a mobile-compatible website on which students from Ahi Evran University Vocational School of Technical Sciences would be able to learn their rooms and seats in midterm exams, final exams and make-up exams was created. Students who enter the website have access to the examination place information about the exam they are going to take when they enter their student numbers.

Method

Accelerating developments in technology accelerates the access to desired information and access to technologies that facilitate life. Getting the tools that provide all these is also becoming easier at the same rate and becoming a part of life. The university students, who are the target masses of the study, are open to innovations and they also focus on smartphone use as a mean of communication [5]. The aim of the research is to determine the internet use status of the vocational school students in obtaining information. In this context, a mobile-compatible website on which students can learn their place and seat in the midterm, final and make-up exams was created. The access records of the students to this system have been collected and various analyzes have been applied and the data has been presented in tables and graphics in the study. The research was applied to students who were studying at Kırşehir Ahi Evran University Vocational High

School during the 2015-2016 academic year. There are 6 departments and 12 programs in the Vocational School. Information such as the type of device, activity date, IP address, browser used, version of the browser, how many minutes before the exam the system was accessed, whether the page can be opened or not was recorded when a total of 725 students access this system. In addition to all these data, the personal information of the students was obtained from the department of student affairs and they were matched with the analyzes made.

Findings

The data are based on the departments and programs of the students. When the number of students is examined by gender, it is seen that female students are fewer. The largest number of female students are found in the Department of Computer Technology and the smallest number of female students are in the Department of Handicrafts and Plant and Animal Breeding. Departments, programs and student numbers by gender are listed in the following table.

Table 1 Department and program names and number of students within the Vocational School

Departments and Programs	Mr	Mrs	Grand Total
Computer Technologies	**120**	**46**	**166**
Computer Programming	57	31	88
Computer Programming (Evening Education)	60	15	75
Computer Technology	3		3
Plant and Animal Breeding	**33**	**12**	**44**
Organic Farming	27	8	35
Greenhouse	2		2
Medical and Aromatic Plants	3	4	7
Handicrafts		**1**	**1**
Trad. **Handicrafts (Evening Education)**		1	1
Electricity and Energy	**157**	**1**	**158**
Electricity	117		117
Electricity (Evening Education)	40	1	41
Electronics and Automation	**91**		**91**
Mechatronics	91		91
Construction	**228**	**37**	**285**
Construction Technology	131	22	153
Construction Technology (Evening Education)	97	15	112
Grand Total	**628**	**97**	**725**

There are partial differences between the classes in Vocational High School students who are first and second grade students. The number of first grade students in Computer Technologies department is 90 while the number of second grade students is 76. The numbers in the related department and program are given in the table below.

Table 2 Grade status of students according to departments and programs

Departments and Programs	1. Grade	2 Grade	Grand Total
Computer Technologies	**90**	**76**	**166**
Computer Programming	46	42	88
Computer Programming (Evening Education)	42	33	75
Computer Technology	2	1	3
Plant and Animal Breeding	**23**	**21**	**44**
Organic Farming	15	20	35
Greenhouse	2		2
Medical and Aromatic Plants	6	1	7
Handicrafts	**1**		**1**
Trad. **Handicrafts (Evening Education)**	1		1
Electricity and Energy	**85**	**73**	**158**
Electricity	62	55	117
Electricity (Evening Education)	23	18	41
Electronics and Automation	**58**	**33**	**91**
Mechatronics	58	33	91
Construction	**118**	**147**	**285**
Construction Technology	78	75	153
Construction Technology (Evening Education)	40	72	112
Grand Total	**375**	**350**	**725**

The age of the students ranges from 18 to 53 years. The average age is 21.18. The most number of students over the age of 26 is in the Construction department. The least number is in Electronics and Automotive departments and Computer Technology departments. The ages and department-programs of the students are listed in the following table.

Table 3 Age distribution of students according to departments and programs

Departments and Programs	18	19	20	21	22	23	24	25	Between 26-53	Grand Total
Computer Technologies	**2**	**31**	**61**	**33**	**10**	**11**	**3**	**7**	**8**	**166**
Computer Programming	1	21	41	12	4	3	1	2	3	88
Computer Programming (Evening Education)	1	10	18	20	6	8	2	5	5	75
Computer Technology			2	1						3
Plant and Animal Breeding	**1**	**5**	**7**	**5**	**4**	**2**	**5**	**2**	**13**	**44**
Organic Farming	1	4	6	4	4	2	3	2	9	35
Greenhouse									2	2
Medical and Arom Plant (Boztepe)		1	1	1			2		2	7
Handicrafts									**1**	**1**
Trad. **Handicrafts (Evening Education)**									1	1
Electricity and Energy	**5**	**42**	**38**	**39**	**17**	**3**	**1**	**2**	**11**	**158**
Electricity	4	38	30	29	9	2			5	117
Electricity (Evening Education)	1	4	8	10	8	1	1	2	6	41
Electronics and Automation	**1**	**17**	**29**	**22**	**10**	**4**	**1**		**7**	**91**
Mechatronics	1	17	29	22	10	4	1		7	91
Construction	**1**	**27**	**60**	**75**	**46**	**17**	**11**	**6**	**22**	**285**
Construction Technology		17	35	43	24	10	7	4	13	153
Construction Technology (Evening Education)	1	10	25	33	22	7	4	2	9	112
Grand Total	**10**	**122**	195	174	**87**	**37**	**21**	**17**	**62**	**725**

A total of 17,082 entry attempts were made to the system. In these attempts, 11,991 had a successful entry and viewed the exam place information, but 921 could not access the information and received errors as they entered student numbers incorrectly. Information is allowed to be displayed 15 minutes before the examination. Nevertheless, 4162 entry attempts were conducted before the time allowed. In addition, 8 students tried to view their information even though they were not entitled to take exams because of having received disciplinary penalties. Below is a table summarizing this situation.

Table 4 System entry attempts and results

Entry Type	Number
Successful Entry	11991
Miswriting of Student Number	921
Entries of students with disciplinary penalty	8
Entries before authorized time	4162
Grand Total	17082

Although students could access the exam information through the system 15 minutes before the exam time, many students tried to view the information even though they knew that there was a long time until they could. The information was tried to be viewed mainly between 18 and 30 minutes before the exam time but failed. It is also seen that some students made attempts between 51 and 4000 minutes before the exam. The number of entry attempts reached the top at 15 minutes left, which is the certain opening time of the system, and they declined from high values at 14 minutes left and 13 minutes left. Student entry attempts to the system are shown in the following graph according to time intervals.

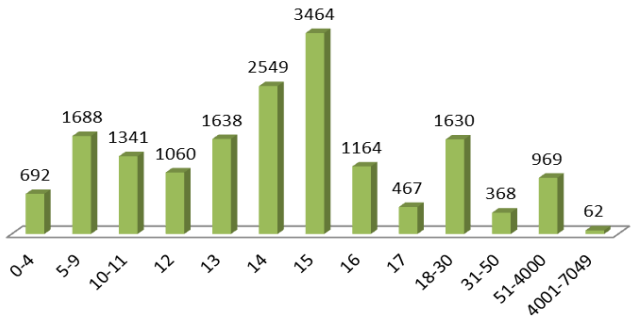

Figure 2 Entry attempts of student into the system according to time intervals

The IP addresses of students were recorded during information viewing and course-based analysis is performed. In addition to English and Turkish language, the exams of Ataturk's Principles and Revolution History courses are taken by all students. For this reason, the information of these courses were taken into consideration in order to analyze from how many devices the entries of the students were made. When the English exam information was viewed, 277 of the 475 students used the device of another person. The number of singular device is 189 in Turkish Language exam, which is the most crowded with 535 students. Similarly, in Ataturk's Principles and Revolution History, there is a 32,38% singular device.

Table 5 Repetition of IP values according to classes

IP values / Course Names	English	Turkish Language	Ataturk's Principles and Revolution History
Repeating IP	277	346	355
Singular IP	198	189	170
Total	475	535	525
Singular Device Ratio	% 41,68	% 35,32	% 32,38

The browsers of the devices used by the students were recorded and in the analyzes made, it was seen that the most number of browsers from 8 different browsers were Chrome with 12.243 entries. Afterwards, the largest number of entries were made with Safari with 3.086 entries. The fewest enties are done with IE and Opera browser. The browsers used by the students while accessing the system and their numbers are given below.

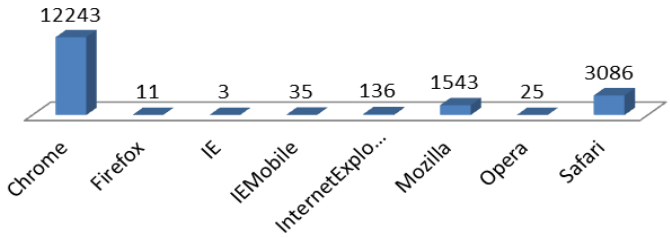

Figure 3 Browsers Used by Students and Entry Numbers

When the version numbers of the browsers used while accessing the system are examined, it is seen that version 50.0 is the most used for Chrome and students mostly uses the versions between 30.0 and 51.0. For the Safari browser, version 9.0 is the most used while versions 7.0 and 8.0 are also used.

Discussion and Conclusion

Through this study, students' access to information has been made online and their access data has been recorded. The records reviewed provide information on student access to information. It seems that students generally use the latest versions of browsers or versions that are close to the latest. It can be said that some browsers are more interested in than others. Even though the students did know what the results they would get while writing the information to access to information, they were still trying to see that result. This situation is considered as a step with the possibility that the students might get a different answer. Similarly, some students did not have the right to take exams because of the disciplinary penalty, but they still tried to access the exam location information. Likewise, although it was known that the information would not be viewed until 15 minutes before the exam time, some entry attempts were made maybe because of clock setting difference or maybe because of the idea that system could allow. However, during the first minute when system was allowed to be entered, students viewed their information intensively. The next majority were between 5 and 9 minutes left. It is thought that this could be because classroom doors were opened 5 minutes before the exam. When the students' access to information on mobile devices or other devices is examined, it is seen that the students accessed the information on the device used by the other half. It is thought that this may be because the devices used by students did not have internet, their batteries died or had low levels, and the students requested from other students to check their information as well since they already opened that page. However, there are no complaints or opinions to draw attention from the students despite low singular use and all other reasons. It is definitely important to take the emotions and thoughts of the students about their views on digital environments in accessing such information as the research done is quantitative. For this reason, we have the idea that it will be useful to perform qualitative data analysis in similar studies to be done in the future and to compare it with this research.

References

1- Li S-M, Chung T-M. Internet function and Internet addictive behavior. Comput Human Behav 2006; 22:1067-1071.
2- Subrahmanyam K, Greenfield P. Online communication and adolescent relationships. Future Child 2008; 18:119-146.
3- TÜİK. Hane Halkı Bilişim Teknolojileri Kullanım Araştırması, 2015 http://www.tuik.gov.tr/
4- Canbek G, Sağıroğlu Ş. Çocukların ve gençlerin bilgisayar ve internet güvenliği. Politeknik Dergisi. 2007; 10: 33–39.
5- ÇAKIR, F., & DEMİR, N. (2014). Üniversite öğrencilerinin akıllı telefon satın alma tercihlerini belirlemeye yönelik bir araştırma. *Dokuz Eylül Üniversitesi İktisadi ve İdari Bilimler Fakültesi Dergisi*, 29 (1): 213-243.

The Mechanical Properties of ZrSbTe and HfSbTe Compounds

Engin Deligöz[a], Hacı Özışık[b], Havva Boğaz Özışık[a]

[a]*Department of Physics, Aksaray University, TR-68100 Aksaray, Turkey*
[b]*BOTE Department, Aksaray University, TR-68100 Aksaray, Turkey*

**e-mail corresponding author*: *edeligoz@yahoo.com*

Keywords: ZrSbte, HfSbTe, Mechanical Properties

ABSTRACT

By means of first principles calculations, we have studied the structural and mechanical properties of the ZrSbTe and HfSbTe compounds. The elastic constants of these compounds are calculated, then bulk modulus, shear modulus, Young's modulus, Possion's ratio and Debye temperature of polycrystalline aggregates have been derived and relevant mechanical properties are discussed. We have found that these compounds have mechanically stable.

1. INTRODUCTION

Thermoelectric materials have acquired increased attention by researchers around the globe owing to the unique capability of such materials to convert heat directly into electricity [1, 2]. As known, these materials have been considered for many important applications from clean energy to photon sensing devices. An important criterion of a suitable thermoelectric is that it should be a semiconductor with a narrow band gap [2, 3].

The best materials for thermoelectric devices at or below room temperature are alloys of bismuth, antimony, and tellurium [4]. Therefore, the ternary antimonides and tellurium have been investigated for their potential use as thermoelectric materials [5–7]. Recently, Soheilnia et al. [8] have synthesized two new antimonide-tellurides which ZrSbTe and HfSbTe compounds. They have reported that these compounds are metallic conductors with a small Seebeck coefficient.

The present work is devoted to the mechanical properties of the ZrSbTe and HfSbTe compounds, using the density functional theory (DFT). Specifically, we address their bulk modulus, shear modulus, Young's modulus, Possion's ratio, Debye temperature. But until now, to our best knowledge, no systematic research has been reported these properties of ZrSbTe and HfSbTe compounds.

2. COMPUTATIONAL METHODS

Our calculations are performed within the framework of the density functional theory (DFT) using the projector augmented wave (PAW) method [9] as implemented in the Vienna ab initio Simulation Package (VASP) [10]. The exchange and correlation are treated within the generalized gradient approximation using the parametrization obtained by Perdew, Ernzerhof and Burke (GGA-PBE) [11]. We used a kinetic energy cutoff of 500 eV for plane-wave expansion of the PAWs. Brillouin-zone sampling has done in the Monkhorst-Pack [12] scheme with a k-point mesh of 8 × 6 × 4 for all compounds.

3. RESULTS AND DISCUSSION

ZrSbTe and HfSbTe crystallize in the orthorhombic structure (space group *Immm*, *NbPS*-type, *Z=4*). We have fully relaxed the cell volume and the ionic positions of atoms in reciprocal coordinates which are

supported by VASP code [9, 10] for these compounds, we have used these relaxed parameters. The calculated lattice parameters are presented in Table 1. It is seen that the present lattice parameters for ZrSbTe and HfSbTe compounds are in good agreement with the experimental values [8].

Table 1. Calculated equilibrium lattice parameters (*a*, b, and *c* in Å) along with the available experimental

Materials	***a***	***b***	***c***	**Refs.**
ZrSbTe	3.916	5.822	13.668	Present
	3.911	5.805	13.463	Exp. [8]
HfSbTe	3.909	5.804	13.517	Present
	3.867	5.7511	13.442	Exp. [8]

The present elastic constants are obtained from the strain-stress relationship [13], and the findings are given in Table 2. For a stable orthorhombic structure, its nine independent elastic constants should satisfy the well-known Born stability criteria [14] $C_{11}>0$, $C_{22}>0$, $C_{33}>0$, $C_{44}>0$, $C_{55}>0$, $C_{66}>0$, $[C_{11}+C_{22}+C_{33}+2(C_{12}+C_{13}+C_{23})]>0$, $(C_{11}+C_{22}-2C_{12})>0$, $(C_{11}+C_{33}-2C_{13})>0$, and $(C_{22}+C_{33}-2C_{23})>0$. Clearly, the calculated elastic constants satisfy the Born stability criteria for considered structures, suggesting that these compounds are mechanically stable.

Table 2. The calculated elastic constants (C_{ij} in GPa).

Materials	C_{11}	C_{12}	C_{13}	C_{22}	C_{23}	C_{33}	C_{44}	C_{55}	C_{66}	**Refs.**
ZrSbTe	127.2	25.0	72.7	203.6	33.1	133.4	50.6	85.3	46.1	Present
HfSbTe	134.4	26.5	77.1	206.3	35.1	141.6	51.4	88.3	46.1	Present

Clearly, the calculated elastic constants satisfy the Born stability criteria, suggesting that these compounds are mechanically stable. Unfortunately, there are no theoretical or experimental results for these compounds for comparing with the present work. Then, our results can serve as a prediction for future investigations. After obtaining elastic constants, the polycrystalline bulk modulus (*B*), shear modulus (*G*) are calculated from the Voigt-Reuss-Hill (VRH) approximations [15]. The Young's modulus (E) and Poisson's ratio (v) are calculated through $E = 9BG/(3B + G)$ and $v= (3B - 2G)/2(3B+G)$. Exploring the mechanical properties, our results have been summarized in Table 3.

Table 3. The calculated isotropic bulk modulus (*B* in GPa), shear modulus (*G* in GPa), Young's modulus (*E* in GPa), Poisson's ratio (v) and Debye Temperature (Θ_D in K)

Materials	***B***	***G***	***E***	***v***	***B/G***	Θ_D	**Refs.**
ZrSbTe	80.3	54.2	132.7	0.22	1.48	304.1	Present
HfSbTe	84.1	55.7	136.8	0.22	1.50	274.4	Present

The bulk modulus measures the resistance of a solid to volume change against external forces. The obtained bulk modulus is lower than 100 GPa, and therefore these compounds should be classified as high compressibility material. According to Pugh formulation [16], a material is brittle (ductility) if the *B/G* ratio is less (high) than 1.75. The value of the *B/G* is lower than 1.75 for these compounds; hence, these compounds will behave in a brittle manner

Young's modulus is defined as the ratio of stress and strain, and is used to provide a measure of the stiffness of the solid. When the value of E is large, the material is stiff. On this context, due to the higher value of Young's modulus (136.8 GPa) for HfSbTe is relatively stiffer the other compounds.

The value of the Poisson's ratio is indicative of the degree of directionality of the covalent bonds. The value of the Poisson's ratio is about 0.1 for covalent materials, whereas for ionic materials a typical value of v is 0.25 [17]. The calculated Poisson's ratios are about 0.20 for these compounds. Therefore, both compounds are ionic materials.

The Debye temperature is known as an important fundamental parameter closely related to many physical properties such as specific heat and melting temperature. We have calculated the Debye temperature by using the common relation given in Refs. [18-20]. According to Table 3, among the compounds ZrSbTe has the highest Debye Temperature (304.1 K).

4. CONCLUSION

The first-principles calculations have been performed to investigate the structural and mechanical properties of ZrSbTe and HfSbTe compounds. The calculated elastic constants showed that these compounds are mechanically stable in considered structure. The polycrystalline elastic parameters have been further calculated within the scheme of Voigt–Reuss–Hill (VRH) approximation. These compounds possess brittle in nature with respect to the *B/G*.

REFERENCES

[1] Rowe D.M., Thermoelectrics Handbook: Macro to Nano, CRC Press, Taylor & Francis Group, Boca Raton, FL, USA, 2006.
[2] Sofo J.O. and Mahan G.D., Phys. Rev. B: Condens. Matter. (1994), 49, 4565–4570.
[3] Thonhauser T., Sol. State Commun. (2004), 129, 249–253
[4] Bell L.E., Science (2008), 321, 1457.
[5] Kleinke H., Chem. Mater. (2010), 22, 604.
[6] Toberer E.S., May A.F., Snyder G.J., Chem. Mater. (2010), 22, 624.
[7] Kanatzidis M.G., Chem. Mater. (2010), 22, 648.
[8] Soheilnia N., Kleinke K.M. and Kleinke H., Chem. Mater. (2007), 19, 1482-1488.
[9] Blöchl P.E., Phys. Rev. B (1994), 50, 17953.
[10] Kresse G. and Furthmuller J., Phys. Rev. B (1996), 54, 11169.
[11] Perdew J.P., Burke K. and Ernzerhof M., Phys. Rev. Lett. (1996), 77, 3865.
[12] Monkhorst H.J. and Pack J.D., Phys. Rev. B (1976), 13, 5188.
[13] Page Y.L. and Saxe P., Phys. Rev. B (2002), 65, 104104.
[14] Born M., Proc. Cambridge Philos. Soc. (1940), 36, 160.
[15] Hill R., Proc. Phys. Soc. London (1952), 65, 349.
[16] Pugh S.F., Phil. Mag. (1954), 45, 823.
[17] Shein I.R. and Ivanovskii A.L., J. Phys.: Condens. Matter. (2008), 20, 415218.
[18] Johnston I., Keeler G., Rollins R. and Spicklemire S., Solid State Physics Simulations, The Consortium for Upper-Level Physics Software, Jhon Wiley, New York, 1996.
[19] Anderson O.L., J. Phys. Chem. Solids (1963), 24, 909.
[20] Schreiber E., Anderson O.L. and Soga N., Elastic Constants and their Measurements, McGraw-Hill, New York, 1973.

The Investigation of Some Probiotics Proporties of Lactic Acid Bacteria Izolated from Traditionally Produced Shalgam Juice in Mersin Region

Esin Kiray

Ahi Evran University, Faculty of Science and Arts, Department of Biology, TR-40100, Kirsehir, Turkey

**esin.kiray@ahievran.edu.tr*

Keywords: Lactic acid bacteria, probiotics, probiotics proporties, shalgam juice

ABSTRACT

Shalgam juice is a traditional fermented beverage, mostly produced and consumed in the southern east parts of Turkey. The main ingredient of shalgam juice is black carrot which is known for its high antioxidant capacity due to the presence of anthocyanins. In this study, *Lactobacillus brevis* was obtained from traditional fermented black carrot juice and was investigated some probiotics proporties such as antibiotics susceptibility, antimicrobial activity, acid and bile resistance and cholesterol lowering ability. *L. brevis* strain demonstrated antimicrobial activity against *Enterecoccus faecalis* ATTC 29212, *Escherichia coli* ATCC 25922 and *Stapylococcus aureus* ATCC 25923 by the agar well assay. Our results showed that this strain is resistant to vancomycin and teicoplanin. Moreover high resistance to low pH and bile salts was also observed. Although shalgam juice's composition is widely studied, further characterization is needed to determine its potential health benefits.

1. INTRODUCTION

Fermented fruit and vegetable juices are non-dairy fermented beverages produced generally by lactic acid fermentation and their microbiological and chemical compositions provide beneficial properties to them. The microbiological composition of lactic acid fermented products consists of mostly lactic acid bacteria (LAB), which are considered to be probiotics due to their beneficial health effects, such as antimicrobial, immunostimulatory and anticarcinogenic properties [1].

More than 3,500 fermented foods and beverages are produced all over the world using several raw materials, manufacturing techniques and microorganisms, and most of these products are traditional products that are only produced in certain regions of the world usually by small scale businesses [2,3].

Shalgam juice is a traditional fermented beverage, mostly produced and consumed in the southern east parts of Turkey. It is defined by Turkish Standards Institution (TSE) in TS 11149 standard as “The product produced by lactic acid fermentation of turnip (Brassica rapa), black carrot (Daucus carota), chilli powder and extract obtained from the lactic acid fermentation of bulgur flour, sourdough, drinking water and salt, which can be heat treated for preservation, if desired” [4].

Determination of the antioxidant capacities of fermented fruits and vegetable juices, as well as identification of beneficial LAB is important in order to understand their health effects and functional properties [5].

LAB are among the most important groups of microorganisms used in food fermentation and also confer some health benefits. LAB are a group of gram positive, facultative anaerobic bacteria, which use hexoses in fermentation to produce lactic acid as the main end-product. Lactic acid gives fermented beverages their flavor and aroma. LAB mostly from the genuses *Lactobacillus* and *Bifidobacterium* are widely investigated as probiotic microorganisms [6].

Probiotics are live microorganisms that when administered in adequate amounts confer a health benefit on the host. Because of these beneficial health effects, the isolation and identification of new LAB strains in natural complex microbial communities is important for their selection as probiotics in fermented products [7].

The probiotic effects of LAB are reported to involve inhibition of pathogenic microorganisms, protection against gastrointestinal diseases, anti-mutagenic and anti-carcinogenic activities, and enhancement of the host immune response. The reduction of cholesterol by LAB has also been demonstrated in humans, mice, and pigs [8].

Potential health effects of shalgam juice as a whole product is not widely known. Therefore, In the present study, the probiotic proporties of *Lactobacillus brevis* isolated from traditionally produced shalgam juice was investigated. Survival to gastrointestinal tract (GI) conditions and adhesion to human intestinal cells were assessed in vitro. In addition, the study focused on its antimicrobial activity, antipathogenic activities, inhibit adhesion of gastrointestinal and urogenital pathogens, and cholesterol lowering ability.

2. RESULTS AND DISCUSSION

2.1. Isolation of *Lactabacillus brevis*

The microbial load of shalgam juice mostly comes from bulgur dough used in fermentation. Ten mL shalgam juice was suspended in 90 mL peptone water and 10-fold serial dilutions were made ($100\text{-}10^{-7}$). After dilutions, *L. brevis* specie was cultivated on Man Rogosa Sharp (MRS) agar, and was incubated at 37°C in a 5% CO_2 incubator for 48 h. The identity of the strain was confirmed by Gram staining (Salubris Gram Staining Kit, USA) and by checking colony morphologies. *L. brevis* was idendified by standard biochemical tests, the API 50 CHL system (BioMérieux- France).

2.2. Acid and bile tolerance of strain

Acid and bile tolerance was tested using the method described by Hyronimus et al. (2000) [9]. Acid tolerance of *L. brevis* was grown in MRS broth at 37°C for 18 h and subcultured in 10 mL of fresh MRS broth, adjusted to pH 2, 2.5 and 3 with HCI. The initial bacterial concentration was 1.0×10^8 CFU/mL, and sample was incubated for 0 and 3 h at 37°C. Strain (1.0×10^8 CFU/mL) was serially diluted in sodium phosphate buffer (PBS) (pH 7.0) to neutralize medium acidity. The plate count method was used to count colony-forming units. Colony forming units were determined by multiplying the number of colonies by the dilution factor. The strain evaluated demonstrated sufficient acid and bile tolerance to be resistant to physiological stomach and intestinal conditions, making them potentially useful candidates for the development of probiotics (Tablo 1).

Tablo 1. The viability (log CFU mL^{-1}) of *L. brevis* strains with in GI conditions.

	pH 2	**pH 2,5**	**pH 3**	**%0.3 oxgal**	**%0.5 oxgal**	**%1 oxgal**
L. brevis	$1.2x10^3$ kob/ml	3.8 ± 10^6 kob/ml	7.6 ± 10^7 kob/ml	$6.7x10^6$ kob/ml	$5.6x10^5$ kob/ml	$3.4x10^3$ kob/ml

2.3. Antibiotic Susceptibility of strains

The antibiotic susceptibility of strain was determined by the disc diffusion method. Strain was grown with MRS broth at 37 ^{o}C for 48 h in anaerobic condition. The discs were placed on the inoculated MRS agar plate. Inhibition zones after incubation were measured, and interpreted to be susceptible, moderately susceptible, or resistant.

Tablo 2. Antibiotic resistance of *L. brevis*

	AM	**RA**	**CAZ**	**TE**	**C**	**VA**	**E**	**TEC**	**P**	**G**
L. brevis	13 mm	20 mm	R	15 mm	22 mm	R	14 mm	R	25 mm	15 mm

*R: Resistant; AM: Ampicillin (10 mg). RA: Rifampin (5 mg). CAZ: Ceftazidime/Clavulanic acid (30/10 mg). TE: Tetracyline (30 mg). C: Chloramphenicol (30 mg). VA: Vancomycin (30 mg). E: Erythromycin (15 mg). TEC: Teicoplanin (30 mg). P: Penicillin (10 mg). G: Gentamicin (10 mg).

2.3. Antagonistic activity of *L. brevis*

The agar well diffusion method was used to determine the antagonistic effect of strain. *L. brevis* was incubated at 37 ^{O}C for 24 h in under anaerobic conditions in a MRS medium [10]. The cultur was centrifuged at 10. 000 g for 10 min, after which time the supernatant was drawn into an injector and passed through a filter with 0.45 µm pore (Millipore, Molsheim, France) diameter. Separately, indicator microorganisms were activated and 0.5 McF of bacterial suspension was inoculated into Muller Hinton agar (Merck, Germany). Wells of 6 mm in diameter was cut and 100 µl of filter-sterilized supernatant was placed into each well and incubated for 18 h at the suitable temperature for indicator strains. Diameter of zones that formed around wells was measured in mm. As show in Tablo 3, the zones of growth inhibition on *E. faecalis* ATCC 29212 and *C. albicans* YN-1200 by supernatant were found 15.6 and 15.8, respectively. This strain is also weak anti-pathogenic activity againts *S. aureus* ATCC 25923.

Tablo 3. The inhibitory effect of *L. brevis* on urogenital pathogens

	E. faecalis **ATCC 29212**	***E. coli*** **ATCC 25922**	***P. aeruginosa*** **ATCC 27853**	***S. aureus*** **ATCC 25923**	***C. albicans*** **ATCC 10098**	***C. albicans*** **YN-1200**
L. brevis	15.6 mm	14.2 mm	14.8 mm	12.1 mm	13.5 mm	15.8 mm

2.4. Cholesterol assimilation by *L. brevis*

Cholesterol assimilation by strains A sample of 500-600 mg dL $^{-1}$ human plasma cholesterol included in MRS and MRS with 0.3 % bile (Oxgall, Sigma) broth was used to test the ability of cholesterol assimilation of strain. After inoculation, cells were incubated at 37 ^{o}C for 24 h in anaerobic conditions and subsequently spin down at 5000 g for 10 min [10]. The remaining cholesterol level was analyzed in supernatant by COBAS Integra® 800 model autoanalyzer (Roche, Germany).

Tablo 4. Reduction of cholesterol by *L. brevis* in vitro

	L. brevis
Control	58±0.5
First value	57±0.8
Last value	42±0.3
Reducing rate %	26.4

3. CONCLUSION

This study was investigated some probiotics proporties of *L. brevis* such as antibiotics susceptibility, antimicrobial activity, acid and bile resistance and cholesterol lowering ability. The strain evaluated demonstrated sufficient acid and bile tolerance to be resistant to physiological stomach and intestinal conditions, making them potentially useful candidates for the development of probiotics. The strain screened strong anti-pathogenic activity against several pathogenic bacteria. *L. brevis* was found to have the highest levels of cholesterol assimilation. In conclusion, although this study provided detailed information about some probiotic proporties of LAB isolated from shalgam juice, the mechanism behind health benefits of shalgam juice is still not clear and needs to be studied. Therefore, this strain would make a good candidate for further investigation through in vivo studies to determine its potential health benefits.

REFERENCES

[1] Ekinci F.Y., Baser G.M., Özcan E., G. Üstündag Ö., Korachi M., Sofu A., Blumberg J. B., C.Y.O. Chen., Eur Food Res Technol. (2016), 242, 1355 – 1368.
[2] Waters D.M., Mauch A., Coffey A., Arendt E.K., Zannini E., Crit Rev Food Sci. (2015), 55, 503 – 520.
[3] Corbo M.R., Bevilacqua A., Petruzzi L., Casanova F.P., Sinigaglia M., Compr Rev Food Sci. (2014), 13(6), 1192 – 1206.
[4] H Erten., H Tanguler., A. Canbaş., (2008), 24(3), 352 – 359.
[5] Başer G.M., Yeditepe University, (2013), 38.
[6] Sip A., Grajek W., Blackwell. Oxford, 2010.
[7] Swain M.R., Anandharaj M., Ray R.C., Rani R.P., (2014), Article ID 250424, 19.
[8] Song M., Yun B., Moon J.H., Park D.J., Lim K., Oh S., Korean J Food Sci Anim Resour. (2015), 35(4), 551 – 556.
[9] Hyronimus B., Le Marrec C., Sassi A.H., Deschamps A., Int. J. Food Microbiol. (2000), 61, 193 – 197.
[10] Tulumoğlu Ş., Kaya H.İ., Şimşek Ö., Anaerobe. (2014), 30, 120 - 125.

All Solution-Based Fabrication of CuO Thin Film/Si Nanowires Heterojunction Devices for Optoelectronic Applications

Funda Aksoy Akgul[a], Guvenc Akgul[b]

[a]*Physics Department, Ömer Halisdemir University, TR-51240 Nigde, Turkey*
[b]*Bor Vocational School, Ömer Halisdemir University, TR-51700 Niğde, Turkey*

**e-mail corresponding author*: fundaaksoy01@gmail.com

Keywords: CuO thin films, Si nanowires, electroless etching method

ABSTRACT

In this study, copper oxide (CuO) thin film/silicon (Si) nanowires p-n heterojunction devices were fabricated and their optoelectronic performances were investigated. Well-aligned dense arrays of vertically oriented n-type Si nanowires were fabricated via electroless etching technique. CuO thin films were synthesized by sol-gel method and deposited onto nanowire arrays of Si through spin-coating. Fabricated nanowire-based heterojunction devices exhibited excellent diode behavior compared to planar control device. Rectification ratios were found to be 10^5 and 10^1 for the nanowire-based and planar heterojunctions, respectively. Improved electrical properties and photosensitivity of the nanowire-based heterojunction devices were observed, which was related to three-dimensional nature of the interface between Si nanowires and CuO thin film. Obtained device characteristics in this work clearly prove the potential of the CuO thin film/Si nanowires heterojunctions for next generation high-performance and low-cost optoelectronic device applications.

1. INTRODUCTION

During the last few decades, semiconductor nanowires have been the subject of extensive interest because of their novel physical and/or chemical properties. Among the vast majority of studied material systems so far, silicon (Si) nanowires have shown a promising potential for photovoltaic and optoelectronic applications because of their superior antireflection characteristics and thus enhanced absorption compared to thin film/planar devices [1]. Various methods have been developed for the synthesis of Si nanowires such as the vapour–liquid–solid method, electroless etching, molecular beam epitaxy and electron beam evaporation. Among these methods, electroless etching is the most simple and cost-efficient method for the fabrication of Si nanowires [2]. In this method, fabricated Si nanowires have the same doping type and level and high-quality crystal structure of the starting Si wafer. It is also possible to control the length of the nanowires.

Promising results from fabrication of Si nanowire-based heterojunction solar cells and photodiodes have recently been obtained. In these device structures, one-dimensional semiconducting Si nanowires are complemented with a layer of organic or inorganic complementary materials to form a p–n heterojunction. Significant efforts have been devoted to developing devices with such a device structure using different semiconducting complementary compounds including metal oxide semiconductors. However, most metal oxides have wide band gaps leading to a limited light absorption in the visible region of solar spectrum and unfavorable energy band levels. Copper oxide (CuO) has emerged as a potential complementary candidate for various applications due to its suitable properties such as p-type conductivity, narrow optical bandgap between 1.2-1.9 eV (ideal for sunlight absorption), high absorption coefficient over a substantial portion of the solar spectrum, direct type bandgap structure and similar electron affinity to Si. A wide range techniques have been employed to prepare CuO thin films [3].

Based on aforementioned considerations, heterojunctions of the two materials could offer additional advantages. Although there are few studies on CuO thin film/Si heterojunctions, to the best of our knowledge, no comparable study has been reported on the fabrication and characterization of CuO thin film/Si nanowire heterojunctions yet. In this study, we report on the synthesis and characterization of CuO thin film/Si nanowire heterojunction devices for optoelectronic applications. The sol-gel method which is versatile and the non-vacuum wet-chemical process was used to synthesis CuO thin films. The fabricated devices consist of vertically aligned Si nanowires fabricated through the electroless etching method which are coated with p-type CuO thin films. Planar heterojunction devices were also fabricated for reference.

2. RESULTS AND DISCUSSION

Fabrication of CuO thin film/Si nanowires heterojunction devices was achieved in two steps. In the first, highly oriented Si nanowire arrays were produced by typical electroless etching method, as discussed in a previous work [2]. Prior to etching, the cleaning process was applied to one side polished Si wafers (400 µm thick, (100) orientation, n-type, resistivity 1–10 Ω.cm) through consecutive sonication in acetone (99.8%), isopropanol (99.8%) and de-ionized baths for 15 min. In the second fabrication step, thin CuO films were deposited onto the as-grown Si nanowire arrays via spin coating in order to create three-dimensional p-n heterojunctions structures. The solution for the deposition of CuO thin films was prepared by dissolving copper acetate ($Cu(CH_3COO)_2$. H_2O, Merck, 99.98%) in ethanol. Afterwards, lactic acid ($C_3H_6O_3$, 85%) and triethylamine ($C_6H_{15}N$, 99.95%) was added into the prepared solution. The spin-coating was applied at 2000 rpm. To avoid cracking in thin films and inhomogeneous coverage, multiple coatings were carried out with drying in between each successive coating. Finally, the samples were annealed in air at 500 ºC to improve crystallinity and to form a single CuO phase. The device fabrication was completed by the thermal evaporation of gold (Au) and aluminum (Al) as ohmic front and back contacts, respectively. Formation of ohmic-type contacts was achieved by subsequent annealing at 180 °C for 30 minutes.

Morphological examination of the fabricated devices was carried out by Nova NanoSEM 430 model field emission scanning electron microscope (FESEM) operated at 10 kV. Cross-sectional SEM image of the fabricated nanowires is provided in Fig. 1(a). The figure shows dense arrays of highly oriented Si nanowires with uniform length of approximately 1 µm, grown successfully and distributed over the Si substrate. In this work, n-type Si wafer was etched for 10 min to obtain about 1 µm long nanowires, vertically aligned on the Si substrate. Fig. 1(b) is the cross-sectional SEM image taken after the CuO layer was deposited on the Si nanowire arrays. A total of 15 consecutive coatings were carried out onto Si nanowires. The same amount of CuO was deposited on the planar Si and the corresponding film thickness was measured to be approximately 500 nm from the cross-sectional SEM images (not shown here). Therefore, any observed difference in the performance of the fabricated devices can be safely ascribed to the properties of Si nanowires. An intimate contact between the Si nanowires and deposited CuO film can be seen in Fig. 1(b). Semiconductor CuO particles interpenetrated within the Si nanowire arrays yielding a combined structure with particles attached to the surface of the nanowires. Empty spaces in between the nanowires were partially filled with these small CuO particles with sizes around 100 nm. The packing of the CuO thin films increases towards the tip of the Si nanowires, resulting in the formation of a continuous film on the top of the Si nanowire arrays.

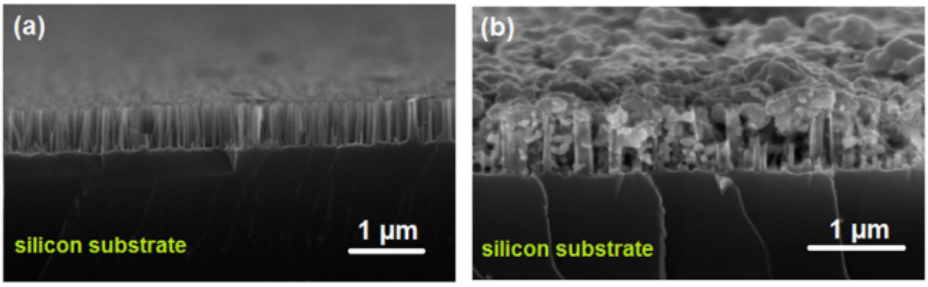

Figure 1. (a) Cross-sectional SEM image of the fabricated Si nanowires on an n-type Si substrate. (b) SEM image of CuO thin film/Si nanowire heterojunction.

In order to determine the electrical properties and optoelectronic characteristics of the constructed naowires-based devices, the typical current-voltage (*I-V*) measurements were carried out in the dark and under illumination conditions at room temperature. *I-V* characteristics of the fabricated devices were

measured by LabVIEW controlled Keithley 2400 source meter and tested with an AM 1.5G solar simulator controlled with Newport *I-V* test software. Fig. 2(a) illustrates a schematic structure of the fabricated nanowire heterojunction devices. The effective area of the devices was 2 cm^2.The semi-logarithmic *I-V* characteristics measured both in the dark and under illumination at room temperature is shown in Fig. 2(b). The diode behavior of the Si nanowire-based heterojunction was observed to be prominently superior compared to the planar heterojunction. The devices exhibited decent diode behavior with a rectification ratio (IF/IR taken at −1 V/1 V) of approximately 105 for the nanowire heterojunction and 101 for the planar junction. Important diode parameter of ideality factor (n) was determined using the standard Shockley-diode model [4]. The ideality factors of the diodes were found to be 1.3 and 2.9 for the nanowire and planar heterojunction devices, respectively. It is well known that the diode ideality factor is 1 when the current is only diffusion type (ideal Shockley diode). The ideality factor of the fabricated CuO thin film/Si nanowires heterojunction device was less than 2, holding promise for optoelectronic applications. However, the obtained ideality factor for the planar heterojunction was too high; probably because of both strong parasitic generation and recombination at the interface states [5].

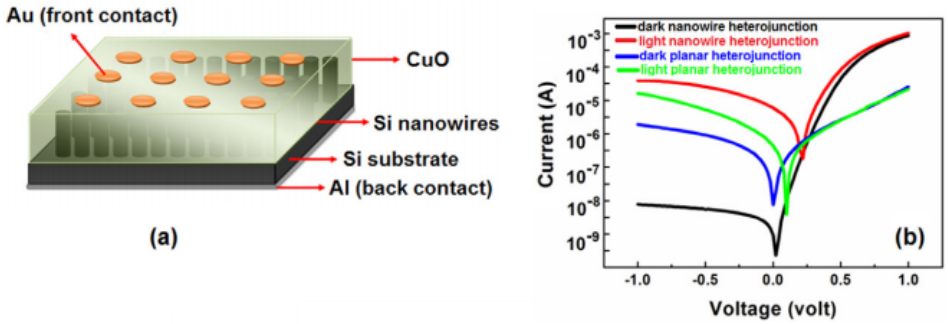

Figure 2. (a) Schematic presentation of the fabricated CuO thin film/Si nanowires devices. (b) Semilogarithmic plot of the I-V characteristics of the nanowire and planar heterojunction photodiodes measured in the dark and under illumination at room temperature.

Fig. 3(a) shows the light ON/OFF characteristics of the nanowire and planar heterojunction photodiodes under 1 V bias. The dark (OFF) current was measured for 10 s without illumination and then the AM 1.5G lamp was turned on for 10 s to measure the light (ON) current. The light (OFF) current for the nanowire junction is almost 40-fold higher than the planar junction and it decreases to 30-fold for the light (ON) current owing to enhanced contact area and shorter carrier diffusion lengths for the nanowire junction. The decrease in the enhancement of the light (ON) currents might be correlated to the enhanced surface recombination at the deep trap levels at the surface of the Si nanowires. Surface passivation might be a solution to prevent this effect. The light ON/OFF characteristics proved that CuO thin film/Si nanowire heterojunctions can be used for photodetection. The rise and relaxation times were found to be less than 1 s for both photodiodes. The photoresponsivity measurements of the nanowire and planar junctions have also been performed. Fig. 3(b) presents the spectral response of the nanowire and planar heterojunction diodes as a function of wavelength in the 400 and 1100 nm range. The variation in photoresponsivity was measured using a calibrated light source under a reverse bias of 1 V at room temperature. The figure shows that the photoresponsivity covers photon energies ranging from ultraviolet to near-infrared (NIR). A high photoresponse enhancement was observed for the nanowire heterojunction diodes with nanowires compared to the planar counterparts. The intensity of the signal was significantly improved for the nanowire-based heterojunction. The maximum responsivity of the nanowire heterostructure was observed around 890 nm (~1.4 eV) matching to the optical band gap of CuO [6]. There is almost a 12-fold higher response at this wavelength proving the enhancement due to the nanowire junction. Therefore, the CuO thin film/Si nanowires heterojunction devices could be used as NIR photodetectors. By comparing our results with previously reported experimental studies, high photoresponsivity observed for the CuO thin film/Si nanowires heterojunction device could be attributed to the improved structural quality of the CuO film deposited on the Si nanowires compared to its counterpart on planar Si [5]. The enhanced interfacial area and the nucleation sites on the surface of the Si nanowires may lead to a better crystal quality. In addition, the flexible three-dimensional structure of the nanowires overcomes the possible lattice mismatch between CuO and Si, leading to low defect densities at the interface. The light trapping nature of the nanowires also contributed to the signal enhancement.

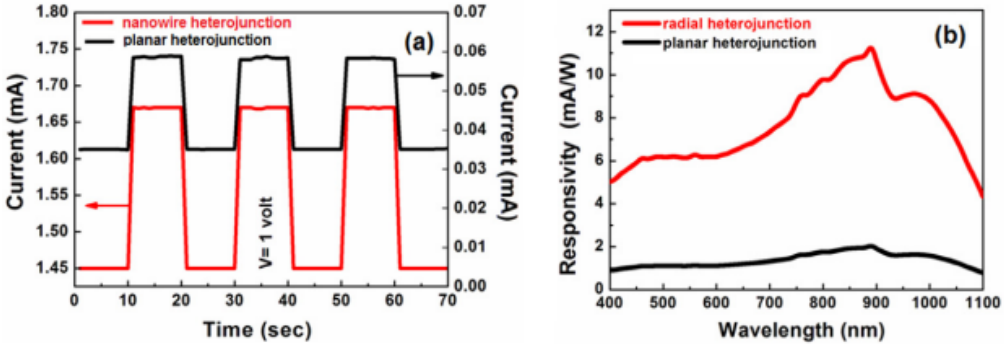

Figure 3. (a) Light ON/OFF characteristics and (b) spectral photoresponsivity of the photodiodes under 1 V bias.

3. CONCLUSION

In this study, Si nanowires-based heterojunction solar cells were fabricated by depositing of p-type CuO films onto the vertically well-aligned n-type Si nanowire arrays via simple and cost-effective chemical bath deposition technique. Constructed solar cell structures demonstrated good p-n characteristics in the dark and illumination conditions. Diode parameters of ideality factor and rectification ratio were calculated to be 1.95 and 10^2, respectively. The optimal short-circuit current density, open-circuit voltage, fill factor and power conversion efficiency were found to be 3.2 mA/cm^{-2}, 337 mV, 37.9 and 0.45%, respectively. The observed performance clearly indicates that the investigated device structure could be a promising candidate for high-performance low-cost new-generation photovoltaic diodes.

4. ACKNOWLEDGEMENTS

F.A.A. and G.A. would like to thanks The Scientific and Technical Research Council of Turkey (TUBITAK) Post-Doctoral Fellowship for financial support.

REFERENCES

[1] Sakalakos L.T., Balch J., Fronheiser J., Korevaar B.A. and Sulima O.R., J. Appl. Phys. Lett. (2007), 91, 233117-1 – 233117-1.
[2] Ozdemir B., Kulakci M., Turan R. and Unalan H.E., Nanotechnology (2011), 22, 155606-1–155606-7.
[3] Aksoy Akgul F., Akgul G., Yildirim N., Unalan H.E. and Turan R., Materials Chemistry and Physics (2014), 147, 987 – 995.
[4] Schroder D.K., Semiconductor Material and Device Characterization, (2006), third ed., John Wiley & Sons, New York.
[5] Kulakci M., Colakoglu T., Ozdemir B., Parlak M., Unalan H.E. and Turan R., Nanotechnology (2013), 24, 375203-1 – 375203-7.
[6] Chen L., Shet S., Tang H., Wang H., Deutsch T., Yan Y., Turnerand J. and Jassim M.A., J. Mater. Chem. (2010), 20, 6962 – 6967.

Preparation of CuO Thin Films by Chemical Bath Deposition Method and Their Solar Cell Application with Si Nanowires

Funda Aksoy Akgul[a], Guvenc Akgul[b]

[a]*Physics Department, Ömer Halisdemir University, TR-51240 Nigde, Turkey*
[b]*Bor Vocational School, Ömer Halisdemir University, TR-51700 Niğde, Turkey*

**e-mail corresponding author*: fundaaksoy01@gmail.com

Keywords: CuO thin films, MACE method, photovoltaic diodes

ABSTRACT

Recently, copper(II) oxide (CuO) has attracted much interest owing to its inexpensive fabrication cost and potential applications. Suitable properties of CuO make it an ideal inorganic semiconductor material for optoelectronic devices. In this study, CuO thin films were deposited onto glass substrates using chemical bath deposition, and post-deposition annealing effects on the properties of the prepared samples were investigated. p-n heterojunction solar cells were constructed by coating of p-type CuO films onto the vertically well-aligned p-type Si nanowires synthesized through metal-assisted chemical etching (MACE) method. Photovoltaic performance of the fabricated devices were determined with current-voltage (*I-V*) measurements under AM 1.5 G illumination. The optimal short-circuit current density, open-circuit voltage, fill factor and power conversion efficiency were found to be 3.2 mA/cm^{-2}, 337 mV, 37.9 and 0.45%, respectively. The observed performance clearly indicates that the investigated device structure could be a promising candidate for high-performance low-cost new-generation photovoltaic cells.

1. INTRODUCTION

One-dimensional Si nanostructures in the form of nanowires have revealed a conspicuous promise for next-generation photovoltaic applications. Up to now, several fabrication methods for the formation of nanowires on Si substrates have been developed [1]. Among them, metal-assisted chemical etching (MACE) of Si substrates is a very easy, powerful and cheap solution-based route.

Tremendous efforts have been made by researchers to fabricate Si nanowires-based photovoltaic devices integrated with different materials including metal oxide semiconductors. Copper(II) oxide (CuO) has emerged as a potential complementary candidate for solar cell applications due to its suitable properties such as p-type conductivity, narrow optical bandgap between 1.2-1.9 eV (ideal for sunlight absorption), high absorption coefficient over a substantial portion of the solar spectrum, direct type bandgap structure and similar electron affinity to Si. A wide range techniques have been employed to prepare CuO thin films [1].

In this study, photovoltaic characterization of CuO thin film/Si nanowires heterojunction structure was reported. p-type CuO thin films were deposited via chemical bath deposition. Structural, optical, and electrical properties of the prepared thin film samples were investigated as a function of post-deposition annealing temperature. n-type Si nanowires were synthesized through facile and cheap MACE method. Finally, Si nanowires-based solar cells were fabricated by coating CuO films onto Si nanowire arrays, and photovoltaic properties of the constructed heterojunction structures were investigated.

2. RESULTS AND DISCUSSION

Fabrication of Si nanowires-based heterojunction solar cells was achieved in two steps. In the first, highly oriented Si nanowire arrays were produced by typical MACE method, as discussed in a previous work [2]. One side polished n-type Si (100) wafers of 1-10 Ω.cm resistivity were used. In the second fabrication step, thin CuO films were deposited onto the as-grown Si nanowire arrays via chemical bath deposition in order to create three-dimensional p-n heterojunctions structures. The solution for the deposition of CuO thin films was prepared by dissolving copper acetate ($Cu(CH_3COO)_2$. H_2O, Merck, 99.98%) in ethanol. Afterwards, lactic acid ($C_3H_6O_3$, 85%) and triethylamine ($C_6H_{15}N$, 99.95%) was added into the prepared solution. The solution was deposited directly onto the Si nanowire arrays by chemical bath deposition. CuO thin films were also deposited onto pre-cleaned commercially available soda-lime silicate glass slides for the characterization of the film properties. Si and glass substrates were dipped vertically into CuO solution for 20 seconds, then dried on a hot plate at 150 °C for 3 minutes in air under ambient conditions. Dipping/drying cycle was repeated as many times as desired in order to get sufficient film thickness. The device fabrication was completed by the thermal evaporation of gold (Au) and silver (Ag) as ohmic front and back contacts, respectively. Formation of ohmic-type contacts was achieved by subsequent annealing at 180 °C for 10 minutes.

Before Si nanowires-based solar cell fabrication, CuO thin films deposited onto glass substrates were investigated. Samples were annealed in a muffle furnace under atmospheric conditions for 20 minutes at different temperatures varied between 200 and 600 ºC to obtain films with better properties. Structural properties of the as-deposited and post-annealed CuO films were evaluated through X-ray diffraction (XRD). XRD measurements were performed using a Rigaku Miniflex diffractometer with Cu Kα radiation (λ = 0.154 nm). XRD patterns of the samples are shown in Fig 1(a).

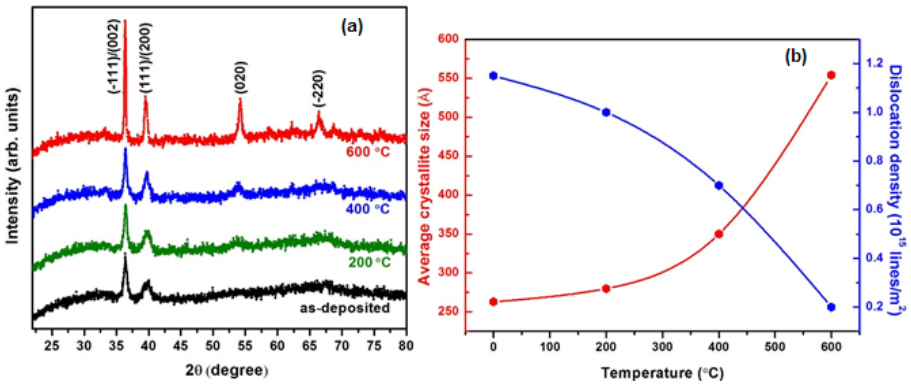

Figure 1. XRD patterns of as-deposited and post-annealed CuO thin films (a) and average crystallite size and dislocation density of CuO thin films as a function of annealing temperature (b).

As-prepared sample exhibits two distinct peaks, indicating polycrystalline structure. The first and second Bragg diffraction peaks at an angle 2θ of 35.6º and 38.7º can be indexed to (-111) or (002) and (111) or (200) reflections, respectively, indicating tenorite phase of CuO [3]. Sharpest XRD peaks were monitored for the thin film annealed at 600 ºC. The Rietveld method was applied to the collected diffraction data to derive structural parameters of CuO samples. Variation of the average crystallite size and dislocation density with post-annealing temperature is demonstrated in Fig. 1(b). The largest crystallite size of 554 Å was estimated when CuO thin film was annealed at 600 ºC. The same thin film sample also exhibited the lowest value for the density of dislocations, as shown in Fig. 1(b). Obviously, thermal energy provided by annealing treatment leads to larger crystallite formation. The observed increase in crystallite size could be correlated with the reduced amount of lattice imperfections in the crystalline structure of CuO.

Optical properties of the thin film samples were analyzed using an optical setup [4] and optical characteristics of the as-deposited and post-annealed thin CuO films were evaluated by the analysis of transmission and reflection spectra. Spectral variation of the transmittance and reflectance of samples with the wavelength of the incident photon is shown in Fig. 2(a) and Fig. 2(b), respectively. Highly absorbing thin films in the visible wavelength region were obtained by applying chemical bath deposition method. Below 800 nm, a sharp absorption fall is noticeable. In the near-infrared region, an average transmittance was found to be 73%. Relatively similar reflectance spectra with low intensity reflectivity were measured

for the as-deposited, 200 ºC-annealed and 400 ºC-annealed thin films. However, high-temperature annealing of CuO films at 600°C caused a rise in the intermediate region of the reflectance curve. Larger crystallites formed at this temperature could lead to enhanced light scattering and more reflection from the film surface. Tauc model was used for estimating optical bandgap energy (E_g) of CuO thin films [5]. To apply this widely used model, the absorption coefficient (α) of the samples was calculated using the following relation:

$$\alpha = \frac{1}{d} ln \left[\frac{(1-R)^2}{2T} + \left(\frac{(1-R)^4}{4T^2} + R^2 \right)^{1/2} \right] \quad (1)$$

where d is the film thickness and T and R are the experimentally measured transmission and reflection spectra, respectively. E_g of the as-deposited and annealed CuO films at 200 °C, 400 °C and 600 °C was estimated to be approximately 1.77, 1.71, 1.54 and 1.45 eV, respectively. Determined bandgap energies are consistent with the reported values of CuO thin films [6].

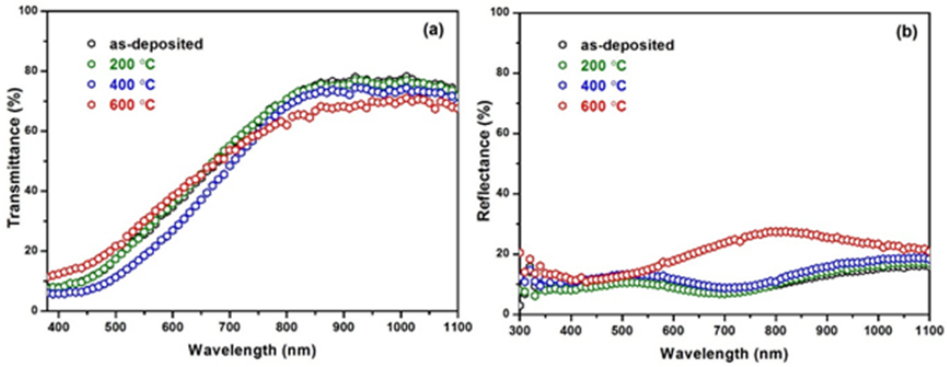

Figure 2. Transmittance (a) and reflectance (b) spectra of as-deposited and post-annealed CuO thin films.

Electrical properties of CuO thin films including carrier concentration and mobility were obtained from Hall Effect measurements by conventional four-point dc Van der Pauw technique. All investigated thin film samples revealed p-type conductivity. Table 1 summarizes the obtained carrier concentration and mobility values for as-deposited and post-annealed films. Experimental results indicate that the electrical properties of the post-annealed CuO films are substantially improved by annealing process compared to as-deposited sample.

Table 1. Electrical properties of as-deposited and post-annealed CuO thin films

Samples	**Carrier concentration (cm^{-3})**	**Mobility ($cm^2 V^{-1}s^{-1}$)**
As-deposited	0.8×10^{13}	1.42
200 ºC-annealed	1.15×10^{13}	4.14
400 ºC-annealed	2.32×10^{16}	10.26
600 ºC-annealed	5.13×10^{16}	25.56

In our study, post-deposition annealing was employed for CuO thin films at various temperatures to develop their structural, optical and electrical properties. The optimal film characteristics were found at an annealing temperature of 600 ºC, based on the obtained results. p-n heterojunction solar cells were constructed by coating of p-type CuO films onto the vertically aligned n-type Si nanowires. Thereafter, fabricated devices were annealed at 600 ºC for 20 minutes. Morphological examination of the fabricated solar cells was carried out by Nova NanoSEM 430 model field emission scanning electron microscope (FESEM). Cross-sectional SEM image of a Si nanowires-based heterojunction device is provided in Fig. 3(a). The image evidently reveals that the deposited film covers the surface of Si nanowires, and a continuous film forms at top of the nanowire arrays. As shown in Fig. 3(a), thin film packing increases from the bottom towards the top, resulting in the formation of matchstick-shaped CuO/Si nanoheterostructures.

In order to determine the electrical properties and photovoltaic characteristics of the constructed naowires-based devices, the typical current-voltage (*I-V*) measurements were carried out in between -1 and +1 V.

I-V characteristics of the fabricated solar cells were measured by LabVIEW controlled Keithley 2400 source meter and tested with an AM 1.5G solar simulator controlled with Newport *I-V* test software. The semi-logarithmic *I-V* characteristics measured both in the dark and under illumination at room temperature is shown in Fig. 3(b). Significant rectifying behavior with a rectifying ratio of 10^2 at ±1 V was observed in the dark. This result confirms the successful formation of p-n heterojunctions within the device structure. Important diode parameters including ideality factor (n) and dark saturation current (I_0) were determined using the standard Shockley-diode model [7], and they were calculated to be 1.95 and 8.75×10^{-6} A, respectively. Photovoltaic performance of the fabricated solar cells were tested with an AM 1.5G solar simulator with an illumination power density of 90 mW.cm^{-2}. The best photovoltaic cell yielded a power conversion efficiency of 0.45%. Other solar cell parameters such as short-circuit current density, open-circuit voltage, fill factor, series resistance and shunt resistance were found to be 3.2 mA/cm^{-2}, 337 mV, 37.9, 460.25 Ω and 98.46 Ω, respectively. The obtained cell efficiency may not be high for a solar cell device, but it can be enhanced by the optimizing the fabrication process of the nanowires, plasmonic effects, refinement of the physical properties of the deposited CuO thin films, inserting a passivation layer in the cell structure and some contact issues.

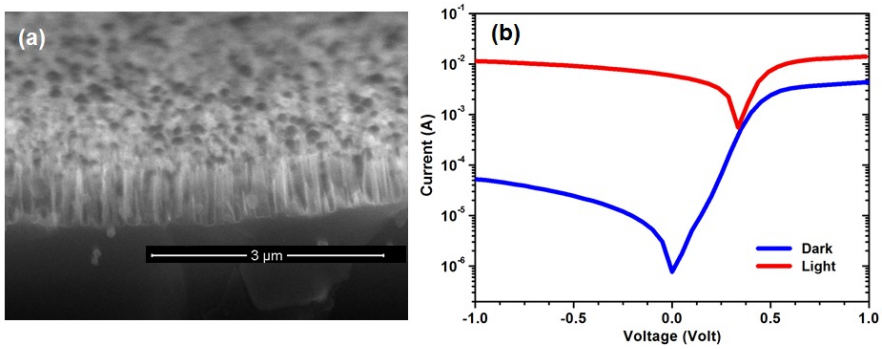

Figure 3. Cross-sectional FESEM image (a) and semi-logarithmic *I-V* characteristics (b) of the fabricated Si nanowires-based solar cells measured in the dark and illumination conditions at room temperature.

3. CONCLUSION

In this study, Si nanowires-based heterojunction solar cells were fabricated by depositing of p-type CuO films onto the MACE-grown vertically well-aligned n-type Si nanowire arrays via simple and cost-effective chemical bath deposition technique. Constructed solar cell structures demonstrated good p-n characteristics in the dark and illumination conditions. Diode parameters of ideality factor and rectification ratio were calculated to be 1.95 and 10^2, respectively. The optimal short-circuit current density, open-circuit voltage, fill factor and power conversion efficiency were found to be 3.2 mA/cm^{-2}, 337 mV, 37.9 and 0.45%, respectively. The observed performance clearly indicates that the investigated device structure could be a promising candidate for high-performance low-cost new-generation photovoltaic diodes.

4. ACKNOWLEDGEMENTS

F.A.A. and G.A. would like to give thanks to Research Projects Unit of Ömer Halisdemir University (The Project Code: FEB 2014/25-BAGEP and The Project Code: FEB 2014/26-BAGEP) for the financial support.

REFERENCES

[1] Akgul G., Aksoy Akgul F., Mulazimoglu E. and Unalan H.E., J. Phys. D: Appl. Phys. (2014), 47, 065106 – 065113.
[2] Ozdemir B., Kulakci M., Turan R. and Unalan H.E., Nanotechnology (2011), 22, 155606-1–155606-7.
[3] Aksoy Akgul F., Akgul G., Yildirim N., Unalan H.E. and Turan R., Materials Chemistry and Physics (2014), 147, 987 – 995.
[4] Akgul G., Aksoy Akgul F., Unalan H.E. and Turan R., Philosophical Magazine (2016), 96, 1093 – 1109.

[5] Tauc J.V., Optical Properties of Solids, (1972), F. Abeles ed., North-Holland Publishing, Amsterdam.
[6] Ramya V., Neyvasagam K., Chandramohan R., Valanarasu S. and A.M.F. Benial, J Mater Sci: Mater Electron (2015), 26, 8489 – 8496.
[7] Schroder D.K., Semiconductor Material and Device Characterization, (2006), third ed., John Wiley & Sons, New York.

Synthesis and Structural Characterization of ZnO and TiO_2 Nanoparticles

Funda Aksoy Akgul[a], Guvenc Akgul[b]

[a]*Physics Department, Ömer Halisdemir University, TR-51240 Nigde, Turkey*
[b]*Bor Vocational School, Ömer Halisdemir University, TR-51700 Niğde, Turkey*

**e-mail corresponding author*: fundaaksoy01@gmail.com

Keywords: ZnO, TiO_2, NEXAFS

ABSTRACT

Transition metal oxides in nano-sized form provide a wide range of functional materials for industrial applications. In this study, titanium dioxide (TiO_2) and zinc oxide (ZnO) nanostructured materials were successfully fabricated by chemical vapor synthesis (CVS). Crystalline and local atomic structures of the prepared samples were examined through X-ray diffraction (XRD), synchrotron-based X-ray absorption near edge structure (XANES) and extended X-ray absorption fine structure (EXAFS) techniques. Based on the XRD results, a second phase(s) was not observed in the both fabricated nanostructures, and single-phase wurtzite and anatase structures were obtained in ZnO and TiO_2, respectively. Ti K pre-edge features of XANES spectrum indicated presence of six-fold coordinated Ti in TiO_2. Obtained results in this study clearly reveals that CVS is quite useful method in order to synthesize highly crystalline and single-phase metal oxide nanoparticles.

1. INTRODUCTION

In recent years, there is a challenge in science to prepare of nanoscale material with high crystalline quality. Nanoparticles with diameters ranging from 1 to 10 nm, consistent crystal structure, size, shape and a high degree of monodispersion have been achieved by means of several techniques. Chemical vapor synthesis (CVS) [1] is a remarkable method to prepare highly crystalline nanoparticles compared to other preparation methods. The process parameters in CVS can be adjusted to form nanoparticles instead of thin films. CVS can be also used to synthesize nanostructured powders with high purity for almost all materials due to the wide range of precursors available.

Transition metal (TM) oxides in nanometer scale have been gathered a lot of scientific interest due to the large variety of applications including catalysis, gas sensors, biochemistry, optoelectronic, spintronic, etc. [2]. Zinc oxide (ZnO) is one of the TM oxides and well known for its use in wide range of application potentials ranging from nano electronic science to UV emitting diodes and chemical sensors. ZnO is also an excellent candidate for room temperature diluted magnetic semiconductor. Doped ZnO can be also considered for spintronic applications. Titanium dioxide (TiO_2) is another promising TM oxide material. Particularly, nanocrystalline TiO_2 is widely used as heterogeneous catalyst, photocatalyst, solar cells, gas sensors, pigments, and various other items and devices. Excellent photocatalytic activity is observed in high crystallized and at particle sizes below 20 nm for TiO_2.

In this work, ZnO and TiO_2 nanoparticles were produced by CVS method. The local structures of the prepared nanoparticles were investigated through X-ray absorption near edge spectroscopy (XANES) and extended X-ray absorption fine structure (EXAFS).

2. RESULTS AND DISCUSSION

Nanosized ZnO and TiO_2 powders were synthesized by CVS. The schematic representation of CVS setup was illustrated in Fig. 1. Firstly, the precursor vapors were created in CVS. Diethylzinc (DEZ) as a zinc precursor and titanium tetraisopropyl (TTIP) as a titanium precursor was used, respectively. Then, the precursor vapors were transported into the hot wall reactor at 900 ºC using helium (1020 sccm) as carrier gas. In the hot wall reactor, the precursor decomposes and reacts with oxygen to form ZnO and TiO_2 nanoparticles. Only DEZ for ZnO nanoparticles and TTIP for TiO_2 nanoparticles were used. In this system, average particle size of synthesized ZnO and TiO_2 nanosamples was about 23 and 9 nm, respectively. The nanosamples were in starch powder and pressed as a pellet uniaxially.

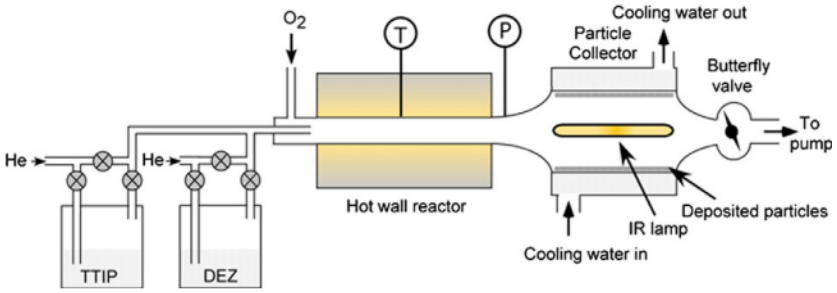

Figure 1. Schematic representation of chemical vapor synthesis setup (P: pressure gauge, T: thermocouple, IR: infrared, TTIP: titanium tetraisopopxide and DEZ: diethylzinc).

Crystal structure of the synthesized nanosamples was determined by X-ray diffraction (XRD) using a PANalytical X-ray diffractometer (X'Pert PRO) with Ni-filtered Cu-K_α (1.5406 Å) radiation produced at 40 kV and 40 mA. The data recorded over the 2θ range from 20º to 120º with a step size of 0.03º and a sampling time of 200 s/step was collected using X'Celerator detector. In Fig. 2, XRD spectra of the produced ZnO and TiO_2 nanoparticles were compared with the standard spectra. The XRD pattern of TiO_2 exhibits four distinctive peaks at 25.4º, 38.1º, 48.1º and 54.7º indicating TiO_2 in the anatase phase [3]. The formation of second phase(s) or impurities was not observed. Considering from this result it can be said that prepared nanosized TiO_2 sample has anatase structure. Also, XRD data of ZnO nanoparticles confirms the presence of single phase of wurtzite structure. The sharpness of XRD peaks demonstrates that the nanosamples have high crystallinity. Crystallite sizes of ZnO and TiO_2 can be calculated using Scherrer equation and were found to be about 11 and 5 nm for ZnO and TiO_2, respectively.

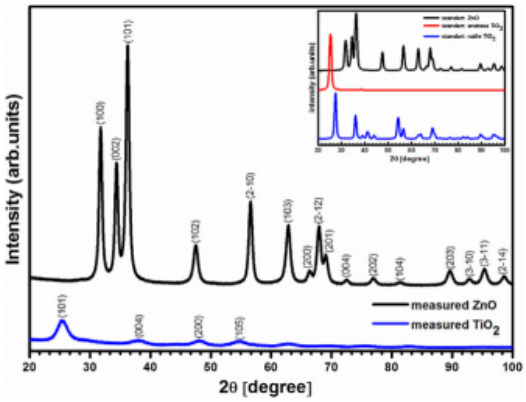

Figure 2. XRD patterns of synthesized nanoparticles and inset shows the standard spectrum of XRD patterns of the ZnO, anatase and rutile TiO_2 structures.

In general, XRD technique is not sensitive to segregation or the formation of small precipitates of second phase(s). Therefore, the prepared nanosamples were also studied by EXAFS to further verify the local structures and to clarify whether a second phase or phases exists or not. Fig. 3 shows normalized XANES spectra and theoretical calculation at Zn K edge of ZnO nanoparticles and Ti K edge of TiO_2 nanoparticles, respectively. XANES spectra of Zn K edge in ZnO do not possess any pre-edge peak as can be seen from the experimental spectra shown in the figure. The absence of pre-edge peaks can be explained based on the fact that all 3d band of Zn is occupied by 3d electrons. This was also confirmed for other sixfold coordinated Zn samples, such as $Zn(OH)_2$ and $ZnCO_3$ [4]. The rising edge energy difference between two main maximum of ZnO nanosample and Zn metal XANES spectrum was measured to be ~10 eV. This energy shift can be correlated with the oxidation state and bonding characteristics. Zinc linked to oxygen atoms

exhibits stronger bonding in the case of ZnO. Consequently, the absorption edge of ZnO shifts to higher photon energy side of XANES spectrum. Fig. 3(b) shows the normalized Ti K edge XANES spectra of the prepared TiO_2 nanosample together with the theoretical spectra of anatase and rutile TiO_2. The features labeled by C, D, and E have been widely studied and are not considered in detail below. We focus our discussion on the pre-edge structures. By comparison with the XANES spectra of ZnO shown in Fig. 3(a) one can see that the measured TiO_2 nanosample has pre-edge structures (A and B). Due to the tetrahedral geometry in TiO_2, the origin of pre-edge peak is not only attributed to 1s–3d transition, but also transition to the p component in p–d hybridized states. In the literature, it has been also concluded that pre-edge features are a powerful fingerprint to assign the coordination number of materials. In Fig. 3(b) the observed experimental spectrum of TiO_2 nanosample is quite similar to that for the theory of anatase structure rather than rutile. Therefore, this obtained result from XANES measurement of TiO_2 nanosample supports the obtained one from XRD data.

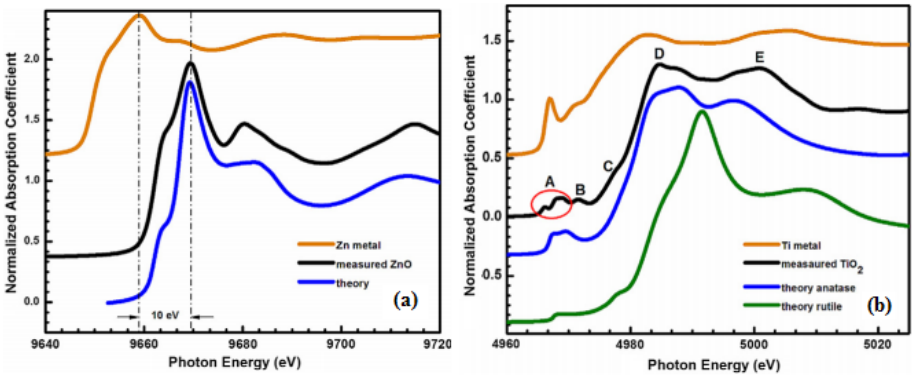

Figure 3. (a) Normalized XANES spectra and theoretical calculation at Zn K edge for ZnO nanoparticles. (b) Normalized XANES spectra and theoretical calculations at Ti K edge for TiO_2 nanoparticles.

EXAFS region reveals detailed information on local atomic structure of interested material complementary to that observed by diffraction methods. EXAFS is also preferred technique to investigate the atomic local structure of nanoparticles due to its excellent sensitivity to the short range order around absorbing atoms. EXAFS data was used to determine the location of the Zn and Ti ions in ZnO and TiO_2 nanosamples. The coordination numbers (N), the interatomic distances (R) and the disorder (Debye–Waller factor, σ^2) of the nanoparticles can be found performing data analysis of the experimental EXAFS spectra. EXAFS spectra were background subtracted and normalized at 9669 eV for ZnO and 4982 eV for TiO_2. Data in the k=3-12 $Å^{-1}$ range was Fourier transformed (FT) and fitted in real space in the R = 1–6 Å range for ZnO and TiO_2 nanosamples using a Hanning window function with k^2-weighted. For ZnO nanoparticles, the $k^2\chi(k)$ spectrum was obtained from the normalized experimental data and the theory obtained using FEFF8 and plotted in Fig. 4(a). The FT curve corresponding to this EXAFS oscillation was obtained after background subtraction and normalization procedure, and presented in Fig. 4(b). The qualitative EXAFS analysis was done by leastsquares fits of phase and amplitude functions generated by the FEFF6 code [5]. The fitting curve corresponding to the experimental data was also given in Fig. 4(b). The first two peaks for the ZnO nanosample were fitted using ARTEMIS including single scattering. The calculated FT showed two major peaks around 1.5 and 2.97 Å. It was used FEFFIT in combination with FEFF8 for data fitting. The ZnO and Zn–Zn bond lengths for first two coordination shells was obtained around 1.96 and 3.22 Å, respectively after the fitting procedure. These results are in accordance with all reported paper on ZnO compound in the single wurtzite type structure. Fig. 4(c) and (d) represents the EXAFS spectrum and corresponding FT curve, respectively. The curve fitting process was also performed in the range of 1–6 Å for TiO_2 nanosample for the best fitting. The best fit analysis of the EXAFS oscillations and the first two peaks in FT were done using the single-scattering approximation. These peaks are corresponding to the first two coordination shells around titanium. The first and second peak in FT which are composed of oxygen and titanium atoms were satisfied good agreement between theory and experimental EXAFS signals. The coordination numbers and interatomic distances in prepared TiO_2 nanosample agree well with the known structural values of anatase type structure of TiO_2. Thus, in addition to XRD, the presence of a crystalline anatase TiO_2 was further supported by XANES and EXAFS measurements. The all calculated values for the structural parameters of ZnO and TiO_2 nanosamples were summarized in Table 1.

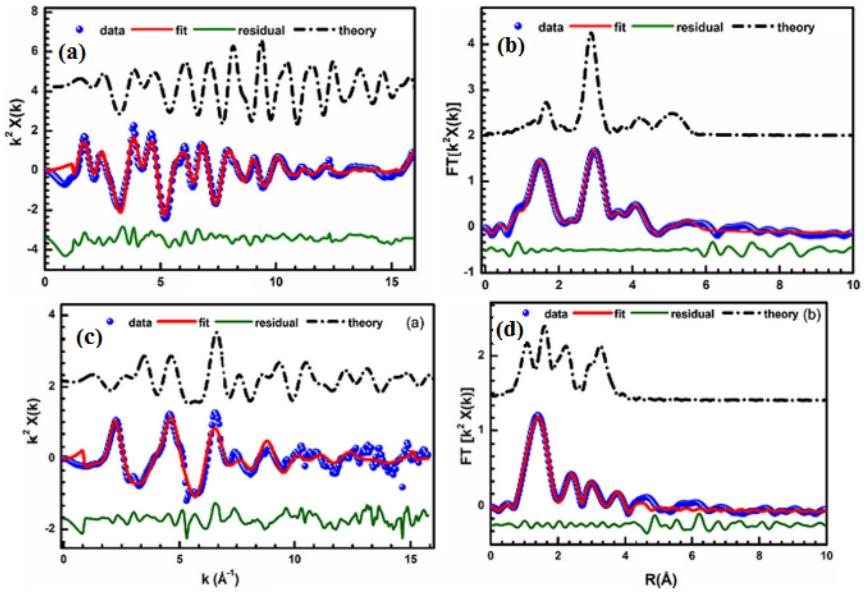

Figure 4. (a) Experimental EXAFS $k^2\chi(k)$ functions, theory and ARTEMIS fit. (b) Fourier transform magnitude of EXAFS data, theory and ARTEMIS fit for Zn K edge ZnO. (c) Experimental EXAFS $k^2\chi(k)$ functions, theory and ARTEMIS fit. (d) Fourier transform magnitude of EXAFS data, theory and ARTEMIS fit for Ti K edge TiO_2.

Table 1. Results of EXAFS data analysis using ARTEMIS for ZnO and TiO_2 nanoparticles

Nanosamples	Shell	Range (Å)	*N*	*R* (Å)	σ^2 (Å^2)
ZnO	Zn–O	1.7–2.2	4.1 ± 0.02	1.96 ± 0.02	0.007 ± 0.02
	Zn–Zn	2.3–4.0	11.5 ± 0.02	3.22 ± 0.02	0.009 ± 0.02
	Zn–O	2.3–4.0	10.5 ± 0.02	3.74 ± 0.02	0.011 ± 0.02
TiO_2	Ti–O	1.5–2.2	6.04 ± 0.02	1.94 ± 0.02	0.098 ± 0.02
	Ti–Ti	2.5–4.0	3.02 ± 0.02	3.04 ± 0.02	0.013 ± 0.02
	Ti–O	2.5–4.0	11.5 ± 0.05	3.81 ± 0.04	0.011 ± 0.02

3. CONCLUSION

In this study, ZnO and TiO_2 nanoparticles were successfully synthesized by CVS. The crystal and local atomic structures of the prepared nanosamples were probed by XRD, XANES, and EXAFS methods. In particular, a careful EXAFS analysis was performed to specify the qualitative information about the structural parameters of the nanosamples. No evidence of any secondary phases has been observed through XRD and EXAFS studies. The results have indicated that the CVS is considerable technique for many applications as a method of producing high crystallized materials with nanosized.

4. ACKNOWLEDGEMENTS

The authors would like to thank Dr. Nadia Leyarovska from APS, Argonne National Laboratory, IL, USA for technical support at the EXAFS beamline.

REFERENCES

[1] Brehm J., Winterer M., Hahn H., J. Appl. Phys. (2006), 100, 064311 – 064319.
[2] Hoffmann M.R., Martin S.T., Choi W., Bahnemann D.W., Chem. Rev. (1995), 95, 69 – 96.
[3] Thamaphat K., Limsuwan P., Ngotawornchai B., Kasetsart J., Nat. Sci. (2008), 42, 357 – 361.
[4] Akgul G., Aksoy Akgul F., Unalan H.E. and Turan R., Philosophical Magazine (2016), 96, 1093 – 1109.
[5] Zabinsky S.I., Rehr J.J., Ankudinov A., Albers R.C., Eller M.J., Phys. Rev. B (1995), 52, 2995 – 3009.

Phenotypic and Genotypic Characterization for Grain Yield in Wheat (*Triticum vulgare* L.)

Mehmet Emin Yazici[a], Ufuk Karadavut[b], Çetin Palta[c], Galip Şimşek[a], Kübra Soğanci[a]

[a]*Graduate School of Natural andAppliedSciences, Ahi Evran University, TR-40100 Kırşehir, Türkiye*
[b] *Department of Biometry and Genetics, Agricultural Faculty, Ahi Evran University, TR-40100 Kırşehir, Türkiye*
[c]*Department of Biosystem Engineering, Necmettin Erbakan University, TR-42150 Konya, Türkiye*

**e-mail corresponding author:galipsimsek@hotmail.com*

Keywords:Wheat, phenotypic and genotypic variance, heritability, genetic gain, yield

ABSTRACT

Genetic variability, heritability and genetic gains are very important for breeders. Selection characters can assist the plant breeder in ascertaining criteria. It can be used for the breeding programmers. Five wheat varieties were evaluated at the Konya Soil, Water and Deserting Control Research Institute. Plats are grown 2008 and 2009 vegetation seasons to estimate genetic variability, heritability and genetic advance of grain yield and its component characters. Genetic variance (δ^2g), genotype × year interaction (δ^2gy) variance, phenotypic variance (δ^2p), genotypic coefficient of variation (GCV) and phenotypic coefficient of variation (PCV) and environmental coefficient of variation (ECV) for grain yield and other related characters evaluated. As results, for heritability; plant height (cm) 95.36, ear height (cm) 93.48, number of grains/ear 94.14, ear weight (t/ha) 88.47, maize yield (t/ha) 97.63. For genetic advance; plant height (cm) 34.12, ear height (cm) 37.16, number of grains/ear 57.48, ear weight (t/ha) 33.64, wheat yield (t/ha) 30.08.

1. INTRODUCTION

Wheat is most important plant in the world. It provides to 35% of human-food. It als provide 20% of food calories. Global climatic change, shortage of water resources and worsening eco-environment effected significantly (Singh and Chaudhary, 2006). The yield of wheat is determined by some factors. These factors are productive spikes per unit area, kernel per spike and kernel weight (Collaku, 1994). One of major factor for its increasing has wheat yield improvement (Hill, 1975). For estimating of genetic variability is often considered a pre-requisite for initiating appropriate breeding procedures (De Vita et. al. 1007) . Therefore, the current study was undertaken with the aim of estimating genetic variability, heritability and genetic advance (Ludlow and Muchow, 1990).

Yield and its component are controlled by polygene. However, polygens are manipulated by environments (Ahmed et al., 2007). The high variation in this crop offers much scope for its improvement. Hence, genetic variation, heritability and genetic advance was succesfully estimated in the available germplasm of wheat (Manju and Sreelathakumary, 2002). The success of wheat improvement programme not only dependent on the amount of genetic variability in the population but also on the extent to which it is heritable, which sets the limit of progress that can be achieved through selection (Ali et. al., 1999; Gupta, 2006). If growing peirods have highly variable rainfall, irrigation won't be done. Since yield has a complex trait and is strongly influenced by the environment, losses can be caused by drought, a stress common in most arid and semiarid areas.

Heritability has predictive function of breeding crops (Songsri et al., 2008).It provides an estimate of genetic advance for breeders under certain environment and the utility of heritability therefore increases when it is used to calculate genetic advance (Atlin et. al., 2006). Thus, genetic advance is another important selection parameter (Shukla et al., 2004). In this study, we aimed to determine heritability and genetic advance for some whaet cultivars. In this study, we aimed to determine genetic variability, heritability and genetic gains for wheat cultivars.

Material and method

This study was conducted in the test field of Konya Soil, Water and Deserting Control Research Institutefor 2 years in 2008 and 2009. In the province of Konya which is located in Central Anatolia Region, it is hot and dry in summers, rainy in springs and harsh and cold in winters. Konya 2002, Ahmetaga, Meram, Gerek and Tosunbey were used as materials. The trials were conducted in the randomized blocks were conducted with 4 repetitions

Sowing were done in November. First year sowings of tests were conducted on 15 November and second year sowings were conducted on 14 November. The sowing procedure was manually made in the areas opened with marker. Along with the sowing, fertilizer was applied in the form of 5 kg pure nitrogen and 5 kg phosphor per decare. Every parcel consisted of 8 rows at the length of 5 meters. The variance analysis was applied in accordance with the test pattern of parcels divided into two years data acquired at the end of test and the differences between the averages were tested in accordance with the LSD multiple comparisons method (DÜZGÜNEŞ ve ark., 1987).

Also, the correlation analysis was applied in order to determine the correlation between the variables. Also heritability and genetic advance were determined every character.

2. RESULTS AND DISCUSSION

The analysis of variance revealed significantly differences. Especially, mean squares of genotypes were significant for all traits. The cultivars have different high degree of genetic variability. This indicates to will be used as a material in breeding programs (Table 1). Gerek cultivar has the most plant height and 1000 seed weight. , 50% heading date and yeild was higher than other characters. Konya cultivar showed better performance under stress conditions. Ahmedag showed the lowest performance. This results show that Ahmetaga will be efficient in terms of reducating producers under stress conditions. Foulkes et al., (2004) explained the adaptability of plants under water stress conditions have less. When wheat plants are deprived of water at vegetative and flowering stages (Holland, 2007)), shorter plants are obtained as a result of low moisture absorption, lower soil absorption, lower soil nutrient uptake, reduced cell size and reduced photosynthesis (Ahmed anr Khalil., 2007). While the coefficient of variation was the lowest in the weight of a thousand, the highest value of it was in the yield. Yields are the most affected by environmental conditions feature. It shows us the impact of the observed variations in climate (Aziz et.al., 1998).

Table 1. The results of Duncan Multiple Comparison Test

Cultivars	Plant Height (cm)	Spike Length (cm)	50% Heating Date (day)	1000 Seed yield (g)	Yield (kg/da)
Konya2002	92.6 b	10.1 a	196 a	27.3 b	263 a
Ahmetaga	87.1 c	9.4 b	192 a	25.8 c	246 b
Meram	97.4 a	10.2 a	201 a	27.1 b	261 a
Gerek	98.4 a	9.4 b	190 a	28.6 a	255ab
Tosunbey	87.5 c	9.5 b	194 a	25.9 c	253 ab
Means	92.6	9.7	194.6	26.9	255.4
CV (%)	7.85	5.42	12.7	1.9	14.2

Table 2. Genetic Correlation amoung the characters under controlled and sressed conditions

Traits	Plant Height (cm)	Spike lenght (cm)	50% Heading date (day)	1000 seed weight (g)	Yield (kg/da)
Plant height (cm)	-	0,363	-0,205	0,378	0,402
Spike lenght (cm)		-	-0,416**	0,562**	0,573**
50% Heading date (day)			-	-0,225	0,466*
1000 seed weight (g)				-	0,783**
Yield (kg/da)					-

Table 3. Genetic Correlation amoung the characters under controlled and sressed conditions

Traits	S_g^2	S_e^2	S_p^2	GCV	PCV	H	GA
Plant height (cm)	87,14	3,87	101,6	10,44	9,87	0,2356	5,78
Spike lenght (cm)	0,42	0,64	1,13	8,41	9,14	0,4709	27,11
50% Heading date (day)	5,12	0,96	2,86	2,33	2,75	0,5677	1,07
1000 seed weight (g)	0,41	0,03	0,17	13,44	13,26	0,6223	18,36
Yield (kg/da)	1,13	0,56	1,02	14,19	15,22	0,7077	21,02

S_g^2: Genotypic varince, **S_e^2:**Environmental variance, **S_p^2:**Phenotypic variance, **GCV:**Genotypic coefficient of variation, **PCV:**Phenotypic coefficient of variation, **H:**Heritability, **GA:**Genetic advance

Plant height has been observed to be heihger Genotypic varince, Environmental variance and Phenotypic variance than other characaters. However, it had the lowest value of heritability. 1000 seed weiht has the lowest values of Genotypic varince, Environmental variance and Phenotypic variance. This results coincided with Ma et. al., (2007). This is perhaps due to differences in breeding material or variation in environment or interaction. genetic advance should be considered along with heritability in coherent selection breeding program.

3. CONCLUSION

The genetic parameters can differ environmental variability. And they are function of environment. Based on the high heritability and high genetic advance revealed 1000 seed weight and grain yield. It can be said that genetic effects and phenotypic expression of these characters are additive type (Hassan, 2004). Yield and yield characters depend on different environments (Collaku, 1994). And for this reason, environmental variables should be controlled and optimized. If they are controlled as possible, the relative effect of genotype and environment interaction will be minimized.

REFERENCES

[1] Ahmed Ncm, Khaliq Imm. The İnheritance Of Yield And Yield Components Of Five Wheat Hybrid Populations Under Drought Conditions. Indonesian J. Agric. Sci., (2007), 8(2): 53-59.

[2] Aziz, K.; Rehman, A.; Rauf, A.. Heritability AndInterrealtionships For Some Plant Traits In Maize Single Crosses.Pak. J. Biol. Sci.(1998), 1(4):313-314.

[3] Collaku A. Selection For Yield And İts Components İn A Winter Wheat Population Under Different Environmental Conditions in Albania. Plant Breed., (1994), 112(1): 40-46.

[4] De Vita, P., O. Li Destri Nicosia, F. Nigro, C. Platani, C. Riefolo et al.,Breeding progress in morpho-physiological, agronomical and qualitative traits of durum wheat cultivars released in Italy during the 20th century. Eur. J. Agron. (2007) 26: 39–53.

[5] Düzgüneş, O., Kesici, T., Kavuncu, O., Gürbüz, F. Araştırma ve Deneme Metotları. Ankara Üniversitesi, Ziraat Fakültesi Yayınları, Ankara, (1987),381s.

[6] Foulkes M, Verma R, Sylvester R, Weightman R, Snap J. Traits For İmproved Drought Tolerance Of Winter Wheat İn The Uk. Proceeding Of The 4 Th İnternational Crop Science Congresses. (2004).

[7] G.N. Atlin, H.R. Lafitte, D. Tao, M. Laza, M. Amante, B. Courtois, Developingricecultivarsforhigh-fertilityuplandsystems in theAsiantropics, FieldCropsResearch, (2006),97, pp. 43–52.

[8] Gupta, P. K., S. Rustgi and N. Kumar, Genetic and molecular basis of grain size and grain number and its relevance to grain productivity in higher plants. Genome.(2006), 49: 565–571.

[9] Hassan G. Diallel Analysis Of Some İmportant Parameters İn Wheat (Triticum Aestivum L.) Under İrrigated And Rainfed Conditions. Phd. Agricultural University, Peshawar, Pakistan. (2004).

[10] Hill, J.,Genotype-environment interactions-a challenge for plant breeding. J. agric. Sci., Camb. (1975), 85: 477–493.

[11] Holland, J. B., Genetic architecture of complex traits in plants. Curr. Opin. Plant Biol.(2007),10: 1–6.

[12] Ludlow, M. M., and R. C. Muchow, A critical evaluation of traits for improving crop yields in water-limited environments. Adv. Agron. (1990),43: 107–153.

[13] M. Ali, C.R. Jensen, V.O. Mogensen, M.N. Andersen, I.E. Henson. Root signaling and osmotic adjustment during intermittent soil drying sustain grain yield of field grown wheat. Field Crops Research, (1999), 62, pp. 35–52

[14] Ma, Z., D. Zhao, C. Zhang, Z. Zhang, S. Xue et al., Molecular genetic analysis of five spike-related traits in wheat using RIL and immortalized F2 populations. Mol. Genet. Genomics. (2007),277: 31–42.

[15] Manju P. R. And I. Sreelathakumary, Genetıc Varıabılıty, Herıtabılıty And Genetıc Advance In Hot Chıllı (*Capsıcum Chınense* Jacq.). Journal Of Tropical Agriculture.(2002),40 (2002): 4-6

[16] Shukla S, Bhargava A, Chatterjee A, Singh S. Estimates Of Genetic Parameters To Determine Variability For Foliage Yield And İts Different Quantitative And Qualitative Traits İn Vegetable Amaranth (A. Tricolor). J. Genet. Breed.(2004),58: 169-176.

[17] Singh G, Chaudhary H. Selection Parameters And Yield Enhancement Of Wheat (Triticum Aestivum L)Under Different Moisture Stress Condition. Asian J. Plant Sci.(2006), 5: 894-898.

[18] Songsri P, Joglloy S, Kesmala T, Vorasoot N, Akkasaeng Cpa, Holbrook C. Heritability Of Drought Resistance Traits And Correlation Of Drought Resistance And Agronomic Traits İn Peanut. Crop Sci.(2008), 48:2245-2253.

Fabrication of CdTe-Si Nanowire Heterojunctions for Photodetector Applications

Guvenc Akgul[a], Funda Aksoy Akgul[b]

[a]*Bor Vocational School, Ömer Halisdemir University, TR-51700 Niğde, Turkey*
[b]*Physics Department, Ömer Halisdemir University, TR-51240 Nigde, Turkey*

**e-mail corresponding author*: guvencakgul@gmail.com

Keywords: CdTe, Si nanowires, RF magnetron sputtering

ABSTRACT

In this study, a facile and inexpensive electroless etching method were applied to synthesize vertically aligned Si nanowires on n-type single crystalline (100)-oriented Si wafer. Three dimensional CdTe/Si heterojunction structures were successfully fabricated by coating of CdTe thin films on the Si nanowire arrays by RF magnetron sputtering, and their optoelectronic characteristics and photodetection properties were investigated. A decent rectifying behavior with a high rectification ratio of 10^5 at ±4 V and a relatively small ideality factor of 1.8 were observed at room temperature in the dark. An open circuit voltage were determined to be 0.12 V under AM 1.5G illumination. A distinct responsivity together with a high detectivity were detected by means of photoresponsivity measurements. The observed properties clearly reveals that the investigated Si nanowire-based heterojunction diodes could be a promising candidate for high-performance and low-cost next-generation optoelectronic devices, near-infrared photodetectors in particular.

1. INTRODUCTION

One-dimensional Si nanostructures such as nanowires reveal noticeable electronic performance in microelectronic devices because of their attractive physical properties which are differ from those of typical bulk counterparts [1]. Utilization of the nanowire junctions instead of typical planar junctions in Si-based thin film devices causes an increase in the amount of absorbed light by the device surface and a decrease the high recombination rate in the junction. In addition, increased surface area of the nanowires can lead to the enhanced optoelectronic properties in the devices. There are numerous successful techniques to fabricate the Si nanowires. Electroless etching is a simple and low-cost process using fewer amounts of materials for the Si nanowires synthesis with ability to control the length of the nanowires [2].

Si nanowires complemented with organic or inorganic materials are of interest for a variety of optoelectronic device applications due to its geometrical advantages relating to the junction area. Different semiconductor materials can be combined with the Si nanowire arrays to form heterostructures which gives them functionalities like p–n heterojunctions. Integration of semiconductor cadmium telluride (CdTe) with Si may be a promising route toward effectively utilization of the solar light for optoelectronic applications. Despite a great number of individual studies on the CdTe and Si, very little effort focusing on combined system of these two materials has been done in the published literature. However, to the best of our knowledge, no comparable study is presented on the fabrication and characterization of the CdTe thin film/Si nanowire heterojunctions in the literature.

This paper presents the fabrication and characterization of CdTe thin film/Si nanowire heterojunction photodiodes. RF magnetron sputtering method was used for the deposition of a thin CdTe layer on the Si nanowire arrays. The fabricated nanowire-based devices consisted of vertically oriented n-type Si nanowires complemented with the p-type CdTe film. The planar heterojunction device was also fabricated

as a reference sample.

2. RESULTS AND DISCUSSION

One side polished n-type Si wafers (400 μm thickness, (100) orientation, 1-10 Ω.cm resistivity) were well cleaned and highly oriented Si nanowire arrays were produced by typical electroless etching method, as discussed in a previous work [2]. Fabricated Si nanowire arrays and a flat Si wafer were immediately placed into the RF sputtering system for the deposition of CdTe thin films. A CdTe target (99.99%, in 3 in. diameter) was used for the deposition. RF power applied for the deposition was 70 W at a deposition rate of 2.5 Å/s. During deposition, substrates were kept at 200 ºC. The fabrication of the heterojunction devices was completed by the thermal evaporation of gold (Au) and silver (Ag) ohmic front and back contacts, respectively. A final annealing treatment at 180 ºC for 10 min was applied to facilitate the formation of ohmic contacts. The average device area was about 4 cm^2.

The surface morphology of the as-grown Si nanowires and fabricated devices were obtained through Nova Nano-SEM 430 model field emission scanning electron microscope (FESEM) operated at 10 kV. A top-view SEM image obtained from the CdTe thin films deposited onto the planar Si substrate is provided in Fig. 1(a). Non-uniform distribution of the CdTe nanoparticles on the planar substrate is evident. The corresponding film thickness was measured to be around 500 nm from the cross-sectional SEM image (see inset of Fig. 1(a)). A cross-sectional SEM image of the CdTe thin film deposited onto Si nanowires is provided in Fig. 1(b). It is quite clear from the image that the CdTe thin film deposited onto nanowire arrays forms a continuous film at top of the nanowire arrays. As clearly, the film packing on the Si nanowires increases from the bottom toward the top, resulting in formation of matchstick-like structures. The cross-sectional SEM image of the as-prepared Si nanowires (length of approximately 1 μm) is provided as an inset in Fig. 1(b), for comparison.

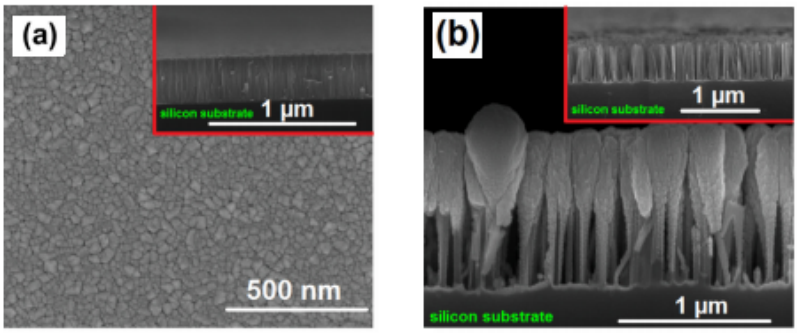

Figure 1. (a) Top-view SEM image of CdTe thin film deposited on planar Si wafer. (b) Cross-sectional SEM image of the CdTe/Si nanowire heterojunction structure. The insets show the cross-sectional SEM image of CdTe thin film deposited onto planar Si wafer and the as-fabricated Si nanowire arrays on n-type Si substrate, respectively.

In order to unveil the electrical properties of the fabricated heterojunction devices, *I-V* measurements were conducted by LabVIEW controlled Keithley 2400 source meter and an AM 1.5G solar simulator controlled with Newport *I-V* test software. Fig. 2(a) shows typical semilogarithmic *I-V* characteristics of the nanowire-based and planar heterojunctions measured both in the dark and under illumination at room temperature. Decent rectifying properties were obtained from both nanowire-based and planar heterojunction devices. Rectifying behaviors indicated the formation of p–n junctions within the devices. Rectification ratios of 10^5 and 10^3 (I_F/I_R taken at ±5V) were obtained for the nanowire-based and planar heterojunction, respectively. It is clear that the diode performance of the heterojunction with nanowires was superior compared to the planar counterpart. The difference between the rectification ratios could be attributed to the enhanced surface area due to the three-dimensional nature of the Si nanowires. In addition, increased interfacial area on the nanowire surfaces can minimize the structural disorders in the thin films such as crystal defects or dislocations leading to a stress relief [2]. Photocurrent to dark current ratio was obtained to be 2339 and 192 at ±5 V for the nanowire-based and planar devices, respectively. This considerable improvement of the current ratio in the nanowire-based device manifests the formation of a remarkable heterojunctions on nanowires. Moreover, reverse leakage currents were found to be approximately 45 and 230 nA for the nanowire-based and planar devices in the dark at a reverse bias of 5 V. The reverse leakage current of the device with nanowires is almost 5-fold lower than that of the planar device. Further and important diode

parameters such as ideality factor (n) and series resistance (R_s) were obtained from the measured I-V characteristics of the devices. The diode properties of the fabricated devices have analyzed using the standard diode equation. The ideality factor of the diodes was found to be 1.9 and 3.2 for the nanowire-based and planar devices, respectively. The ideality factor of the planar heterojunction was found to be higher than $n = 1$. This is due to the parasitic generation and recombination at the interface states [3]. The values of I_0 were found to be 2.06 and 15.2 nA for the nanowire-based and planar diodes, respectively. I-V characteristics of the diodes are strongly affected by the parasitic resistances such as series resistance (R_s). The value of the R_s was calculated to be 1.84 kΩ for the nanowire-based diode, and 58 kΩ for the planar diode. It is clear that the use of nanowires for the fabrication of heterojunction devices significantly decreased the R_s. High series resistance is known to cause non-ideal diode behavior, deteriorating the device performance.

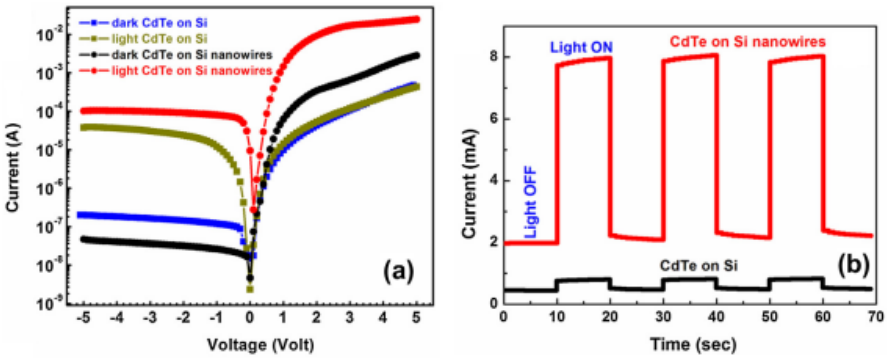

Figure 2. a) Semilogarithmic plot of current–voltage (I-V) characteristics measured in the dark and under AM 1.5 G illumination at room temperature. (b) Light ON/OFF characteristics of Si nanowire-based and planar heterojunction diodes.

The reflection of the light from the device surface is the one of the loss mechanisms that decreases the efficiency of the photodetectors. Mostly, anti-reflection coatings are used to minimize such losses [4]. Reflection of fabricated heterojunction diodes are provided in Fig. 3(a). The nanowire-based device exhibited an average reflectance of less than 4%, in comparison to 35% for the planar device within the investigated wavelength range. Improved antireflective performance of the devices with Si nanowires could also contribute to the enhanced optoelectronic performance of the devices.

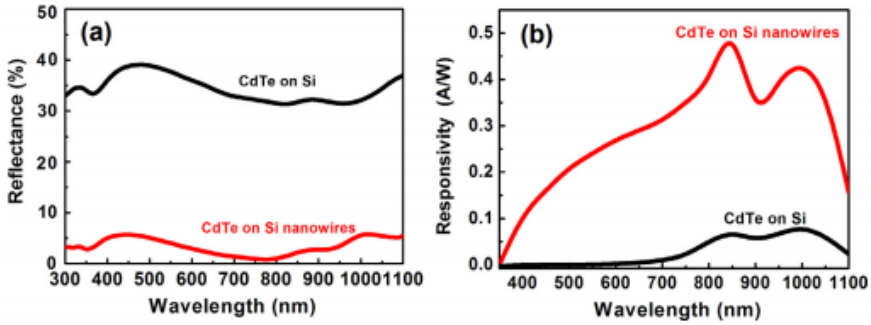

Figure 3. (a) Reflectivity and (b) responsivity of Si nanowire-based and planar heterojunction diodes.

The responsivity of a photodiode is defined as the ratio of photocurrent density to the intensity of incident light at a certain wavelength and shows the photoelectric sensitivity of the diode to incident light energy. Fig. 3(b) shows the spectral response of the fabricated heterojunction diodes measured using a calibrated light source under a reverse bias of 2 V. Two pronounced device features shows two humps located at 845 nm and 1000 nm are evident in the spectra which are associated with the absorption edges of p-type CdTe thin film and n-type Si, respectively. The planar reference device shows a photoresponse within the wavelength range of 700–1000 nm, and no response is obtained for the incoming photons with the wavelengths shorter than 700 nm. The maximum responsivity is 0.08 A W^{-1} at the wavelength around 1000 nm. On the other hand, a large enhancement in responsivity over the broad spectral range is observed for the nanowire-based heterojunction diode. Both the range of detection and signal intensity are substantially higher as opposed to planar control sample. The detection window is extended to the ultraviolet region.
The detectivity (D) and external quantum efficiency (EQE) for a photodiode are a figure of merits used for the characterization of the device performance. The detectivity characterizes normalized signal to noise

performance of a detector and can be determined using the equation in ref. [5]. Fig. 4(a) shows the spectral detectivity of fabricated devices. The detectivity was found to be higher for the CdTe thin film/Si nanowire heterojunction device as compared to the planar reference sample. External quantum efficiency (EQE) of the fabricated heterojunction photodiodes was estimated using the relation in ref. [5]. The obtained spectral EQE (%) curve is shown in Fig. 4(b). It was noticed that the EQE is higher for the nanowire-based device than that of the planar control device over the entire wavelength range. The high EQE of the nanowire-based device indicates the effect of enhanced light absorption within the Si nanowire arrays (as shown in Fig. 3(a)) resulting in effective electron–hole pair generation, separation in the junction, and transportation of the photogenerated charge carriers toward metallic contacts, and consequently efficient collection leading to a higher photocurrent.

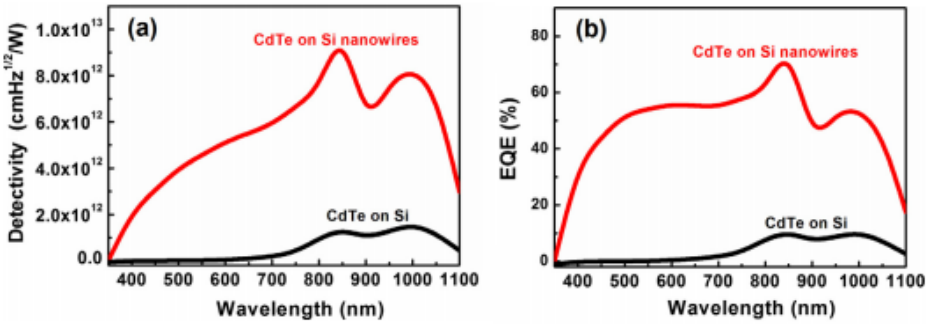

Figure 4. Calculated (a) detectivity and (b) external quantum efficiency (EQE) of Si nanowire-based and planar heterojunction diodes at a reverse bias of 2 V at room temperature.

3. CONCLUSION

In summary, heterojunction diodes composed of CdTe thin films and vertically well-oriented Si nanowire arrays were successfully fabricated and their photodiode properties were systematically characterized. Si nanowire-based device clearly demonstrated exceptional improvements in the electrical and optoelectronic properties. The higher rectifying ratio, lower ideality factor, reduced reverse leakage current and series resistance were obtained. A relatively fast photoresponse (<1 s) was measured. Photoresponsivity measurements revealed that the device with Si nanowire arrays was sensitive to near-infrared wavelengths and showed approximately seven times higher sensitivity (at 845 nm). In this respect, we believe that the CdTe thin film/Si nanowire heterojunction device structure with significant improvement in sensitivity and detectivity could be a promising alternative to existing optoelectronic devices.

4. ACKNOWLEDGEMENTS

G.A. and F.A.A. would like to thanks The Scientific and Technical Research Council of Turkey (TUBITAK) Post-Doctoral Fellowship for financial support.

REFERENCES

[1] Peng K.Q., Wang X., Li L., Wu X.L., Lee S.T., J. Am. Chem. Soc. (2010), 132, 6872 – 6873.
[2] Akgul G., Aksoy Akgul F., Mulazimoglu E., Unalan H. E. and Turan Rasit, J. Phys. D: Appl. Phys. (2014), 47, 3065106-1 – 3065106-7.
[3] Kulakci M., Colakoglu T., Ozdemir B., Parlak M., Unalan H.E., Turan R., Nanotechnology (2013), 24, 375203 – 375210.
[4] Srivastava S.K., Kumar D., Singh P.K., Kar M., Kumar V., Husain M., Sol. Energy Mater. Sol. Cells (2010), 94, 1506 – 1511.
[5] Katiyar A.K., Sinha A.K., Manna S., Aluguri R., Ray S.K., Phys. Chem. Chem. Phys. (2013), 15, 20887 – 20893.

Ga-doped ZnO/Si Heterojunction Nanodiodes: Fabrication and Characterization

Guvenc Akgul[a], Funda Aksoy Akgul[b]

[a]*Bor Vocational School, Ömer Halisdemir University, TR-51700 Niğde, Turkey*
[b]*Physics Department, Ömer Halisdemir University, TR-51240 Nigde, Turkey*

**e-mail corresponding author*: guvencakgul@gmail.com

Keywords: Ga-doped ZnO thin films, Si nanowires, heterojunction diodes

ABSTRACT

In this study, temperature-dependent electrical properties of n-type Ga-doped ZnO thin film/p-type silicon (Si) nanowire heterojunction diodes were reported. Facile and cost-effective metal-assisted chemical etching (MACE) process was performed to synthesize Si nanowires. Ga-doped ZnO thin films were then deposited onto Si nanowires through chemical bath deposition (CBD) technique to build three-dimensional nanowire-based heterojunction diodes. Fabricated devices revealed significant diode characteristics in the temperature range of 220 - 360 K. Electrical measurements shown that diodes had a well-defined rectifying behaviour with a good rectification ratio of 10^3 ±3 V at room temperature in dark condition. A relatively low values for the ideality factor (*n*) were found at all temperatures and they changed from 2.2 to 1.2 with increasing temperature.

1. INTRODUCTION

Semiconductor p-n heterojunction structures are basic elements in modern microelectronic and energy conversion devices, and play crucial roles as either functional or interconnecting elements [1]. Nanoscale heterojunctions showing advantages with respect to their conventional film and bulk conjugates have promoted device applications of the nanostructures. Particularly, silicon (Si) nanowire based heterojunctions have been regarded as novel and promising for their potential applications in solar cells and photodetectors [2]. In order to investigate the potential applications of the Si nanowires, several kinds of heterojunction structures have been designed and a variety of organic or inorganic compounds including metal oxides have been used in these structures as complementary materials. Particularly, transparent metal oxide thin films have recently become one of the attractive materials and are strong candidates that can be integrated into Si nanowires due to the combination of their excellent electrical properties. Most previous studies have focused on the development of gallium doped zinc oxide (Ga-doped ZnO) transparent metal oxide thin films for display, optoelectronic and solar cell applications. However, few studies have focused on the characteristics of solution-based derived Ga-doped ZnO semiconductor thin films [3].

In this study, p-n heterojunction nanodiodes were fabricated by deposition of n-type Ga-doped ZnO thin films onto the vertically aligned Si nanowires by chemical bath deposition (CBD) technique, and temperature-dependent electrical properties of the fabricated devices were analyzed in detail. It is inevitable that the results will be very important as a starting point for further applications in transparent electronics.

2. RESULTS AND DISCUSSION

All chemicals were purchased from Merck and used without further purification. Ga-doped ZnO semiconductor films were prepared by CBD method. Firstly, 0.22 g zinc acetate [$Zn(CH_3COO)_2.2H_2O$] was dissolved in 100 ml I-propanol ($CH_3CH_2CH_2OH$). Afterwards, 0.012 g gallium nitrate ($Ga(NO_3)_3.H_2O$) was added to the mixed solution as dopant source. Each complex solution was stirred for 45 min. using magnetic stirrer. The resultant solution was aged for 24 h. at room temperature. For Si nanowires fabrication, metal-assisted chemical etching (MACE) method was reported in previous study [4]. Before the deposition, p-type Si substrates (B-doped, (100) orientation, 1-10 Ω.cm resistivity) were well cleaned as reported elsewhere. Si nanowire substrates dipped vertically into the prepared solution in order to construct Si nanowire based p-n heterojunction nanodiodes. The substrates were taken out from the bath after 5 min. The samples were exposed to a heat-treatment process at 150 ºC for 5 min. for better adhesion of the thin films onto Si nanowires. Dipping/drying cycle was repeated as many times as desired in order to get sufficient film thickness.

The surface morphology and cross-sectional images of the as-grown Si nanowires and fabricated devices were obtained through Nova Nano-SEM 430 model field emission scanning electron microscope (FESEM) operated at 10 kV. Cross-sectional FESEM images were obtained from the cleaved edges of Si wafer substrates. Fig. 1(a) and Fig. 1(b) show top-view and cross-sectional FESEM image of the fabricated bare Si nanowires, respectively. A p-type Si wafer was etched for 10 min. to synthesize 1 µm long nanowires. It is clearly seen from the images that the nanowires are highly densely and vertically well-oriented on the Si substrate.

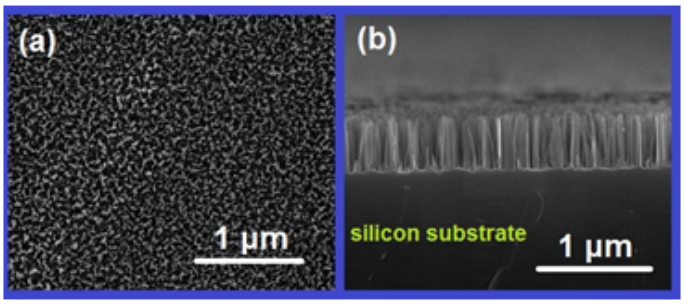

Figure 1. Top-view (a) and cross-sectional (b) FESEM image of bare Si nanowires.

Prior the deposition of the complementary Ga-doped ZnO films onto the fabricated Si nanowires, the substrates were meticulously cleaned to remove native oxide layer. Afterwards, Ga-doped ZnO thin films were deposited onto Si nanowire arrays by CBD technique in order to build p-n heterojunction structures. Finally, the fabricated devices were subsequently annealed at 500 °C for 10 min. before the thermal evaporation of front and back metallic contacts. Fig. 2(a) and (b) show top-view and cross-sectional FESEM image of Ga-doped ZnO coated Si nanowire arrays, respectively.

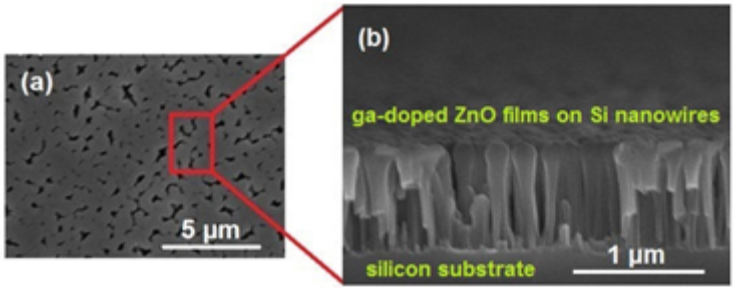

Figure 2. Top-view and (a) and (b) cross-sectional FESEM image of Ga-doped ZnO thin film coated Si nanowire arrays.

It is obvious from Fig. 2 that Ga-doped ZnO films cover the nanowire surfaces from their bottom to their top. The film packing on Si nanowire arrays increases from the bottom towards the top, resulting in the formation of matchstick-like nanosized heterojunctions. In this study, Ga-doped ZnO thin films were

deposited onto Si nanowire arrays and glass substrates during the same amount time under identical processing conditions. The corresponding thickness of Ga-doped ZnO film deposited onto glass substrates was measured to be about 200 nm. The apparent thickness of the thin film on the Si nanowires was different than that of the films deposited onto glass substrates because of the three dimensionality (3D) and high roughness of Si nanowire surfaces. 3D nature of the junction interface within the nanowire-based devices causes an interface closer to the thin film surface.

Electrical characteristics of the Si nanowire based heterojunction nanodiodes were determined by current-voltage (*I-V*) measurements. The measurements were taken in the temperature range of 220 - 360 K with applied voltage at ± 3V in the dark. Fig. 3(a) and (b) show the room temperature (300 K) typical and semi-logarithmic *I-V* characteristics of the fabricated nanodiodes, respectively. At room temperature, good rectifying *I-V* behavior was observed from the fabricated nanodevices. This result confirms the successful formation of p-n junctions for Ga-doped ZnO thin film/Si nanowires heterojunction structure. The rectification ratio up to 10^3 (I_F/I_R taken at ± 3V) was obtained under dark condition. This observation clearly demonstrates the formation of highly effective depletion region between the deposited thin film and Si nanowire surfaces.

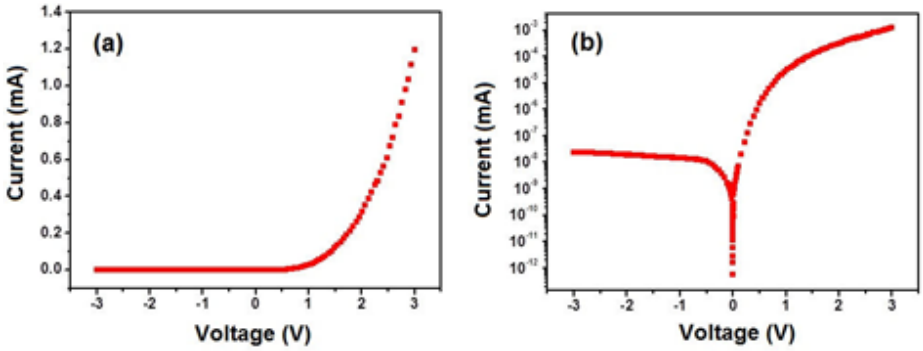

Figure 3. Typical (a) and semi-logarithmic (b) *I-V* characteristics of the fabricated nanodiodes at room temperature.

Diode parameters such as ideality factor (n), dark saturation current (I_0) and barrier height (Φ_B) can be obtained from the measured *I-V* characteristics of the heterojunction nanodevices under dark conditions. For the relatively low forward bias voltages, the *I-V* characteristics can be described by the conventional diffusion-recombination model [5]. *I-V* characteristics of the fabricated devices in the temperature range of 220 - 360 K were measured and are provided in Fig. 4 to determine the device parameters of the heterojunction nanodiodes.

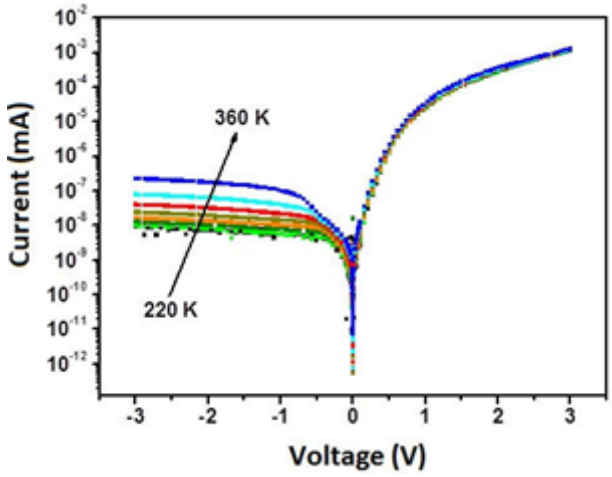

Figure 4. Semi-logarithmic *I-V* plots of fabricated heterojunction nanodiodes at different temperatures.

The device parameters of the heterojunction nanodiodes calculated from the temperature dependent *I-V* analysis are listed in Table 1. Table 1 shows that the Φ_B values increase with increasing temperature since

more carriers have enough energy to overcome the barriers and contributed to the conduction with increasing temperature that is the reason of increasing potential barrier height with the temperature. In addition, the ideality factor n values decreases with increasing temperature on the contrary to the Φ_B. The n could be utilized to achieve the information about current transport mechanism of the fabricated heterojunction devices. It can be seen that the calculated n values are higher than one. This indicates that there could be other transport mechanisms different from the pure thermionic emission mechanism in which $n = 1$ [6].

Table 1. Device parameters of fabricated heterojunction nanodiodes calculated from the temperature dependent *I-V* analysis

T (K)	n	I_0 [A]	Φ_B [eV]
220	2.21	9.8×10^{-11}	0.67
240	1.64	1.1×10^{-10}	0.73
260	1.45	2.3×10^{-10}	0.78
280	1.4	2.7×10^{-10}	0.83
300	1.32	4.2×10^{-10}	0.89
320	1.3	5.2×10^{-10}	0.94
340	1.22	8.4×10^{-10}	0.98
360	1.16	2.1×10^{-9}	0.99

3. CONCLUSION

In this study, temperature-dependent electrical characteristics of Ga-doped ZnO thin film/Si nanowires heterojunction nanodiodes were investigated. p-type Si nanowires were synthesized by the MACE method, and high-quality n-type Ga-doped ZnO films were successfully deposited onto the nanowire arrays using the CBD to construct heterojunction nanodiodes. Fabricated nanodevices showed a good p-n characteristics in the dark conditions at room temperature. The diode parameters such as ideality factor, reverse saturation current and effective potential barrier height of the fabricated nanodiodes were obtained from the temperature-dependent *I-V* measurements. The observed diode performance in this study clearly showed that the fabricated device structure could be a promising alternative candidate for high-performance low-cost optoelectronic device applications in future.

4. ACKNOWLEDGEMENTS

G.A. and F.A.A. would like to give thanks to Research Projects Unit of Ömer Halisdemir University (The Project Code: FEB 2014/25-BAGEP and The Project Code: FEB 2014/26-BAGEP) for the financial support.

REFERENCES

[1] Yang C., Barrelet C.J., Capasso F. and Lieber C.M., Nano Letters (2006), 6, 2929 – 2934.
[2] Cui Y., Zhong Z., Wang D., Wang W.U. and Lieber C.M., Nano Letters (2003), 3, 237 – 241.
[3] Park W.J., Shin H.S., Ahn B.D., Kim G.H., Lee S.M., Kim K.H. and Kim H.J., Appl. Phys. Lett. (2008), 93, 083508-1 – 083508-3.
[4] Akgul G., Aksoy Akgul F., Mulazimoglu E., Unalan H. E. and Turan Rasit, J. Phys. D: Appl. Phys. (2014), 47, 3065106-1 – 3065106-7.
[5] Schroder D.K., Semiconductor Material and Device Characterization, (2006), 3rd ed., John Wiley & Sons, New York, NY.
[6] Aurang P., Demircioglu O., Es F., Turan R. and Unalan H.E., J. Am. Ceram. Soc. (2013), 96, 1253 – 1257.

Structural Characterization of Zinc Titanates Nanocomposites by X-Ray Absorption Spectroscopy

Guvenc Akgul[a], Funda Aksoy Akgul[b]

[a]*Bor Vocational School, Ömer Halisdemir University, TR-51700 Niğde, Turkey*
[b]*Physics Department, Ömer Halisdemir University, TR-51240 Nigde, Turkey*

**e-mail corresponding author*: guvencakgul@gmail.com

Keywords: Zinc Titanates, XRD, EXAFS

ABSTRACT

Zinc titanates ($ZnTiO_3$ and Zn_2TiO_4) are crucial materials for technologial applications and play important role in industry. Especially, they are used as a regenerable catalyst, a pigment and dielectric materials for microwave frequencies, etc. Focus of this study is to obtain local atomic structural information of zinc titanates nanocomposites accurately. Nanosamples have been synthesized through ball-milling process using mixture of highly pure ZnO and TiO_2 powders. X-ray diffraction (XRD), synchotron based X-ray absorption near edge structure (XANES) and extended X-ray absorption fine structure (EXAFS) techniques have been used to probe the crystal and local atomic structures of the synthesized nanocomposites. Obtained results have showed that ball-milling is a quite effective method to fabricate highly crystalline nanocompositestemperature.

1. INTRODUCTION

Zinc titanates (especially $ZnTiO_3$ and Zn_2TiO_4) are crucial compounds for material science and play an important role in industry [1]. Zinc titanates are used as regenerable catalysts, pigments and dielectric materials for microwave frequencies, etc. [2]. Particularly, Zn_2TiO_4 is currently an attractive material as sorbent for removing sulfur from hot coal gasification products. There are few techniques to synthesize zinc titanates, and the processes are generally complicated and the reagents used are very expensive. In this study, $ZnTiO_3$ and Zn_2TiO_4 powder synthesis using ball milling method was attempted. This process is usually used for producing metallic and ceramic nanomaterials and it is simple and cheap in comparison with other methods. In addition, ball milling of mixture of ZnO and TiO_2 powders leads to much higher homogeneity and hence single phase of zinc titanates can be obtained.

Structural investigation of the zinc titanates attracts major interest in science. Therefore, it is very important to accurately understand the local atomic structures of these materials. The present study aimed to elucidate the crystal and local atomic structures of $ZnTiO_3$ and Zn_2TiO_4 powders produced by the ball milling method.

2. RESULTS AND DISCUSSION

ZnO and TiO_2 powders (as starting materials, 99.99% high pure) supplied by Sigma–Aldrich were used to synthesize $ZnTiO_3$ and Zn_2TiO_4. The materials were mixed in a stoichiometric ratio 1:1 with 5 mm zirconia balls in ethanol, and the ball to powder ratio was estimated to be 20:1. Fritsch Planetary mill P5 was used for milling. The milling speed was kept at a rotation rate of 400 rpm and the mixtures were milled for 24 h. After the milled time, the milling was stopped to collect the samples. The homogeneous mixtures of the powders were calcined especially at 800 ºC and 950 ºC for 24 h to obtain optimal $ZnTiO_3$ and Zn_2TiO_4 phases.

Fabricated powders were characterized for crystal structure by X-ray diffraction (XRD) using a PANalytical X-ray diffractometer (X'Pert PRO) with Ni-filtered Cu K_α (0.15406 nm) radiation produced at 40 kV and 40 mA. The data, recorded over the 2h range from 20º to 80º with a step size of 0.03º and a sampling time of 200 s/step are collected using an X'Celerator detector. Fig. 1 shows the XRD traces of the produced samples. The sharpness of XRD peaks demonstrates that the nanosamples have high crystallinity. The average grain sizes of the powders can be estimated using Scherrer equation which is defined as $d = (0.94\lambda)/(\beta\cos\theta)$ where d is the average grain size, λ is the X-ray wavelength (0.15406 nm), β is the full-width at half maximum (FWHM), and θ is the diffraction angle. The strongest peaks (104) and (311) in XRD were used to calculate the grain size for $ZnTiO_3$ and Zn_2TiO_4. Applying Scherrer's formula, the grain sizes were found to be 45 nm and 20 nm for $ZnTiO_3$ and Zn_2TiO_4, respectively.

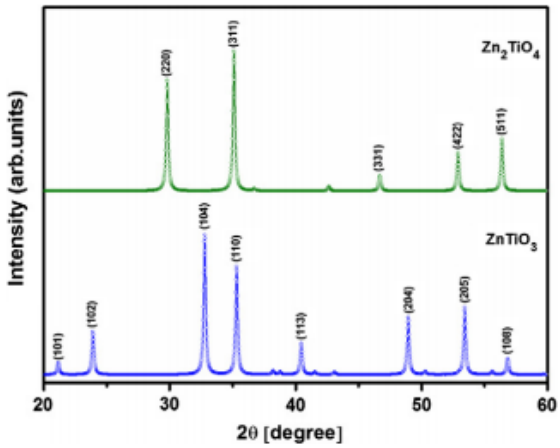

Figure 1. XRD patterns of synthesized $ZnTiO_3$ and Zn_2TiO_4 powders.

Fig. 2(a) compares normalized Zn K edge experimental XANES spectra for the $ZnTiO_3$ and zinc foil (99.95% pure) which was measured simultaneously as reference in an open-air environment at room temperature. Fig. 2(a) also shows the calculated XANES spectrum for the $ZnTiO_3$ using FEFF 8.2 to compare with experimental data. A shift of 1.1 eV in the edge position to higher photon energy was observed for the $ZnTiO_3$ in comparison with zinc metal foil. This energy shift can be correlated with the oxidation state and bonding characteristics. Zinc linked to oxygen atoms exhibits stronger bonding in the case of $ZnTiO_3$. Consequently, the absorption edge of $ZnTiO_3$ shifts to higher photon energy side of the XANES spectrum.

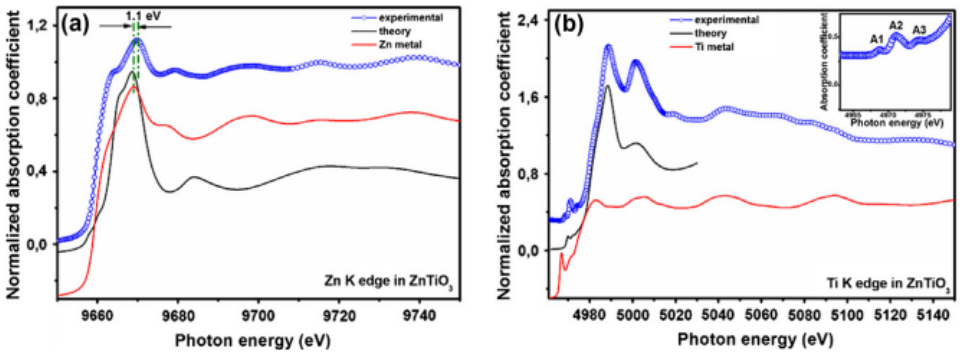

Figure 2. Measured XANES spectra of $ZnTiO_3$ and Zn metal at Zn K edge (a) and Ti K edge (b) with theoretical calculations. Inset shows a magnified view of the corresponding pre-edge peak at Ti K edge.

The XANES spectrum of Zn K edge in $ZnTiO_3$ does not possess any pre-edge peak feature as shown in Fig. 2(a). The reason is that all 3d bands of Zn are occupied by 3d electrons. The absence of pre-edge peak was also confirmed for other six-fold coordinated Zn samples, such as $Zn(OH)_2$ and $ZnCO_3$ [3]. To determine the atomic structure of $ZnTiO_3$ Ti K edge XANES and EXAFS data analysis was also performed. The normalized Ti K edge experimental XANES spectra, titanium foil (99.95% pure), and theoretical calculation for $ZnTiO_3$ are shown in Fig. 2(b). The XANES spectrum of Ti K edge in $ZnTiO_3$ exhibits significantly different structure from the reference Ti foil. By comparison with spectra in Fig. 2(a) one can see that the sample has a triplet pre-edge structure. This peak is a powerful fingerprint to assign the

coordination number of the materials. This feature can be also attributed to transition of 1s electron to p–d hybridized states in tetrahedral symmetry. In order to make quantitative calculation of Ti coordination in the prepared $ZnTiO_3$, the peak intensities were used. The inset of Fig. 2(b) shows the pre-edge peak region (4967–4975 eV) of $ZnTiO_3$ for Ti K edge. The normalized peak parameter is defined by A_2/A_{AT} where A_{AT} denotes the sum of A_1, A_2, and A_3 peak heights. This parameter was calculated to be 0.35 using the intensities of each of them. The pre-edge structure and obtained peak parameter agree well with the results found by other researchers [3]. Therefore, it is concluded that the stabilized $ZnTiO_3$ has a perovskite structure and only contains six coordinated Ti^{4+} ions. Fig. 3(a) and (b) demonstrates experimental XANES spectra of Zn_2TiO_4 at Zn K edge and Ti K edge with their theoretical calculations, respectively. The pre-edge peak of Zn_2TiO_4 for Ti K edge can be seen from Fig. 4(b). Generally, this peak is assigned as a transition from 1s to the unoccupied 3d states hybridized with the 4p character, and its intensity is enhanced by the local atomic configuration. This prominent pre-edge peak indicates Ti K edge XANES spectra of Zn_2TiO_4 containing six coordinated titanium.

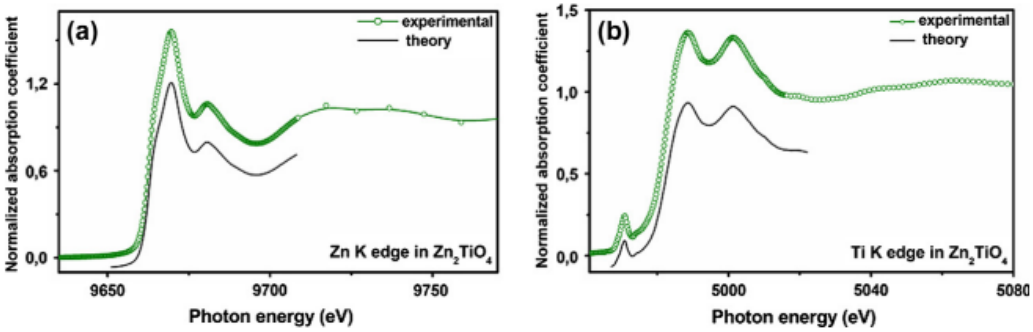

Figure 3. Measured XANES spectra of Zn_2TiO_4 at Zn K edge (a) and Ti K edge (b) with theoretical calculations.

The local atomic structure of the $ZnTiO_3$ is typically characterized by EXAFS measurements. Fourier transform (FT) spectra are commonly used to determine the structural information contained in the EXAFS spectrum. Thus, detailed information about the local atomic structure of the $ZnTiO_3$ can be extracted by data analysis from the experimental EXAFS spectra. For ZnTiO3, the $k^2\chi(k)$ spectrum was obtained from the experimental data and plotted in Fig. 4(a). The FT curve corresponding to this EXAFS oscillation is presented in Fig. 4(b).

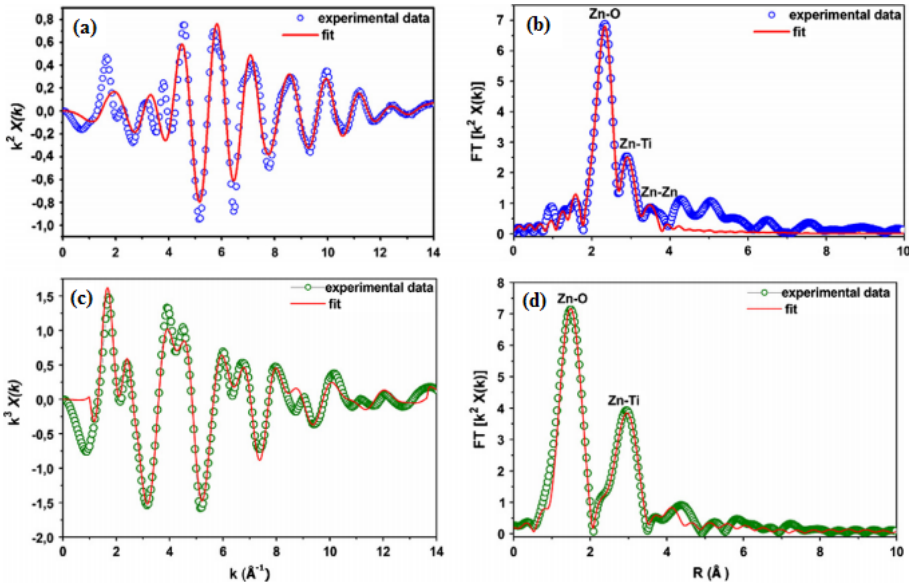

Figure 4. (a) The EXAFS functions $k^2\chi(k)$ and fit at Zn K edge for $ZnTiO_3$ and (b) the Fourier transform magnitudes of EXAFS spectra of k^2 weighted $\chi(k)$ data and fit at Zn K edge for $ZnTiO_3$. (c) The EXAFS functions $k^2\chi(k)$ and fit at Zn K edge for Zn_2TiO_4 and (d) the Fourier transform magnitudes of EXAFS spectra of k^2 weighted $\chi(k)$ data and fit at Zn K edge for Zn_2TiO_4.

The fitting curves corresponding to the experimental data are also given in Fig. 4a and b. The first three peaks for the $ZnTiO_3$ sample were fitted using ARTEMIS including single and multiple scattering, and it can be seen in Fig. 4(b) that the first peak in the FT is assigned to scattering from the nearest-neighbor O

coordination shell (Zn–O). Quantitative results of structural parameters obtained from the fitting procedure such as the numbers of the nearest atoms, inter atomic distances of $ZnTiO_3$ are listed in Table 1. Fig. 4(c) and (d) represents the EXAFS spectrum and corresponding FT curve for Zn_2TiO_4. The curve fitting process was also performed in the range of 1–4 Å for Zn_2TiO_4 sample for the best fit. The best fit analysis of the EXAFS oscillations and the first two peaks in FT were done using the single-scattering approximation. These peaks correspond to the first two coordination shells around zinc. The first and second peaks in FT are composed of oxygen and titanium atoms. The coordination numbers and inter atomic distances in the Zn_2TiO_4 sample agree well with the known structural values of cubic structure of Zn_2TiO_4 [4]. The all calculated values of the structural parameters of Zn_2TiO_4 were also summarized in Table 2.

Table 1. Fitting results of EXAFS data analysis using ARTEMIS for synthesized $ZnTiO_3$ powder at Zn K edge and Ti K edge

Compound	Shell	Number of nearest atoms	Type of nearest atoms	Distance (Å)	Debye–Waller factor (Å^2)
$ZnTiO_3$	Zn–O[a]	5.9 ± 0.01	O	2.15 ± 0.02	0.02 ± 0.02
	Zn–Ti[a]	0.9 ± 0.01	Ti	2.91 ± 0.02	0.03 ± 0.02
	Zn–Zn[a]	2.9 ± 0.01	Zn	3.02 ± 0.02	0.01 ± 0.02
	Zn–O[a]	3.0 ± 0.01	O	3.40 ± 0.02	0.03 ± 0.02
	Ti–O[b]	6.1 ± 0.01	O	2.05 ± 0.02	0.09 ± 0.01
	Ti–Zn[b]	0.9 ± 0.01	Zn	2.91 ± 0.02	0.08 ± 0.02
	Ti–Ti[b]	2.9 ± 0.01	Ti	2.96 ± 0.02	0.08 ± 0.02

Table 2. Fitting results of EXAFS data analysis using ARTEMIS for synthesized Zn_2TiO_4 powder at Zn K edge and Ti K edge

Compound	Shell	Number of nearest atoms	Type of nearest atoms	Distance (Å)	Debye-Waller factor (Å^2)
Zn_2TiO_4	Zn–O[a]	3.8 ± 0.02	O	1.98 ± 0.02	0.05 ± 0.02
	Zn–Ti[a]	11.5 ± 0.02	Ti	3.50 ± 0.02	0.04 ± 0.02
	Zn–O[a]	11.8 ± 0.02	O	3.52 ± 0.02	0.04 ± 0.02
	Zn–Zn[a]	3.8 ± 0.02	Zn	3.67 ± 0.02	0.02 ± 0.02
	Ti–O[b]	5.9 ± 0.02	O	2.04 ± 0.02	0.06 ± 0.01
	Ti–Ti[b]	5.8 ± 0.02	Ti	3.01 ± 0.02	0.08 ± 0.02
	Ti–Zn[b]	6.0 ± 0.02	Zn	3.51 ± 0.02	0.07 ± 0.02

3. CONCLUSION

In the present study, zinc titanates nanopowders have been successfully synthesized using the ball milling method. Ideal conditions (800 ºC and 950 ºC for 24 h) have been used to form $ZnTiO_3$ and Zn_2TiO_4 phases. XRD method was used to assess the crystallinity and average grain size of the prepared samples. The local atomic structures of the zinc titanates samples were determined by XANES and EXAFS methods. No evidence of any secondary phase(s) has been observed through XRD and EXAFS studies. EXAFS results have indicated that ball milling is a technique that can be considered for many applications, as a method of producing crystallized nanosized powders.

4. ACKNOWLEDGEMENTS

G.A. and F.A.A. would like to thank the APS team, Argonne National Laboratory, IL, USA for help at the 12-BM-B EXAFS beamline.

REFERENCES

[1] Dulin F.H., Rase D.E., J. Am. Ceram. Soc. (1960), 43, 125 – 131.
[2] Kim H.T., Nahm S., Byun J.D., Kim Y., J. Am. Ceram. Soc. (1999), 82, 3476 – 3480.
[3] Yamamoto T., X-Ray Spectrom. (2008), 37, 572 – 584.
[4] Chang Y., Chen I., Chen G., Chai Y., Fang T., Wu S., Ceram. Int. (2004), 30, 2183 – 2189.

Cytogenetic Effects of different concentrations and different time periods of Strontium onto *Lens culinaris* Medik.

Hakan Sepet[a], Murat Çanlı[b]

[a]*Engineering and Architecture Faculty, Department of Environmental Engineering, Ahi Evran University, TR-40100 Kırşehir, Turkey*
[b]*Mucur Vocational School, Department of Chemistry and Chemical Processing Technologies, Ahi Evran University, TR-40500 Mucur, Kırşehir, Turkey*

**e-mail corresponding author*: hakansepet@gmail.com

Keywords: Chromosome Abnormalities, Lens culinaris, Cytogenetic effects, Strontium

ABSTRACT

The purpose of this study is to investigate the cytogenetic effect of different concentrations and different contact time periods of strontium on *Lens culinaris* Medik. Sr solutions were prepared in different concentrations such as 0.05M, 0.1M, 0.25M, 0.50M, and 1.00M, and in different contact time period such as ¼, ½, 1, 2, 4, 8, 12, 16, 20, and 24 hours. All those concentrations were exposed to the seeds of *Lens culinaris* for 12 hours. All contact time treatments were done at 1.0 M concentration of strontium. The focus on microscopic examination was to clarify the cell division of chromosomal abnormalities. Microscopic examinations showed that some abnormalities occurred in the cells of seedlings as chromosome breakings, bridge chromosome, chromosome dispersion, chromosome adherence, and ring chromosome. Those abnormalities were seen in several times at each treatment depending on the different time periods. The variety and number of the abnormality were usually seen increasing with the increase of treatment time. Then, the results were evaluated statistically.

1. INTRODUCTION

Strontium (Sr) composes about 0.04% of the Earth's crust, ranking 15th among elements in abundance. Sr is an alkaline earth metal element with bright white material. 12 of its radioactive isotopes decay in a few minutes or days. Sr that can replace calcium in some foods can accumulate in bones and teeth. Some investigations into the effect of heavy metal pollution in plants demonstrated that these elements can move to plants from water and soil.

Cytogenetics studies are vital to understand plants behavior against outside effects. Cytogenetic effects of metals, especially heavy metals, still are in the focus of research efforts because of huge amount of environmental pollution caused by metal based.

Lentil experiences are being preferred because it is showing off abiotic stresses, salinity, drought, and metal toxicity on its growth and yield. Lens culinaris has 14 (2n) chromosomes. Chromose preparation is achieved from meristematic cells of roots of Lens culinaris as suggested in Plant Cytogenetics.

Table 1. The Mitotic Index of Root Tip Cells of *Lens culinaris* at Different Time periods

Time (Hour)	*Mitotic Index ± *S.D.*	*Time (Hour)*	*Mitotic Index ± *S.D.*
1/4	*18.80±7.75*	*8*	*3.42±1.94*
1/2	*16.09±4.90*	*12*	*-*
1	*10.22±3.82*	*16*	*-*
2	*7.63±2.28*	*20*	*-*
4	*6.52±2.22*	*24*	*-*
Control Group	*19.12±6.35*		

Table 2. The Mitotic Index of Root Tip Cells of Lens culinaris at the Different concentrations

Concentrations (M)	*Mitotic Index ± *S.D.*	*Time (Hour)*
0.05	*17.25±6.25*	*12*
0.1	*15.37±5.20*	*12*
0.25	*11.32±4.10*	*12*
0.5	*-*	*12*
1.0	*-*	*12*
Control Group	*19.12±6.35*	

2. RESULTS AND DISCUSSION

The purpose of this study is to investigate the cytogenetic effect of different concentrations and different contact time periods of strontium on *Lens culinaris* Medik. Sr solutions that were prepared in different concentrations such as 0.05M, 0.1M, 0.25M, 0.50M, and 1.00M were exposed to the seeds of *Lens culinaris* for 12 hours, and all contact time treatments were done at 1.0 M concentration of strontium in different contact time period such as ¼, ½, 1, 2, 4, 8, 12, 16, 20, and 24 hours.

After exposure, the seeds were left for seedling. Then, the seeds were washed by distilled water, and germinated in petri dishes at 20–25 ºC. For *fixation*, the root tips are cut the 1.5-2 cm end of it, and placed directly into fixative (in the ratio of 3:1, 100 % ethyl alcohol: glacial acetic acid). Stock root tips were stained by Feulgen method to get ready them for microscopic examination. Homologous areas were chosen on these preparations for cytogenetic examination. The cells in homologous areas were counted and the number of mitotic cells was also detected (Table 1 and 2). Any occurred chromosomal abnormalities were tried to be detected in the cells, and they are also counted. The preparations were photographed with motorized Leica DM 3000 microscope. The images from different preparations which are prepared by

exposure of strontium in different concentrations and time periods onto the root tips of *Lens culinaris* seeds were compared to each other, and the results were analyzed.

In the cells of the root tips of the seeds treated with Sr, various chromosomal abnormalities as fish bones chromosome adherence, chromosome dispersions, chromosomal adherence, bridge chromosome, chromosome breaking, chromosome shrinking, ring chromosome at different stages of mitotic division were detected (Table 3).

Table 3. Frequencies of Investigated chromosome abnormality

Investigated Abnormality(number of occurence)								
Dose Treated (M)	Treatment Time(Hour)	Fish Bones	Chromosome Dispersion	Chromosome Adherence	Chromosome Breaking	Bridge Chromosome	Chromosome Shrinking	
1	1/4	19.10	19.10	12.73	6.37	12.73	6.37	0
1	1/2	19.04	12.69	6.35	12.69	6.35	6.35	0
1	1	36.40	9.10	18.20	9.10	18.20	9.10	0
1	2	26.88	13.44	26.88	0	13.44	40.32	1
1	4	30.40	30.40	15.20	15.20	15.20	15.20	0
1	8	23.47	11.74	11.74	11.74	0	35.21	1

Investigated Abnormality (number of occurence)								
Dose Treated (M)	Treatment Time(Hour)	Fish Bones	Chromosome Dispersion	Chromosome Adherence	Chromosome Breaking	Bridge Chromosome	Chromosome Shrinking	
0.05	12	19.10	19.10	12.73	6.37	12.73	6.37	0
0.1	12	19.04	12.69	6.35	12.69	6.35	6.35	0
0.25	12	36.40	9.10	18.20	9.10	18.20	9.10	0
0.5	12	-	-	-	-	-	-	-
1.0	12	-	-	-	-	-	-	-

3. CONCLUSION

The results show that Sr concentration over 0.25 mol/L has inhibited seedling on the plant. None of the chromosomal abnormality has the shape of ring chromosome. Over 8 hours exposure of 1 mol/L Sr concentration, plant seedling was inhibited. All plants which have seedling showed different types of chromosomal abnormality. There is no sequence between chromosomal abnormalities and Sr exposure level. It is concluded that in every level of Sr exposure there is at least one type of chromosomal abnormalities occurred in seedling.

REFERENCES

[1] Çelik A., Kartal A., Akdoğan A., and Kaska Y. Environmental International, (2004), 31(1), 105-112.
[2] İnceer H., Ayaz S., Beyazoğlu O., and Entürk E. Turkish Journal of Biology. (2003), 27, 43–46.
[3] Kıran Y. and Şahin A. Gazi University Journal of Science, (2005), 18(1), 17–25.
[4] Özdemir A., Bozdağ B., Sepet H., Parlak Y., Kocabaş O., Ereeş F.S., and Özdemir C. Caryologia, (2015), 68 (3), 200–206.
[5] Sepet H., Çanlı M., Özdemir A., Bozdağ B., and Özdemir C. Pakistan Journal of Botany, (2014), 46(1), 101-110.

Comparison of Cytogenetic Effects of Barium and Strontium in different concentrations onto *Lens culinaris* Medik.

Hakan Sepet[a], Murat Çanlı[b]

[a]*Engineering and Architecture Faculty, Department of Environmental Engineering, Ahi Evran University, TR-40100 Kırşehir, Turkey*
[b]*Mucur Vocational School, Department of Chemistry and Chemical Processing Technologies, Ahi Evran University, TR-40500 Mucur, Kırşehir, Turkey*

**e-mail corresponding author*: hakansepet@gmail.com

Keywords: Chromosome Abnormalities, Lens culinaris, Cytogenetic effects

ABSTRACT

This study aims to investigate cytogenetic effects of strontium and barium on meristematic cells of root tips belonging to the plant (*Lens culinaris* Medik.). Seeds of the plant, prepared were kept in barium and strontium solutions were prepared in different concentrations such as 0.05M, 0.1M, 0.25M, 0.50M, and 1.00M., and the root tips obtained were prepared for microscopic examination. The preparations were characterized by using microscopic objectives with 40 x magnified. The focus on microscopic examination was to clarify the cell division of chromosomal abnormalities. Microscopic examinations showed that some abnormalities occurred in the cells of seedlings as chromosome breakings, bridge chromosome, chromosome dispersion, chromosome adherence, and ring chromosome. Those abnormalities were seen in several times at each treatment depending on the different time periods. The variety and number of the abnormality were usually seen increasing with the increase of treatment time. Then, the results were evaluated statistically.

1. INTRODUCTION

Barium (Ba) toxicity for plant has become increasingly important because of its presence in the environment. Barium ions find their way in plants directly by vegetation, water and soil. Animals also consume Ba enriched plants. The most noticeable harmful effect is on growth of plants. The critical threshold level of Ba for growth inhibition of each plant is quite variable. The inhibition of growth is an outcome of its damage to the physiological, cytological and biochemical processes. In addition, small amounts of water-soluble barium may be the reason for breathing difficulties, increased blood pressures, heart rhythm changes, stomach irritation, muscle weakness, changes in nerve reflexes, swelling of brains and liver, kidney and heart damage. Strontium composes about 0.04% of the Earth's crust, ranking 15th among elements in abundance. Strontium (Sr) is an alkaline earth metal element with bright white material. Mass numbers of stable isotopes are 84, 86, 87, 88, and 90. The most stable and found isotope of Sr is ^{88}Sr. 12 of its radioactive isotopes decay in a few minutes or days.^{90}Sr that has 28-year half-life time is a good beta-ray transmitter. This isotope is the most hazardous component of radioactive fallout. ^{90}Sr that can replace calcium in some foods can accumulate in bones and teeth. Although the metals did not affect maize radicle protrusion, they inhibited seed germination in the following order: Cd > Ni ≈ Pb > Sr. The major effects of heavy metals on seeds are manifested by overall abnormalities and decrease in germination, reduced root and shoot elongation, dry weight, total soluble protein level, oxidative damage, membrane alteration, altered sugar and protein metabolisms, nutrient loss all contributing to seed toxicity and productivity loss.

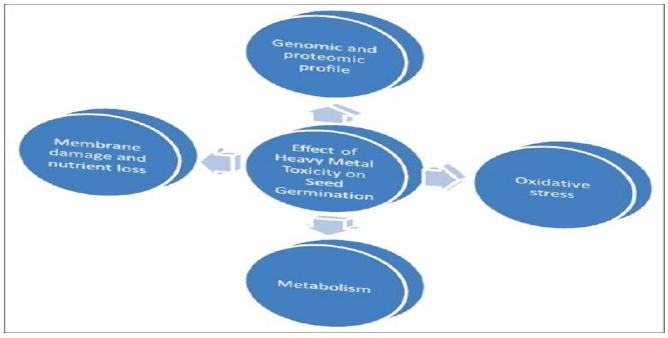

Figure 1. Effect of heavy metals on plants

Cytogenetics studies are vital to understand plants behavior against outside effects. Cytogenetic effects of metals, especially heavy metals, still are in the focus of research efforts because of huge amount of environmental pollution caused by metal based.

Table 1. The Mitotic Index of Root Tip Cells of *Lens culinaris* at the Different concentrations

Concentrations (M)	Mitotic Index ± *S.D. (for Barium)	Mitotic Index ± *S.D. (for Strontium)	Time (Hour)
0.05	16.70±6.75	18.80±7.75	12
0.1	14.09±3.90	16.09±4.90	12
0.25	11.22±3.62	10.22±3.82	12
0.5	-	-	12
1.0	-	-	12
Control Group	18.12±6.35	19.12±6.35	

2. RESULTS AND DISCUSSION

This study aims to investigate the similarities and differences of the effects of barium and strontium on *Lens culinaris* Medik. For this reason, barium and strontium solutions were prepared in different concentrations such as 0.05M, 0.1M, 0.25M, 0.50M, and 1.00M. All those concentrations were exposed to the seeds of *Lens culinaris* for 12 hours. After exposure, the seeds were left for seedling. Then, the seeds were washed by distilled water, and germinated in petri dishes at 20–25 ºC. For *fixation*, the root tips are cut the 1.5-2 cm end of it, and placed directly into fixative (in the ratio of 3:1, 100 % ethyl alcohol: glacial acetic acid). Stock root tips were stained by Feulgen method to get ready them for microscopic examination. Homologous areas were chosen on these preparations for cytogenetic examination. The cells in homologous areas were counted and the number of mitotic cells was also detected. Any occurred chromosomal abnormalities were tried to be detected in the cells, and they are also counted. The preparations were photographed with motorized Leica DM 3000 microscope. The images from different preparations which are prepared by exposure of barium and strontium in different concentrations onto the root tips of *Lens culinaris* seeds were compared to each other, and the results were analyzed.

In the cells of the root tips of the seeds treated with Sr and Ba, various chromosomal abnormalities as fish bones chromosome adherence, chromosome dispersions, chromosomal adherence, bridge chromosome, chromosome breaking, chromosome shrinking, ring chromosome at different stages of mitotic division were detected (Table 2 and 3).

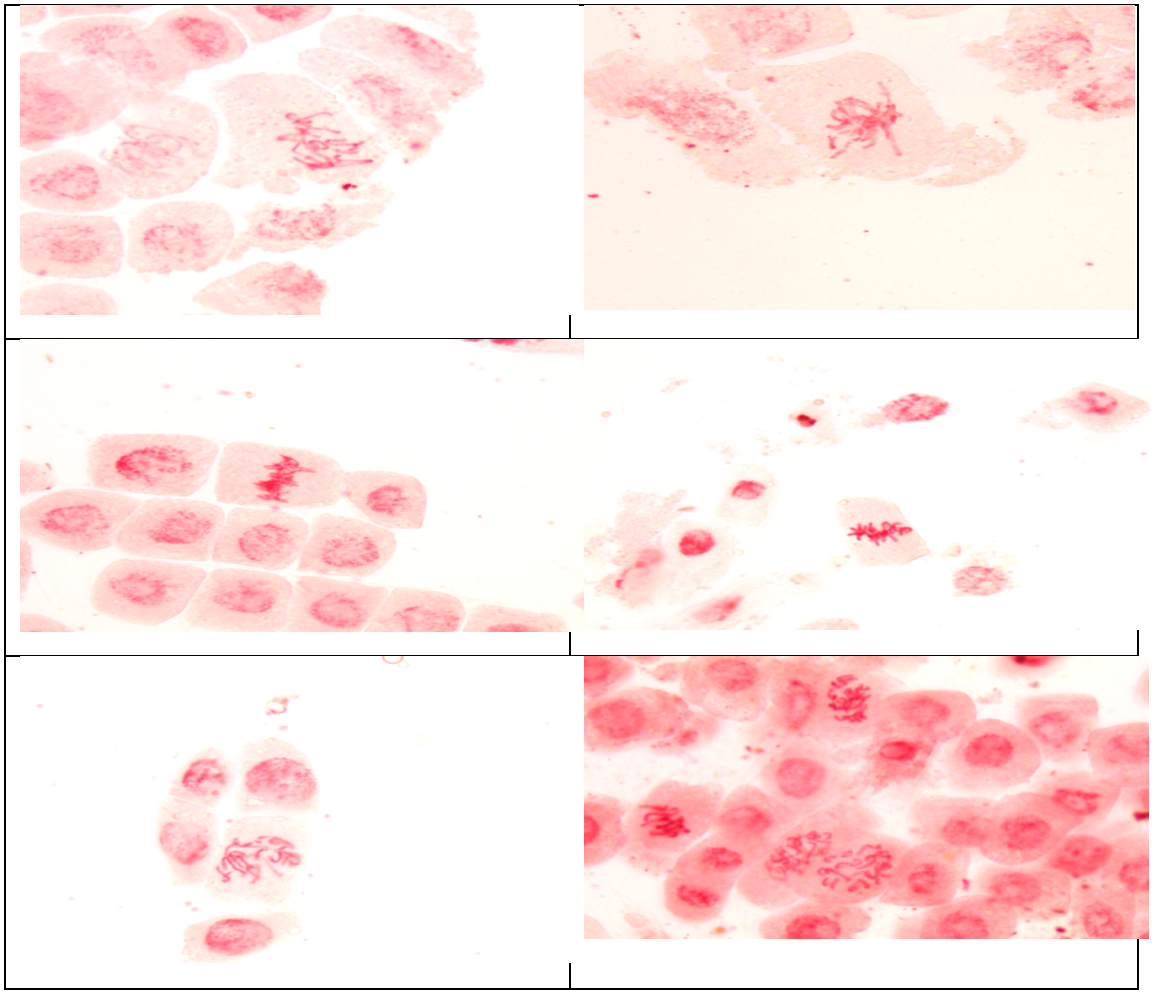

Figure 2. Investigated chromosome abnormality

3. CONCLUSION

The results show that the effect on mitotic cell division is in the following order: Sr gives higher damage to the plant than Ba (Sr>Ba).

Table 2. Chromosome Abnormality on The Root Tip Cells of *L. Culinaris* (Barium)

Investigated Abnormality(%)								
Dose Treated (M)	Treatment Time(Hour)	Fish Bones	Chromosome Dispersion	Chromosome Adherence	Chromosome Breaking	Bridge Chromosome	Chromosome Shrinking	Ring Chromosome
0.05	12	14.10	9.10	11.73	7.37	12.73	6.37	0
0.1	12	17.04	10.69	16.35	5.69	6.35	6.35	0
0.25	12	36.40	7.10	18.20	5.10	10.20	9.10	0
0.5	12	-	-	-	-	-	-	-
1.0	12	-	-	-	-	-	-	-

Table 3. Chromosome Abnormality on The Root Tip Cells of *L. Culinaris (Strontium)*

Investigated Abnormality(%)								
Dose Treated (M)	Treatment Time(Hour)	Fish Bones	Chromosome Dispersion	Chromosome Adherence	Chromosome Breaking	Bridge Chromosome	Chromosome Shrinking	Ring Chromosome
0.05	12	19.11	19.00	12.63	6.37	10.52	8.53	0
0.1	12	19.22	12.91	6.35	12.69	7.15	4.86	0
0.25	12	43.43	9.10	17.15	9.10	18.10	7.18	0
0.5	12	-	-	-	-	-	-	-
1.0	12	-	-	-	-	-	-	-

REFERENCES

[1] Çelik A., Kartal A., Akdoğan A., and Kaska Y. Environmental International, (2004), 31(1), 105-112.
[2] İnceer H., Ayaz S., Beyazoğlu O., and Entürk E. Turkish Journal of Biology. (2003), 27, 43–46.
[3] Kıran Y. and Şahin A. Gazi University Journal of Science, (2005), 18(1), 17–25.
[4] Özdemir A., Bozdağ B., Sepet H., Parlak Y., Kocabaş O., Ereeş F.S., and Özdemir C. Caryologia, (2015), 68 (3), 200–206.
[5] Sepet H., Çanlı M., Özdemir A., Bozdağ B., and Özdemir C. Pakistan Journal of Botany, (2014), 46(1), 101-110.

Electronic Properties and Reactivity Descriptors of 5-chloro-2-amino benzophenone

Hamit Alyar

Department of Physics, Faculty of Sciences, Çankırı Karatekin University, TR-18100 Çankırı, Turkey

halyar@karatekin.edu.tr

Keywords: NLO, reactivity descriptors, MEPs, DFT

ABSTRACT

In this study, structure of 5-chloro-2amino benzophenone is optimized using Density Functional Theory (DFT) method. Nonlinear optical (NLO) properties examined by the theoretically predicted values of dipole moment (μ), polarizability (<α>), anisotropic polarizability ($\Delta\alpha$) and first static hyperpolarizability (β_{tot}). Besides, molecular electrostatic potential surface (MEPs), the highest occupied molecular orbital (HOMO) energies, the lowest unoccupied molecular orbital (LUMO) energies of 5-chloro-2amino benzophenone was analyzed. HOMO-LUMO energy band gap and some reactivity descriptors (such as ionization energy, electron affinity, chemical softness, chemical hardness, electronegativity, chemical potential and electrophilicity index) were computed with B3LYP/6-311++G (d,p) level of theory. All calculations performed with Gaussian 09 and Gauss View 5.0 package.

1. INTRODUCTION

Investigation of the nonlinear optical properties of the materials is so important due to the keyfunctions of frequency shifting, optical modulation, optical switching, optical logic and optical memory for the emerging technologies in areas such as in telecommunications, information storage, signal processing [1] and THz wave generation [2].

The THz region, which lies in between microwaves and infrared region of the electromagnetic spectrum, offers diverse applications such as wireless communications, inspection of drugs, spectroscopy and imaging [3]. Due to measures in the field of technology, there is an increasing interest in designing new organic materials with desired nonlinear optical properties.

In this study nonlinear optical properties (<α>, Δα, β_{tot}), molecular electrostatic potential surface, frontier molecular orbital energies, HOMO-LUMO energy band gap and some reactivity descriptors (such as ionization energy, electron affinity, chemical softness, chemical hardness, electronegativity, chemical potential and electrophilicity index) were computed with B3LYP/6-311++G (d,p) level of theory. All calculations performed with Gaussian 09 and Gauss View 5.0 package.

2. RESULTS AND DISCUSSION

2.1 Nonlinear optical (NLO) properties

The dipole moment (μ), the static polarizability (<α>), anisotropic polarizability (Δα) and first static hyperpolarizability (β_{tot}) are related directly to the nonlinear optical (NLO) activity of structures. The calculated values of the mean polarizability, anisotropic polarizability and the hyperpolarizabilities from Gaussian 03 output were converted from atomic units into electrostatic units (α: 1a.u = $0.1482*10^{-24}$esu; β: 1a.u = $8.6393*10^{-33}$esu) [4].

The total static dipole momen, μ is defined as; $\mu = (\mu_x^2 + \mu_y^2 + \mu_z^2)^{1/2}$. The calculations of static polarizability (<α>) and first static hyperpolarizability (β_{tot}) from the Gaussian output have been stated in detail previously [5] as follows:

$$<\alpha> = 1/3\ (\alpha_{xx} + \alpha_{yy} + \alpha_{zz}\ )$$

$$\Delta\alpha = 1/2^{1/2}\ [(\alpha_{xx} - \alpha_{yy})^2 + [(\alpha_{xx} - \alpha_{zz})^2 + [(\alpha_{yy} - \alpha_{zz})^2]^{1/2}$$

$$\beta_{tot} = [(\beta_{xxx} + \beta_{xyy} + \beta_{xzz})^2 + (\beta_{yyy} + \beta_{yzz} + \beta_{yxx})^2 + (\beta_{zzz} + \beta_{zxx} + \beta_{zyy})^2]^{1/2}$$

The optimized structure of 5-choloro-2-amino benzophenone calculated by DFT levels with the B3LYP/6-311++G (d,p) basis set in accordance with the atomic numbering scheme given in Fig 1. The first static hyperpolarizability (β_{tot}), mean polarizability (<α>), anisotropic polarizability (Δα) and the ground state dipole moment (μ) results for 5-chloro-2-aminobenzophenone presented at Table 1.

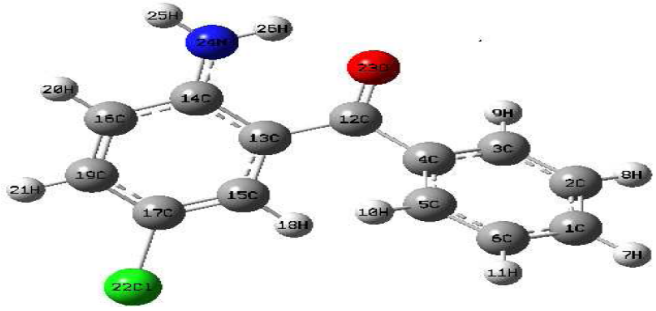

Figure 1. Optimized molecular structure of 5-choloro-2-amino benzophenone

Table 1. The electric dipole moment μ (D), the mean polarizability <α> (x 10^{-24}esu), anisotropic polarizability(Δα) and the first static hyperpolarizability β_{tot} (x10^{-33}esu) of 5-chloro-2-amino benophenone by DFT B3LYP/6-311++G(d,p) method

Parameter	B3LYP	Parameter	B3LYP
μ_x	-1.20	$ß_{xxx}$	245.10
μ_y	1.72	$ß_{xxy}$	-2375.81
μ_z	-0.08	$ß_{xyy}$	-1062.63
M	2.09	$ß_{yyy}$	181.42
α_{xx}	37.34	$ß_{xxz}$	-1105.83
α_{xy}	-0,75	$ß_{xyz}$	-17.28
α_{yy}	23.86	$ß_{yyz}$	146.87
α_{xz}	0.95	$ß_{xzz}$	181.42
α_{yz}	1.28	$ß_{yzz}$	285.10
α_{zz}	18.52	$ß_{zzz}$	-25.92
<α>	26.53	β_{tot}	2242.45
Δα	11.88		

α,Δα: 1a.u = 0.1482*10^{-24} esu
β: 1a.u = 8.6393*10^{-33} esu

The hyperpolarizability plays an important role to understanding of the nonlinear optical activity in materials to use them for the fabrication the technologically important nonlinear optical devices. The first static hyperpolarizability of title compound was computed to be 2242.45 x10^{-33} esu. It found that, the first static hyperpolarizability of 5-chloro-2-amino benzophenone is six times larger than that of urea (0.3728x 10^{-30}esu). The value of total dipole moment is found to be 1.68 D and the highest value of component of μ

is μ_y (= 1.13 D) which is a major contributor to it. Also, the value of mean polarizability (<α>) and anisotropic polarizability (Δα) are found to be 26.53 x 10^{-24} esu and 11.88 x 10^{-24} esu, respectively.

2.2. MEP analysis

The MEP plot of 5-choloro-2-amino benzophenone molecule provides the useful information about molecular level. The MEP for the title compound was composed by DFT calculation using the optimized geometry at the B3LYP/6-311++G(d,p). Our aim is to investigate reactive sites for electrophilic and nucleophilic attack, the regions of the MEP. As shown in Fig. 2, while the blue colors indicate for partial positive regions to nucleophilic reactivity (where is the electron-poor region), red and yellow colors indicated for the negative regions of the MEP (where is the electron-rich region) are related to electrophilic reactivity.

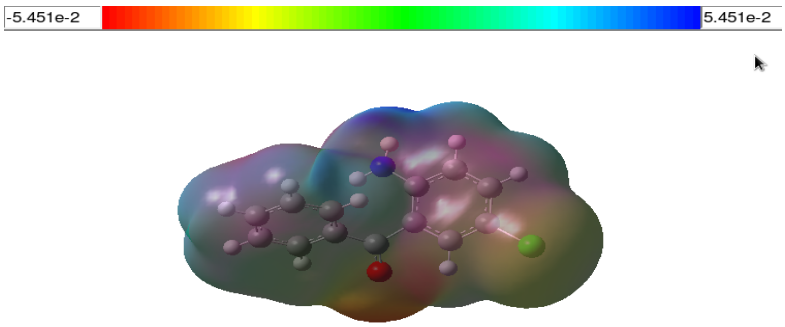

Figure 2. Molecular electrostatic potential (MEPs) 3D contour map for 5-choloro-2-amino benzophenone

The MEPs of title molecule in 3D contour plots are presented in Fig. 2. The potential values decreases from blue to red color. The colors line up in the range of -5.451e^{-2} a.u. and 5.451e^{-2} a.u. for studied molecule. While the blue colors represent strongest attraction, the red colors represent repulsion.

3.3 HOMO-LUMO analysis and reactivity descriptors

The frontier molecular orbital distributions and energy levels of the HOMO and LUMO, which computed at B3LYP/6-311++G(d,p) level of title molecule were shown in Fig. 3. The frontier molecular orbitals (FMOs) help for physicists and chemists for the main orbital taking part in chemical reaction. While the HOMO is directly related to the ionization potential, the LUMO is directly related to the electron affinity. The molecules with a larger $\Delta E_{HOMO\text{-}LUMO}$ band gap should be less reactive than one having a smaller gap [6].

The calculated values of HOMO and LUMO energies and $\Delta E_{HOMO\text{-}LUMO}$ band gaps of title molecule were listed in Table 2. As shown in Fig. 3 and Table 2, the difference between HOMO and LUMO energy levels of studied molecule ($\Delta E_{HOMO\text{-}LUMO}$) was found to be 3.80 eV at B3LYP/6-311++G(d,p) in gas phase. The ionization energy and electron affinity can be expressed through HOMO and LUMO orbital energies according to the Koopman's theorem [7];

$I = -E_{HOMO}$

$A = -E_{LUMO}$

In the past, the hardness has been associated with the stability of chemical system [8]. The chemical hardness corresponds to the gap between the HOMO and LUMO orbitals. The larger the HOMO-LUMO energy gap the harder molecule.

$\eta = \frac{1}{2}(E_{LUMO} - E_{HOMO})$

The chemical softness is as follows,

$S = \frac{1}{2\eta}$

Electro negativity is a measure of the tendency of an atom to atrcat a bonding pair of electrons.

$\chi = \frac{1}{2}(I+A)$

Electronic chemical potential μ defined by Parr and Pearson [9] as follow;

$\mu = -\frac{1}{2}(I+A) = \frac{1}{2}(E_{HOMO} + E_{LUMO})$

The global electrophilicity index ω was introduced by Parr [10] and calculated as follow equation;
$\omega = \mu^2/2\eta$

All the calculated parameters were given in Table 2.

Table 2. Calculated values for frontier orbital energies, energy band gap (ΔE), ionization energy (I), electron affinity(A), electronegativity(χ), chemical hardnesses (η) and chemical softness (S), chemical potential(μ) and electrophilicity index (ω) of 5-choloro-2-amino benzophenone

Physical properties	B3LYP/6-311++G(d,p)
E_{HOMO} (eV)	-6.00420
E_{LUMO} (eV)	-2.16210
$\Delta E=E_{HOMO-LUMO}$ (eV)	3.84210
I (eV)	6.00420
A (eV)	2.16210
χ (eV)	4.92315
η(eV)	1.92105
S (eV^{-1})	0.26027
μ(eV)	-4.92315
ω(eV)	6.30837

3. CONCLUSION

In this study, nonlinear optical properties of 5-choloro-2-amino benzophenone were investigated by DFT B3LYP/6-311++G(d,p) level of theory. The <α>, $\Delta\alpha$ and β_{tot} are found to be 26.53 x 10^{-24} esu, 11.88 x 10^{-24} esu and 2242.45 x10^{-33} esu, respectively. The β_{tot} value for 5-chloro-2-amino benzophenone at molecular level is found to be about six times larger than that of urea (0.3728x 10^{-30}esu). ΔE energy band gap is found to be about 3.84 eV. MEPs, ionization energy, electron affinity, chemical softness, chemical hardness, electronegativity, chemical potential and electrophilicity index) were computed with same level of theory.

REFERENCES

[1] Andraud C., Brotin T., Garcia C., Pelle F., Goldner P., Bigot B., Collet A., J. Am. Chem. Soc. (1994), 116, 2094–2102.
[2] Krishnakumar V., Nagalakshmi R., Physica B (2008), 403, 1863–1869.
[3] Ramaclus J.V., Thomas T., Ramesh S., Sagayaraj P., Michael E. A., Cryst. Eng. Comm. (2014), 16, 6889-6895.
[4] Sundaraganesan N., Kavitha E., Sebastian S., Cornard J. P., Martel M., Spectrochemica Acta Part A (2009), 74,788–797.
[5] Alyar H., Kantarci Z., Bahat M., Kasap E., J. Mol. Struc. (2007), 834-836, 516-520.
[6] Kurtaran R., Odabasoğlu S., Azizoğlu A., Kara H., Atakol O., Polyhedron, (2007), 26, 5069-5074.
[7] Koopmans T., Physica (1933), 1, 104-113.
[8] Pearson R. G., J. Chem.Sci. (2005), 117, 369-377.
[9] Parr R. G., Pearson R. G., *J. Am. Chem. Soc*. (1983), 105, 7512-7516.
[10] Roy R. K., Choho K.,. De Proft F, Geerlings P., *J. Phys. Org. Chem.* (1999), 12, 503-509.

The Magnetic and Electronic Properties of $Ce_{1-x}Pr_xIn_3$ Compounds

Havva Bogaz Ozisik[a], Haci Ozisik[b], Engin Deligoz[a]

[a]*Department of Physics, Faculty of Arts and Sciences, Aksaray University, 68100 Aksaray, Turkey*
[b]*BOTE Department, Faculty of Education, Aksaray University, 68100 Aksaray, Turkey*

**e-mail corresponding author: havvaoz@aksaray.edu.tr*

Keywords: magnetic properties, electronic properties, ab initio

ABSTRACT

The ab initio total energy calculations have been performed to investigate the structural, magnetic, and electronic properties of the Pr doped $CeIn_3$ compound in $AuCu_3$ structure. Spin-polarized electronic band structure and density of states (DOS) were calculated and interpreted. The magnetic moments of the Pr doped $CeIn_3$ compound was calculated. The obtained data were compared with the available experimental and theoretical work.

1. INTRODUCTION

The rare earth intermetallic compound $ReIn_3$ have attracted attention due to their interesting properties [1-3]. Magnetic interaction is important in the appearance of these properties [1]. Among the $ReIn_3$ compounds, $CeIn_3$ is key compound for understanding characteristics of strongly correlated systems [2]. $CeIn_3$ shows Kondo-type as well as superconducting behavior when pressure is applied [2].

İlkhani et al. have studied the impacts of pressure on the structural and electronic properties of $CeIn_3$ [3]. The low temperature heat capacity of $(R_xEr_{1-x})In_3$ (R = Y, Ce, Pr, and Dy) has been studied by Hale et al. [4]. Knebel et al. have studied the phase diagram of the antiferromagnetic Kondo-lattice compound $CeIn_3$ under pressure up to 100 kbar by the resistivity measurements [5]. The pressure dependency of localization degree in heavy fermion $CeIn_3$ using density functional theory have been studied [1]. The magnetic structure of $CeIn_3$ with Neutron diffraction measurements has been studied by Benoit et al. [6]. Kletowski has studied the transverse and longitudinal magnetoresistances of $LaIn_3$, $CeIn_3$, $PrIn_3$ and $SmIn_3$ in magnetic fields up to 32 T [7].

The diverse experimental and theoretical studies have been carried out to determine the magnetic and electronic properties. To our best knowledge, the structural, magnetic, and electronic properties of the Pr doped $CeIn_3$ compound are not studied. Therefore, in this paper the first-principles calculations of Pr doped $CeIn_3$ have been performed.

2. THE CALCULATION METHOD

All calculations were carried out using the Vienna Ab initio Simulation Package (VASP) [8-11] and performed for cubic $AuCu_3$ structure in 2 × 2 × 2 supercell. The exchange and correlation terms are described in the generalized gradient approximation (GGA) with the Perdew-Burke-Ernzerhof (PBE) [12] and the electron-ion interaction is considered in the form of the projector-augmented-wave (PAW) method [10, 13]. The kinetic energy cutoff was set at 425 eV. 9 x 9 x 9 k-point grid were used to sample the Brillouin zone [14]. The optimization was performed until the total energy tolerance and maximum force tolerance was below 1.0 x 10^{-7} eV and 1.0 x 10^{-5} eV/Å, respectively. Also, spin-polarization effects have been included in the calculations.

2. RESULTS AND DISCUSSION

$ReIn_3$ rare earth intermetallic compounds are crystalized in $AuCu_3$-type structure (Space Group: Pm-3m, No: 221) and crystal view of Pr doped $CeIn_3$ compound are given in Figure 1 for the interested concentrations. The calculated lattice constants are given in Table 1 for $Ce_{1-x}Pr_xIn_3$ compound.

Table 1. The calculated lattice constant (a in Å) and magnetic moment (M in μ_B/atom) values of $Ce_{1-x}Pr_xIn_3$ compound with available values.

x	***a***	M_{Ce}	M_{Pr}	***Ref.***
0.00	4.7122	0.690	-	Present
	4.689	0.48±0.08		Exp. [6]
	4.6894			Exp.[4]
		0.65±0.1		Exp. [15]
	4.691	0.658		AFM [3]
	4.702	0.713		AFM+SOC [3]
	4.707	0.855		AFM+SOC+GGAU [3]
0.25	4.7117	0.706	2.134	Present
0.50	4.7048	0.058	2.150	Present
0.75	4.7103	0.726	2.149	Present
1.00	4.7096	-	2.149	Present
	4.6717			Exp. [4]

It is seen that the present lattice parameters do agree with the other available experimental values. The calculated lattice parameter is about %1 larger than the available values. This is expected for GGA-PBE calculations. Also, the calculated magnetic moment values of $Ce_{1-x}Pr_xIn_3$ compound are given in Table 1. The calculated magnetic moment value for Ce and Pr is agreement with the experimental and theoretical values. The total magnetic moment increases as the Pr contribution increases.

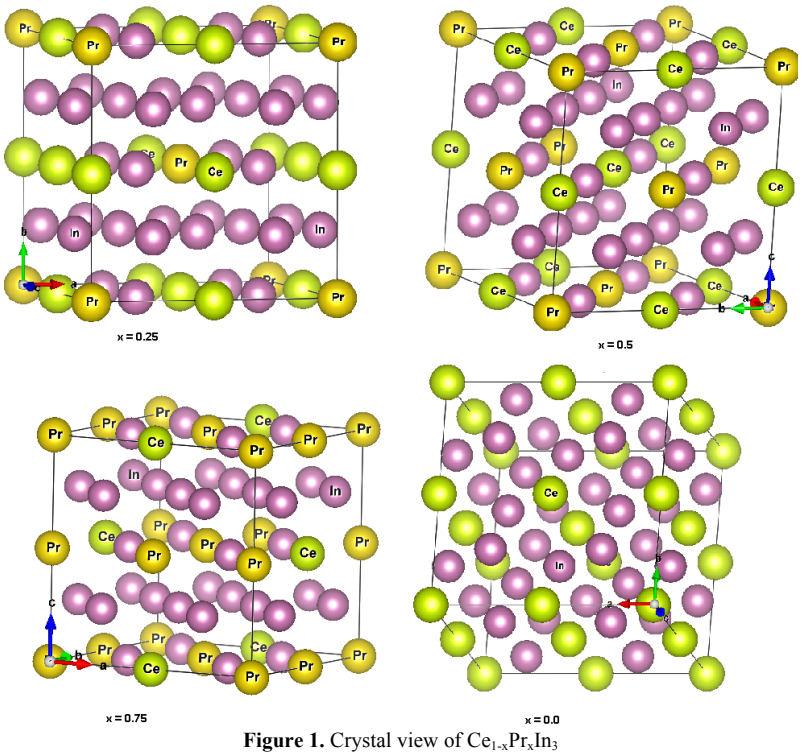

Figure 1. Crystal view of $Ce_{1-x}Pr_xIn_3$

The total density of states (TDOS) of $Ce_{1-x}Pr_xIn_3$ compounds along the high symmetry directions are calculated and given in Figure 2. The energy shift between the spin up and spin down causes the occurrence of the magnetic polarization. It seen that $Ce_{1-x}Pr_xIn_3$ compounds exhibit metallic character.

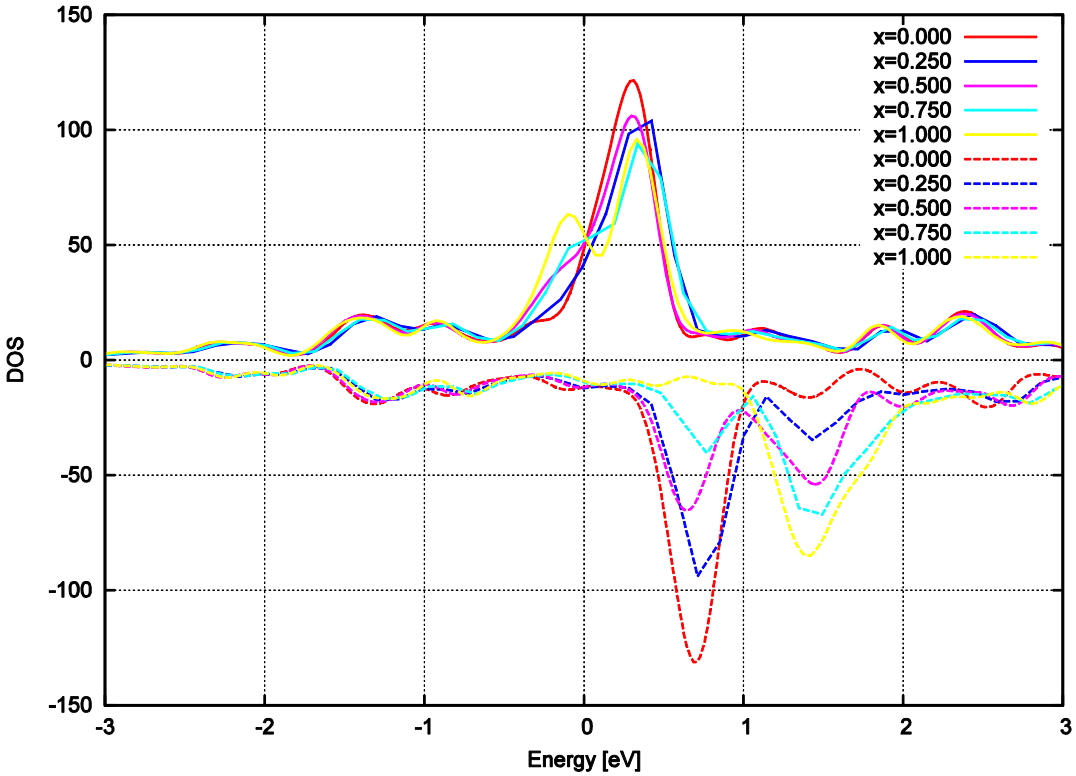

Figure 2. The calculated TDOS of $Ce_{1-x}Pr_xIn_3$

3. CONCLUSION

The structural, magnetic, and electronic properties of the Pr doped CeIn3 compound are calculated using density functional theory. The calculated lattice constant and magnetic moment values for $Ce_{1-x}Pr_xIn_3$ compound are accord with the other available experimental and theoretical values. The DOS of $Ce_{1-x}Pr_xIn_3$ reveals the metallic character.

REFERENCES

[1] Yazdani-Kachoei M., Jalali-Asadabadi S., Ahmad I., and Zarringhalam K., Scientific Reports. (2016), 6, 31734.
[2] Cabrera-Pasca G.A., Mestnik-Filho J., Carbonari A.W., and Saxena R.N., Journal of Applied Physics. (2013), 113, 17E133.
[3] Ilkhani M., Abolhassani M.R., and Aslaninejad M.., Eur. Phys. J. B. (2008), 65, 21–28.
[4] Hale L., Gschneidner Jr. K.A., Pecharsky V.K., Mudryk Y., Journal of Alloys and Compounds. (2009) 472, 24–29.
[5] Knebel G., Braithwaite D., Canfield P.C., Lapertot G., and Flouquet J., Physical Review B. (2001), 65, 024425.
[6] Benoit A., Boucherle J.X., Convert P., Flouquet J., Palleau J.,and Schweizer J., Solid State Communications. (1980), 34, 293-295.
[7] Kletowski Z., Journal of Magnetism and Magnetic Materials. (1998), 186, L7-L9.
[8] Kresse G. and Hafner J., Phys. Rev. B. (1993), 47, 558.
[9] Kresse G. and Furthmuller J., Comput. Mater. Sci. (1996), 6, 15-50.
[10] Kresse G. and Joubert D., Phys. Rev. B. (1999), 59, 1758.

[11] Kresse G. and Furthmüller J., Phys. Rev. B. (1996), 54, 11169.
[12] Perdew J.P., Burke K. and Ernzerhof M., Phys. Rev. Lett. (1996), 77, 3865.
[13] Blöchl P.E., Phys. Rev. (1994), 50, 17953.
[14] Monkhorst H.J. and Pack J.D., Phys. Rev. (1976), 13, 5188.
[15] Lawrence J.M. and Shapiro S.M., Phys. Rev. B. (1980), 22, 4379.

Hysteresis Behavior of GaAs Semiconductor in an IR Image Converter

Hilal Kurt[a]

[a]*Department of Physics, Faculty of Science, Gazi University, 06500 Teknikokullar, Ankara, Turkey*

**e-mail:hkurt@gazi.edu.tr*

Keywords: hysteresis,GaAs,IR image converter

ABSTRACT

Hysteresis behavior was studied in an IR image converter with GaAs cathode in the pressure range between 28 Torr and 690 Torr. Hysteresis is related to the electron capture mechanism in the semiconductors when the applied voltage is higher than the critical value. It has been also observed that hysteresis depends on the plasma pressure for the interelectrode distance d changing from 45 μm to 500 μm. Fig.1 shows the hysteresis behavior under voltage changing for up and down situation.

1. INTRODUCTION

GaAs is combined by Gallium and Arsenic and this semiconductor compound forms the main core material for the technology [1]. The products such as *GPS* navigation units, fiber optic equipments, digital mobile phones, satellite units and wireless networks frequently include *GaAs* [1]. Therefore, semiconductor technologies based on *GaAs* circuitry form the high amount of wireless and wi-fi consumer products. According to recent studies, *III-V* group semiconductors have numerous technical and energy applications. Indeed, it attracts much attention in the qualified fabrication techniques with different electronic and physical features

2. RESULTS AND DISCUSSION

The hysteresis curves are obtained in both cases under backward and forward voltage as shown in Fig. 1. It is believed that the formation of electric field domains moving from the cathode to anode plays an important role to create such hysteresis for both materials. The voltage sweeping in upward and downward direction is performed from 200 V to 2000 Volt and 2000 to 200 V by 5 V steps. Current - voltage measurements on the semiconductor plasma device are of great importance to uncover the electrical properties of the devices and materials. In order to understand the stable region in terms of discharge voltage, that gives tremendous knowledge.

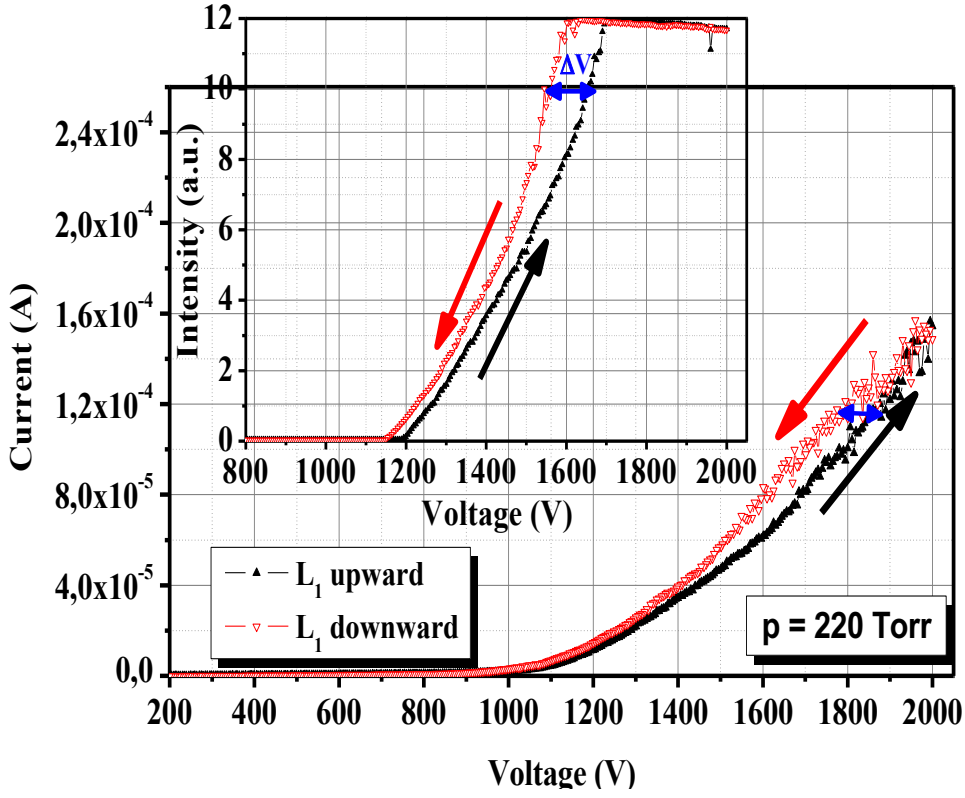

Figure1. Hysteresis behavior of GaAs in an IR image converter

Fig. 1 shows such hysteresis curves for CVC and DLE, when GaAs semiconductor is used. The variations of CVC and DLE depending on the applied voltages are shown for backward and forward directions. Hysteresis as nonequilibrium phenomena is related to electron capture and emission from EL2 deep centers [2,3], when the semiconductor electrode is subjected to forward and reverse driven voltage.

3. CONCLUSION

Indeed the IR irradiation also plays important role on that mechanism, since the curves for different illuminations provide different results. That process also results with a non-volatile memory effect in electrically programmable read only memory for the large hysteresis curves in SI GaP materials with N-shaped CVC curves points [3]. Indeed, the localized natures of the surface states indicate different behavior by charging and discharging in that manner.

REFERENCES

[1] Fu. C.Z., Yong. D., Guan,X.Q., Hui .Z. T., J. Appl. Phys.(2000), 87, N3-1482.
[2] Niedernostheide F.J., Nonlinear dynamics and pattern formation in semiconductors and Devices (Berlin, Springer, 1995)
[3] Kurt H.Y., Sadıq Y., Salamov B.G., Phys. Status Solidi A . (2008), 205, 321.

Low Pressure Argon Discharges in a Microdischarge Cell with Gap Cathode

Hilal Kurt[a]

[a]*Department of Physics, Faculty of Science, Gazi University, 06500 Teknikokullar, Ankara, Turkey*

**e-mail:hkurt@gazi.edu.tr*

Keywords: Argon, GaP, gas discharge

ABSTRACT

Low pressure Ar discharges are studied in microdischarge cell with GaP cathode both experimentally and theoretically. High purity commercial Argon was used to fill the gas discharge cell at pressures between 2 Torr and 100 Torr. Townsend's first ionization coefficient α and second ionization coefficient γ are calculated for different interelectrode distance and pressure p. Paschen´s curves are obtained varying the distance between GaP cathode and SnO_2 covered glass electrodes.

1. INTRODUCTION

Microdischarge unit is the main part of an IR image converter and it was invented in 1970s [1]. In such converter systems, a micro gap filled by a gas, a high-resistivity semiconductor cathode (sensitive to IR region), and a glass plate coated with a transparent film are mainly used. It has crucial importance to choose the convenient semiconductor materials for specified by good sensitivity and high speed of operation [2]. The operation principle of such a device is based on controlling the gas discharge via a high-resistivity semiconductor electrode [3]. The spatial distribution of the discharge light emission and current and in the discharge gap is proportional to the semiconductor conductivity, which is controlled by means of incident IR radiation projected onto the photodetector; it is converted into visible glow of the gas [3]. Gas discharges are mainly classified as a Townsend, glow and arc discharges [3].

Experimental setup

The properties of planar semiconductor- gas discharge cell are explored for various interelectrode gaps d= 50 μm–500 μm and relatively high pressures p = 3 Torr -20 Torr, experimentally. Both pressure and interelectrode gap are important for the characterization of microdischarges. For instance, the characterization is valuable for UV radiation sources in microreactors or purification of gases [1]. The experimental structure is a multilayer geometry as shown in Fig. 1.

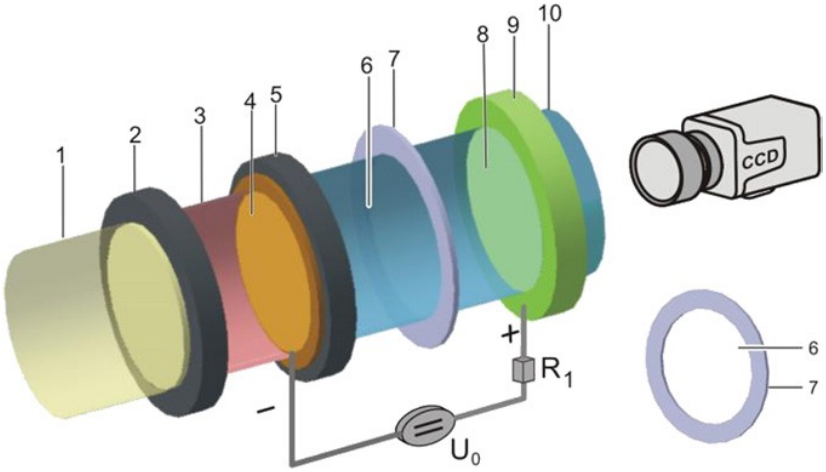

Figure 1. The gas discharge cell of IR image converter is sketched in Figure: 1—Light beam; 2—Si filter; 3— IR light beam; 4—semi transparent Au contact; 5—GaP cathode; 6— The diameter of the gas discharge gap D ; 7— insulator mica layer; 8. Semitransparent SnO2 contact; 9—glass disc;10—UV–visible light beam.

2. RESULTS AND DISCUSSION

In our experiments, we used IR sensitive high resistivity semiconductor electrodes that exhibit linear CVCs in the whole applied voltage range and different illumination intensities. The spatial distribution of the current and the brightness in the gap during the discharge are proportional to the conductivity of the cell. The current and discharge values strongly depend on the type of the semiconductor and also the studied gas plasma in the investigated structure. The discharge experiments have been performed with two high-resistivity GaP semiconductor cathode at room temperature in a maximal range of a 60 μA cm−2 [3]. Detailed information regarding to the CVCs for variable interelectrode gaps d and cathode diameter D are represented in Fig. 2 for Ar plasma.

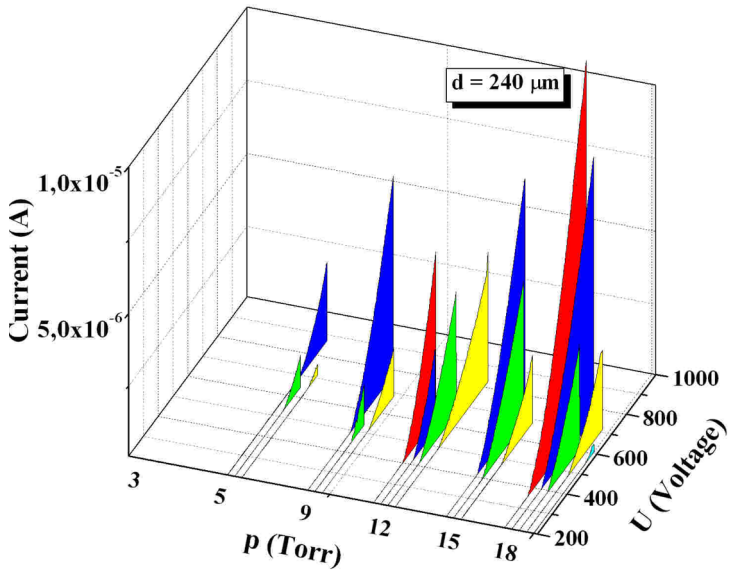

Figure 2. Current voltage characteristic for low pressure discharge in the case of different cathode diameter (5-18mm);
18 mm 15 mm 12 mm 9 mm 5 mm

3. CONCLUSION

We have focused on the Current voltage characteristic for GaP at the same electrode gap sizes and different gap diameters D to determine the conditions under which the electrons have maximum speeds with the lowest gap distance and highest voltage over a low pressure range (i.e.3 Torr to 18 Torr). In these curves, the CVCs increase with D, for GaP. The optical feature of GaP is interesting since it operates in visible (VIS), MWIR or LWIR spectral ranges [4]. Although it is not best choice for the optical devices, it can have certain advantages over other semiconductors by its high chemical resistance, mechanical strength, hardness and thermal conductivity.

REFERENCES

[1] Kasymov Sh. S and Paritskii L. G. 1973 Device for tracking images Russian Authors' Certificate 1798020/18-10
[2]Portsel L .M., Astrov Yu. A, Reimann I., Ammelt E. and . Purwins H.G, J. Appl. Phys.(1999), 85, 3960.
[3] Astrov Yu. A., Lodygin A. N. and Portsel,L.M ., J. Phys. D: Appl. Phys. (2016), 49, 095202.
[4] Vaclavík J., Vapenka D., EPJ Web of Conferences. (2013),48, 00028.

Comparison of the Electronic Properties of the II-VI ZnS and ZnSe Cathodes in Plasma-Semiconductor Structure

Hilal Kurt[a]

[a]*Department of Physics, Faculty of Science, Gazi University, 06500 Teknikokullar, Ankara, Turkey*

**e-mail:hkurt@gazi.edu.tr*

Keywords: ZnS, ZnSe, gas discharge, Argon

ABSTRACT

In this study, the electrical properties of the ZnS and ZnSe semiconductor materials are investigated in a plasma semiconductor structure by using COMSOL multiphysics programme theoretically in a wide parameter range for Argon media. Space charge densities, electron densities, thermal electron velocities, secondary electron coefficients γ, and electron mobilities are calculated for both semiconductor materials. The wide-bandgap II-VI group semiconductors are important for optoelectronic application and they promise the infrared spectral range due to their proper band gaps.

1. INTRODUCTION

II–VI group semiconductor materials such as ZnS, ZnSe, and ZnTe and their prototypes with cubic phase are found in nature as mineral complexes (i.e. zinc-blende structure) [1]. Having importance for various optical and electronic device applications and promising for blue diode lasers and electro - acoustic devices, ZnSe can be used as solar cell window in the photovoltaic measurements with 2.70 eV band gap, which is suitable for nonlinear optical devices [2], displays [3], and sensors [2-3]. ZnSe is one of the most studied semiconductor compounds with an optical transmittance range of 0.5-22 mm [4]. From the theoretical manner, many authors have studied ZnS and ZnSe in order to explore their electronic properties, using various computational methods. Most of the previous theoretical studies on transport properties of ZnS and ZnSe have realized based on the Monte Carlo method [5]. According to previous studies [reference], the refractive index of ZnSe has been measured by Hattori and co-workers in the spectral region from 10 to 100 cm−1 [6]. Jensen and Torabi [7] have reported the same index by using a quantum mechanical calculation of the dielectric constant of a compound semiconductor. Besides, Li [8] has made important explorations about the optical properties of ZnSe [9].

2. RESULTS AND DISCUSSION

Most of the previous theoretical studies on transport properties of ZnS and ZnSe have realized based on the Monte Carlo method. In the present work, electronic properties of SI ZnS and ZnSe compound semiconductors have been studied using a COMSOL physics programme in a wide interelectrode distance in the range of 50 mm to 500 mm and pressure are the possibility their to be used as an IR photodetector materials in IR image converters, which are difficult to attain with other materials at room temperature in particular for near-infrared. The calculated transport parameters of these materials are also compared with accordance to the pressure p, interelectrode distance d and voltage. Our results prove that the predicted values of electronic properties of these semiconductors agree fairly well with the known values over a wide range of energy gap.

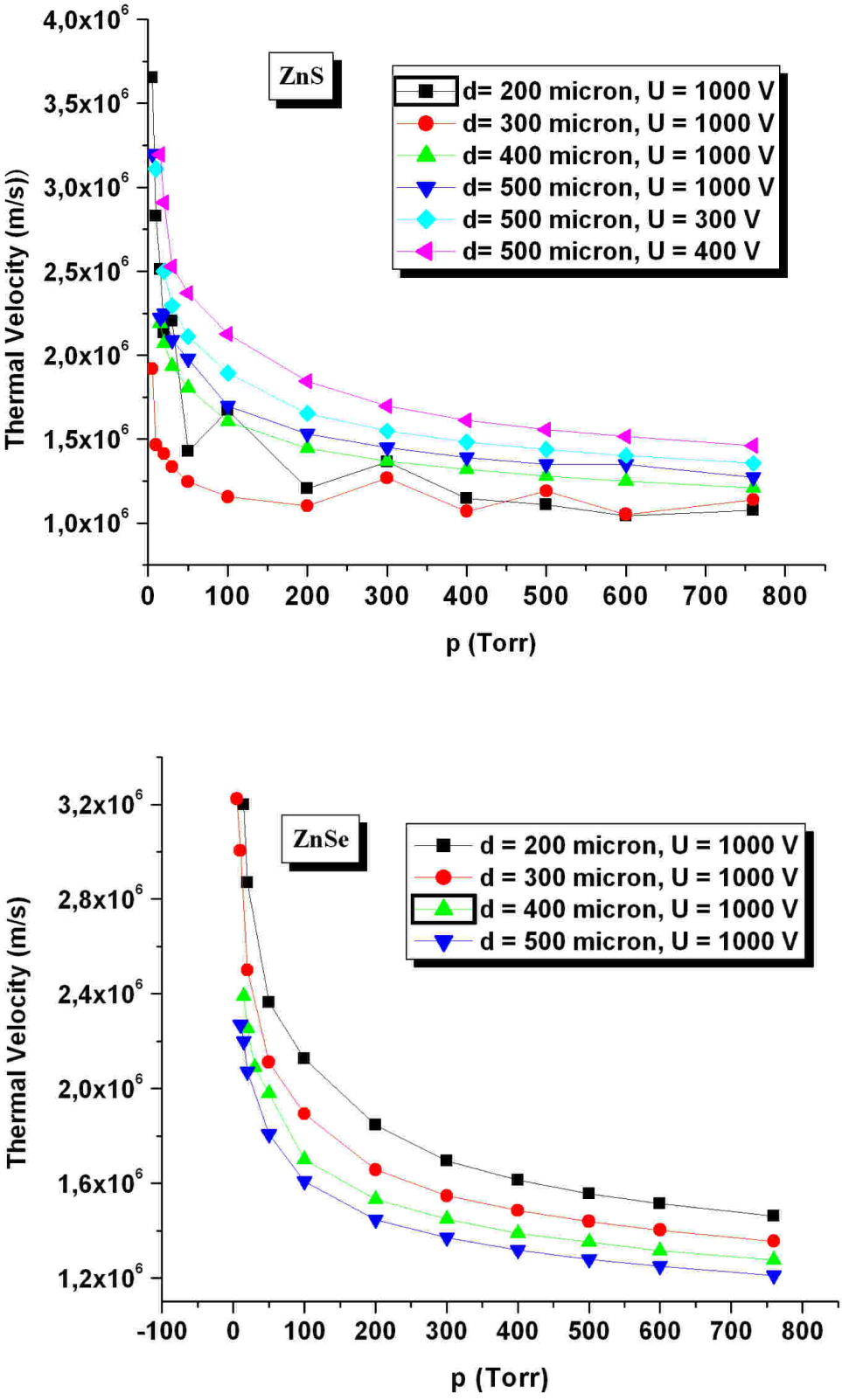

Figure1. Termal velocities with respect to the different d distances in ZnSe and ZnS.

ZnSe under narrower band gap has higher thermal velocity in the low p compared to wider band gap ZnS. The saturation velocity for ZnSe is equal to that of ZnS, and this value is calculated between $1x10^{6}$ and $2x10^{6}$m/s .

3. CONCLUSION

A theoretical study on the discharge features of two semiconductor cathodes has been carried out. The cathodes were made by ZnS and ZnSe. According to the simulations, these cathodes indicate some similar electrical features, although some other features differ. The explorations have been realized the pressure dependence of the thermal velocities indicate similar behaviour.

REFERENCES

[1] Benkabou F., Aourag H., Certier M., Materials Chemistry and Physics .(2000), 66, 10–16.
[2] Mirov S., Fedorov V., Moskalev I., Mirov M., Martyshkin D., Journal of Luminescence.(2013), 133, 268– 275.
[3] Duan Y.L., Yao S.L., Dai C., Liu X.H., Xu G.F., Trans. Nonferrous Met.Soc. China.(2014), 24, 2588−2597.
[4] Mahmood Q., Hassan M., Faridi M.A., Sabir B., Murtaza G., Mahmood Asif, Current Applied Physics. (2016), 16, 549-561.
[5] Benkabou F. , Aourag H., Certier M., Materials Chemistry and Physics.(2000), 66, 10–16.
[6] Mirov S., Fedorov V., Moskalev I., Mirov M., Martyshkin D., Journal of Luminescence.(2013), 133, 268– 275.
[7] Jensen B., Torabi A., Infrared Phys. (1983), 23, 359–361.
[8] Qi H., Zhanga X., Jiang M., Liu C., Wang Q., Li D., Optik. (2016), 127, 5576–5584.
[9] Vasilyev S., Moskalev I., Mirov M., Smolsky V., Mirov S. and Gapontsev V., Laser Technik Journal. 4 (2016), 24.

Parameter Estimation of Weibull Growth Model in Maize

Mehmet Emin Yazıcı[a], Ufuk Karadavut[b], Kübra Soğancı[a] , Galip Şimşek[a]

[a] *Graduate School of Natural and Applied Sciences, Ahi Evran University, Kırşehir, Türkiye*
[b] *Department of Biometry and Genetics, Agricultural Faculty, Ahi Evran University, Kırşehir, Türkiye*

**e-mail corresponding author*: *kubra.soganci.92 @gmail.com*
Keywords: Weibull model, growth curve, maize plants, parameter estimation

ABSTRACT

Weibull growth model is a dynamic model. Because of this feature, its use is increasing constantly. In this study was conducted to estimate Weibull growth curve parameters of maize plants. It is investigated phenotypic and genotypic correlations between growth curve parameters. In this study, Weibull models with 2, 3 and 4 parameters were used to evaluate growth curve parameters and weights at different times. The maize plants are grown in experimental areas of Konya Soil, Water and Deserting Control Research Institute. Plants were grown under the same conditions. Sowing time, irrigation time, weed control time and another work was done at the same time. In 5 plants were used to measurement. As comparison criteria were used Determination coefficient and root mean square error. As results, Determination coefficients were found 96.12 % for fresh matter and 95.88 % for dry matter. Weibull model with four parameters has the best definition in fresh matter and dry matter. These results have shown to us that can be used successfully in the Weibull with 4-parameter model in the growth study.

1. INTRODUCTION

Estimates of crop yield and production is very important on regional and national scales. Improvement of yield is becoming increasingly important in developing countries. However, food prices, food security and for other crucial decisions affect agricultural policy and trade. As generally, estimation of yield is done with crop simulation models. Data obtained from crop simulation models allow government agencies, private industry, and researchers to estimate yield before harvest (Wall et al., 2008). Limitations and potential capabilities of the approach may not be detected at large scales and further assessment should be performed at field scales.

Growth studies in plant growth have shown that nonlinear functions are more complex if the range of the independent variable encompasses growth stage (Philip 1994). A function with a sigmoid form, ideally its origin at (0,0), a point of inflection occurring early in the adolescent stage and either approaching a

maximum value, an asymptote, or peaking and falling in the senescent stage, is justified (Fekedulegn, 1999). Weibull model can be given as example. Nonlinear growth models provide the basis for an objective method of estimating growth potential, yield and the sustainable yield of a crop. Nonlinear models are more difficult to estimate than linear models. Because solutions of growth stages are determined iteratively (Ratkowsky 1983). In this study, we aimed to estimate with Weibull model growth by using 2, 3 and 4 parameter models in maize growth.

Material and method

This research was carried out in 2009-2010 growing season in Konya, Turkey. TTM 8119 maize cultivar was tested in a completely randomized parcels design with four replications. Each plot was 4.0 m * 6.0 m = 24 m^2. Planting distance was 0.75 m between rows and 0.25 m between plants and a plant population was 53 333 plants ha^{-1} . Four-row plots were used for data collection for all other traits. Weed control were practiced two times by hand on the exit and before flowering. The data were recorded ten weeks. For each measurement, 5 plants were randomly selected. Weibull growth model with two, three and four parameters were used in this study. These models are shown in Table 1.

Table 1. Different parameters of Weibull models and growth features

	Different parameters of Weibull models		
Charecters	Two parameters $Y = a(1 - e^{(-ct)})$	Three parameters $Y = a(1 - e^{(-ct^d)})$	Four parameters: $Y = a(1 - be^{(-ct^d)})$
Growth rate	$GR = ace^{-ct}$	$GR = acdt^{d-1}e^{-ct^d}$	$GR = bcdt^{d-1}e^{-ct^d}$
Inflection point	$IP = a - be^{\frac{1-d}{d}}$	$IP = a - ae^{\frac{1-d}{d}}$	No inflection point
Starting point of growth	$SPG = a - b$	$SPG = 0$	$SPG = 0$
Upper asymptote	$UA = a$	$UA = a$	$UA = a$
	Comparison criteria		
R^2	$R^2 = 1 - \frac{SS_{Error}}{SS_{Total}}$		
RMSE	$RMSE = \sqrt{\frac{\sum_{i=1}^{n}(X_{obs,i} - X_{model,i})^2}{n}}$		
X^2	$\chi^2 = \sum_{j=1}^{k}\frac{(G_j - B_j)^2}{B_j}$		

2. RESULTS AND DISCUSSION

The results obtained in this study are given in Table 2. Analyzing the Table, it is seen that as time progresses growth increases up to a certain point. After this point that expressed as the inflection point begins decreasing in the growth rate. The Weibull shape parameter, β, is also known as the Weibull slope. This is because the value of β is equal to the slope of the line in a probability plot. Different values of the shape parameter can have marked effects on the behavior of the distribution (Anderson, 1991). In fact, some values of the shape parameter will cause the distribution equations to reduce to those of other distributions. In many applications however the usual assumption of constant shape parameter β cannot be appropriate. The two-parameter Weibull model at the workshop had less success in identifying than the other models. One studies with fatigue of materials, usually, it is assumed that the shape parameter of the Weibull distribution depends on the stress levels (Meeter and Meeker, 1994; Hirose, 1993; Chan, 1999).

Table 2. Estimation of Weibull models for different parameters

Week	**Dry Matter**	**Weibull with two parameters**	**Weibull with three parameters**	**Weibull with four parameters**
1	15,63	13,60	14,02	16,02
2	37,41	34,58	35,68	38,47
3	52,61	49,61	49,88	51,26
4	84,12	77,74	79,12	85,09
5	101,55	94,58	97,15	100,36
6	128,57	119,67	121,86	125,17
7	148,24	142,55	145,64	145,24
8	176,38	169,94	170,22	177,33
9	195,24	188,47	191,52	195,66
10	192,53	187,23	190,27	193,51
a		197,94	201,23	200,15
b		155,44		
c		0,334	0,238	0,267
d		5,264	4,966	
R^2		0,94	0,97	0,99
RMSE		12,36	10,27	8,12
χ^2		4,25	3,84	1,02
GR		6,38	26,79	20,45
IP		128,621	110,41	No inflection point
SPG				
UA		42,5	0	0
		197,94	201,23	200,15

The main Focus of this study is to discuss some properties of the Weibull models and estimate the parameters. Weibull model estimated succssfully appropriate statistical outputs from agricultural traitments. Good initial estimates are required to estimate the parameters from any iteration method and to specify good initial estimates of the parameters one should know the properties of the parameters (Mahanta and Borah, 2014). This study developed some expressions the initial values of the parameters based on the definitions and properties of the parameter of the Weibull models (Karadavut et. al., 2010; Mahanta and Borah, 2014). These expressions will be very useful to specify growth characteristics values for Weibull models in maize.

3. CONCLUSION

As results, Weibull with four parameters defined as a successful more than other models. However, there isn't inflection point parameter of it. For this reason biological interpretation is difficult. Weibull with three parameters model has made a successful identification for growth. Biological be explained due to the inflection point. Weibull with two parameters have similar characteristics in the Weibull with two parameters. But it was taken to evaluate is poor in comparison criteria.

REFERENCES

[1] Wall, L., Larocque, D., & Léger, P. M. (2008). The early explanatory power of NDVI in crop yield modelling. International Journal of Remote Sensing, 29(8), 2211-2225.

[2] Philip, M.S. 1994. Measuring trees and forests. 2nd edition. CAB Int., Wallingford, UK.310 p.

[3] Fekedulegn, D., Mac Siurtain, M.P., & Colbert, J.J. 1999. Parameter estimation of nonlinear growth models in forestry. Silva Fennica 33(4): 327–336.

[4] Ratkowsky, D.A. 1983. Nonlinear regression modelling. Marcel Dekker, New York. 276 p

[5] Growth and Leaf Area Index Simulation in Maize (Zea mays L.) under Small-Scale Farm Conditions in a Sub-Saharan African Region Jean-Claude Lukombo Lukeba1 , Roger Kizungu Vumilia2,3, Kabwe C.

[6] K. Nkongolo4*, Moïse Lufuluabo Mwabila5 , Mbungu Tsumbu6 American Journal of Plant Sciences, 2013, 4, 575-583

[7] J. J. Hanway, "Internode Lengths at Different Developmental Stages of Corn," Agronomy Journal, Vol. 62, No. 1, 1970, pp. 116-117.

[8] M. R. Thiagarajah and L. A. Hunt, "Effects of temperature on Leaf Growth in Corn (Zea mays)," Canadian Journal of Botany, Vol 60, No. 9, 1982, pp. 1647-1652.

[9] J. R. Porter, P. D. Jamieson and D. R. Wilson, "Comparison of the Wheat Simulation Models AFRCWHEAT2, CERES-Wheat and SWHEAT for Nonlimiting Conditions of Crop Growth," Field Crops Research, Vol. 33, No. 1-2, 1993, pp. 131-157.

[10] Anderson, M.K. (1991). A nonproportional hazards Weibull accelerated failure time regression model, Biometrics, 47, 281–288.

[11] Josmar Mazucheli, Francisco Louzada-Neto and Jorge Alberto Achcar 2003. Lifetime Models with Nonconstant Shape Parameters. https://www.ine.pt/revstat/pdf/rs030103.pdf

[12] Meeter, C.A. and Meeker, W.Q. (1994). Optimum accelerated life tests with a nonconstant scale parameter, Technometrics, 36, 71–83.

[13] Hirose, H. (1993). Estimation of threshold stress in accelerated life-testing, IEEE Transactions on Reliability, 42, 650–657.

[14] Chan, C.K. (1991). Temperature-dependent standard deviation of log(failure time) distributions, IEEE Transactions on Reliability, 40, 2, 157–160.

[15] International Journal of Mathematics Trends and Technology – Volume 8 Number 3 – April 2014 ISSN: 2231-5373 http://www.ijmttjournal.org Page 157 Parameter Estimation of Weibull Growth Models in Forestry Dimpal Jyoti Mahanta1,* and Munindra Borah2

[16] U. Karadavut, K. Kokten and Z. Kavurmaci, "Comparison of relative growth rates in silage corn cultivars," Asian Journal of Animal and Veterinary Advances, vol. 5, no. 3, pp. 223-228, 2010

CERAMIC FILTER SIMULATION MANUFACTURING BY POWDER INJECTION MOLDING METHOD

Levent Urtekin[a]

[a]*Department of Mechanical Engineering, Faculty of Engineering and Architecture, Ahi Evran University, TR-40100 Kırşehir, Turkey*

**e-mail corresponding author*: levent.urtekin@ahievran.edu.tr

Keywords: Ceramic Injection Molding, Rheology, Moldflow

ABSTRACT

In this study; the feedstock was obtained by mixing zirconium-based powder with suitable binders. Rheology experiments of feedstocks were carried out by capillary rheometer. One of the most critical processes in powder injection molding method is known the flow properties of feedstock inside the mold. For this purpose, it was determined the injection pressure, holding pressure, mold closing force and the molding temperature of zirconium filter designed by Autodesk Modlflow design simulation program. The filter design and the obtained of solid model was performed by SolidWorks program. The solid model is then transferred to Moldflow program and embedded in the mold. The flow properties of the feedstock was examined using the proper gating design. The mold filling time, injection pressure, flow rate and the cylinder temperature of the ceramic filter was determined.

1. INTRODUCTION

Powder Injection molding method is a net-shape process for the manufacturing. Metal (MIM) and ceramic (CIM) powder injection method used variety of industry. Final products are used medical, dental device, firearms, aerospace, and automotive. The PIM process is basically four step, (I) feedstock preparing (mixing, granulation), (II) injection molding, (III), debinding (solvent, thermal) and (IV) sintering. For proper molding of feedstock, feedstock flow behavior and viscosity are the most important feature [1-4]. Powder Injection molding process given in Figure 1.

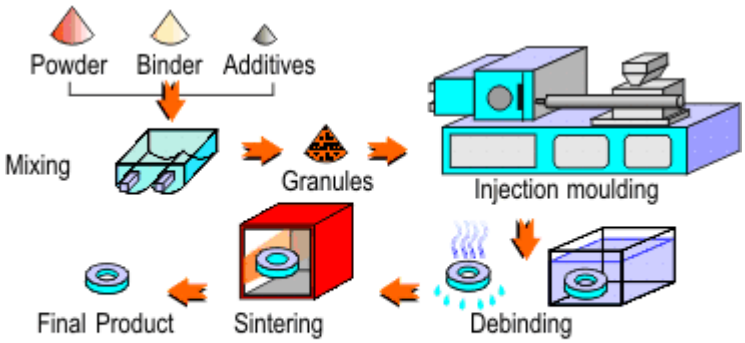

Figure 1. The powder injection moulding process [5]

2. RESULTS AND DISCUSSION

Rheological tests were carried out in a custom built capillary rheometer to determine the behavior of feedstocks. Water based binder of composition (wt. %) 65 % PEG 8000, 30 % Polyethylene (PE) and 5 % stearic acid (SA) was used to prepare feedstocks. Rheological properties of each feedstock were measured at six temperatures from 225 ºC to 240 ºC and under pressures of 1.36 MPa (197 psi) and 1.88 MPa (272 psi). Designated pressure was applied to the feedstock under constant temperature and thus the feedstock was pushed by plunger through the capillary tube and the flow time was recorded. Pressure applied during rheological tests is not critically affecting the viscosity. The tests for this feedstock were repeated at temperatures 225 to 240 ºC. In Figure 2. given rheology analysis.

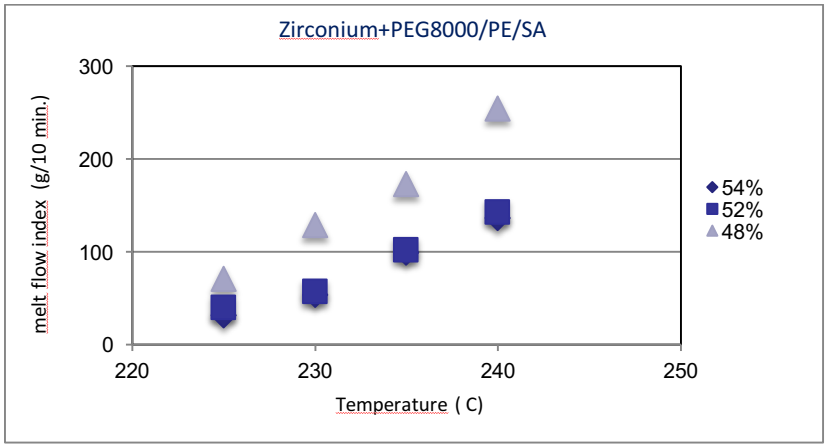

Figure 2. Melt Flow Index Versus Temperature For 48-54 vol. % Zirconium Loading

Flow properties was determined the injection pressure, holding pressure, mold closing force and the molding temperature of zirconium filter designed by Autodesk Modlflow design simulation program. The filter design and the obtained of solid model was performed by SolidWorks program. The solid model is then transferred to Moldflow program and embedded in the mold. The flow properties of the feedstock was examined using the proper gating design. The mold filling time, injection pressure, flow rate and the cylinder temperature of the ceramic filter was determined. Figure 3. was given simulation analysis.

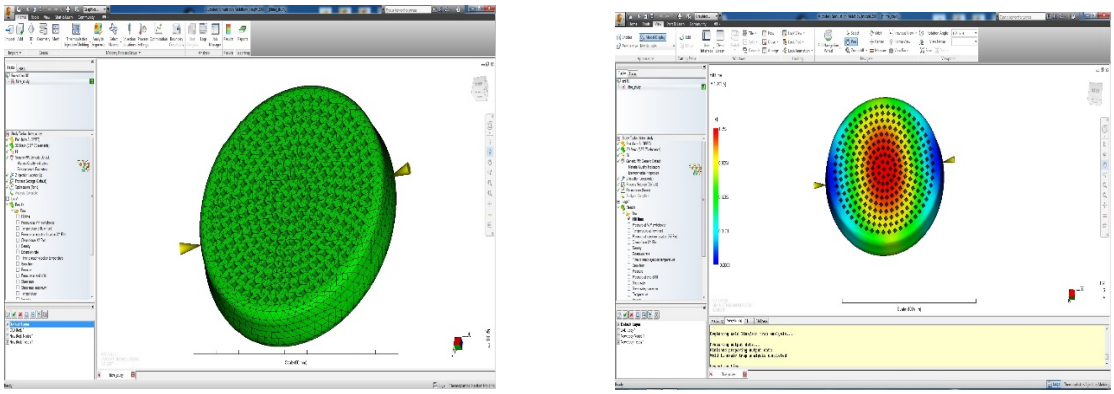

Figure 3. Moldflow Simulation

3. CONCLUSION

- Maximum solid loading with the PEG-based binder is 54 vol. %.
- Temperature ranges 225 to 240 °C are suitable for molding of PEG-based feedstock.
- Moldflow Simulation Analysis: Viscosity 525 < 1000 Pa.s (critical value), Temperature 237-240.3 °C, Filling time 1.252 s, Shrinkage 17.94 %.

REFERENCES

[1] German, R.M., "Powder Injection Molding", New Jersey, USA, (1990).
[2] German, R.M., Bose, A., "Injection Molding of Metals and Ceramics", Metal Powder Industries Federation, New Jersey, (1997).
[3] Karataş, Ç. ve Sarıtaş, S., "Toz Enjeksiyon Kalıplama: Bir Yüksek Teknoloji İmalat Metodu", Gazi Ünv. Müh-Mim. Fak. Dergisi, (1998), 13 (2): 193.
[4] Karatas C., Kocer A., Unal H.I., Sarıtas S., Rheological Properties of Feedstocks Prepared with Steatite Powder and Polyethlene-Based Thermoplastic Binders, J. Materials Processing Technology, (2004),152 77-83.
[5] Azom Materials-http://www.azom.com/article.aspx/ArticleID=1080

Species of Microfungi Isolated From *Buxus sempervirens* L. in Küre Mountains National Park Forest Ecosystems

Makbule Erdoğdu

[b]*Department of Biology, Faculty of Arts and Sciences, AhiEvran University, TR-40100 Kırşehir, Turkey*

**e-mail corresponding author*: *merdogdu@ahievran.edu.tr*

Keywords: Buxus sempervirens, microfungi, new record

ABSTRACT

The material of this study comprises microfungi specimens collected on *Buxus sempervirens* in Kastamonu Küre Mountains National Park in the years 2005 and 2006. As a result of field and laboratory studies, a total 7 species of micromycetes identified on *Buxus sempervirens* L. *Cyanonectria buxi* (Fuckel) Schroers is reported for the first time from Turkey.

1. INTRODUCTION

Mycobiota is an important component of an ecosystem, ensuring its formation and stability: fungi play important role in organic matter decomposition and soil formation, participate in nutrient cycling both directly and by assisting nutrient uptake by plants, regulate plant communities both by mutualistic and biotrophic life modes (Kutorga et al. 2012). Pathogenic fungi depend on living trees for at least a portion of their nutrition. Many have saprophytic ability as well or live on the dead parts of live trees, but others are obligate parasites that thrive on vigorous trees. These fungi have have coevolved with their host and exist in an often delicate balance with them. Just as the saprophytic and symbiotic fungi play essential roles in the forest, so the pathogens manage many ecocystem interactions. In a forest without disease, succession would be slowed and plant and animal diversity lowered, with special losses among cavity-dwelling birds and mammals. Disease, caused mostly by fungi, results in more economic destruction in forest than insects and fire combined (Hansen and Lewis 1997). Floristic studies of the microfungal biota are the first and the most important step to controlling the fungal diseases in a country.

Küre Mountains National Park is located within the Kastamonu and Bartın Provinces. Kastamonu Province is situated in the Euro – Siberian phytogeographic region. This region lies to the northern Turkey and constitutes an important National Park. According to the grid square system adopted by Davis, Kastamonu is located in the squares A4. The climate of the province is oceanic. It is rainy during all 4 seasons. The Kastamonu province was chosen as a research area, because its climatic conditions (especially high humidity) and plant distributions are very suitable for the growth of microfungi.

There are about 90 species of boxwood from Eurasia, Africa, the Caribbean, and Central America. It is known that of box tree (*Buxus balearica* Lam. and *Buxus sempervirens* L.) grow in natural conditions of Turkey. *Buxus sempervirens* is a small native tree mostly growing along the coastal areas of Marmara and Black Sea regions of Turkey on approximately 1000 hectares. The present taxonomic research is based on the microfungi collected on *Buxus sempervirens* in Kastamonu Küre Mountains National Park.

2. MATERIALS & METHODS

Infected plant specimens were collected from Küre Mountains National Park in Kastamonu province of Turkey. The host specimens were prepared according to established herbarium techniques. The fungal material for examination were isolated from the host plants by obtaining thin sections or scraping. For microscopic examination and microphotographs a Leica DM E light microscope was used. A Leica EZ4D stereo microscope was used for close-up photographs of the acervuli on the leaf surface. Spores were

measured using a Leica DM E light microscope. The microfungi were identified using relevant literature (Dennis 1981; Ellis and Ellis 1987; Grove 1935; Ignatavičiūtė and Treigienė 1998; Saccardo 1881-1931; Smitskaya et al. 1986; Sutton 1980; Vasil'yeva ve Mitrofanova 1974; Wilson ve Henderson 1966). All specimens examined were deposited in the mycological collection of the Department of Biology, Faculty of Arts and Science, Ahi Evran University, Kırşehir province of Turkey.

3. LIST OF TAXA

The list of microfungi with their host plant, collection sites, coordinates, altitudes, dates and the numbers of the collector (ME = Makbule Erdogdu) is arranged below according to the systematics given in Index Fungorum (www.indexfungorum.org).

Ascomycota
Dothideomycetes
Capnodiales
Mycosphaerellaceae
***Mycosphaerella buxicola* (DC.) Tomilin**
Material examined: Turkey, Kastamonu, Pınarbaşı District, Ilıca Waterfall, 726 m, 30.08.05, 41°41'893''N, 33°07'861''E, on leaves of *Buxus sempervirens*, ME 1745.

Pleosporales
Melanommataceae
***Melanomma pulvis-pyrius* (Pers.: Fr.) Fuckel**
Material examined: Turkey, Kastamonu, Pınarbaşı District, Ilıca Waterfall, 726 m, 30.08.05, 41°41'893''N, 33°07'861''E, on branches of *Buxus sempervirens*, ME 1745 (Figure 1).

Sordariomycetes
Amphisphaeriales
Bartaliniaceae
***Truncatella angustata* (Pers.) S. Hughes**
Material examined: Turkey, Kastamonu, Pınarbaşı District, Ilıca Waterfall, 726 m, 30.08.05, 41°41'893''N, 33°07'861''E, on branches of *Buxus sempervirens*, ME 1745.

Hypocreales
Nectriaceae
***Cyanonectria buxi* (Fuckel) Schroers**
Material examined: Turkey, Kastamonu, Pınarbaşı District, Ilıca Waterfall, 726 m, 30.08.05, 41°41'893''N, 33°07'861''E, on branches of *Buxus sempervirens*, ME 1745.

***Pseudonectria buxi* (DC.) Seifert, Gräfenhan & Schroers**
Material examined: Turkey, Kastamonu, Pınarbaşı District, Ilıca Waterfall, 726 m, 30.08.05, 41°41'893''N, 33°07'861''E, on leaves of *Buxus sempervirens*, ME 1745; Turkey, Kastamonu, Pınarbaşı District, Horma Canyon, 970 m, 27.06.05, 41°44'015''N, 33°051'506''E, on leaves of *Buxus sempervirens*, ME 1646 (Figure 2).

Xylariales
Hyponectriaceae
***Hyponectria buxi* (Alb. & Schwein.) Sacc.**
Material examined: Turkey, Kastamonu, Pınarbaşı District, Ilıca Waterfall, 726 m, 30.08.05, 41°41'893''N, 33°07'861''E, on leaves of *Buxus sempervirens*, ME 1745; Turkey, Kastamonu, Pınarbaşı District, Horma Canyon, 970 m, 27.06.05, 41°44'015''N, 33°051'506''E, on leaves of *Buxus sempervirens*, ME 1646; Turkey, Kastamonu, Cide District, Ovacık Village, 421 m, 22.08.06, 41°49'37''N, 32°53'18''E, on leaves of *Buxus sempervirens*, MK 1920 (Figure 3).

Basidiomycota
Pucciniomycetes
Pucciniales
Pucciniaceae
***Puccinia buxi* DC.**

Material examined: Turkey, Kastamonu, Pınarbaşı District, Ilıca Waterfall, 726 m, 30.08.05, 41°41'893''N, 33°07'861''E, on leaves of *Buxus sempervirens*, ME 1745; Turkey, Kastamonu, Pınarbaşı District, Kurtgirmez Mountain, 1310 m, 18.08.06, 41°36'90''N, 33°12'32''E, on leaves of *Buxus sempervirens*, MK 1825; Turkey, Kastamonu, Cide District, Ovacık Village, 421 m, 22.08.06, 41°49'37''N, 32°53'18''E, on leaves of *Buxus sempervirens*, MK 1920.

4. RESULTS AND DISCUSSION

The material of this study comprises microfungi specimens collected on *Buxus sempervirens* in Kastamonu Küre Mountains National Park in the years 2005 and 2006. As a result of field and laboratory studies, a total 7 species of micromycetes identified on *Buxus sempervirens* (*Cyanonectria buxi* (Fuckel) Schroers, *Hyponectria buxi* (Alb. & Schwein.) Sacc., *Melanomma pulvis-pyrius* (Pers.: Fr.) Fuckel, *Mycosphaerella buxicola* (DC.) Tomilin, *Pseudonectria buxi* (DC.) Seifert, Gräfenhan & Schroers, *Puccinia buxi* Sowerby and *Truncatella angustata* (Pers.) S. Hughes). *Cyanonectria buxi* (Fuckel) Schroers is reported for the first time from Turkey.

The recorded microfungi revealed different consort relationships with their host plants. This consort relationships were positive, negative, indifferent and antagonistic. Although fungi develop on edificators in indifferent consortive relations, hosts can continue their normal development and seed. Microfungus consort in negative consortive relations are generally represented with obligate parasites and sometimes with facultative parasites or pathogens. *Pseudonectria buxi* (DC.) Seifert, Gräfenhan & Schroers, *Hyponectria buxi* (Alb. & Schwein.) Sacc. and *Puccinia buxi* DC. with *Buxus sempervirens* L. is example of microfungi and host that have negative relations. In positive consortive relations, microfungi enable fragmentation of organic components (lignin, pektit, cellulose) until simple mineral components and ensure continuity of energy flow in biocoenosis. Saprotroph microfungi that play an active role in substance cycle by creating a humus-like substance by crumbling wood are in a positive relation with their hosts. There are positive consortive relations between *Melanomma pulvis-pyrius* (Pers.: Fr.) Fuckel, *Truncatella angustata* (Pers.) S. Hughes, *Mycosphaerella buxicola* (DC.) Tomilin and *Cyanonectria buxi* (Fuckel) Schroers with *Buxus sempervirens* L. Antagonistic relations were not registered in study area.

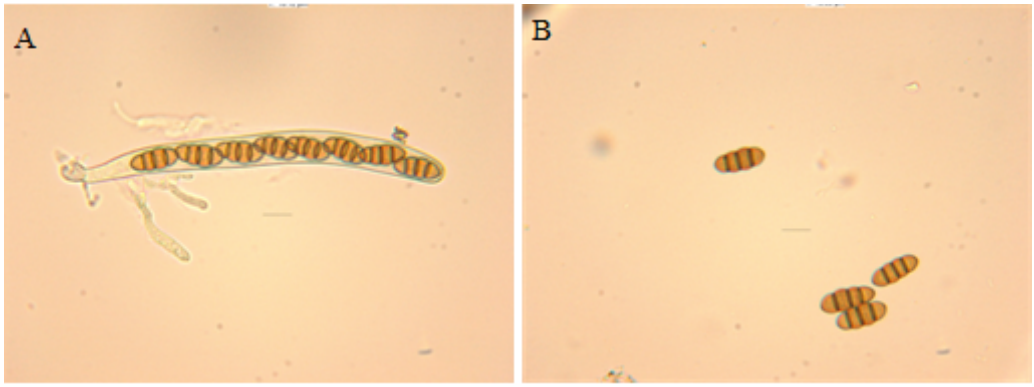

Figure 1. *Melanomma pulvis-pyrius* (Pers.: Fr.) Fuckel: A. Ascus, B. Ascospores

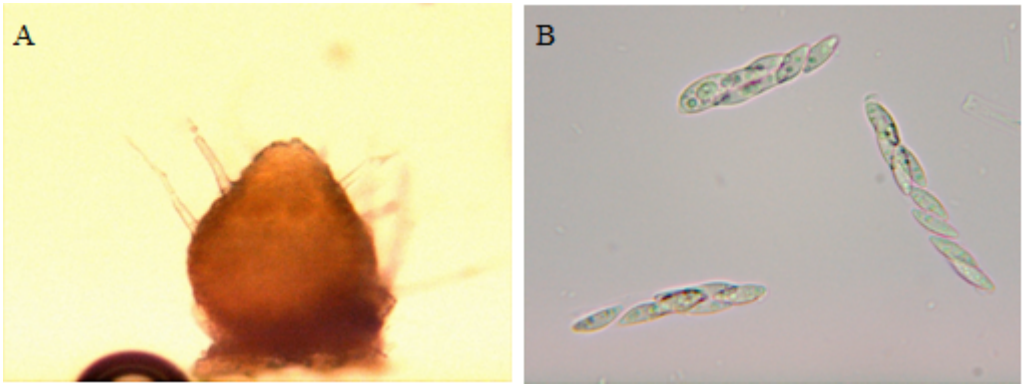

Figure 2. *Pseudonectria buxi* (DC.) Seifert, Gräfenhan & Schroers: A. Perithecium, B. Asci and ascospores

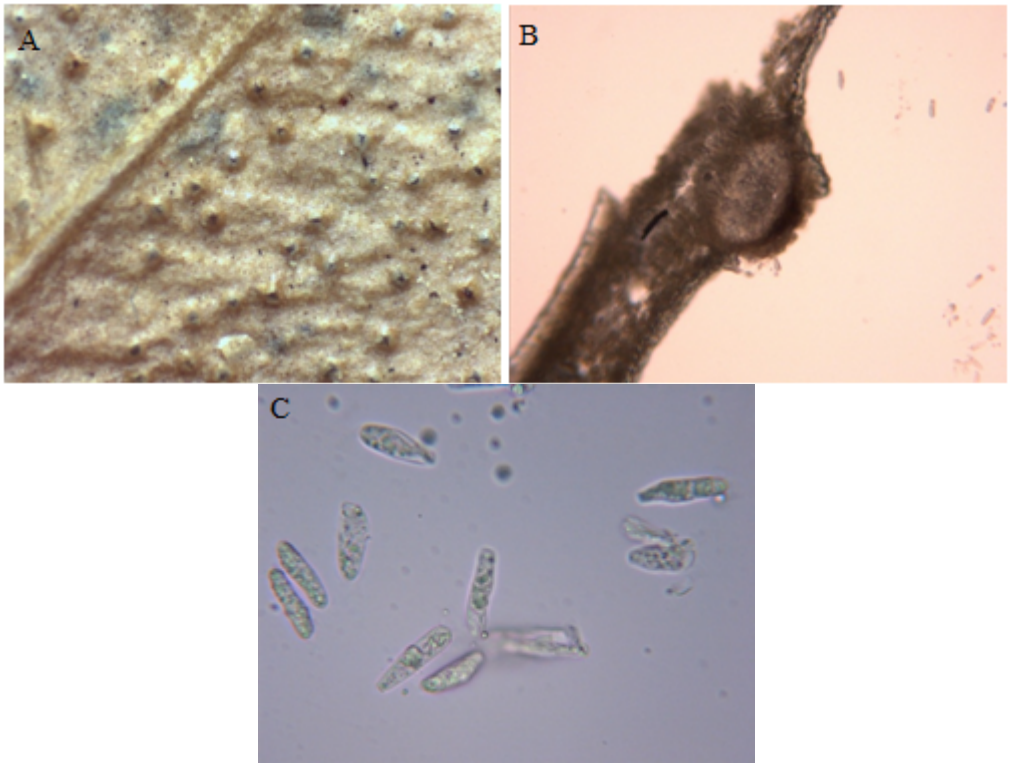

Figure 3. *Hyponectria buxi* (Alb. & Schwein.) Sacc.: A. General appearance of infected leaf, B. Vertical section of the pycnidium, C. Conidia.

REFERENCES

[1] Dennis R.W.G. British Ascomycetes, Cramer, Stutgard. (1981).
[2] Ellis B.M. and Ellis J.P. Microfungi on Land Plants, Croom Helm, London & Sydney. (1987).
[3] Grove W.B. British stem–and leaf fungi. Coelomycetes, Vol: 1, At the Universty Pres, Cambridge. (1935).
[4] Hansen E.M., Lewis K.J. (eds.). Compendium of conifer diseases. American Phytopathological Society Press, St. Paul, Minn. (1997).
[5] Ignatavičiūtė M. and Treigienė A., Mycota Lithuaniae, Vol: 9, Melanconiales, UAB Vaslstıečıu Laıkraštıs, Vılnıus. (1998).
[6] Kutorga E., Adamonytė G., Iršėnaitė R., Kasparavičius J., Markovskaja S., Motiejūnaitė J. and Treigienė A., Botanica Lithuanica. (2012), 18(1): 66 – 79.
[7] Saccardo P.A., Sylloge Fungorum omnium hucusque cognitorum, Vol: 1-25, Pavia, (1881-1931), Johnson reprint corporation, New York, London, Vol: 26. (1972).
[8] Smitskaya M.F., Smyk L.W. and Merezhko T.A., Opredelitel' pirenomitsetov, Naukova Dumka, Kiev. (1986).
[9] Sutton B.C., The Coelomycetes Fungi Imperfecti with Pycnidia, Acervuli and Stromata, Common Wealth Mycol. Institute, Kew, Surrey, England. (1980).
[10] Vasil'yeva L.I. and Mitrofanova O.B., Glavneyşiye bolezni dekorat Kustarn. Krıma i meri borbı snimi, Yatla. (1974).
[11] Wilson L.M. and Henderson D.M., British Rust Fungi, At the University Pres, Cambridge. (1966).

Temperature Dependent Electrical Characteristics of Au/p-CuO/n-Si/Ag Structures

Muhammmet Kaya[a], Funda Aksoy Akgul[a], Guvenc Akgul[b]

[a]*Physics Department, Ömer Halisdemir University, TR-51240 Nigde, Turkey*
[b]*Bor Vocational School, Ömer Halisdemir University, TR-51700 Niğde, Turkey*

**e-mail corresponding author*: fundaaksoy01@gmail.com

Keywords: p-type CuO, chemical bath deposition, heterojunction diodes

ABSTRACT

In this work, p-type CuO thin films were deposited onto n-type (100)-oriented crystalline Si wafer through cost-effective chemical bath deposition technique in order to construct p/n heterojunction diodes. Temperature-dependent current – voltage (I–V) characteristics of the fabricated structures were investigated in the range of 220 – 360 K under dark conditions. Important diode parameters such as ideality factor (n), dark saturation current (I_0) and barrier height ($q\Phi_B$) were evaluated as a function temperature. Electrical measurements revealed that the diodes have a well-defined rectifying behavior with a good rectification ratio of ~10^2 at ±2 V and a relatively small ideality factor of n = 2.1 at room temperature. The estimated values of the n, I_0 and $q\Phi_B$ were found to be between 1.7 – 3.1, 6.2×10^{-8} – 2.1×10^{-9} A and 0.6 – 0.9 eV, respectively.

1. INTRODUCTION

Semiconductor p-n heterojunction structures are basic elements in modern microelectronic and energy conversion devices, and play crucial roles as either functional or interconnecting elements [1]. Tremendous efforts have been made by researchers to fabricate Si-based optoelectronic devices integrated with different materials including metal oxide semiconductors [2]. Copper oxide (CuO) has emerged as a potential complementary candidate for optoelectronic applications due to its suitable properties such as p-type conductivity, narrow optical bandgap between 1.2-1.9 eV (ideal for sunlight absorption), high absorption coefficient over a substantial portion of the solar spectrum, direct type bandgap structure and similar electron affinity to Si. A wide range techniques have been employed to prepare CuO thin films such as reactive evaporation, thermal oxidation, chemical vapor deposition, chemical bath deposition and sol-gel [3].

Development of p–n junction with high-quality interface is among the most challenging problems for the heterojunction devices. In this study, p-type CuO thin films were deposited onto n-type (100)-oriented crystalline Si wafers through cost-effective chemical bath deposition technique in order to construct p/n heterojunction diodes and electrical characterization of fabricated structures was reported in the temperature range of 220 – 360 K.

2. RESULTS AND DISCUSSION

Fabrication of heterojunction diodes was achieved in two steps. In the first, thin CuO films were deposited onto the one side polished crystalline n-type Si (100) wafers of 1-10 Ω.cm resistivity via chemical bath deposition in order to create three-dimensional p-n heterojunctions structures. The solution for the deposition of CuO thin films was prepared by dissolving copper acetate ($Cu(CH_3COO)_2$. H_2O, Merck, 99.98%) in ethanol. Afterwards, lactic acid ($C_3H_6O_3$, 85%) and triethylamine ($C_6H_{15}N$, 99.95%) was added

into the prepared solution. The solution was deposited directly onto the Si wafers by chemical bath deposition. CuO thin films were also deposited onto pre-cleaned commercially available soda-lime silicate glass slides for the characterization of the film properties. Crystalline Si and glass substrates were dipped vertically into CuO solution for 20 seconds, then dried on a hot plate at 150 °C for 3 minutes in air under ambient conditions. Dipping/drying cycle was repeated as many times as desired in order to get sufficient film thickness. The second step of device fabrication was completed by the thermal evaporation of gold (Au) and silver (Ag) as ohmic front and back contacts, respectively. Formation of ohmic-type contacts was achieved by subsequent annealing at 180 °C for 10 minutes.

Before the fabrication of heterojunction diodes, CuO thin films deposited onto glass substrates were investigated. Samples were annealed in a muffle furnace under atmospheric conditions for 20 minutes at different temperatures varied between 200 and 600 ºC to obtain films with better properties. Structural properties of the as-deposited and post-annealed CuO films were evaluated through X-ray diffraction (XRD). XRD measurements were performed using a Rigaku Miniflex diffractometer with Cu Kα radiation (λ = 0.154 nm). XRD patterns of the samples are shown in Fig 1.

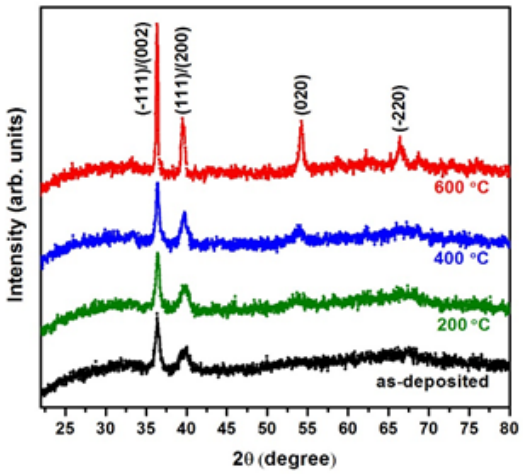

Figure 1. XRD patterns of as-deposited and post-annealed CuO thin films as a function of annealing temperature.

As-prepared sample exhibits two distinct peaks, indicating polycrystalline structure. The first and second Bragg diffraction peaks at an angle 2θ of 35.6º and 38.7º can be indexed to (-111) or (002) and (111) or (200) reflections, respectively, indicating tenorite phase of CuO [3]. Sharpest XRD peaks were monitored for the thin film annealed at 600 ºC. The Rietveld method was applied to the collected diffraction data to derive structural parameters of CuO samples. The largest crystallite size of 554 Å was estimated when CuO thin film was annealed at 600 ºC. The same thin film sample also exhibited the lowest value for the density of dislocations. Obviously, thermal energy provided by annealing treatment leads to larger crystallite formation. The observed increase in crystallite size could be correlated with the reduced amount of lattice imperfections in the crystalline structure of CuO. Optical properties of the as-deposited and post-annealed thin CuO films were evaluated by the analysis of transmission and reflection spectra. Tauc model was used for estimating optical bandgap energy (E_g) of CuO thin films [4]. E_g of the as-deposited and annealed CuO films at 200 °C, 400 °C and 600 °C was estimated to be approximately 1.77, 1.71, 1.54 and 1.45 eV, respectively. Determined bandgap energies are consistent with the reported values of CuO thin films [5]. Transport properties of CuO thin films including carrier concentration and mobility were obtained from Hall Effect measurements by conventional four-point dc Van der Pauw technique. All investigated thin film samples revealed p-type conductivity. Experimental results indicate that the electrical properties of the post-annealed CuO films are substantially improved by annealing process compared to as-deposited sample.

In our study, the optimal film characteristics were found at an annealing temperature of 600 ºC, based on the obtained results. p-n heterojunction diodes were constructed by coating of p-type CuO films onto the n-type (100)-oriented crystalline wafers. Thereafter, fabricated devices were annealed at 600 ºC for 20 minutes. In order to determine the electrical properties of the constructed devices, the current – voltage (I–V) measurements were carried out in between -2 and +2 V over the temperature range of 220 – 360 K. Temperature dependent I–V characteristics of the fabricated diodes were measured by LabVIEW controlled

Keithley 2400 source meter and Janis liquid nitrogen VPF series cryostat system. The temperature of the diodes was controlled by a LakeShore-331 temperature controller. The typical and semi-logarithmic *I–V* characteristics measured in the dark at room temperature is shown in Fig. 2. Significant rectifying behavior with a rectifying ratio of ~10^2 at ±2 V was observed at 300 K. This result confirms the successful formation of p-n heterojunctions within the heterojunction structure.

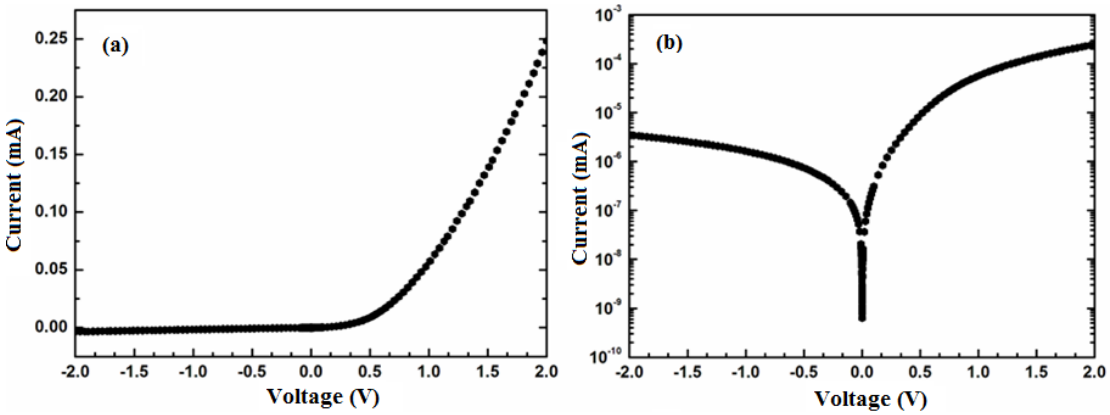

Figure 2. Typical (a) and semi-logarithmic *I–V* characteristics (b) of the fabricated Au/p-CuO/n-Si/Ag structures measured at room temperature.

I–V characteristics of the fabricated devices in the temperature range of 220 – 360 K were analyzed, and important diode parameters including ideality factor (n), dark saturation current (I_0) and zero-bias barrier height ($q\Phi_B$) were determined using the standard Shockley-diode model [6]. Obtained results for the fabricated heterojunction devices are listed in Table 1. As can be seen from Table 1 below, the value of $q\Phi_B$ increases with increasing temperature since more carriers have enough energy to overcome the barriers and contributed to the conduction with increasing temperature. In addition, the ideality factor n decreases with increasing temperature on the contrary to the $q\Phi_B$. The n could be useful to achieve the information about current transport mechanism of the fabricated heterojunction diodes. It can be seen that the calculated n values are higher than one. This result indicates that there could be other transport mechanisms different from the pure thermionic emission mechanism in which $n = 1$.

Table 1. Electrical properties of as-deposited and post-annealed CuO thin films

Temperature [K]	Rectification Ratio	Ideality Factor, n	Saturation Current, I_0 [A]	Barrier Height, $q\Phi_B$ [eV]
220	1.2 x 10^3	3.06	2.06 x 10^{-9}	0.62
240	1.1 x 10^3	2.65	2.72 x 10^{-9}	0.69
260	7.8 x 10^2	2.43	5.61 x 10^{-9}	0.75
280	4.9 x 10^2	2.21	8.87 x 10^{-9}	0.79
300	2.2 x 10^2	2.06	2.11 x 10^{-8}	0.83
320	1.8 x 10^2	1.94	2.32 x 10^{-8}	0.86
340	1.1 x 10^2	1.85	3.48 x 10^{-8}	0.88
360	0.8 x 10^2	1.74	6.21 x 10^{-8}	0.91

3. CONCLUSION

In this study, Au/p-CuO/n-Si/Ag heterojunction diodes were fabricated by depositing of p-type CuO films onto the n-type Si wafers via simple and cost-effective chemical bath deposition technique. Constructed devices demonstrated good p-n characteristics in the dark condition. Diode parameters of ideality factor (n), rectification ratio and zero-bias barrier height ($q\Phi_B$) were calculated to be 2.1, ~10^2 and 0.91 eV, respectively, at room temperature. The obtained values for n, I_0 and $q\Phi_B$ were found to be strongly temperature dependent. The observed diode performance clearly shows that the investigated device structure could be a promising candidate for high-performance low-cost new-generation diodes.

4. ACKNOWLEDGEMENTS

M.K., F.A.A. and G.A. would like to give thanks to Research Projects Unit of Ömer Halisdemir University (The Project Code: FEB 2014/25-BAGEP and The Project Code: FEB 2014/26-BAGEP) for the financial support.

REFERENCES

[1] Yang C., Barrelet C.J., Capasso F. and Lieber C.M., Nano Letters (2006), 6, 2929 – 2934.
[2] Akgul G., Aksoy Akgul F., Mulazimoglu E. and Unalan H.E., J. Phys. D: Appl. Phys. (2014), 47, 065106 – 065113.
[3] Aksoy Akgul F., Akgul G., Yildirim N., Unalan H.E. and Turan R., Materials Chemistry and Physics (2014), 147, 987 – 995.
[4] Tauc J.V., Optical Properties of Solids, (1972), F. Abeles ed., North-Holland Publishing, Amsterdam.
[5] Ramya V., Neyvasagam K., Chandramohan R., Valanarasu S. and A.M.F. Benial, J Mater Sci: Mater Electron (2015), 26, 8489 – 8496.
[6] Schroder D.K., Semiconductor Material and Device Characterization, (2006), third ed., John Wiley & Sons, New York.

Electrical Characterization of p-type CuO Thin Film/n-type Si Nanowire Heterojunction Diodes

Muhammmet Kaya[a], Funda Aksoy Akgul[a], Guvenc Akgul[b]

[a]*Physics Department, Ömer Halisdemir University, TR-51240 Nigde, Turkey*
[b]*Bor Vocational School, Ömer Halisdemir University, TR-51700 Niğde, Turkey*

**e-mail corresponding author*: fundaaksoy01@gmail.com

Keywords: CuO thin films, MACE method, p-n heterojunctions

ABSTRACT

This study presents results on the fabrication and electrical characterization of cupric oxide (CuO) coated silicon (Si) nanowire-based heterojunction diodes prepared by solution-based low-cost methods. Dense arrays of vertically well-aligned Si nanowires were synthesized on n-type (100)-oriented Si wafer through metal-assisted chemical etching (MACE) technique. p-type CuO thin films were then deposited onto Si nanowire arrays via chemical bath deposition to construct three-dimensional heterostructures. Electrical properties of the diodes were determined with the current – voltage (I–V) measurements over the temperature range of 220 – 360 K. Main diode parameters including ideality factor (n), dark saturation current (I_0) and zero-bias barrier height ($q\Phi_B$) were evaluated as a function temperature. I–V measurements exhibited that the fabricated diodes have a well-defined rectifying behavior with a good rectification ratio of ~10^3 at ±3 V and a relatively small ideality factor of n = 1.6 at room temperature. The obtained values for n, I_0 and $q\Phi_B$ were found to be strongly temperature dependent.

1. INTRODUCTION

One-dimensional Si nanostructures in the form of nanowires have revealed a conspicuous promise for next-generation optoelectronic applications due to their interesting optical and electronic characteristics including high surface-to-volume ratios, direct conduction pathway for charge transport, intrinsic antireflection effect and thus high light absorption. Up to now, several fabrication methods for the formation of nanowires on Si substrates have been developed. Among these methods, chemical vapour deposition (CVD), vapor liquid solid (VLS), molecular beam epitaxy (MBE), thermal evaporation and electron beam evaporation can be recognized as the most commonly used bottom-up approaches. Other top-down alternatives are lithographical methods and a novel metal-assisted chemical etching (MACE) [1, 2]. Metal-assisted chemical etching of Si substrates is a very easy and powerful solution-based route. Facile and relatively cheap process equipments, adaptability to large area applications, controlled density and length, same crystal quality and uniform doping type with pristine Si substrate can be major advantageous of MACE over other methods.

Tremendous efforts have been made by researchers to fabricate Si nanowires-based optoelectronic devices integrated with different materials including metal oxide semiconductors. Copper(II) oxide (CuO) has emerged as a potential complementary candidate for optoelectronic applications due to its suitable properties such as p-type conductivity, narrow optical bandgap between 1.2-1.9 eV (ideal for sunlight absorption), high absorption coefficient over a substantial portion of the solar spectrum, direct type bandgap structure and similar electron affinity to Si. A wide range techniques have been employed to prepare CuO thin films such as reactive evaporation, thermal oxidation, chemical vapor deposition, chemical bath deposition and sol-gel [3].
Development of p–n junction with high-quality interface is among the most challenging problems for the heterojunction devices. In this study, fabrication and electrical characterization of cupric oxide (CuO)

coated silicon (Si) nanowire-based heterojunction diodes were reported in the temperature range of 220 – 360 K.

2. RESULTS AND DISCUSSION

Fabrication of Si nanowires-based heterojunction diodes was achieved in two steps. In the first, highly oriented Si nanowire arrays were produced by typical MACE method, as discussed in a previous work [2]. One side polished n-type Si (100) wafers of 1-10 Ω.cm resistivity were used. In the second fabrication step, thin CuO films were deposited onto the as-grown Si nanowire arrays via chemical bath deposition in order to create three-dimensional p-n heterojunctions structures. The solution for the deposition of CuO thin films was prepared by dissolving copper acetate ($Cu(CH_3COO)_2$. H_2O, Merck, 99.98%) in ethanol. Afterwards, lactic acid ($C_3H_6O_3$, 85%) and triethylamine ($C_6H_{15}N$, 99.95%) was added into the prepared solution. The solution was deposited directly onto the Si nanowire arrays by chemical bath deposition. CuO thin films were also deposited onto pre-cleaned commercially available soda-lime silicate glass slides for the characterization of the film properties. Si and glass substrates were dipped vertically into CuO solution for 20 seconds, then dried on a hot plate at 150 °C for 3 minutes in air under ambient conditions. Dipping/drying cycle was repeated as many times as desired in order to get sufficient film thickness. The device fabrication was completed by the thermal evaporation of gold (Au) and silver (Ag) as ohmic front and back contacts, respectively. Formation of ohmic-type contacts was achieved by subsequent annealing at 180 °C for 10 minutes.

Before Si nanowires-based diode fabrication, CuO thin films deposited onto glass substrates were investigated. Samples were annealed in a muffle furnace under atmospheric conditions for 20 minutes at different temperatures varied between 200 and 600 ºC to obtain films with better properties. Structural properties of the as-deposited and post-annealed CuO films were evaluated through X-ray diffraction (XRD). XRD measurements were performed using a Rigaku Miniflex diffractometer with Cu Kα radiation (λ = 0.154 nm). XRD patterns of the samples are shown in Fig 1.

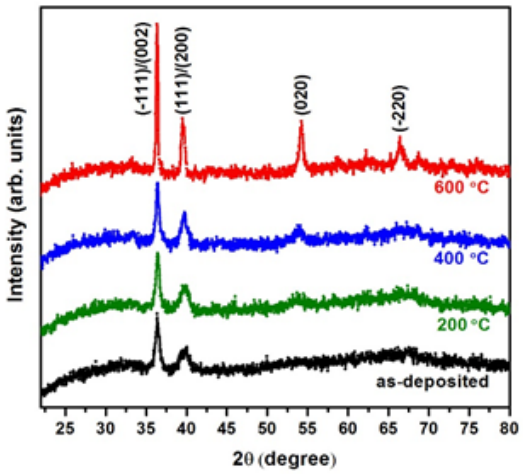

Figure 1. XRD patterns of as-deposited and post-annealed CuO thin films as a function of annealing temperature.

As-prepared sample exhibits two distinct peaks, indicating polycrystalline structure. The first and second Bragg diffraction peaks at an angle 2θ of 35.6º and 38.7º can be indexed to (-111) or (002) and (111) or (200) reflections, respectively, indicating tenorite phase of CuO [3]. Sharpest XRD peaks were monitored for the thin film annealed at 600 ºC. The Rietveld method was applied to the collected diffraction data to derive structural parameters of CuO samples. The largest crystallite size of 554 Å was estimated when CuO thin film was annealed at 600 ºC. The same thin film sample also exhibited the lowest value for the density of dislocations. Obviously, thermal energy provided by annealing treatment leads to larger crystallite formation. The observed increase in crystallite size could be correlated with the reduced amount of lattice imperfections in the crystalline structure of CuO. Optical properties of the as-deposited and post-annealed thin CuO films were evaluated by the analysis of transmission and reflection spectra. Tauc model was used for estimating optical bandgap energy (E_g) of CuO thin films [4]. E_g of the as-deposited and annealed CuO

films at 200 °C, 400 °C and 600 °C was estimated to be approximately 1.77, 1.71, 1.54 and 1.45 eV, respectively. Determined bandgap energies are consistent with the reported values of CuO thin films [5]. Transport properties of CuO thin films including carrier concentration and mobility were obtained from Hall Effect measurements by conventional four-point dc Van der Pauw technique. All investigated thin film samples revealed p-type conductivity. Experimental results indicate that the electrical properties of the post-annealed CuO films are substantially improved by annealing process compared to as-deposited sample.

In our study, the optimal film characteristics were found at an annealing temperature of 600 ºC, based on the obtained results. p-n heterojunction diodes were constructed by coating of p-type CuO films onto the vertically aligned n-type Si nanowires. Thereafter, fabricated devices were annealed at 600 ºC for 20 minutes. Morphological examination of the fabricated heterojunction diodes was carried out by Nova NanoSEM 430 model field emission scanning electron microscope (FESEM). Cross-sectional SEM image of a Si nanowires-based heterojunction device is provided in Fig. 2. The image evidently reveals that the deposited film covers the surface of Si nanowires, and a continuous film forms at top of the nanowire arrays. As shown in Fig. 2, thin film packing increases from the bottom towards the top, resulting in the formation of matchstick-shaped CuO/Si nanoheterostructures.

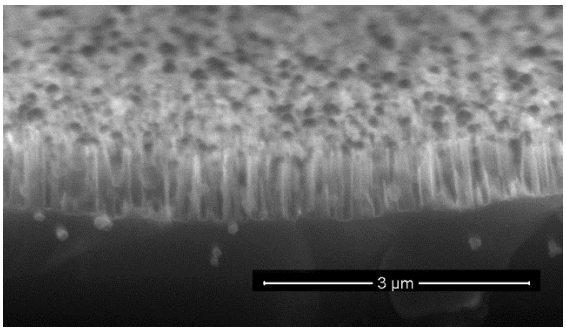

Figure 2. Cross-sectional FESEM image of the fabricated Si nanowires-based heterojunction diodes.

In order to determine the electrical properties of the constructed nanowires-based devices, the current – voltage (*I–V*) measurements were carried out in between -3 and +3 V over the temperature range of 220 – 360 K. Temperature dependent *I-V* characteristics of the fabricated diodes were measured by LabVIEW controlled Keithley 2400 source meter and Janis liquid nitrogen VPF series cryostat system. The temperature of the diodes was controlled by a LakeShore-331 temperature controller. The typical and semi-logarithmic *I-V* characteristics measured in the dark at room temperature is shown in Fig. 3. Significant rectifying behavior with a rectifying ratio of ~10^3 at ±3 V was observed at 300 K. This result confirms the successful formation of p-n heterojunctions within the heterojunction structure.

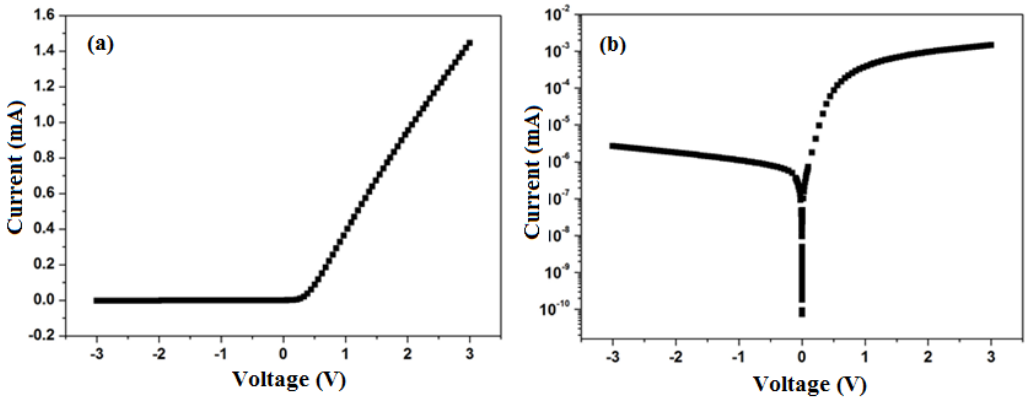

Figure 3. Typical (a) and semi-logarithmic *I–V* characteristics (b) of the fabricated p-type CuO thin film/n-type Si nanowire heterojunction diodes measured at room temperature.

I-V characteristics of the fabricated devices in the temperature range of 220 – 360 K were analyzed, and important diode parameters including ideality factor (n), dark saturation current (I_0) and zero-bias barrier height ($q\Phi_B$) were determined using the standard Shockley-diode model [6]. Obtained results for the

fabricated heterojunction devices are listed in Table 1. As can be seen from Table 1 below, the value of $q\Phi_B$ increases with increasing temperature since more carriers have enough energy to overcome the barriers and contributed to the conduction with increasing temperature. In addition, the ideality factor n decreases with increasing temperature on the contrary to the $q\Phi_B$. The n could be useful to achieve the information about current transport mechanism of the fabricated heterojunction diodes. It can be seen that the calculated n values are higher than one. This result indicates that there could be other transport mechanisms different from the pure thermionic emission mechanism in which $n = 1$.

Table 1. Electrical properties of as-deposited and post-annealed CuO thin films

Temperature [K]	Rectification Ratio	Ideality Factor, n	Saturation Current, I_0 [A]	Barrier Height, $q\Phi_B$ [eV]
220	$3.5x10^3$	2.1	$7.65x10^{-9}$	0.58
240	$2.5x10^3$	1.85	$1.02x10^{-18}$	0.64
260	$1.5x10^3$	1.73	$2.39x10^{-8}$	0.67
280	$8.3x10^2$	1.65	$6.36x10^{-8}$	0.7
300	$5.5x10^2$	1.56	$1.58x10^{-7}$	0.73
320	$3.1x10^2$	1.45	$3.63x10^{-7}$	0.76
340	$2.1\ x10^2$	1.37	$8.23x10^{-7}$	0.79
360	$1.2\ x10^2$	1.32	$2.13\ x10^{-6}$	0.81

3. CONCLUSION

In this study, Si nanowires-based heterojunction diodes were fabricated by depositing of p-type CuO films onto the MACE-grown vertically well-aligned n-type Si nanowire arrays via simple and cost-effective chemical bath deposition technique. Constructed structures demonstrated good p-n characteristics in the dark condition. Diode parameters of ideality factor (n), rectification ratio and zero-bias barrier height ($q\Phi_B$) were calculated to be 1.6, ~10^3 and 0.81 eV, respectively, at room temperature. The obtained values for n, I_0 and $q\Phi_B$ were found to be strongly temperature dependent. The observed diode performance clearly shows that the investigated device structure could be a promising candidate for high-performance low-cost new-generation diodes.

4. ACKNOWLEDGEMENTS

M.K., F.A.A. and G.A. would like to give thanks to Research Projects Unit of Ömer Halisdemir University (The Project Code: FEB 2014/25-BAGEP and The Project Code: FEB 2014/26-BAGEP) for the financial support.

REFERENCES

[1] Akgul G., Aksoy Akgul F., Mulazimoglu E. and Unalan H.E., J. Phys. D: Appl. Phys. (2014), 47, 065106 – 065113.
[2] Zhang M.L., Peng K.Q., Fan X., Jie J.S., Zhang R.Q., Lee S.T., Wong N.B., J. Phys. Chem. C (2008), 112, 4444 – 4450.
[3] Aksoy Akgul F., Akgul G., Yildirim N., Unalan H.E. and Turan R., Materials Chemistry and Physics (2014), 147, 987 – 995.
[4] Tauc J.V., Optical Properties of Solids, (1972), F. Abeles ed., North-Holland Publishing, Amsterdam.
[5] Ramya V., Neyvasagam K., Chandramohan R., Valanarasu S. and A.M.F. Benial, J Mater Sci: Mater Electron (2015), 26, 8489 – 8496.
[6] Schroder D.K., Semiconductor Material and Device Characterization, (2006), third ed., John Wiley & Sons, New York.

Comparison of Cytogenetic Effects of Titanium and Strontium in different time periods onto Fabaceae

Murat Çanlı[a], Hakan Sepet[b]

[a]*Mucur Vocational School, Department of Chemistry and Chemical Processing Technologies, Ahi Evran University, TR-40500 Mucur, Kırşehir, Turkey*
[b]*Engineering and Architecture Faculty, Department of Environmental Engineering, Ahi Evran University, TR-40100 Kırşehir, Turkey*

**e-mail corresponding author*: muratbdm@gmail.com

Keywords: Chromosome Abnormalities, Fabaceae, Cytogenetic effects

ABSTRACT

This study aims to investigate the similarities and differences of the effects of titanium and strontium on *Lens culinaris* Medik. from Fabaceae family. For this reason, 1.0 M titanium and 1.0 M strontium solutions were exposed to the seeds in different time periods such as ¼, ½, 1, 2, 4, 8, 12, 16, 20, and 24 hours. After exposure, the seeds were left for seedling. Then, the seeds were washed by distilled water, and germinated in petri dishes at 20–25 ºC. For *fixation*, the root tips are cut the 1.5-2 cm end of it, and placed directly into fixative (in the ratio of 3:1, 100 % ethyl alcohol: glacial acetic acid). Stock root tips were stained by Feulgen method to get ready them for microscopic examination. The focus on microscopic examination was to clarify the cell division of chromosomal abnormalities. Microscopic examinations showed that some abnormalities occurred in the cells of seedlings as chromosome breakings, bridge chromosome, chromosome dispersion, chromosome adherence, and ring chromosome. Those abnormalities were seen in several times at each treatment depending on the different time periods. The variety and number of the abnormality were usually seen increasing with the increase of treatment time. Then, the results were evaluated statistically.

1. INTRODUCTION

48Titanium (48Ti) with atomic number 22 is a lightweighted, strong, bright, corrosion-resistant transition metal. The most useful properties of titanium in metal form are being resistant to corrosion and having high strength-weight ratio among all metals. About 95% of titanium ore extracted from the Earth is used for production of titanium dioxide (TiO_2). The Ti distribution in soil profiles depends mainly on the geological processes and on soil-forming processes.

In terrestrial plants, titanium accumulates in a species-specific and organ-specific pattern, with increased concentrations in senescent leaves. Some researchers also emphasize that titanium fertilizer, applied through roots or leaves in growth experiments stimulates plant growth in a species-specific manner. It can stimulate chlorophyll content, enzyme activities and uptake of major and minor nutrients.

As a soil-to-plant transfer, all the treatments containing titanium increase the tree performance (branch elongation, flowering and fruit setting intensities) and fruit size. While harvested fruits from the Ti-treated trees show improved resistance to compression and penetration, there is a decrease in weight-loss during postharvest storage. In a study, 3 morphologically different varieties of lentil (*Lens culinaris* Medik.) and one cultivar of naked spring barley (*Hordeum vulgare* ssp. *nudum* L.) as monocrops and substitutive mixture were investigated. There have been several studies about titanium and other metals cytogenetic effects.

Janas *et al*. (2010) have investigated cytogenetic effects of copper ions on root cells of *Lens culinaris* (Medik.). They detected that this compound was accumulated particularly in vacuoles and the cell wall. Researchers made contributions about the intake and distribution of some radioactive elements by plants. Researchers have focused on the effects of heavy metal pollution on plants, resulted from different factors at environment and entrance of these elements into soil and plant.
Strontium (Sr) composes about 0.04% of the Earth's crust, ranking 15th among elements in abundance. Strontium is an alkaline earth metal element with bright white material. Mass numbers of stable isotopes are 84, 86, 87, 88, and 90. The most stable and found isotope of Sr is 88Sr. 12 of its radioactive isotopes decay in a few minutes or days. 90Sr that has 28-year half-life time is a good beta-ray transmitter. This isotope is the most hazardous component of radioactive fallout. 90Sr that can replace calcium in some foods, can accumulate in bones and teeth.

Some investigations into the effect of heavy metal pollution in plants demonstrated that these elements can move to plants from soils. Lentil experiences are being preferred because it is showing off abiotic stresses, salinity, drought, and metal toxicity on its growth and yield. Lens culinaris has 14 (2n) chromosomes. Chromose preparation is achieved from meristematic cells of roots of Lens culinaris as suggested in Plant Cytogenetics.

Table 1. The Mitotic Index of Root Tip Cells of Lens culinaris at the Period of Different Time (Titanium)

Time (Hour)	Mitotic Index ± *S.D.	Time (Hour)	Mitotic Index ± *S.D.
¼	15.25±4.62	8	7.79±1.66
½	11.17±4.07	12	9.59±2.19
1	11.66±3.08	16	10.12±2.60
2	8.77±2.95	20	10.86±2.81
4	8.32±1.60	24	11.43±1.81
Control Group	16.25±3.78		
***S.D: Standard Deviation**			

Table 2. The Mitotic Index of Root Tip Cells of *Lens culinaris* at the Period of Different Time (Strontium)

Time (Hour)	**Mitotic Index ± *S.D.**	**Time (Hour)**	**Mitotic Index ± *S.D.**
¼	18.80±7.75	8	8.42±1.94
½	16.09±4.90	12	-
1	10.22±3.82	16	-
2	7.63±2.28	20	-
4	6.52±2.22	24	-
Control Group	19.12±6.35		

2. RESULTS AND DISCUSSION

The focus on microscopic examination was to clarify the cell division of chromosomal abnormalities. Microscopic examinations showed that some abnormalities occurred in the cells of seedlings as chromosome breakings, bridge chromosome, chromosome dispersion, chromosome adherence, and ring chromosome. Those abnormalities were seen in several times at each treatment depending on the different

time periods. The variety and number of the abnormality were usually seen increasing with the increase of treatment time. Then, the results were evaluated statistically.

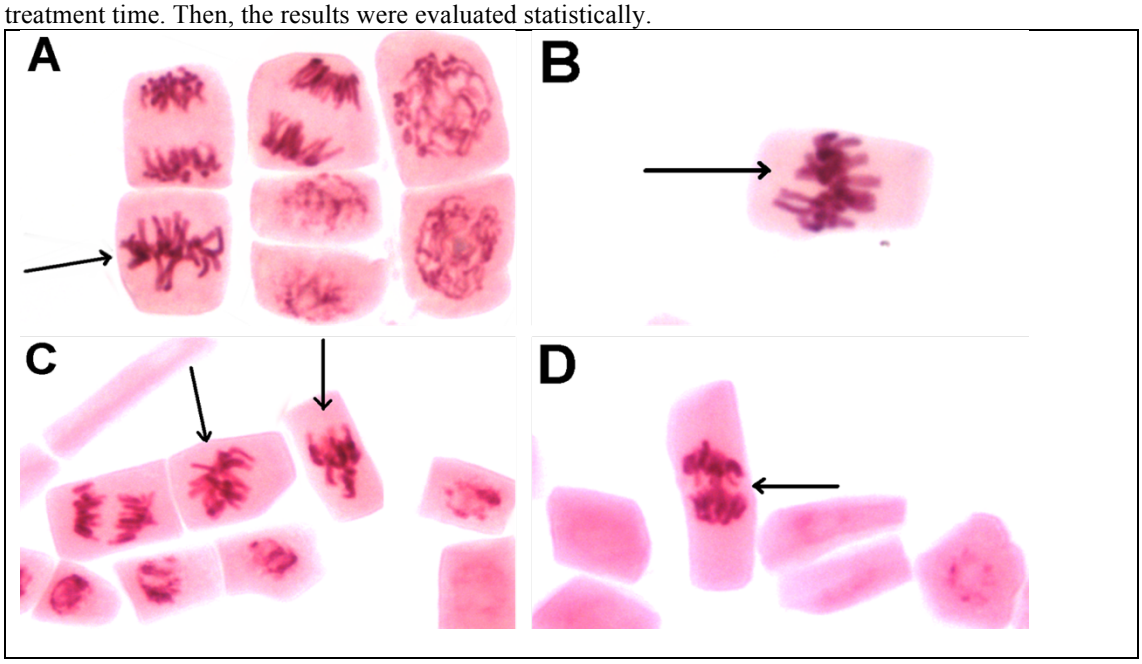

Figure 1. Investigated chromosome abnormality (Titanium)

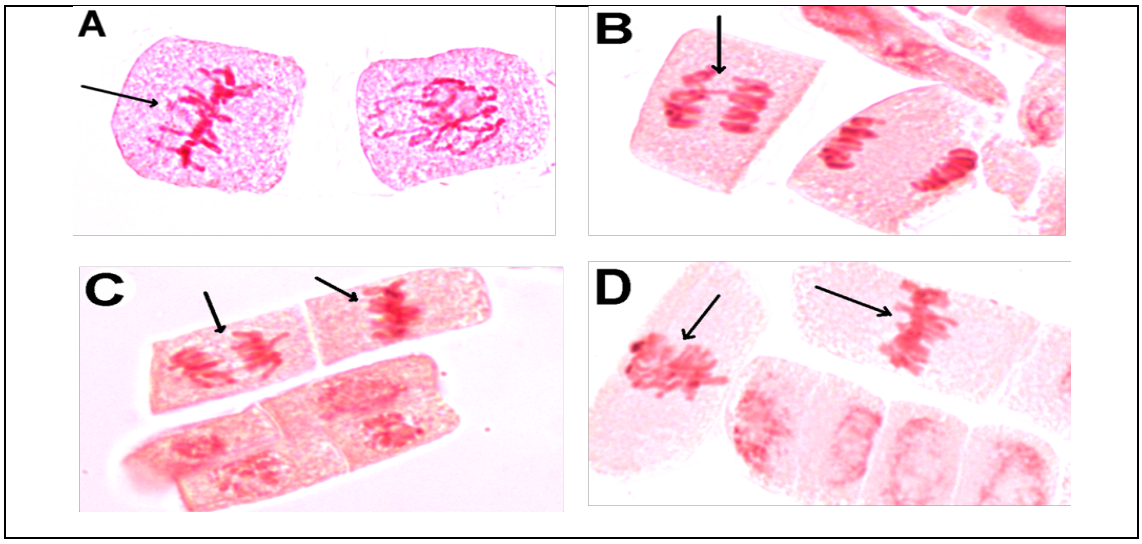

Figure 2. Investigated chromosome abnormality (Strontium)

3. CONCLUSION

As a conclusion, strontium is effective after 8 hours treatment, and the cell division stops over 8 hours treatment of strontium. On the other hand, titanium has no effect on cell division in any treatment time period. Both metals have caused cytogenetic effects and chromosomal abnormalities on Fabaceae.

REFERENCES

[1] Janas K.M., Zielińska-Tomaszewska J., Rybaczek D., Maszewski J., Posmyk M.M., Amarowicz R., and Kosinska A. Journal of Plant Physiology, (2010), 167(4): 270-276.
[2] İnceer H., Ayaz S., Beyazoğlu O., and Entürk E. Turkish Journal of Biology. (2003), 27, 43–46.
[3] Kozhevnikova, A. D., Seregin, I. V., Bystrova, E. I., Belyaeva, A. I., Kataeva, M. N., and Ivanov, V. B., Russian Journal of Plant Physiology, (2009), 56(2), 242–250.

[4] Özdemir A., Bozdağ B., Sepet H., Parlak Y., Kocabaş O., Ereeş F.S., and Özdemir C. Caryologia, (2015), 68 (3), 200–206.
[5] Sepet H., Çanlı M., Özdemir A., Bozdağ B., and Özdemir C. Pakistan Journal of Botany, (2014), 46(1), 101-110.

Cytogenetic Effects of different concentrations of Barium onto Monocotyledon (*Triticum aestivum* L.) and Dicotyledon (*Lens culinaris* Medik.)

Murat Çanlı[a], Hakan Sepet[b]

[a]*Mucur Vocational School, Department of Chemistry and Chemical Processing Technologies, Ahi Evran University, TR-40500 Mucur, Kırşehir, Turkey*
[b]*Engineering and Architecture Faculty, Department of Environmental Engineering, Ahi Evran University, TR-40100 Kırşehir, Turkey*

**e-mail corresponding author*: muratbdm@gmail.com

Keywords: Chromosome Abnormalities, Monocotyledon, Dicotyledon, Cytogenetic effects

ABSTRACT

The purpose of this study is to investigate the cytogenetic effect of different concentrations of barium on *Lens culinaris* Medik. and *Triticum aestivum* L. For this goal, strontium solutions were prepared in different concentrations such as 0.05M, 0.1M, 0.25M, 0.50M, and 1.00M. All those concentrations were exposed to the seeds of *Lens culinaris* and *Triticum aestivum* for 12 hours. After exposure, the seeds were left for seedling. Then, the seeds were washed by distilled water, and germinated in petri dishes at 20–25 ºC. For *fixation*, the root tips are cut the 1.5-2 cm end of it, and placed directly into fixative (in the ratio of 3:1, 100 % ethyl alcohol: glacial acetic acid). Stock root tips were stained by Feulgen method to get ready them for microscopic examination. Homologous areas were chosen on these preparations for cytogenetic examination. The cells in homologous areas were counted and the number of mitotic cells was also detected. Any occurred chromosomal abnormalities were tried to be detected in the cells, and they are also counted. The preparations were photographed with motorized Leica DM 3000 microscope. The images from exposure of barium concentrations on the seeds of *Lens culinaris* Medik. and *Triticum aestivum* L. were compared to each other, and the results were analyzed.

1. INTRODUCTION

Barium is surprisingly abundant in the Earth's crust, being the 14th most abundant element. High amounts of barium may only be found in soils and in food, such as nuts, seaweed, fish and certain plants. Because of the extensive use of barium in the industries human activities add greatly to the release of barium in the environment. As a result barium concentrations in air, water and soil may be higher than naturally occurring concentrations on many locations. The amount of barium that is detected in food and water usually is not high enough to become a health concern.

Barium (Ba) toxicity for plant and animal growth has become increasingly important because of its presence in the environment. It finds its way in plants directly by foliage and via water and soil and eventually into animals when they consume Ba enriched plants. The main source of barium accumulation in plants is from the soil. Of the harmful effects, the most pronounced is on plant growth. The critical threshold level of BaCl2 for plant growth inhibition is quite variable. In mungbean, complete growth inhibition is reported at 40 mM Ba2, in rice at 100mM, in maize 50% germination is inhibited and 90% shoot growth is observed at 100mM, in wheat 50% shoot inhibition occurred at 40mM. Ba has been reported to accumulate upto 4000 ppm in Brasillian nut. The inhibition of growth is an outcome of the damage to the physiological, cytological and biochemical processes.

Table 1. The Mitotic Index of Root Tip Cells of *Lens culinaris and* ***Triticum aestivum*** **L.** at the Different concentrations

Concentrations (M)	Mitotic Index ± *S.D. (Lens culinaris)	Mitotic Index ± *S.D. (Triticum aestivum L)	Time (Hour)
0.05	16.70±6.75	16.25±4.62	12
0.1	14.09±3.90	13.17±4.07	12
0.25	11.22±3.62	10.66±3.08	12
0.5	-	7.23±2.46	12
1.0	-	5.85±2.27	12
Control Group	18.12±6.35	18.25±3.78	

2. RESULTS AND DISCUSSION

The focus on microscopic examination was to clarify the cell division of chromosomal abnormalities. Microscopic examinations showed that some abnormalities occurred in the cells of seedlings as chromosome breakings, bridge chromosome, chromosome dispersion, chromosome adherence, and ring chromosome. Those abnormalities were seen in several times at each treatment depending on the different concentrations. Mitotic index values decreased with increasing concentration of Ba. Over 0.5 M concentration of Ba, mitotic index showed zero for *Lens culinaris* while *Triticum aestivum* showed seed germination in each concentration.

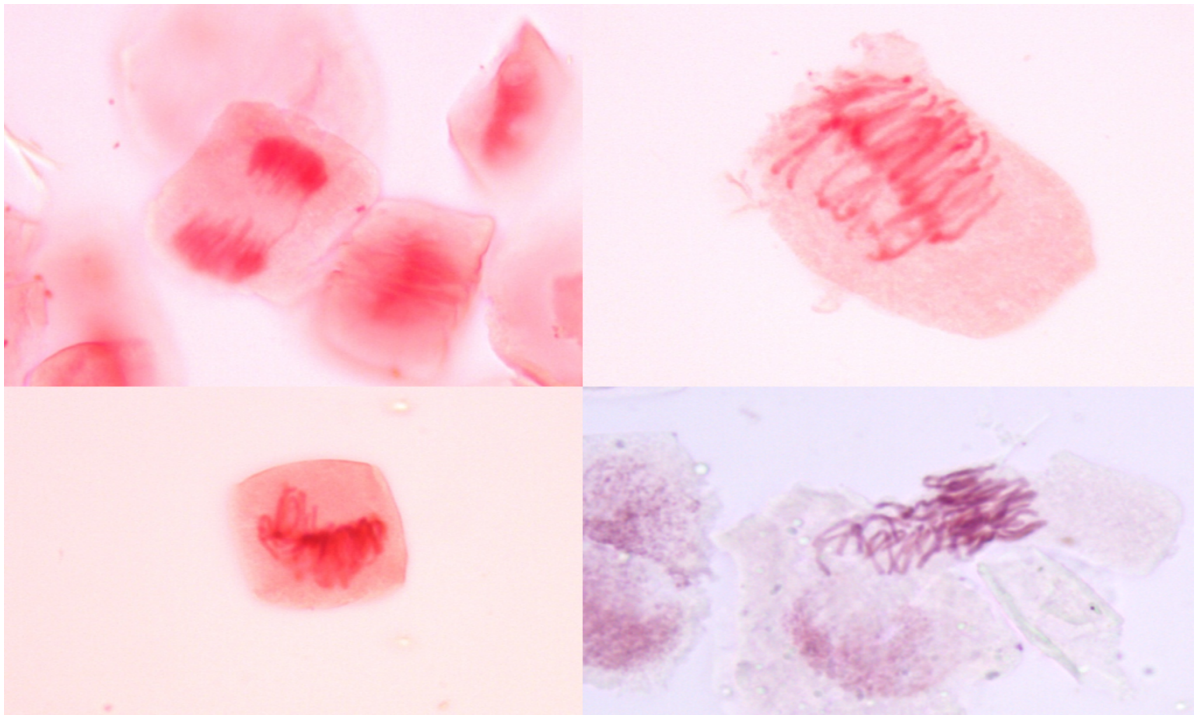

Figure 1. Investigated chromosome abnormality (Monocotyledon)

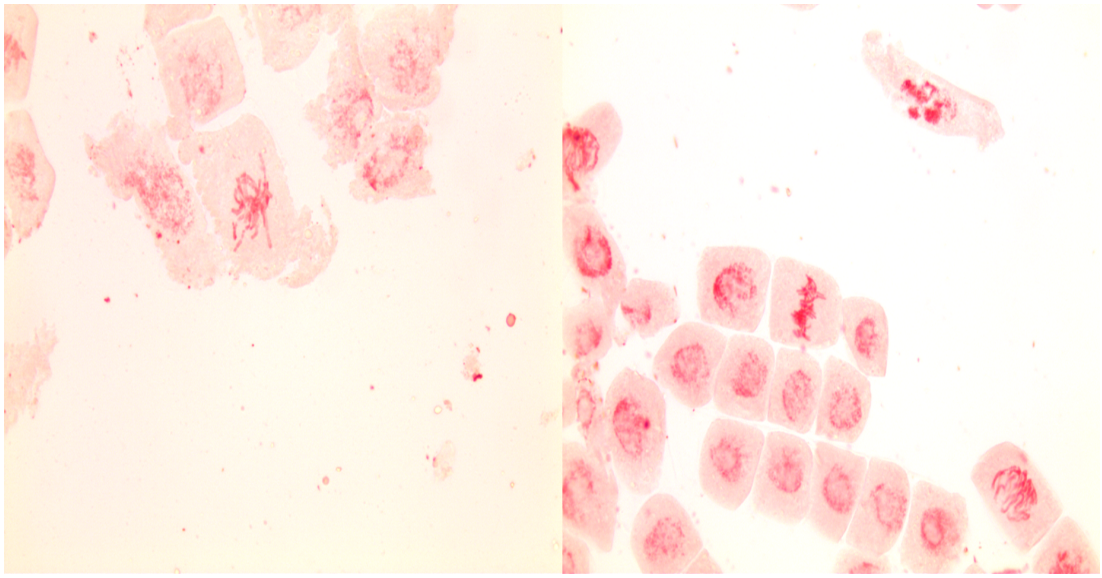

Figure 2. Investigated chromosome abnormality (Dicotyledon)

3. CONCLUSION

Both plant had chromosomal abnormalities in each concentration. The amount of those abnormalities is different for *Lens culinaris* and *Triticum aestivum.*In the end, it can be clearly said that Ba is more effective on dicotyledon than monocotyledon.

REFERENCES

[1] Özmen A., Sümer Ş. 2004. Caryologia, 57 (3): 290-293.
[2] Pesnya D.S. 2013. Caryologia, 66 (3): 275-281.
[3] Saxena P.N., Murthy R.C., Gupta S.K. 2009. Toxicological & Environmental Chemistry, 91(3): 577-594.
[4] Talukdar D. 2013. International Journal of Pharma and Bio Sciences, 4(1): 694–701.
[5] Sepet H., Çanlı M., Özdemir A., Bozdağ B., and Özdemir C. Pakistan Journal of Botany, (2014), 46(1), 101-110.
[6] Janas K.M., Zielińska-Tomaszewska J., Rybaczek D., Maszewski J., Posmyk M.M., Amarowicz R., and Kosinska A. Journal of Plant Physiology, (2010), 167(4): 270-276.
[7] Kozhevnikova, A. D., Seregin, I. V., Bystrova, E. I., Belyaeva, A. I., Kataeva, M. N., and Ivanov, V. B., Russian Journal of Plant Physiology, (2009), 56(2), 242–250.
[8] Özdemir A., Bozdağ B., Sepet H., Parlak Y., Kocabaş O., Ereeş F.S., and Özdemir C. Caryologia, (2015), 68 (3), 200–206.

Applying Ishihara Pseudoisochromatic Plates on a Computer

Murat Işık[a], Mustafa Yağcı[b]

a Vocational Collage of Technical Sciences, Ahi Evran University, TR-40100 Kırşehir, Turkey
b Faculty of Education, Ahi Evran University, TR-40100 Kırşehir, Turkey

**e-mail corresponding author*: isikmurat06@gmail.com

Keywords: Colour blindness, colour deficiency, ishihara, computerized test

ABSTRACT

Today, 10% of the World population suffer from colour deficiency which is also called colour-blindness. There are so many tests to diagnose colour-blindness in relevant literature. Ishihara pseudoisochromatic plates commonly used in the world for Clinical diagnosis due to ease of use, fast and practical results. In this paper, the pictures scanned from a brand new Ishihara 24 plates with 1000 dpi scanner has been applied on 12 subjects having normal colour vision and 12 subjects having colour deficiency though a computer screen and the results have been examined. We achieved 100% sensitivity and 100% specificity by way of our study. The conclusion of our study has been compared to similar studies in relevant literature.

1. INTRODUCTION

Ishihara pseudoisochromatic plates commonly used in the world [1,2,3,4] for Clinical diagnosis since 1917 [5,6,7]. But Ishihara test does not give enough digital results for further analysis and studies. So it can be said that Ishihara test is not exactly suitable for today's technology.

Computers having modern display technologies with high performance hardware, [9,10] light and ergonomic casings, low cost parts and along with advanced information systems enable colour-blindness tests applying on them feasible.

Using Ishihara test over many times causes many disadvantages such as listed:

- Discolour [7],
- Wear and tear [7,11],
- Finger-marks,

This question that has to be asked is these disadvantages could cause a significant colour changes that can affect the colour blindness test results. It has been aimed to use modern technology for colour blindness diagnosis to resolve all flaws listed above. In this study, a brand new Ishihara 24 plates version have been scanned by 600 dpi scanner and applied on subjects. With the benefit of the new test, some Ishihara's disadvantages in matter of this study have been eliminated completely.

Method

The scanned plates have been applied on 12 subjects having normal colour vision and 12 subjects having colour blindness through a computer screen. All the subjects consist of males aged of 18 to 35 years old. The subjects have no permanent disease such as diabetes, eye disease, heart condition etc.

The test has been applied on a hp monitors with 1920x1080 pixels resolution and full brightness. 75 cm distance have been adjusted between the subject and monitor. If a subject has more than seven wrong answers to the plates considered as a colour-blind. Figure 1 shows a screen shot from the scanned Ishihara plates on the monitor. The Ishihara test plates and scanned plates applied on the subjects in exact numerical order 1 to 24.

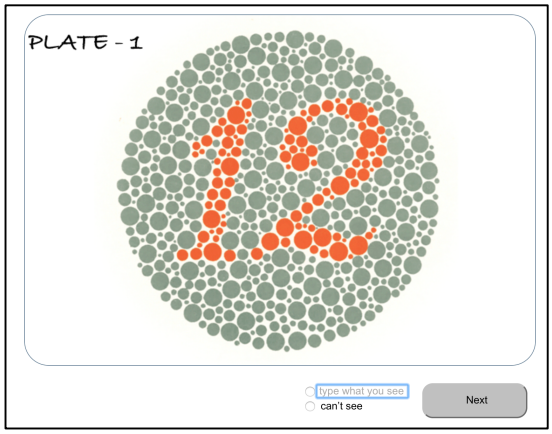

Figure 1. A screen shot from the scanned Ishihara plates on the monitor.

2. RESULTS AND DISCUSSION

With the new test, it has been achieved 100% sensitivity and 100% specificity through Ishihara results. If a subject is colour blind according to the Ishihara results than he/she is colour blind according to the new test too. All the results gathered from subjects are the same with Ishihara test. Table 1 shows count of the wrong answers to both Ishihara and the scanned plates.

Marey et al have presented similar paper and they have also achieved 100% sensitivity and 100% specificity with their study [8]. Gündoğan et al also have a related paper. In their study, they designed a computerized new test based Farnsworth-Munsell 100 Hue. Their test achieved 100% sensitivity and 100% specificity. Although, there are some similar studies on the web, their sensitivity and specificity are unknown. As a result, it can be said that computers technologies enable colour-blindness tests applying on them feasible.

Table 1. Comprasion between Ishihara test and the scanned version of Ishihara

Plate No	Traditional Ishihara		Scanned Ishihara	
	CD*	NCV*	CD*	NCV*
1	0	0	0	0
2	9	0	9	0
3	5	0	5	0
4	6	0	6	0
5	11	0	11	0
6	10	0	10	0
7	5	0	5	0
8	6	0	6	0
9	8	0	8	0
10	12	0	12	0
11	11	0	11	0
12	11	0	11	0
13	12	0	12	0
14	12	0	12	0
15	4	0	4	0
16	6	0	6	0
17	6	0	6	0
18	2	12	2	12
19	1	12	1	12
20	0	12	0	12
21	2	12	2	12
22	5	0	5	0
23	7	0	7	0
24	6	0	6	0

*Legend: CD stands for colour deficiency an NCV stands for normal colour vision

3. CONCLUSION

The test should be used on different monitors and hardware. Another new test can be designed based on Ishihara technics to collect more results concerning the colour that a colour blind person couldn't able to see. All the answers to the plates cloud be memorized by the subjects because scanned plates applied on the subjects without waiting any time. At least changing the order of the scanned plates could improve accuracy of the new test.

REFERENCES

[1] Lambrant, A. (2015). A preferred visual appearance for game avatars based on color theory.
[2] Vu, B. L., Easterbrook, M., & Hovis, J. K. (1999). Detection of color vision defects in chloroquine retinopathy. Ophthalmology, 106(9), 1799-1804.
[3] Bouvier, S. E., & Engel, S. A. (2006). Behavioral deficits and cortical damage loci in cerebral achromatopsia. Cerebral Cortex, 16(2), 183-191.
[4] Shrestha, R. K., & Shrestha, G. S. (2016). Assessment of Color Vision Among School Children: A Comparative Study Between The Ishihara Test and The Farnsworth D-15 Test. Journal of Nepal Medical Association, 53(200), 266-269.
[5] Dain, S. J., & AlMerdef, A. (2016). Colorimetric evaluation of iPhone apps for colour vision tests based on the Ishihara test. Clinical and Experimental Optometry, 99(3), 264-273.
[6] Sarmiento, M. C. E., Andino, M. M., Chavez, J. P. G., Cruzat, J. G., Geducos, S. D., & Caiga, B. T. (2015). Awareness on Medical Examinations and their Importance to Maritime Students. Asia Pacific Journal of Maritime Education, 1(1).
[7] S. Ishihara, 1917, Tests for Color-blindness, Handaya, Tokyo, Hongo Harukicho.
[8] Marey HM, Semary NA, Mandour SS, (2015) Ishihara Electronic Color Blindness Test: An Evaluation Study, Ophthalmology Research: An International Journal, 3, 67-75.
[9] Hesselink, L., Rizal, D., & Bjornson, E. S. (2016). U.S. Patent No. 9,348,864. Washington, DC: U.S. Patent and Trademark Office.
[10] Reddy, K. P. (2014). U.S. Patent No. 8,793,518. Washington, DC: U.S. Patent and Trademark Office.
[11] Yates, J. T., Heikens, M.-F., (2001) "Colour Vision Testing – Methodologies: Update and Review", Research and Technology Organization / North Atlantic Treaty Organization, Neuilly-sur-Seine,
[12] Gündoğan NÜ, Durmazlar N, Altintaş AK, Gümüş K, Durur I, Geyik PÖ, (2003) Bilgisayara Uyarlanmış Yeni Bir Renk Körlüğü Testi, Turkiye Klinikleri Journal of Medical Sciences, 23(2), 120-128.

Realise and Design of Application Development Kit for PIC

Murat Işık [a], Mustafa Yağcı [b]

a Vocational Collage of Technical Sciences, Ahi Evran University, TR-40100 Kırşehir, Turkey
b Faculty of Education, Ahi Evran University, TR-40100 Kırşehir, Turkey

**e-mail corresponding author*: isikmurat06@gmail.com

Keywords: Test kit for PIC, developing application with microcontroller, PIC, microcontroller

ABSTRACT

In recent years, microcontrollers widely used in industrial solutions and Analog/Digital applications to perform process control and automation. Therefore, it is vital that students of the relevant department learn how to enhance applications with microcontrollers. To do this, the students taking relevant courses have to perform applications to consolidate their training and acquisitions. In this study, a training kit, which students can develop applications on it, has been designed and implemented. The new kit has been compared other kits being in market and relevant literature. An instruction for use which explains the kit & its' modules and contains examples of application have been prepared for the students. The main motivation of this study is to provide students making more consolidate knowledge and experiment in microcontroller-based courses.

1. INTRODUCTION

In recent years, to accomplish automation systems and process control, microcontrollers widely used [5] in industrial solutions and Analog/Digital applications. So, it is important for students of the relevant department to learn how to enhance applications with microcontrollers.

In the market, there are many kind of microcontrollers [6]. Besides, PIC family based on reduced instruction set computer (RISC) [7,8,9] which is more easy to develop software and less complex structure of programing, PIC microcontrollers are widely used under favour of their low cost, extensive availability, great user base, extensive collection of application notes, availability of free development tools and re-programmable Flash-memory capability.

Occupational courses in Vocational School of Technical Sciences contain too much abstract contents to acquire them entirely [10]. Because they cover essential knowledge and skills, students in the related department needs for the future. Besides, microcontrollers lesson is one of mentioned occupational course, it is compulsory lessons for the department such as mechatronic, electronic, electric, computer etc. In this paper, a low cost training kit, which students can develop applications on it, has been designed and implemented. The new kit has been compared with other kits in terms of cost and feasibility of the courses. To develop varies kind of applications, the new kit has 18 different modules listed below:

- MMC/SD card support
- USB/RS232/İ2C Connection modules
- Stepper Motor Control Unit
- Servo Motor Control Unit
- DC Motor Control Unit
- Hall Effect Sensor Module
- Infrared Module
- Breadboard Part
- Opt-coupler application Module
- Analog Input/output Module
- Relay and Buzzer Modules

- Graphic LCD
- Dot Matrix LCD 2x16
- Matrix Display
- BCD Display
- Button/Switch Modules
- LED Modules
- Time Control Unit

2. METHOD and AIM

The main motivation of this study is to consolidate the students' knowledge about microcontroller-based courses. To achieve our motivation, the new training kit has been designed to includes all applications in the course books which contains all curriculum of IKMEB which is widely used in most Vocation Schools of Technical Sciences in Turkey.

The dimensions of the kit are 240 mm by 300 mm so it's nearly a 15-inch laptop size and can be carried easily. In the kit, PIC16F877 which has enough capacity for the content of the courses has been chosen as a main microcontroller to develop applications. An electronic schematic program has been used for design. In the kit, every application module has its own DIP switch to enable/disable the module. An instruction for use which explains the kit & its' modules and includes examples have been prepared for the students.

3. LITERATURE SURVEY

In 2002, Bay and Görgünoğlu has presented an educational set to be helpful understanding of courses based on microcontrollers. Their design for 8051 microcontroller [1] not for PIC family. Ozcan and Gunay also has presented a similar set for PIC microcontrollers in 2009 [2] but their set has so limited application modules comparing with this study. Burunkaya and Yorulmaz has designed a similar set in 2009. Their set is only for music and doesn't contain all application in the course books [3]. Engin has presented a training kit in 2007, but the kit was only compatible with Atmel microcontrollers [4].

4. RESULTS and CONCLUSION

Table 1. A comparison of cost between the new kit and other kits in the market

Name	Cost (TL)*
The new kit	285
PIC Lab	875
PIC Lab Pro	451,5
PIC Prog/Deka 2	490
MDS P2-PIC	1250
Exp-Kits	354

*Selling price in the market by year of 2016

Table 1 shows a comparison of the cost between our kit and the other popular kits in the market and the related literature. As it can be seen, the cost of the new kit is a very low comparing other kits. Besides some of the kits has a couple of extra modules which are not the part of the curriculum of the lessons, the other of kits is lack of application modules needed. Consequently, a PIC based training kit, which meets all the requirements of the student to consolidate their knowledge by performing applications on it in the related courses, has been designed and implemented with a very low cost. The new kit is completely appropriate to the curriculum of IKMEB which is almost used all Vocational Schools of Technical Sciences in Turkey.

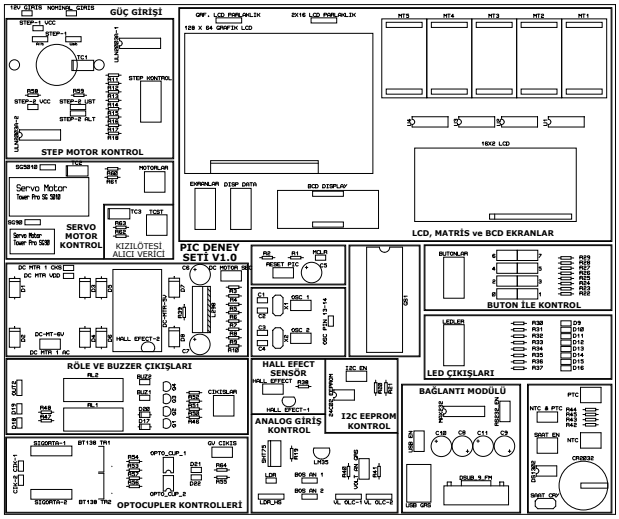

Figure 1. A block diagram of the new kit

Figure 1 shows a block diagram of the new kit. Every module needs their controller units to perform with PIC microcontroller. In other word, microcontrollers cannot control and drive a module alone without other electronical equipment. As it can be seen on the figure 1, the PCB circuit has been separated to some certain of areas to combine modules and their control equipment together. In this way, students can develop applications easily without confusing.

As a result, a training set has been provided for students to consolidate their knowledge in some certain of vocational courses based on microcontrollers. With the benefit of the new kit, students in the related department develop a deeper understanding of the occupational courses like microcontrollers and comprehend their theoretical knowledge.

4. ACKNOWLEDGEMENTS

This work was supported by the Ahi Evran University Scientific Research Projects Coordination Unit. (Project Number: EGF.4006.12.004).

REFERENCES

[1] Bay, Ö. F., & Görgünoğlu, S. (2002). 8051 Ailesi Mikrodenetleyici Eğitim Setinin Tasarimi Ve Gerçekleştirilmesi. Politeknik Dergisi, 5(3).

[2] Özcan, M., & Günay, H., (2009), Mikrodenetleyici Geliştirme Seti Tasarim Ve Uygulamalari, Journal of Technical-Online, Volume 8, Number:3-2009

[3] Burunkaya, M., & Yorulmaz, F., (2009), Mikrodenetleyici Tabanli Elektronik Nota Eğitim Seti Tasarimi Ve Yapimi Design And Construction Of A Microcontroller Based Electronic Note Education Set, 5. Uluslararası İleri Teknolojiler Sempozyumu (IATS'09)

[4] Engin, M., & Engin, D., (2007), Mikroişlemciler Dersi Laboratuvarı Için Yeni Deney Seti Tasarımı, CBÜ Soma Meslek Yüksekokulu Teknik Bilimler Dergisi, Cilt 2, Sayı 8

[5] Cüneray, K., Canal, M. R., & Topaloğlu, N., (2011), PSoC 1 ile Elektronik Uygulamaları için Deney Seti Tasarımı ve Gerçekleştirilmesi, 6th International Advanced Technologies Symposium (IATS'11)

[6] Vieira, M. A. M., Coelho, C. N., da Silva, D. C., & da Mata, J. M. (2003, September). Survey on wireless sensor network devices. In Emerging Technologies and Factory Automation, 2003. Proceedings. ETFA'03. IEEE Conference (Vol. 1, pp. 537-544). IEEE.

[7] Erol, Y., Balik, H. H., Inal, S., & Karabulut, D. (2007). Safe and secure PIC based remote control application for intelligent home. IJCSNS, 7(5), 179.

[8] PIC16F877, D. S. (1998). Microchip Technology Inc.

[9] Petchjatuporn, P., Ngamkham, W., Khaehintung, N., Sirisuk, P., Kiranon, W., & Kunakorn, A. (2005, November). A Solar-powered battery charger with neural network maximum power point tracking

implemented on a low-cost PIC-microcontroller. In TENCON 2005-2005 IEEE Region 10 Conference (pp. 1-4). IEEE.

[10] Işık, M., & Yağcı, M. (2012), "E-Learning Techniques With Support For Formal Education", Education Sciences, 7(1), 426-432.

Absorption Coefficient of Hydrothermally Synthesized Barium Titanate Reacted at Different Temperatures and Varying Reaction Times in a Highly Alkaline Solution

Songül Akbulut[a,b], Murat Özen[c], Saynur Kurtuluş[b], Mehmet Şahin[b]

[a]Bursa Technical University, Department of Energy Systems Engineering, 16310 Bursa, Turkey
[b]Recep Tayyip Erdogan University, Department of Physics, 53100 Rize, Turkey
[c]Laboratory of Adsorption and Catalysis (LADCA), University of Antwerp, Department of Chemistry, B-2610 Wilrijk, Belgium

**e-mail corresponding author: murat.ozen@outlook.com, murat.oezen@uantwerpen.be*

Keywords: Barium Titanate; Hydrothermal Synthesis; Absorption Coefficient

ABSTRACT

In this work, the absorption coefficient of hydrothermally synthesized barium titanate ($BaTiO_3$) was calculated. $BaTiO_3$ was prepared via the peroxo-hydroxide method and hydrothermally synthesized at 80°C, 100°C, 150°C, 200°C and reacted for varying reaction times between 15 min up to 120 h. Absorption coefficient measurements were done with a coaxial HPGe gamma detector (Ortec, GEM55P4-95) with a working range in the X-ray energy region. The samples were made into pellets of 10 mm and were exposed to ^{241}Am radioisotopes at an energy of 59.54 keV for 300 s. FT-Raman revealed that increasing the hydrothermal temperature and the reaction time promoted the formation of phase pure $BaTiO_3$ with a mainly tetragonal crystal structure. At the early stages of the hydrothermal reaction secondary barium titanate phases ($BaTi_2O_5$ and Ba_2TiO_4) were observed which affected the absorption coefficient values. It was observed that the formation of these secondary barium titanate phases was in conjunction with the calculated mass absorption coefficient values.

1. INTRODUCTION

X-rays are electromagnetic radiation with energies in the 100 eV to 100 keV range which translates to wavelengths between 0.01 nm and 10 nm. X-ray spectroscopy techniques are used extensively in material characterization due to their relatively highly penetrating character.[1]
Mass attenuation coefficients or mass absorption coefficients are usually determined to study the shielding properties of non-biological materials or to see the level of damage to biological materials.[2,3] The attenuation length of X-rays in matter can also provide valuable information with regard to the amount and distribution of the studied compositions. The intensity of the incoming X-rays decreases exponentially as explained by the Beer-Lambert law:

$$I = I_0\, e^{-\mu x} \tag{1}$$

with x (cm) the thickness of the sample, I (counts per second, cps) the intensity of the outgoing X-rays, I_0 (cps) the intensity of the incoming X-rays, and μ (cm^{-1}) the linear absorption coefficient. The absorption coefficient is an intrinsic property of atoms/molecules. The mass absorption coefficient of a composition comprising of different elements a, b, c,… etc can be written as:

$$\mu_m = \mu / \rho = W_a\,(\mu_a/\rho_a) + W_b\,(\mu_b/\rho_b) + W_c\,(\mu_c/\rho_c) + \ldots \tag{2}$$

with W_i the mass fraction of element i.

In this study, the synthesized hydrothermal samples were mixed with cellulose due to the hydrophilic nature of the hydrothermal samples. To account for the presence of cellulose the mass absorption coefficient (μ_m) was used instead of the linear absorption coefficient (μ) and the x factor in Eq. (1) was replaced by t:

$$t = m / A \tag{3}$$

with A (cm^2) the surface area of the pellet, and m (g) the mass of either the cellulose or the sample. A pure cellulose sample was measured first to determine $\mu_{m,cellulose}$ with the formula: $I_{cellulose} = I_0 e^{-\mu_{m,cellulose} t_{cellulose}}$.
$I_{cellulose}$ was then subtracted from the measured intensity I of the pellet: $I_{corr} = I - I_{cellulose}$. In this way the effect of the hydrothermal sample was singled out.
Next, the μ_m of the hydrothermal sample was calculated:

$$I_{corr} = I_0 e^{-\mu_m t_{sample}} \leftrightarrow \mu_m = -\frac{\ln\left(\frac{I_{corr}}{I_0}\right)}{t_{sample}} \tag{4}$$

The barium titanate precursor material was hydrothermally synthesized at different temperatures (80°C, 100°C, 150°C and 200°C) and varying reaction times. The reader is referred to the work of Özen et al.[4] for the detailed synthesis procedure. This work presents the mass absorption coefficient of the hydrothermally synthesized barium titanate samples with the aim of studying the crystallization process of $BaTiO_3$.

2. RESULTS AND DISCUSSION

The hydrothermal samples were made into pellets of 10 mm and were exposed to ^{241}Am radioisotopes (X-ray source) at an energy of 59.54 keV for 300 s. The samples were placed between the X-ray source and the coaxial HPGe gamma detector (Ortec, GEM55P4-95) with a working range in the X-ray energy region.

Figure 1 depicts the FT-Raman spectra of the hydrothermal samples. As can be seen in Figure 1, crystalline $BaTiO_3$ was formed after a certain period of hydrothermal reaction time. The FT-Raman spectra of samples produced at 100°C were specifically chosen to study the reaction process, i.e. the crystallization process from precursor to secondary phases to crystalline $BaTiO_3$. The presence of the secondary barium titanate phases were also confirmed by XRD measurements: the reader is referred to [4].

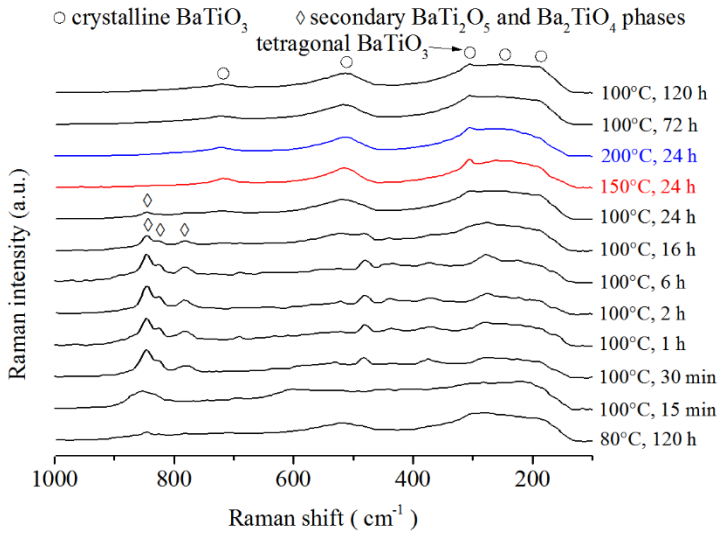

Figure 1. FT-Raman (Nicolet Nexus 670 bench from Thermo Fisher Scientific Inc) spectra of hydrothermal samples produced at different temperatures and varying reaction times.

The mass absorption coefficient values of the hydrothermal samples are shown in Table 1. The theoretical mass absorption coefficients for $BaTiO_3$, Ba_2TiO_4, and $BaTi_2O_5$ are also given in Table 1. The presence of Ba_2TiO_4 and $BaTi_2O_5$ will lead to, respectively, the increase and decrease of μ_m due to the linear nature of the absorption coefficient, see Eq. (2). FT-Raman measurements showed phase pure $BaTiO_3$ for samples prepared at 150°C (24 h) and 200°C (24 h) (see Figure 1). μ_m of samples 150°C (24 h) and 200°C (24 h) were, respectively, 5.43 $cm^2\ g^{-1}$ and 5.33 $cm^2\ g^{-1}$ which concurred well with the theoretical μ_m for $BaTiO_3$. The relatively low μ_m (3.27 $cm^2\ g^{-1}$) for 80°C (120 h) showed that this sample was still not fully crystallized into $BaTiO_3$ and probably contained certain amounts of the low density uncrystallized precursor material. The rather broad bands in FT-Raman for sample 80°C (120 h) confirmed this statement.

Table 1. Mass attenuation coefficients (μ_m) and experimental parameters of the hydrothermally synthesized samples ($I_{cellulose}$ = intensity of the outgoing X-ray intensity for cellulose, I = outgoing X-ray intensity for sample+cellulose, I_{corr} = corrected outgoing X-ray beam intensity, $t_{cellulose}$ = the pure cellulose's contribution to the pellet, t_{sample} = the hydrothermal sample's contribution to the pellet).

Sample*	**I_{corr} (cps)**	**I (cps)**	**$I_{cellulose}$ (cps)**	**$t_{cellulose}$ (g cm^{-2})**	**t_{sample} (g cm^{-2})**	**μ_m ($cm^2\ g^{-1}$)**
80°C / 120 h	46914	45680	64586	0.212	0.106	**3.27**
100°C / 15 min	27250	26658	63944	0.257	0.206	**4.25**
100°C / 30 min	28147	28732	63937	0.254	0.203	**3.94**
100°C / 1 h	25559	24859	62652	0.306	0.245	**3.77**
100°C / 2 h	31653	31148	62847	0.218	0.175	**4.01**
100°C / 3 h	34197	33579	62734	0.163	0.109	**5.73**
100°C / 6 h	29083	28515	62784	0.250	0.200	**3.95**
100°C / 16 h	31482	30999	63835	0.212	0.169	**4.27**
100°C / 24 h	31073	30596	63829	0.206	0.164	**4.47**
100°C / 72 h	32626	32219	63759	0.177	0.142	**4.81**
100°C / 120 h	30025	29542	63835	0.210	0.168	**4.59**
150°C / 24 h	41124	40115	64361	0.174	0.087	**5.43**
200°C / 24 h	37777	37218	62793	0.147	0.098	**5.33**
Cellulose ($C_6H_{10}O_5$)	59285	0	0	0.365	0.000	**0.182 0.192****
Ba_2TiO_4						**6.174****
$BaTi_2O_5$						**4.016****
$BaTiO_3$						**5.208****

*Precursor concentration: [Ba] + [Ti] = 0.05 M

**Theoretical mass absorption coefficients (NIST, XCOM). Values taken from NIST: X-Ray Mass Attenuation Coefficients http://www.nist.gov/pml/data/xraycoef/index.cfm.[5,6]

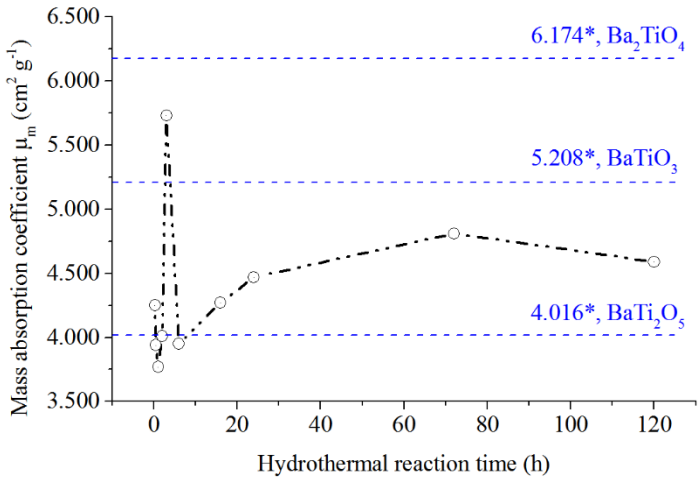

*Theoretical mass absorption coefficients (NIST, XCOM).[5]

Figure 2. Mass absorption coefficient μ_m vs hydrothermal reaction time for hydrothermal samples produced at 100°C.

The crystallization at 100°C was relatively slow with respect to 150°C and 200°C which made it possible to follow the crystallization process. As can be seen from the FT-Raman spectra in Figure 1, at low reaction times the secondary barium titanate phases were developed first. However, it was difficult to establish which of the two secondary phased ($BaTi_2O_5$ or Ba_2TiO_4) was formed first from FT-Raman alone. The mass absorption coefficient values, however, could provide more data on this matter. Figure 2 depicts the calculated mass absorption coefficients for the hydrothermal samples produced at 100°C for varying reaction times. A relatively low μ_m was observed (closer to $BaTi_2O_5$) at the beginning of the reaction followed by a sharp peak at 2 h (closer to Ba_2TiO_4). The sharp peak dropped back to about 4 $cm^2\ g^{-1}$ (close to $BaTi_2O_5$) and continued to increase to values close to the theoretical mass absorption coefficient for $BaTiO_3$.

The mass absorption coefficients revealed that the crystallization process was actually a kinetic process between the secondary Ba_2TiO_4 and $BaTi_2O_5$ phases with the formation of $BaTi_2O_5$ at the early stages of the hydrothermal reaction followed by the formation of Ba_2TiO_4. As the reaction proceeded the thermodynamically stable crystalline $BaTiO_3$[4] was eventually formed.

3. CONCLUSION

Since mass absorption coefficients (μ_m) pertain information on an atomic level, μ_m of hydrothermally synthesized samples were determined to follow the crystallization process from precursor to crystalline $BaTiO_3$. The hydrothermal samples were prepared at different hydrothermal temperatures and varying reaction times.
The calculated μ_m for samples prepared at 150°C (24 h) and 200°C (24 h) were very close to the theoretical μ_m value for $BaTiO_3$. This validated the experimental setup and method of calculation used in this study.
Due to the relatively slow kinetics at 100°C the mass absorption coefficients for hydrothermal samples prepared at 100°C were determined to study the crystallization process of $BaTiO_3$. The reaction started off with relatively low μ_m values, close to the theoretical μ_m value for $BaTi_2O_5$, followed by a sharp peak close to the theoretical μ_m value for Ba_2TiO_4. The mass absorption coefficients leveled off in time to a fairly constant μ_m value close to the theoretical μ_m value for $BaTiO_3$.
Hence, the calculated μ_m values showed that the hydrothermal reaction process of $BaTiO_3$ consisted of a kinetic aspect whereby $BaTi_2O_5$ was formed first followed by Ba_2TiO_4. Eventually the thermodynamically stable crystalline $BaTiO_3$ phase was formed at relatively long reaction times.

4. ACKNOWLEDGEMENTS

Synthesis of barium titanate and characterization: The Flemish Institute for the Promotion of Scientific Technological Research in Industry (IWT, SBO-PROMAG contract, grant number 60056) is acknowledged for the financial support. The research was also performed within the framework of a GOA-BOF project supported by the University of Antwerp. Prof. Dr. Pegie Cool (LADCA, Dept. Chemistry) from the University of Antwerp is acknowledged for the hydrothermal synthesis and FT-Raman measurements.

REFERENCES

[1] Van Grieken R. and Markowicz A., eds., Handbook of X-Ray Spectrometry, 2nd ed., rev and expanded, Marcel Dekker, New York, 2002.
[2] Elmahroug Y., Tellili B. and Souga C., Ann. Nucl. Energy (2015), 75, 268-274.
[3] Akça B. and Erzeneoğlu S.Z., Sci. Technol. Nucl. Install. (2014), 2014, 1-8.
[4] Özen M., Mertens M., Snijkers F. and Cool P., Ceram. Int. (2016), 42, 10967–10975.
[5] NIST: X-Ray Mass Attenuation Coefficients, http://www.nist.gov/pml/data/xraycoef/index.cfm.
[6] Hubbell J.H. and Seltzer S.M., Radiation Physics Division, PML, NIST (2004).

Friction Stir Spot Welding of Aluminium 6061 T6

Mustafa Sudağ[a], Adnan Akkurt[b]

[a]Ahi Evran Üniversitesi, Mucur Meslek Yüksekokulu, Bilgisayar Teknolojileri, Kırşehir

[b]Gazi Üniversitesi, Teknoloji Eğitimi Fakültesi, Endüstriyel Tasarım Mühendisliği Bölümü, Ankara

**e-mail corresponding author: mustafa.sudag@ahievran.edu.tr*

Key Words: Friction Stir Spot Welding, Aluminium, Tensile Strenght, Tool Geometry

ABSTRACT

In this study, effects of different tool geometries on tensile strength of friction stir spot welded AA 6061 T6 sheets in different thicknesses were investigated. Process time, tool rotational speed and shoulder plunge depth were used as constant parameters. The quality of the friction stir spot welded sheets were evaluated by the joining efficiency as a result of the tensile tests. The experimental results showed that the tool geometry had significant effect on mechanical properties.

1. INTRODUCTION

Resistance spot welding is genereally used to join metal sheets which form the automobile's body structure. Resistance spot welding which is used widely for joining metal steel, does not work as well for these light alloys. The higher electrical and thermal conductivities of aluminium relative to steel lead to higher energy consumption, necessitating high capacity electrical systems and associated infrastructure. The need for frequent electrode dressing and reduced electrode life are other disadvantages [1].

A spot welding process using friction stir welding (FSW) technique has been newly developed, which is called friction stir spot welding (FSSW) or friction spot joining (FSJ). This method is expected to apply to joining for body parts made of aluminium sheet in transportation systems, particularly in automotive industry, because of its advantages such as low heat distortion, excellent mechanical properties and little waste or pollution compared with conventional RSW [2].

Friction stir spot welding (FSSW) is a variant of the friction stir welding. A non- consumable rotating tool is plunged into the workpieces to be joined. Upon reaching the desired plunge depth, the rotating tool is held in that position for a pre-determined finite time (sometimes referred to as dwell period). Subsequent to that, the rotating tool is then retracted from the welded joint leaving behind a friction stir pot weld. The tool has two distinct parts shoulder and pin. The shoulder generates bulk of the frictional or deformational heat. The pin assists in material flow between the workpieces [3]. The tool rotational speed which parameter also has significant importance on tensile strenght[4]. The tensile strenght of friction spot joining is an important index to welding quality [5].

Experiments were performed on plates of 6061- T6 aluminium alloys of 4 mm thickness; chemical compositions of this alloy was 0.22Cr- 0.3Cu-0.51Fe-1Mg- 0.05Mn-0.59Si-0.02Ti-0.01Zn- rest Al (wt %) . The workpieces of the 6061-T6 aluminium alloy were cut into the dimensions of 40 x 150 x 4 mm for

FSSW. In order to develop the friction stir spot welding tests, clamping fixtures were used. Also proper backing plates were used in order to obtain lap joints. A specimen had a 40 x 40 mm overlap area as shown in Figure 1.

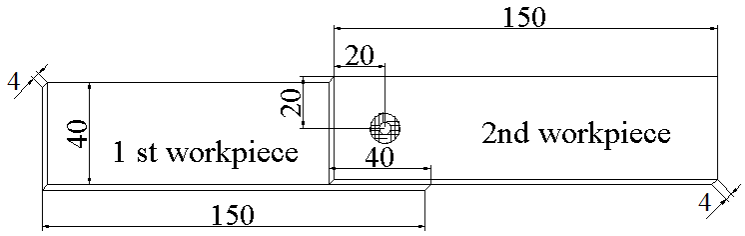

Fig. 1. Plates had a 40 x 40 mm overlap area as shown in figure

The specimens were welded in a milling machine with three different tool. Fig. 3 a, b and c shows a scheamatic illustration of the tool with different probe geometries. The tools were manufactured from hot work tool steels and heat-treated to 52 HRC.

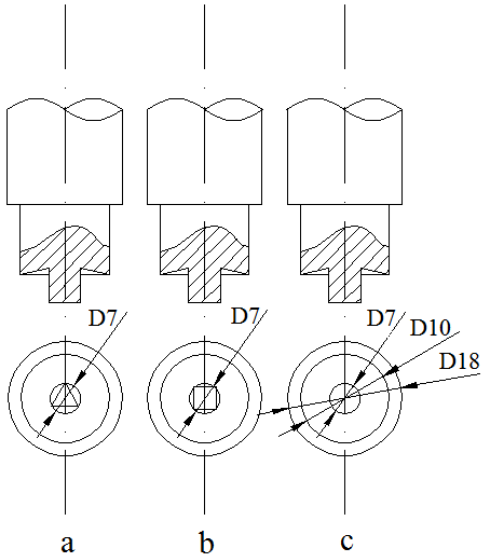

Fig. 2. Probe geometries of tools employed. (a)Triangular (b)Square (c)Cylindirical .

Semi-automatic milling machine is used to weld specimens. In all cases tool plunge depth and dwell time is applied as a constant. Tool geometry parameters and process parameters are seen in table 1.

Table 1. Tool geonetry parameters and process parameters

Parameteres	**Probe profile**			
	Triangular	*Square*		*Cylindir*
Probe lenght (mm)	7	7		7
Probe diameter / Probe diagonal (mm)	7	7		7
Shoulder diameter(mm)	10	10		10
Probe surface (mm^2)	78,26	88,99		104,46
Probe plunge depth(mm)	5,4			
Dwell time (sn)	2			
Tool rotational speed (rpm)	2525	3000	3552	4214

2. RESULTS AND DISCUSSION

Tensile test specimens were tested on an Instron 8503 Universal test machine at the room temperature. The load values recorded during the test. Tensile strength was obtained by averaging the strength of six specimens, which were welded with identical welding parameters. It can be seen on figure 3 that tensile strength increases with increasing probe surface.
Highest tensile strength was achieved with the tool wich had cylindir probe and 3000 rotational tool speed. On the other hand lowest tensile strength value was got with the tool which has triangular probe and so with the tool which has lowest probe surface.

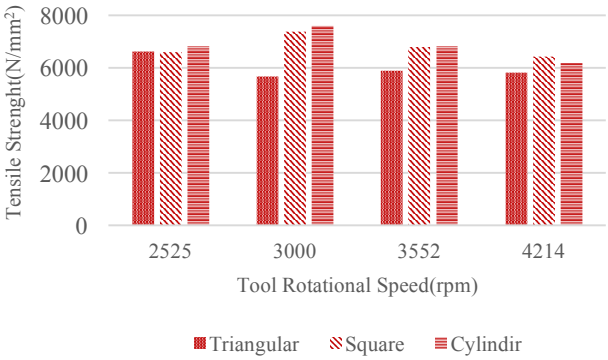

Fig. 3. Comparison of tensile strenght values of tool profiles versus tool rotational speeds

Surface area of the tool is the other important parameter for tensile strenght. Because of increasing the tool surface and tool rotational speed generates higher heat input. And the sufficient heat input during the FSSW process leads to more extensive stirring.

3. CONCLUSION

This study was performed based on the evaluating of tool rotational speed and tool geometry effect on tensile strenght of FSSW joinings

The results obtained indicate that Friction Stir Spot Welding tool shape has a great impact on tensile strenght values of joinings.

Friction stir spot welds have been produced for the AA6061 T6 sheets with the different probe geometries and different tool rotational speeds.

Higher strenght properties yielded with using of friction stir spot parameters of 3000 rpm(tool rotational speed) and the tool which has cylindir geometry compared with other joints.

4. ACKNOWLEDGEMENTS

We would like to thank Scientific Research Projects of Gazi University for financial support.

REFERENCES

[1] Lathabai S., Painter M. J., Cantin G.M.D., Tyagi V.K., Scripta Materialia 55 (2006) 899–902
[2] Uematsu Y., Tokaji K., Tozaki Y., Kurita T., Murata S., International Journal of Fatigue 30 (2008) 1956–1966
[3] Hirasawa S., Badarinarayan H., Okamoto K, Tomimura T., Kawanami T., Journal of Materials Processing Technology 210 (2010) 1455–1463
[4] Merzoug M., Mazari M., Berrahal L., Imad A., Materials and Design 31 (2010) 3023–3028

[5]Badarinarayan H., Yang Q., Zhu S., Int. J. of Machine Tools & Manufacture 49 (2009) 142–148
[6] Sudag M., Ovali I., Bilgin M. B., Akkurt A, International conference on welding technologies and exhibiton (2012) 668-674
[7] Uematsu Y., Tokaji K., Tozaki Y., Nakashima Y., Procedia Engineering 2 (2010) 193–201
[8]Sudag M., Ovali I., Bilgin M. B., Akkurt A., International conference on welding technologies and exhibiton (2012) 376-382
[9]Lee J., Um K., Optics and Lasers in Engineering 34 (2000) 149-158
[10] Malafaia, A. M. S, Milan, M.T., Oliveira, M. F., Spinelli, D., Procedia Engineering 2 (2010) 1815–1821
[11] Buffa G., Fratini L., Piacentini M, J. of Materials Processing Technology 208 (2008) 309–317
[12]M. Sudağ, A. Akkurt, 3rd International Conference on Welding Technologies and Exhibition, ICWET'14, 21-23 May Manisa/Turkey, (2014), 847-855
[13]Ovali I., Mavi A., JESTECH 16(1), 1-10, (201

Experimental and Theoretical Studies on Theobromine Dimers and Theobromine-DMSO Complexes

Mustafa Tuğfan Bilkan[a]

[a]*Department of Physics, Faculty of Sciences, Çankırı Karatekin University, TR-18100 Çankırı, Turkey*

**e-mail corresponding author:mtbilkan@gmail.com*

Keywords: Solvent-ligand complexes; Hydrogen bonds; Vibrational Spectra; DFT; Electronic and thermal properties

ABSTRACT

The solvent effects on physical and chemical properties of theobromine were examined by using Density Functional Theory(DFT) method a hybrid functional Becke's Three Parameter Hybrid Functional Using the Lee-Yang-Parr Correlation Functional (B3LYP)with 6-311++ G(d,p) basis set in Dimethylsulfoxide (DMSO) solvent. DFT/B3LYP combined with polarized continuum model (PCM) [1] was employed to characterize the solvent effects. The optimized molecular structures were determined in vapor and solvation phases. The wavenumbers and intensities of the vibrational frequencies were also computed. Furthermore, the highest occupied molecular orbital (HOMO) and the lowest unoccupied molecular orbital (LUMO) energies were calculated. Experimental FT-IR spectrum in DMSO solution were recorded and compared with solid phase data. The results show that the structural, vibrational and electronic properties of theobromine are affected by the solvent effect. The stable equilibrium energy of theobromine is decreased in solvent media depending on the dielectric constant. Besides results show also that theobromine is found in dimeric form in solid phases.

1. INTRODUCTION

Theobromine (TBR) is a common known alkaloid and it is found in structures of cacao, tea, coffee etc. With a general description, TBR is expressed as methyl bounded xanthine (3,7-dimethylxanthine). It has been investigated by scientists for many years because of its commercial and scientific importance [2-3]. TBR is also known with biological and pharmacological activities for living organisms [4]. Although there are many published study about vibrational and structural properties of free TBR, to the best of our knowledge, there are no published studies on solvent effects, solvent-ligand complexes and dimer structures of TBR. Hence, in this study, we have investigated vibrational, chemical and electronic properties of theobromine dimers (TBR-TBR) and theobromine-dimethyl sulfoxide (TBR-DMSO) complexes by DFT/B3LYP method with 6-311++G(d,p) basis set..

2. RESULTS AND DISCUSSION

The calculations of all chemical properties of TBR have been performed by using Gaussian03 program. Firstly, the optimized molecular structures of TBR in vacuum and solvent medium were performed using by 6-311++G(d,p) basis set. Secondly, based on the optimized structure, physical and chemical properties were calculated. The fundamental vibrational modes were characterized by their PED (potential energy distribution). When examining the solvent effects on TBR, only PCM implicit solvation model calculations on structure of TBR was named as Model I. Both implicit and explicit solvation model calculations on TBR-DMSO complexes was named Model II. In the experimental section, a commercial sample of TBR was purchased from Aldrich and used without further purification. 1 mmol TBR (180 mg) was solved in 1 ml DMSO and the solution was stirred for five minute in room temperature. The infrared spectrum of the solutions free ligand and the pure solvent were recorded between 3700-550 cm-1 by Bruker FT-IR spectrometer and MIRacle ATR (Attenuated total reflection) equipment.

Molecular structure of TBR

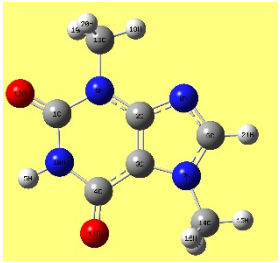

Figure 1. Optimized molecular structure of TBR in vacuum medium

The optimized molecular structure of TBR is presented in Figure 1. Calculated bond lengths and angles were tabulated in Table 1.

Table 1. Selected geometric parameters of TBR in DMSO medium.

	Bond Lengths	Vacuum	DMSO	Exp.*	Bond Angles	Vacuum	DMSO	Exp.*
1	1C-9N	1.393	1.385	1.377	9N-1C-10N	115.34	115.79	116.37
3	1C-12O	1.215	1.223	1.231	9N-1C-12O	122.68	122.57	122.10
4	2C-3C	1.383	1.386	1.364	10N-1C-12O	121.99	121.64	121.53
5	2C-8N	1.371	1.370	1.363	3C-2C-8N	110.77	110.80	112.72
7	3C-4C	1.434	1.429	1.426	3C-2C-9N	122.86	122.89	122.40
8	3C-7N	1.403	1.403	1.388	2C-3C-4C	122.84	122.39	122.94
9	4C-10N	1.411	1.407	1.397	3C-4C-11O	128.58	128.74	128.63
10	4C-11O	1.220	1.226	1.225	7N-6C-8N	116.50	116.78	114.30
11	10N-5H	1.012	1.013	0.856	3C-7N-6C	103.93	103.87	105.62
12	6C-7N	1.343	1.339	1.343	1C-9N-2C	119.23	119.09	118.91
13	6C-8N	1.292	1.296	1.339	2C-9N-13C	122.04	122.11	121.76
16	9N-13C	1.465	1.467	1.473	1C-10N-4C	130.05	129.72	129.10
17	13C-18H	1.087	1.086	1.039	1C-10N-5H	114.16	114.43	116.67
19	13C-20H	1.092	1.090	0.971				
22	14C-17H	1.090	1.089	1.034				

*Data were taken from Acta Crystallogr., 1998, C54, 1980-1983

From Table 1, one can see that 6-311++G(d,p) calculated and experimental data are very compatible. Deviations from the experimental values are quite small for the calculated ones in gas phase. Because of low scattering factors of hydrogen atoms in X-ray diffraction, experimental bond lengths of N-H and C-H bonds are shorter than the calculated ones. There are dramatic deviations in calculated and experimental values of C-N bond lengths. The essential reason of all small deviations in bond lengths and bond angles is that TBR molecules in the crystal structure are firmly located under periodic boundary conditions (PBC) but in the theoretical calculation PBC is ignored. In the solvent medium, geometric parameters of TBR are slightly different from gas phase. The most considerable changes for TBR are determined at the carbonyl sites of the molecule. Similar situations are valid for all of C-N and C-C bonds. As seen from the table, solvent medium has caused significant changes in all bond lengths. The experimental and calculated bond angles are also presented in Table 1, too. In general, most of the bond angles are in good agreement with the experimental data. While some calculated values are smaller than experimental, some values are larger. Some of bond angles showed large deviations from the experimental ones. The cause of these deviations in molecular parameters is due to phase difference between the theoretical and experimental conditions

Vibrational frequencies and assignments

TBR has 21 atoms and according to the rule of 3N-6 normal modes it has 57 vibrational modes. All of DFT/B3LYP-6311++G(d,p) calculated harmonic vibrational frequencies and intensities are given in Table 2 together with experimental data. N-H stretching modes are normally seen around 3300-3500 cm^{-1} for free N-H bond. If N-H is bonded with the hydrogen bond, this stretching mode is decreased until 3100-3150 cm^{-1}. Hydrogen bonding interactions causes N-H band to shift lower wavenumbers. In this case, we can say that TBR may exist in the form of dimer in solid phase. Almost all of the vibration mode are affected by the solvent environment. Especially, N-H stretching mode is the most affected band by the solvent media. Solvent medium is shifted N-H stretching mode about 300 cm^{-1}. Similar changes are valid for C-H stretching bands, too.

Table 2. Selected vibrational frequencies and assignments of TBR in vacuum and DMSO media.

Mode	Exp.	Vacuum		DMSO		(%) PED
		Freq.	I_{IR}	Freq.	I_{IR}	
17	614s	615	8.26	601	3.78	$\Gamma_{HNCC}(70)+\Gamma_{CNCN}(18)$
19	681s	694	1.42	689	0.82	$\Gamma_{ONCC}(35)+\Gamma_{NCNC}(25)+\Gamma_{CCNC}(20)$
20	731s	710	1.46	713	1.67	$\delta_{OCN}(53)+\delta_{NCN}(13)$
21	750s	734	2.80	732	2.05	$\Gamma_{ONNC}(66)$
22	762m	756	1.93	756	1.50	$\Gamma_{ONCC}(47)+\Gamma_{ONNC}(23)+\Gamma_{CCNC}(19)$
24	860s	823	1.53	844	1.00	$\Gamma_{HCNC}(85)+\Gamma_{CNCN}(12)$
32	1173m	1186	1.46	1184	1.88	$\delta_{HCN}(30)+V_{CN}(10)$
33	1222s	1212	11.29	1210	10.87	$\delta_{HCN}(30)+V_{CN}(15)+\delta_{NCN}(10)$
41	1423m	1435	1.28	1430	0.83	$\delta_{HCH}(72)+\Gamma_{HCNC}(20)$
45	1487m	1477	1.80	1473	2.53	$\delta_{HCH}(46)+V_{CN}(16)$
46	1546s	1519	14.46	1513	13.00	$\delta_{CCN}(30)+V_{C-C}(19)+V_{CN}(13)$
47	1591s	1555	15.42	1548	8.74	$V_{C=C}(49)+V_{CN}(23)$
48	1661vs	1683	100.00	1611	100.00	$V_{CO}(63)$
49	1687vs	1694	78.02	1635	62.11	$V_{CO}(72)$
52	3014m	3022	1.33	3020	0.57	$V_{CH}(99)$
57	3150w	3489	10.01	3166	22.76	$V_{NH}(100)$

The C=O stretching modes for TBR are calculated at 1694 and 1683 cm^{-1} for vacuum medium while experimental values are 1687vs and 1667vs. In DMSO solvent medium, these vibrations are calculated 1635 and 1611 cm^{-1}. As can be seen from these results, the solvent medium is affected too much all stretching vibrations of TBR.

Dimer form analysis of TBR

Dimerization is hydrogen-bonded structure of two monomers. In the Figure 2, we present the possible N-H···O type dimer structures of TBR with their energies differences and intermolecular hydrogen bond lengths. We think TBR is in dimer form in the solid phase because it has bonded N-H stretching mode. All of the hydrogen bonded dimer structures of TBR are in binary connected structure. The interaction energies of dimers are computed as 13.45, 13.66, 13.66 and 13.68 kcal/mol, respectively. Furthermore, all of the N-H···O hydrogen bond lengths are between 1.86-1.88 Å.

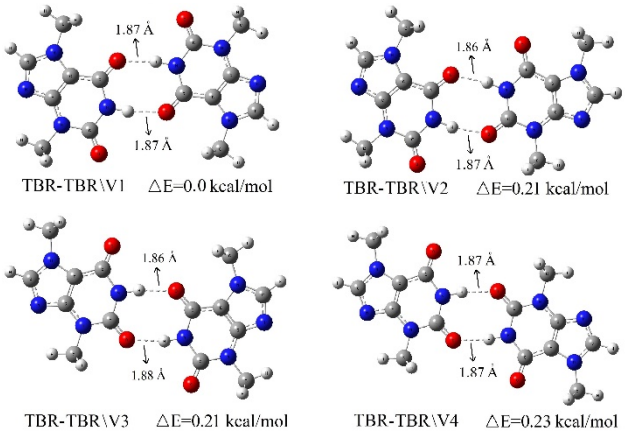

Figure 2. Possible dimer structures of TBR optimized by B3LYP.

Some important vibrational modes of the most stable dimer structure of TBR are given in Table 3. The N-H stretching mode is calculated about at 3200 cm^{-1}. This is evidence of the presence of dimer in solid phase. Furthermore, many of the experimental bands are more compatible with the dimer structure calculations.

Table 3. Selected vibrational frequencies and assignments of TBR-TBR/V1 in gas phase.

Freq.	I_{IR}	Exp.	(%) PED	Freq.	I_{IR}	Exp.	(%) PED
721	1.10	731s	$\delta_{OCN}(28)+V_{CN}(15)$	1460	1.68	1454s	$\delta_{HCH}(42)$
723	1.46	750s	$\Gamma_{ONCC}(34)+\Gamma_{CNNC}(16)$	1474	1.73	1487m	$\delta_{HCH}(46)$
862	5.41	860s	$\Gamma_{HNCC}(33)+\Gamma_{CNHO}(32)$	1527	10.21	1546s	$\delta_{CCN}(13)$
1185	1.38	1173m	$\delta_{HCN}(28)$	1666	83.76	1661vs	$V_{CO}(57)+\delta_{HNC}(12)$
1215	6.27	1222s	$\delta_{HCN}(34)$	1706	46.02	1687vs	$V_{CO}(76)$
1337	3.89	1334m	$V_{CN}(24)$	3014	0.97	3014m	$V_{CH}(98)$
1372	2.78	1366m	$V_{CN}(24)$	3211	100.00	3150w	$V_{NH}(100)$

TBR-Solvent complexes

We have also investigated some physical and chemical properties of hydrogen bonded TBR-solvent complexes. Possible TBR-DMSO complexes were studied in detail by using theoretical and experimental methods. Experimental FT-IR spectrum of TBR in DMSO solution was recorded and plotted in Figure 3 with the possible DMSO-TBR complexes optimized by B3LYP.

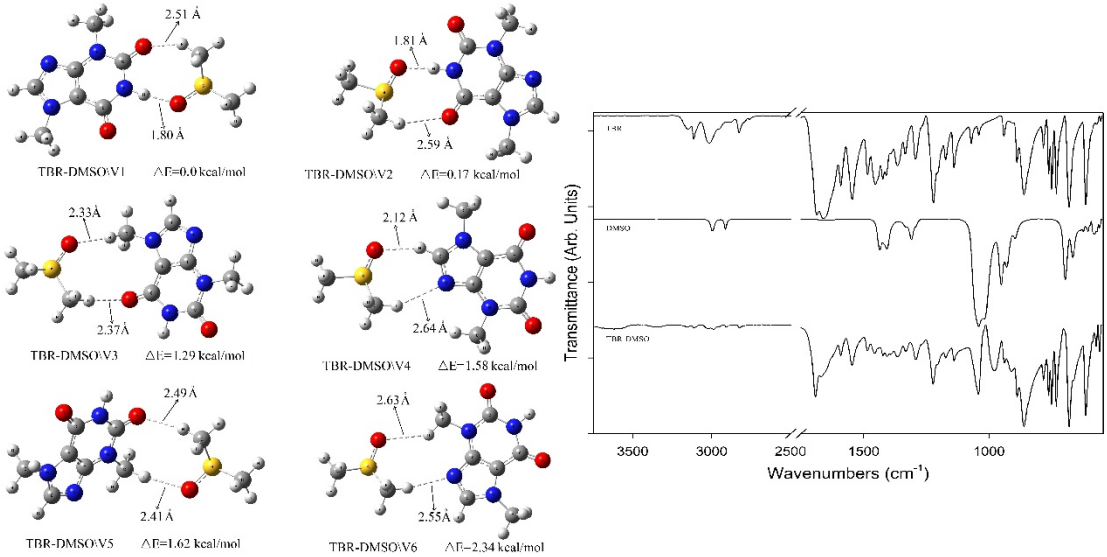

Figure 3. Experimental FT-IR spectra of solid TBR, pure DMSO and TBR-DMSO solution.

When experimental FT-IR spectra of the solutions are recorded, pure solvent spectra were also recorded and were used as background. Nevertheless, when we compared the experimental spectra of the solutions with the solid phase experimental data, we have seen that the vibrational bands are shifted and new bands arise. This indicates there is an interaction between solvent molecules and ligand molecules. In the table 4, bold ones are the modes seen in the FT-IR spectrum of both the free solvent and the solution.

Table 4. Selected vibrational frequencies and assignments of most stable TBR-DMSO (V1) complex.

Mode	Model II		Model I		Exp.	Pure DMSO		(%) PED
	Freq.	I_{IR}	Freq.	I_{IR}		Calc.	Exp.	
28	623	0.21	-	-	**638w**	617	624vw	$V_{SC}(94)$
30	660	0.53	-	-	**662m**	651	666m	$V_{SC}(83)$
38	889	0.34	-	-	**888s**	880	-	$\delta_{HCS}(34)+\Gamma_{HCSC}(28)$
39	902	13.55	-	-	**909m**	912	895w	$V_{SO}(78)$
40	921	0.78	917	0.48	938w	913	930w	$\delta_{CNC}(23)+V_{NC}(21)$
42	972	6.28	-	-	**978m**	972	951m	$\Gamma_{HCSC}(26)+\Gamma_{HCSO}(20)+V_{SO}(18)$
43	1010	2.29	-	-	**994sh**	999	1017s	$\delta_{HCS}(34)+\Gamma_{HCSC}(26)$
45	1047	1.26	1048	1.50	**1043s**	-	1041s	$V_{NC}(16)+\delta_{NCN}(14)+\delta_{HCH}(11)$
64	1424	0.95	1430	0.83	1423w	1412	1436w	$\delta_{HCH}(76)+\Gamma_{HCNC}(13)$
87	3088	100.00	3166	22.76	3152vw	-	-	$V_{NH}(96)$

Table 5. Selected vibrational frequencies and assignments of most stable TBR.

Entropy (cal/mol.K)	108.332 (vacuum)	106.901 (DMSO)
Heat capacity (cal/mol.K)	41.881 (vacuum)	41.823 (DMSO)
Dipole moment (Debye)	4.7479 (vacuum)	6.3663 (DMSO)

3. CONCLUSION

In this study, we have investigated vibrational and structural some properties of TBR, TBR-TBR and TBR-DMSO complexes by using theoretical and experimental methods. As result of this study, we saw that TBR is affected by the solvent effect, seriously. Additionally, the TBR may found in dimeric form in solid phases.

REFERENCES

[1] Miertuš, S.;Scrocco, E.;Tomasi, J. Chem. Phys. (1981), 55,117-124.
[2] Asanuma, H.; Ban, T.; Gotoh, S.; Hishiya, T.; Komiyama, M. Macromolecules, (1998), 31, 371-377.
[3] Huck, C. W.; Guggenbichler, W.; Bonn, G. K. Anal. Chim. Acta, (2005), 538, 195-203.
[4] Oettl, K.; Reibnegger, G. Biochim. Biophys. Acta., (1999), 1430, 387-394.

Frequency and gate voltage effects on the dielectric properties and electrical conductivity of Al/Co-PVC/p-Si structures

İlbilge DÖKME

Science Education Department, Faculty of Gazi Education, Gazi University, Ankara, TR-06560 Turkey

ilbilgedokme@gazi.edu.tr

Keywords: Schottky barrier diode; capacitance-voltage characteristics; Al/Co-PVC/p-Si

ABSTRACT

Dielectric properties and electrical conductivity of Al/Co-PVC/p-Si Schottky barrier diode (SBD) in the frequency range of 50 kHz-3 MHz and gate voltage range of (-4V)-(10V) have been investigated in detail by using experimental capacitance-voltage (*C-V*) and conductance-voltage (*G/w-V)* measurements. Dielectric constant (ε'), dielectric loss (ε''), electrical conductivity (σ_{ac}), the real part of electric modulus (M'), the imaginary part of electric modulus (M'') are plotted as a function of frequency and applied voltage. Experimental results show that the values of the dielectric constant (ε'), dielectric loss (ε'') and $\tan\alpha$ obtained from the experimental *C-V* and *G/w-V* measurements were found a function of frequency and applied voltage. It is also discussed in this paper that Co-PVC interfacial layer at metal and semiconductor effect and change the dielectric properties of Al/Co-PVC/p-Si structures.

1. INTRODUCTION

A growing body of research studies on Schottky diodes support that insulator layer forming on semiconductor wafer are important component of these device by virtue of the fact that the insulator layer between metal and semiconductor can change device electrical and dialectical characteristics [1-3]. The formed a nonnative insulating layer causes barrier height between metal and semiconductor and affects on the device electrical parameters [4]. During the recent years considerable attention was given polymer as an interfacial layer for the fabrication and electrical characterization of Schottky barrier diodes SBDs[5-8]. Poly vinly chloride(PVC) used an interfacial layer in this study is a polar molecule and one of the most important commercially available polymer due to its light, electrical & chemical resistant. PVC has the ability to get mixed with other to produce verity of compounds which has a wide range of physical & chemical properties.[7]. Therefore, this study makes a major contribution to research on polymer based Schottky device technology by presenting the detailed analysis of dielectric characteristics.

2. EXPERİMENTAL PROCEDURE

Al/Co-PVC/p-Si Schottky barrier diode (SBD) was fabricated on the 2 in. (1.5 cm) diameter flat zone p-type (Boron doped) single crystal Si wafer (100) having thickness of 350 μm with ≈ 0.7 Ωcm. After the cleaning steps immediately high purity Al metal (99.999%) with a thickness of about 2000 Å was thermally evaporated onto the whole back side of Si wafer in the system having the vacuum value of 10^{-6} torr. In order to perform a low resistivity ohmic back contact, Si wafer was sintered at 450 $^{\circ}$C for 5 min in N_2 atmosphere. Low-molecular weight PVC (with average molecular weight of 48,000, having K value of 55–57, and density of 1.4 g mL−1 at 25◦C as white-color fine powder) was obtained from Sigma-Aldrich; Tetrahydrofuran (THF) was obtained from Merck. Powders of 0.345 g PVC were slowly added to approximately 30 mL of THF in a volumetric flask during gentle stirring with magnetic stirrer on hot plate at 20◦C. After stirring about 30 min. the volume was completed to 50.0 mL by adding the sufficient volume of THF. After volume completion, the solution was stirred while it was gently heated to 40◦C on hot plate for about an hour. After completely dissolving, content of flask was allowed to cool to room temperature

while it was stirring. Then, Cobalt (Co) doping was performed by using the Fluka atomic spectroscopy standard solutions for Co having the metal ion concentration of 1 gL−1 in well-defined solution characteristics. Co doping processes were performed after testing the precipitation possibility of metal ions in selected solvent. If precipitation was established on this step some of the solution characteristics such as pH, type of solvent, water ratio, etc were rearranged. After regulation of solution content in order to have precipitated Co ion, sufficient volume (4.0% to total volume) from "as regulated" Co ion source was taken and mixed with the solution of PVC in THF. Surface of p-type Si wafer was modified with coating of "as prepared" solution of PVC in THF by spin-coating method with 3000 rpm for 1 min. After the formation of Co-PVC interfacial layer, the rectifier/Schottky contacts were formed in thermal evaporation system by using metal shadow mask on the front surface of the p-Si wafer and Al dots having diameter of 1.5 mm. The *C-V* ang *G/ω-V* measurements were performed in the frequency range of 50 kHz-3 MHz by using a HP 4192A LF impedance analyzer and small sinusoidal test signal of 20 $mV_{p-p.}$ from the external pulse generator is applied to the sample in order to meet the requirement. All measurements were carried out with the help of a microcomputer through an IEEE-488 ac/dc converter card.

3. RESULTS AND DISCUSSION

Fig 1 shows the voltage dependence of the ε' and ε'' of the Al/Co-PVC/p-Si SBD at various frequencies. The complex permittivity can be written [9] as

$$\varepsilon^* = \varepsilon' - i\varepsilon'' \quad (1)$$

where ε' and ε'' are the real and imaginary of complex permittivity, and i is the imaginary root of $\sqrt{-1}$. The complex permittivity formalism has been employed to describe the electrical and dielectric properties. In the ε^* formalism, in the case of admittance Y^* measurements, the following relation holds

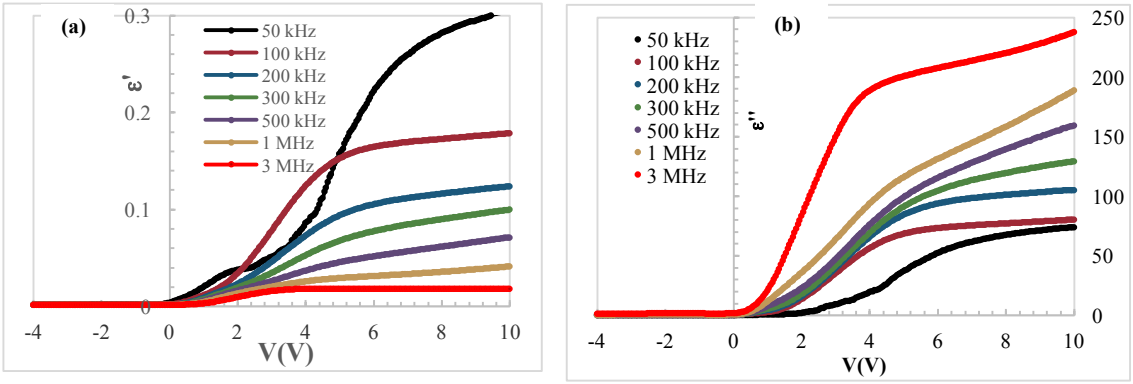

Figure 1. The variations of the (a) dielectric constant and (b) dielectric loss vs. applied voltage for various frequencies of Al/Co-PVC/p-Si at room temperature.

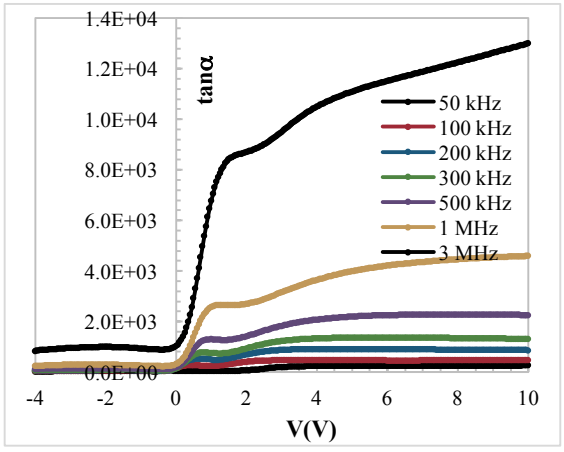

Figure 2. The variations of the tangent loss vs. applied voltage for various frequencies of Al/Co-PVC/p-Si at room temperature.

$$\varepsilon^* = \frac{Y^*}{j\omega C_o} = \frac{C}{C_o} - i\frac{G}{\omega C_{o_i}} \quad (2)$$

where, C and G are the measured capacitance and conductance of the device, ω is the angular frequency ($\omega=2\pi f$) of the applied electric field [10]. The real part of the complex permittivity, the dielectric constant (ε'), at the various frequencies is calculated using the measured capacitance values at the strong accumulation region from the relation [9],

$$\varepsilon' = \frac{C}{C_o} = \frac{C\, d_i}{\varepsilon_o A} \tag{3}$$

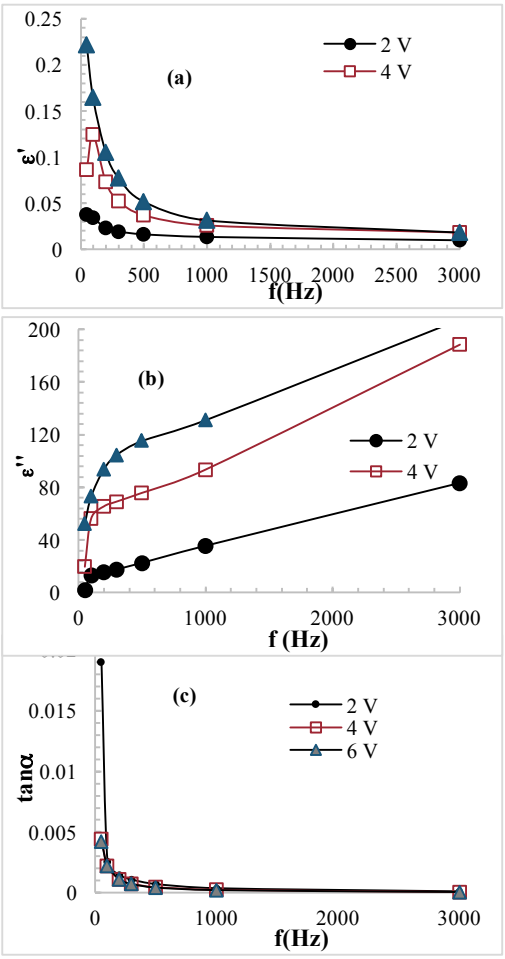

Figure 3. The variation of the (a) dielectric constant, (b) dielectric loss and (c) tangent loss vs. frequency at various applied voltage for Al/Co-PVC/p-Si at room temperature.

where $C_o = \varepsilon_o A/d_i$ is capacitance of an empty capacitor, A is the rectifier contact area of the structure in cm^{-2}, d_i is the interfacial layer thickness and ε_o is the electric permittivity of free space ($\varepsilon_o = 8.85\text{x}10^{-14}$ F/cm). In the strong accumulation region, the maximal capacitance of the structure corresponds to the insulator capacitance ($C_{ac} = C_i = \varepsilon' \varepsilon_o A / d_i$). The imaginary part of the complex permittivity, the dielectric loss (ε''), at the various frequencies is calculated using the measured conductance values from the relation[7-9],

$$\varepsilon'' = \frac{G}{\omega C_o} = \frac{G d_i}{\varepsilon_o \omega A} \tag{4}$$

The loss tangent ($\tan\delta$) can be expressed as follows [9],

$$\tan\alpha = \frac{\varepsilon''}{\varepsilon'} \tag{5}$$

The ac electrical conductivity (σ_{ac}) of the dielectric material can be given by the followidng equation [3],

$$\sigma_{ac} = \omega C \tan\delta (d/A) = \varepsilon'' \omega \varepsilon_o \tag{6}$$

The complex impedance (Z^*) and complex electric modulus (M^*) formalisms were discussed by various authors with regard to the analysis of dielectric materials [9]. Analysis of the complex permittivity (ε^*) data in the Z^* formalism ($Z^* = 1/Y^* = 1/i\omega C_o \varepsilon^*$) is commonly used to separate the bulk and the surface phenomena and to determine the bulk dc conductivity of the material. Many authors prefer to describe the dielectric properties of these devices by using the electric modulus formalize [10].

The complex impedance or the complex permittivity ($\varepsilon^* = 1/M^*$) data are transformed into the M^* formalism using the following relation[9]

$$M^* = i\omega C_o Z^* \tag{7}$$

or

$$M^* = \frac{1}{\varepsilon^*} = M' + jM'' = \frac{\varepsilon'}{\varepsilon'^2 + \varepsilon''^2} + j\frac{\varepsilon''}{\varepsilon'^2 + \varepsilon''^2} \tag{8}$$

The real component M' and the imaginary component M'' are calculated from ε' and ε''. It is clearly seen in Fig. 1(a) that the values of ε' decrease with increasing frequency. The decrease in ε' with increasing frequency may be attributed to the polarization decreasing with increasing frequency that can be explained to Maxwell- Wagner type interfacial polarization, i.e. the fact that inhomogeneities give rise to a frequency dependence of the conductivity because charge carries accumulate at the boundaries of less conducting regions, thereby creating interfacial polarization [5-10]. Fig. 1(b) and 2 show the voltage dependence of dielectric loss (ε'') and the loss tangent ($\tan\delta$) of the Al/Co-PVC/p-Si SBD at various frequencies. As can be seen in these figures, the values of ε'' and $\tan\delta$ are strongly dependent on both frequency and applied

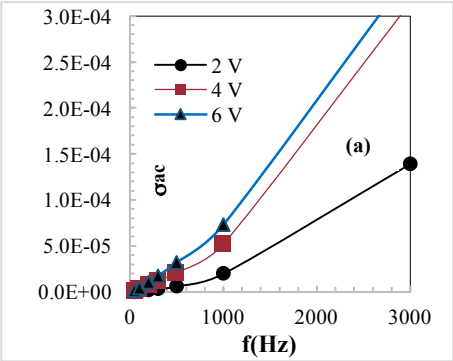

bias voltage. It is well known that the capacitance and conductance are extremely sensitive to the interface properties due to the fact that the interface states respond differently to low and high frequencies. [3-10]. The frequency dependence of the ε', ε'' and tanδ of Al/Co-PVC/p-Si SBD at different voltage are presented in Fig. 3 (a), (b) and (c), respectively. The values of the ε', ε'' and tanδ obtained from the measured capacitance and conductance were found a strong function of applied voltage especially at low frequencies. As shown in Fig. 4 (a) and (b), the values of ε' sharply decrease with increasing frequency while the values of ε'' increase with increasing frequency at each voltage. On the other hand tanδ values for each voltage are much close each other. It may be inferred that all the four types of polarization processes, i.e., the electronic, ionic, dipolar, and interfacial or surface polarization contribute to the values of ε' and ε'' [3-8].

The behavior of ac electrical conductivity (σ_{ac}) of the Al/Co-PVC/p-Si SBD at various voltage is presented in Figure 4(a). It is noticed that the electrical conductivity increases with increasing frequency at each voltage. This electrical conductivity contributes only to the dielectric loss, which becomes infinite at zero frequency and not important at high frequencies. As the frequency increases electrical conductivity increase because of the polarization is decreasing with increasing frequency. The increase of the electrical conductivity lead to an increase of the eddy current which in turn increases the energy loss tangα. This result is corresponded with the decreasing in ε'' with increasing frequency. The variation of the real part of electric modulus, M' and their imaginary part of M'' of Al/Co-PVC/p-Si SBD as a function of frequency at various bias voltages are given in Fig. 4 (b) and (c), respectively.

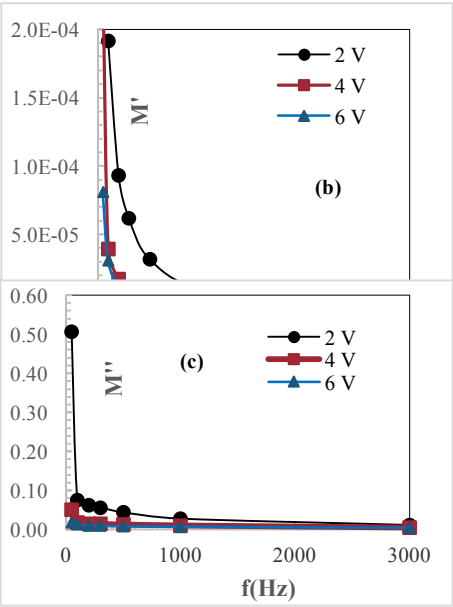

Figure 3. The variation of the (a) σac, (b) M′ and (c) M″ vs. frequency at various applied voltage for Al/Co-PVC/p-Si at room temperature.

4. CONCLUSION

The dielectric characteristics of Al/Co-PVC/p-Si SBD have analyzed in this study. The polarization decreasing with increasing frequency in the Co-PVC interface and also an increase of the eddy current caused by additional charge carriers due to the origin of the SBD. It is conclude that the dielectric properties of Al/Co-PVC/p-Si SBD are strongly depend on both the frequency and applied bias voltage.

5. ACKNOWLEDGEMENTS

This work was supported financially by Scientific ResearchUnit of Gazi University [grant number 04/2016-5]

REFERENCES

[1] Sze S. M., *Physics of Semiconductor Devices*, 2nd ed. New York, NY, USA: Willey, 1981, ch. 7.
[2] Card H. C. and Rhoderick E. H., J., Phys. D. Appl. Phys. (1971), 4, 1589-1595.
[3] Ersöz G., Y. İbrahim, Azizian-Kalandaragh Y., Orak İ. and Altındal Ş., IEEE Trans.on Electr. Dev. (2016), 63, 2948-2955
[4] Singh A., Reinhardt K. C. and Anderson W. A., J. Appl.Phys. (1990), 68, 3475-3482.
[5] Gökçen M., Tunç T., Altındal Ş., and Uslu İ., Mater. Sci. Eng. B. (2012), 177, 416–420.
[6] Kaya A., Vural Ö., Tecimer H., Demirezen S. and Altındal Ş, Current Appl. Phys. (2014), 14, 322-330.

[7] Yücedağ İ., Ersöz G., Gümüş A. and Altındal Ş., Int. J. Mod. Phys. B (2015), 29, 1550075.
[8] Orak İ., Koçyiğit A. And Türüt A., Journal of Alloy Comp. (2017), 691, 8733-879.
[9] Symth C. P., Dielectric Behaviour and Structure, McGraw-Hill, New York, 1955.
[10] Mattsson M. S., Niklasson G. A., Forsgren K. and Harsta S., J. Appl. Phys. (1999), 85, 2185-2193.

Current-Voltage characteristics of Al/Co-PVC/p-Si structures

İlbilge DÖKME

Science Education Department, Faculty of Gazi Education, Gazi University, Ankara, TR-06560 Turkey

ilbilgedokme@gazi.edu.tr

Keywords: MIS structure; current-voltage; Al/Co-PVC/p-Si

ABSTRACT

The purpose of present study is to fabricate the Metal/Insulator/Semiconductor (MIS) with Cobalt dopped Polyvinyl Chloride (PVC) interfacial layer and determine electrical characteristics of this device. The current-voltage (*I-V*) have been measured for fabricated Metal/Co-PVC/Semiconductor electronic structures. Device parameters such as ideality factor (n), saturation current (I_o), zero bias barrier height (Φ_B), series resistance (R_s), interface states density (N_{ss}) have been calculated from *I-V* data. It has been found that Co-PVC as an interfacial layer effect the diode current-voltage characteristics and diode parameters.

1. INTRODUCTION

Future electronics for any complex circuits involve in a Schottky diode which has many advantages such as very low forward voltage drop and switching speeds making them usable for power supplies. Metal-semiconductor Schottky barrier diodes (SBDs) are fabricated with a metal and a semiconductor, creating a thin interfacial native oxide layer between the metal and the semiconductor[1]. The presence of a nonnative insulating layer converts the SBD into a metal-insulator-semiconductor SBD [2] that influences on the device electrical parameters [3]. In recent years, considerable attention was given polymer as an interfacial layer for the fabrication and electrical characterization of SBDs[4-8]. Poly vinly chloride(PVC) which used as an interfacial layer in present work is a polar molecule and one of the most important commercially available polymer due to its light, electrical & chemical resistant. PVC has the ability to get mixed with other to produce verity of compounds which has a wide range of physical & chemical properties.[6]. Therefore, this study makes a major contribution to research on polymer based Schottky device technology by presenting the detailed analysis with comparing experimental and theoretical results.

2. EXPERİMENTAL PROCEDURE

Al/Co-PVC/p-Si Schottky barrier diode (SBD) was fabricated on the 2 in. (1.5 cm) diameter flat zone p-type (Boron doped) single crystal Si wafer (100) having thickness of 350 μm with ≈ 0.7 Ωcm. After the cleaning steps immediately high purity Al metal (99.999%) with a thickness of about 2000 Å was thermally evaporated onto the whole back side of Si wafer in the system having the vacuum value of 10^{-6} torr. In order to perform a low resistivity ohmic back contact, Si wafer was sintered at 450 °C for 5 min in N_2 atmosphere.

Low-molecular weight PVC (with average molecular weight of 48,000, having K value of 55–57, and density of 1.4 g mL−1 at 25◦C as white-color fine powder) was obtained from Sigma-Aldrich; Tetrahydrofuran (THF) was obtained from Merck. Powders of 0.345 g PVC were slowly added to approximately 30 mL of THF in a volumetric flask during gentle stirring with magnetic stirrer on hot plate at 20◦C. After stirring about 30 min. the volume was completed to 50.0 mL by adding the sufficient volume of THF. After volume completion, the solution was stirred while it was gently heated to 40◦C on hot plate

for about an hour. After completely dissolving, content of flask was allowed to cool to room temperature while it was stirring. Then, Cobalt (Co) doping was performed by using the Fluka atomic spectroscopy standard solutions for Co having the metal ion concentration of 1 gL−1 in well-defined solution characteristics. Co doping processes were performed after testing the precipitation possibility of metal ions in selected solvent. If precipitation was established on this step some of the solution characteristics such as pH, type of solvent, water ratio, etc were rearranged. After regulation of solution content in order to have precipitated Co ion, sufficient volume (4.0% to total volume) from "as regulated" Co ion source was taken and mixed with the solution of PVC in THF. Surface of p-type Si wafer was modified with coating of "as prepared" solution of PVC in THF by spin-coating method with 3000 rpm for 1 min.

After the formation of Co-PVC interfacial layer, the rectifier/Schottky contacts were formed in thermal evaporation system by using metal shadow mask on the front surface of the p-Si wafer and Al dots having diameter of 1.5 mm. *I–V* measurements were performed by the use of a Keithley 220 programmable constant current source, a Keithley 4200 electrometer at room temperature.

3. RESULTS AND DISCUSSION

Forward bias *I-V* characteristic of Al/Co-PVC/p-Si SBD was investigated between the potential range from -6 to + 6 V. Fig. 1 shows the semi-logarithmic forward bias *I–V* plots of Al/Co-PVC/p-Si SBD at room temperature. According to the thermionic emission theory, the forward bias *I–V* relationship for SBD is given as follows [2,3]:

$$I = I_o \left[exp \frac{qV_D}{nkT} \right] \quad (1)$$

where V is the definite forward bias voltage, n is the ideality factor, k is the Boltzmann constant and T is temperature in Kelvin and I_o is the reverse saturation current. The value of I_o can be obtained from the y-exis intercept of the linear region of the semi-log-forward bias *I-V* plots and expressed as

$$I_o = A^* A T^2 exp(-q\Phi_B / kT) \quad (2)$$

Here, the quantities A^*, A, Φ_B are the effective Richardson constant and equals to 32 A/cm^{2}K^2 for p-type Si, the diode area and, the zero-bias barrier height respectively.

The experimental values of Φ_B and n of Al/Co-PVC/p-Si SBD were calculated from Eq. 1 and 2 by using the y-exis intercept and slope of the linear region of the semi-log-forward bias *I-V* plots. Φ_B and n were found 0.8 eV and 3.0 respectively. As can be in Fig.1, deviation from linearity in forward bias characteristics is more clear and this characteristics have quite small linear region. This case can be attributed to series resistance (R_s) and interface states (N_{ss}) with dopping with co-PVC in interfacial layer [9]. Series resistance values can be determined by analysis of Cheung and Cheung [10] method. This provide the analysis in the large current range where the *I–V* characteristic is not linear. V_D in Eq.1 is reorganized as $V_D = V - IR_S$ to use this method. Here, V is forward bias voltage, IR_s is voltage drop caused by series resistance.

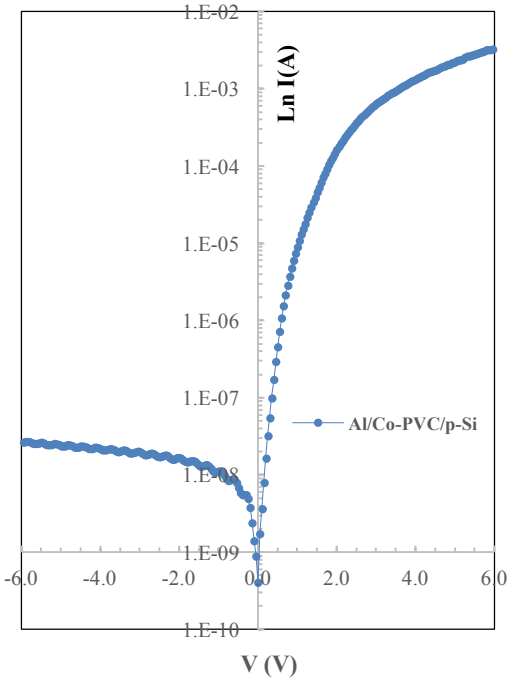

Figure 1. Experimental forward bias *I-V* characteristics of Al/Co-PVC/p-Si SBD at room temperature.

According to this method and from Eq. (1) the following function can be written as

$$\frac{dV}{dLnI} = n\frac{kT}{q} + R_s I \qquad (3)$$

In Fig. 2, experimental dV/d(LnI) vs I plots are presented for Al/Co-PVC/p-Si SBD. Eq. (3) should give a straight line that will give R_s as the slope and nkT/q as the y-axis intercept. Thus, the calculation of R_s in downward curvature region in the forward bias I-V characteristic in Fig.1 is possible. From the Fig. 2, using Eq. (3), the values of R_s was found 1138,9 Ω.

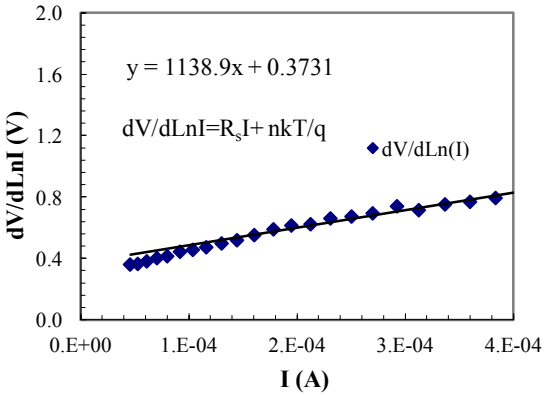

Figure 2. dV/d(LnI) vs I plots of Al/Co-PVC/p-Si SBD at room temperature.

It is expected that experimental results about Schottky diodes are supported thermionic emission (TE) theory with Eq(1). Pure thermionic theory required straight line in the plots of V vs LnI that found LnI_o by y-axis intercept and q/nkT slope of the linear line. Thus, Eq. (1) can be rewritten as follows:

$$LnI = LnI_o + \frac{q}{nkT}V_D \qquad (4)$$

Figure 3 presents detail analysis theoretical and experimental data. The black line in Fig. 3 was plotted with Eq.(4) using experimental value of I_o, and V_D. Dark blue plots were drawn by using $V_D = V - IR_S$ in Eq.(4) with R_s=1138,9 Ω. As can be seen in this figure, dark blue plots are linear up to ≈ 1.6 V and then curve downward due to the effect of series resistance. Both two graphs are have larger linear region than experimental plots with red blank circle. Which effect cause early curvature in experimental plots in Figure3 Interface states (N_{ss}) ensure another effect to consider the deviation from TE theory.

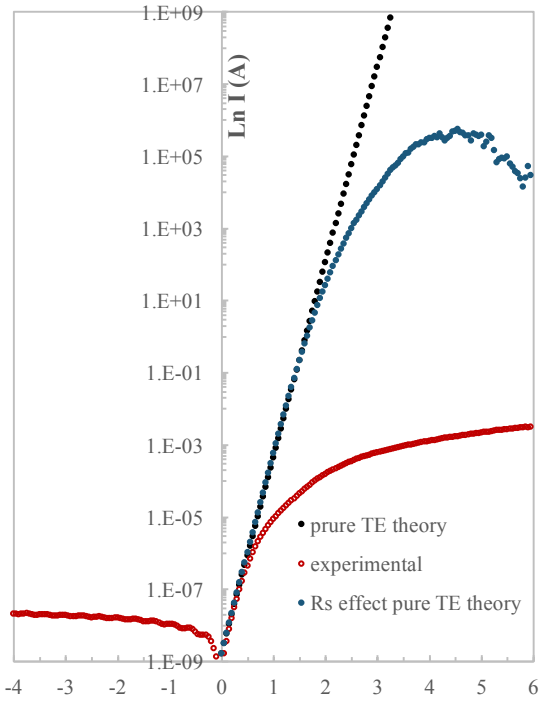

Figure 3. V vs LnI characteristics for experimental, pure TE theory and R_s effect pure TE theory.

Here, we obtained the energy density distribution profile of N_{ss} from the forward I-V characteristics of the fabricated Al/Co-PVC/p-Si SBD. For a SBD with interface states governed by the semiconductor, the expression for the density of interface states as deduced by Card and Rhoderick [1] can be written following equations

$$n(V) = \frac{q}{kT}\left[\frac{V}{Ln(\frac{I}{I_o})}\right] \qquad (5)$$

$$\Phi_e = \Phi_B + \beta(V) = \Phi_B + \left(1 - \frac{1}{n(V)}\right)V \qquad (6)$$

$$N_{ss}(V) = \frac{1}{q}\left[\frac{\varepsilon_i}{\delta}(n(V) - 1) - \frac{\varepsilon_s}{W_D}\right] \quad (7)$$

where $\beta(V)$ is the voltage coefficient of the effective barrier height Φ_e, δ is the thickness of interfacial layer obtained from capacitance-voltage measurements. W_D is the width of the space charge region, ε_i and ε_s are permittivity of the interfacial insulator layer and the semiconductor, respectively. N_{ss} is the density of the interface states in equilibrium with the semiconductor. The energy of the interface states E_{ss} (for *p*-type semiconductors) with respect to the top of valance band at the surface of semiconductor is given by [1]

$$E_{ss} - E_v = q(\Phi_e - V) \quad (8)$$

Figure 4 shows the energy distribution profile of the N_{ss} obtained from the forward bias *I-V* characteristics of Al/Co-PVC/p-Si SBD. The energy values of the density distribution the N_{ss} are in the range (E_V +0.43) to (E_V +0. 51) eV. The values of the N_{ss} in (E_V +0.43) to (E_V +0. 51) eV are 4.46x10^{13} and 1.66x10^{13} eV^{-1} cm^{-2}.

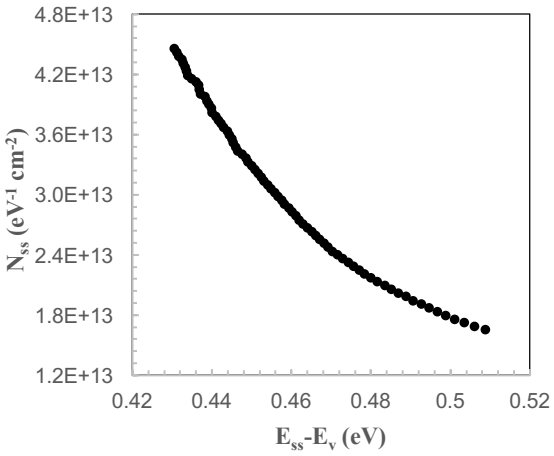

Figure 4. The interface states energy distribution curves of Al/Co-PVC/p-Si SBD at room temperature.

4. CONCLUSION

Al/Co-PVC/p-Si SBD were fabricated and *I–V* characteristics of these devices were measured at room temperature. Experimental forward bias *I–V* characteristics of Al/Co-PVC/p-Si SBD analyzed in detailed based on the thermionic emission theory. It is found that experimental result match up with only narrow linear region in forward bias *I–V* characteristics of Al/Co-PVC/p-Si SBD. The deviation of theory is attributed to series resistance and interface stat density between co-PVC interface and semiconductor.

5. ACKNOWLEDGEMENTS

This work was supported financially by Scientific Research Unit of Gazi University [grant number 04/2016-5]

REFERENCES

[1] Card H. C. and Rhoderick E. H., J., Phys. D. Appl. Phys. (1971), 4, 1589-1595.
[2] Singh A., Reinhardt K. C. and Anderson W. A., J. Appl.Phys. (1990), 68, 3475-3482.
[3] Türüt A., Sağlam M., Efeoğlu E., Yalçın N., Yıldırım M., and Abay B., Physica B. (1995), 205, 41-48.
[4] Yakuphanoğlu F., J. Alloys Compounds. (2010), 494, 45-455.
[5] Gökçen M., Tunç T., Altındal Ş., and Uslu İ., Mater. Sci. Eng. B. (2012), 177, 416–420.
[6] Kaya A., Vural Ö., Tecimer H., Demirezen S. and Altındal Ş, Current Appl. Phys. (2014), 14, 322-330.
[7] Yücedağ İ., Ersöz G., Gümüş A. and Altındal Ş., Int. J. Mod. Phys. B (2015), 29, 1550075.
[8] Yücedağ İ., Kaya A., Altındal Ş. and Uslu İ., Chin. Phys. B. (2014), 23, 047304.
[9] Orak İ., Koçyiğit A. And Türüt A., Journal of Alloy Comp. (2017), 691, 8733-879.
[10] Cheung S. K. and Cheung N. W., Appl. Phys. Lett. (1986), 49, 85-89.

The first principle study of mechanical properties of Rh_3Sc compound

Osman Örnek[1], Mustafa Özduran[2] and Nihat Arıkan[3]

[1]*Department of Metallurgy and Material Engineering, Engineering and Architecture Faculty, Ahi Evran University, 40100- Kırşehir/TURKEY*
[2]*Physics department, Science and Art Faculty, Ahi Evran University 40100-Kırşehir/TURKEY*
[3] *Science education department, Education Faculty, 40100-Kırşehir/TURKEY*

Abstract

The structural, electronic, mechanical and dynamic properties of Rh_3Sc compound in the $L1_2$ phase have been investigated. The calculated lattice constants, bulk modulus and elastic constants for this compound are in good agreement with the available theoretical and experimental data. The brittleness and ductility properties of Rh_3Sc are determined by Poisson's ratios criterion and Pugh's criterion.

Keyword: DFT, ab inito, band structure

1. INTRODUCTION

Rhodium plays an important role as three way catalyst [1].The Rh3Sc compound of L12 phase is widely used in structural applications where ceramics are now contemplated for use. Recently, several groups have studied the structural, mechanical, elastic, electronic, and phase transition of Rh3Sccompound, employing different experimental and theoretical methods [2–4]. The electronic structure of the Rhodium based intermetallic Rh3Sc compound has been studied using the Self Consistent Tight Binding Linear Muffin Tin Orbital (TB-LMTO) method by Sundareswari and Rajagopalan [2]. Popoola and Oluyamo [3] have investigated the physical properties of Rh3Sc compound that this compound evaluates within the quantum mechanical density functional theory framework. Munieswaran et al. [4] have investigated the electronic structure of Rh4 and Rh3X (X= Scand V) by using density functional theory (DFT). The current work focuses on the theoretical study of the structural and electronic properties of Rh3Sc in the $L1_2$ phase, with particular emphasis on phonon properties, by employing the DFT. The phonon properties are necessary for a microscopic understanding of the lattice dynamics. The knowledge of the phonon spectrum plays a significant role in determining various material properties such as phase transition, thermodynamic stability, transport and thermal properties. The band structure has been obtained by applying the plane-wave pseudopotential method within the Generalized Gradient Approximation (GGA). These results are then used, within a linear-response approach, to calculate the phonon dispersion curves and the density of states.

2. METHOD OF CALCULATION

We have employed a plane-wave pseudopotential method in the framework of the density functional theory with the Generalized GradientApproximation (GGA) using the Perdew-Burke-Ernzerhof (PBE) [5] parameterization for the exchange-correlation potential. The electron–ion interaction was described by ultrasoft pseudopotential [6]. The wave functions were expanded in a plane-wave basis set with a kinetic energy cut-off of 40 Ry. The electronic charge density was evaluated up to the kinetic energy cut-off 400 Ry. Brillouin-zone integrations were performed using a 10x10x10 **k**-points mesh. Integration up to the Fermi surface was performed using the smearing technique [7] with smearing parameter r = 0.02 Ry. Having obtained self-consistent solutions of Kohn–Sham equations, the lattice-dynamical properties were calculated within the framework of the self-consistent density functional perturbation theory [8,9]. All calculations have been made by using the Quantum-ESPRESOO code [10].

3. RESULTS AND DISCUSSION

The considered binary intermetallic Rh_3Sc compound was examined herein in the $L1_2$ phase. In the $L1_2$ phase, Rh_3Sc compound is isostructural with Cu_3Au and crystallize in a cubic structure with the space group P*m*3*m* (No 221 inthe X-Ray Tables). The crystalline structure of Rh_3Sc can be seen as four interpenetrating simple cubic sub-lattices, three occupied by Rh atoms and one by Sc atoms. The atoms are positioned at the following Wyckoff positions: Rh: 3*c* (0, 1/2, 1/2) and Sc: 1*a* (0, 0, 0).The theoretical lattice constants and bulk modulus in this section are obtained through fitting the total energy data with the Murnaghan equation of state [11]. The calculated structural properties (lattice constant a, bulk modulus, and the pressure derivative of the bulk modulus, dB/dP) of AgMg and AgZn are summarized in Table 1.Our results have been compared with the available theoretical and experimental results in this table. The calculated lattice parameters reasonably concur with earlier experimental and theoretical values for this material.

Table 1. Calculated lattice constant a (in Å), bulk modulus B (in GPa) and elastic constants Cij (GPa) for Rh_3Sc compound, compared with the available experimental and theoretical data.

Material	Ref.	*a*	*B*	*B′*	C_{11}	C_{12}	C_{44}
Rh_3Sc	This work	3.945	188.63	3.41	377.25	94.31	565.915
	FP- LAPW[2]	3.862	233.1				
	Exp. [2]	3.899					

For cubic crystals, the mechanical stability requires the elastic constants to satisfy the well-known Born stability criteria [12]:

$C_{44}> 0$; $C_{11}-C_{12}> 0$, $C_{11}+C_{12}> 0$ and $B > 0$:

We have used the formulas and procedures for the calculation of elastic constants and bulk modulus in a previous publication [13]. Our calculated elastic constants are suitable values according to Born stability criteria. The experimental values of the elastic constants of this material are not available in the literature. Thus, further experimental studies are needed to compare with these calculated results for Rh_3Sc.

The electronic band structures of the Rh_3Sc compound are shown in Fig. 1 along the highsymmetry directions in the first Brillouin zone.According to Fig. 1, there is no band gap at the Fermi level. Valance and conduction bands overlap significantly at the Fermi level. Consequently, Rh3Sc exhibits a metalliccharacter.

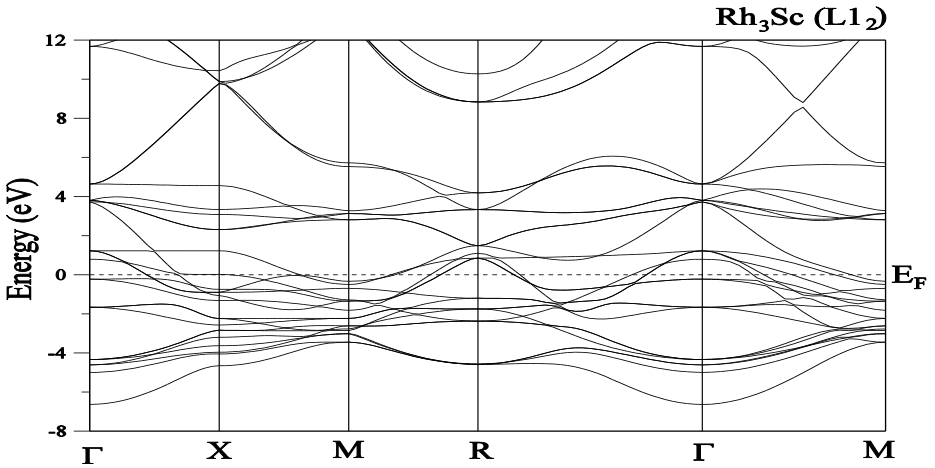

Fig. 1. The electronic band structures of Rh_3Sc compounds in $L1_2$ phase.

The character of the band states for these alloys has been identified by calculating their total and partial densities of the states (DOS) (in Fig. 2). The predominant contributions to the density of states at the Fermi level comes from the Rh-4dand Sc- 3dstates for this material.

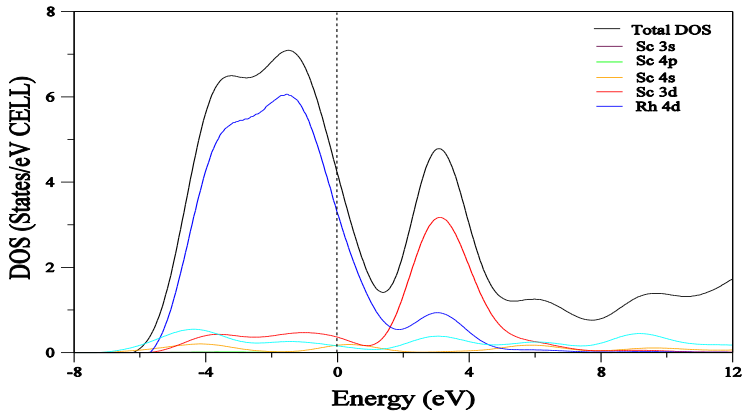

Fig. 2. The total and partial density of states (DOS) of Rh_3Sc compounds in $L1_2$ phase.

4. CONCLUSION

In this study, the structural, electronic, elastic, vibration properties of Rh_3Sc in $L1_2$ phase have been calculated, using the ab initio pseudopotential method, within the GGA of the density functional theory. For Rh_3Sc, the lattice parameters compared well with the experiments. The electronic band structures were calculated for this material, in the $L1_2$ phase.

REFERENCES

[1] Satterfield, C.N.,HeterogeneousCatalysis in IndustrialPractice, 2nd ed. Krieger, Malabar, 1996.
[2] M. Sundareswariand M. Rajagopalan, Eur. Phys. J. B. 49, 67-75 (2006)
[3] A. I. Popoolaand S. S. Oluyamo, Journal of ScienceandTechnology 43, 47-54 (2014)
[4] P. Munieswaran, S. Seenithurai, R. K. Pandyan, S. V. Kumar. M. Mahendran, International Journal of ChemTechResearch 17, 1223-1229 (2014-2015).
[5] P. Perdew, K. Burke, and M. Ernzerhof, Phys. Rev. Lett. 77, 3865 (1996).
[6] D. Vanderbilt, Phys. Rev. B 41, 7892 (1990).
[7] M. Methfesseland A.T. Paxton, Phys. Rev. B 40, 3616 (1989).
[8] S. Baroni, P. Giannozzi, and A. Testa, Phys. Rev. Lett. 58, 1861 (1987).
[9] S. Baroni, S. de Gironcoli, A. Dal Corso, and P. Giannozzi, Rev. Mod. Phys. 73, 515 (2000).
[10] S. Baroni, A. dal Corso, S. de Gironcoli, P. Giannozzi, C. Cavazzoni, G. Ballabio, S. Scandolo, G. Chiarotti, P. Focher, A. Pasquarello, K. Laasonen, A. Trave, R. Car, N. Marzari, A. Kokalj, <http://www.quantum-espresso.org>.
[11] F.D. Murnaghan, Proc. Natl. Acad. Sci. USA 50 (1944) 697.
[12] M. Born, K. Huang, DynamicalTheory of CrystalLattices, Clarendon, Oxford,1954.
[13] S. Uğur, N. Arikan, F. Soyalp, G. Uğur, Comput. Mater. Sci. 48 (2010) 866.

Interpreting Out-of-Control Signals in Multivariate Processes Using Artificial Neural Network

Özkan Sarıkaya[a*] and M. Akif Bakır[b]

[a]*Department of Nursing, College of Health, Ahi Evran University, Kırşehir, Turkey*
[b]*Department of Statistics, Faculty of Science, Gazi University, Ankara, Turkey*

**e-mail corresponding author*: *ozkansrky@gmail.com*

Keywords: Multivariate Process, Artificial Neural Network, Out-of Control Signal, Mean shift

ABSTRACT

Modern data equipment used during production process, it is common to monitor or control several correlated quality characteristics simultaneously in multivariate process. Multivariate control charts are important tools for monitoring multivariate processes. One difficulty encountered with multivariate control charts is the identification of the variable or group of variables that cause an out-of-control signal. Identifying the variable(s) responsible for the mean shifts has become an important research issue in multivariate process control, inducing researchers to continue developing effective methods to interpret the out-of-control signal. There are many approaches to solve the problem, from graphical methods to more analytic approaches in literatures. In this study we suggested an artificial neural network model that can identify the variable(s) that cause an out-of-control signal. The correct identification ratios are calculated using both traditional methods and suggested artificial neural network model with various factors. We showed that the results obtained using the proposed artificial neural network model are in general greater correct identification ratios than those obtained using the traditional methods. Suggested artificial neural network model can provides effective solution for this problem.
.

1. INTRODUCTION

In modern production process, it is prevalent to simultaneous control or monitor more than one quality variables, which are generally correlated with each other. Independently monitoring of these quality variables may be specious. Monitoring and control of these processes is named as multivariate statistical process control. The multivariate control charts are the most important assets of the multivariate process control. [1]. Multivariate process control techniques were firstly demonstrated by Hotelling. He acquainted the problem of correlation between the quality variables of a process and devised the admitted T^2 statistic to determine whether the entire process is out of control. However, the greatest disadvantage of the multivariate control charts like Hotelling T^2 control chart is not providing information on the variable(s) that cause the out of control signal, even though they are able to determine the out of control situation in the process.

There are many approaches to solve this problem in literatures. The operations of graphical approaches are tedious and cumbersome. Nonetheless, the primary problem is that a graphical approach requires the expert interpretation [2].

Bersimis et al. [1] and Das and Prakash [3] take a comparison among traditional analytical methods for interpreting the out of control signal and conclude that each of the methods has its advantages and disadvantages. The most commonly utilized method for determining which variable(s) caused the out of control signal, in the process average vector control, is the Mason-Tracy-Young (MTY) Decomposition Method [4]. Moreover many researches, such as [5]-[6], use MTY method as a benchmark for their comparisons. So that special interest to the MTY method consists of decomposing the T^2 value into

independent components, each of which reflects the contribution of an individual variable. The drawback of this method is the extensive computation and its sensitivity to the number of variables.

Recently many scholars have examined the application of artificial neural network to multivariate statistical process control [7], [8], [5], [9]. Special interest in Aparisi et. al [5] show that the percentage of correct classifications of the MTY method is generally worse in comparison with the suggested artificial neural network (ANN) approach. ANN is a heuristic method and their proposed ANN is applied when the T^2 control chart detect an out-of-control situation to identify which variables have shifted.

Statistical learning methods, such as ANN, whose characteristics consist in that they include two phrases: First, training phrase, in which a classifier is learned from the training set; second, testing phrase, in which an instance is recognized using the classifier learned in the first phrase. The use of ANN in multivariate statistical process control is a recent development with the papers of Noorossana et al [10], Hwarng [11] Chen and Wang [8], Niaki and Abbasi [12], Aparisi et al [5] among others. Atashgar [13] takes an in-depth comparison among ANN approaches.

Our first aim is to develop an ANN that has higher correct classification percentage than MTY method. The proposed ANN is applied not only when the T^2 chart displays an out-of-control signal to identify the source of it but also classifies the observations into in-control situation and out-of-control situaition simultaneously. The proposed ANNs were designed which calculated correct classification percentage which depends on the factors of: sub-sample size, the magnitude of the shift, the number of variables and correlation between variables.

In this paper, two ANNs have been designed for determine the source of the out-of-control signals when two and three variables are monitored simultaneously (p = 2 and 3). These ANNs will detect the out-of-control situation and will classify the variables in the groups “no shift”/ “which variables responsible for the shift”. In the idea mentioned above, ANN is not only a substitute for Hotelling T^2 control chart, but also a tool for determination of the source of out-of-control signal.

Here we explained the procedure followed to simulate the cases employed to train the ANNs. We used a scaled conjugate gradient backpropagation training algorithm. There is no an exact procedure to choose the optimum number of hidden layers and neurons of these layers to design a neural network for optimize the solution. Several network configurations were tested in order to achieve the maximum correct classification percentage. The best results were obtained with the architecture 2-3-4 for the two variable cases. The configuration is a three-layer (one input-one hidden-one output) network in which all the neurons located between the layers are connected to one another. The input layer of the model requires a gaussian activation function and other layers use a sigmoid function. The input data for the network consist of raw sample means. The output consists of four neurons and an output of one for the first neuron indicates no-shift. An output of one for the second neuron indicates a shift in the first variable, an output of one for the third neuron indicates a shift in the second and an output of one for the third neuron indicates a shift in both variables.

For the three-variable case, designed NN model have a three-layer network (3-7-8), with three nodes in the input layer, seven nodes in the hidden layer, and eight nodes in the output layer. The input data for the network consist of raw sample means. An output of one for the first neuron indicates no-shift. An output of one for the second neuron indicates a shift in the first variable, an output of one for the third neuron indicates a shift in the second variable and an output of one for the fourth neuron indicates a shift in third variable. An output of one for the fifth neuron indicates a shift in both first and second variables, an output of one for the sixth neuron indicates a shift in both first and third variables and an output of one for the seventh neuron indicates a shift in both second and third variables. An output of one for the eighth neuron indicates a shift in both three variables.

Design of the training cases is a major factor of the performance of a backpropagation neural network. The procedure followed to obtain the cases to train the neural network consists of the simulation of a productive process. For example, let us follow the case were two variables are monitored. An ANN is simulated, i.e., generated 200 values for each random sample from a bivariate normal distribution and the means of the variables are set to 20 and the standard deviation is set to 2. At the same time, a sample size, a correlation coefficient and a magnitude of the shift have to be specified in the simulation. For case of 1σ shift, for

generating training data sets, we shift the mean vector as $(\mu_1 + 1\sigma_{11}, \mu_2)$, $(\mu_1, \mu_2 + 1\sigma_{22},)$ and $(\mu_1 + 1\sigma_{11}, \mu_2 + 1\sigma_{22},)$ in bivariate process. Simulation runs were repeated a hundred times for each situations.

The following cases were allowed for in order to achieve a complete set of possible shifts:
• Sample size, *m*: 1, 3, 5, 7 and 200 values each sample.
• Relationship Level, (Correlation coefficient) ρ: 0.1(Low), 0.5(Medium), and 0.9(High).
• Magnitude of the shift from the mean: 1σ, 1.5σ, 2σ, 2.5σ and 3σ.

The performance of the ANNs, have been compared regarding the factors of: the number of variables, *p*, relationship level, *low-medium-high*, the sample size, *m*, and the magnitude of shift, *1σ, 1.5σ, 2σ, 2.5σ* and *3σ.* For analysis the ANN effectiveness in terms of the percentage of success in the classification of the variables that have actually shifted in the process, all results have been recalculated under same conditions using MTY method which procedure has been widely referenced in literature.

2. RESULTS AND DISCUSSION

We discussed the correct classification percentages obtained using both the artificial neural network approach and the MTY method when all of the factors are considered i.e., Relationship level, sample size, magnitude of shift and number of variables.

It is clear that the ANN approach had higher correct classification percentage than MTY method in almost all situations. The ANN approach clearly outperforms the MTY method especially for small sample sizes and small magnitude of shifts. On the other hand, the use of larger sample size (m=5, 7) and larger magnitude of shift (2.5σ, 3σ) both methods shown similar performance. When relationship level increased, correct classification percentage have increased for both methods.

For the case of three variables ($P = 3$), the same procedure for two variables has been followed, and similar results were observed. For example, with the sample size of m = 1, when small magnitude of shifts occurred (1σ, 1.5σ), the percentages of MTY method are 6.14% and 10.43% , and ANN approach are 58.12% and 67.53%, respectively. The ANN approach clearly outperforms the MTY method especially for small sample sizes and small magnitude of shifts for this case. Increasing the relationship level performance of both methods had also increased. For experiment ANN approach with sample size of m=5, 2σ shift, the percentages for low, medium and high relationship level, respectively, 77.14%, 81.53% and 82.11%. For MTY method, percentages resulted in 33.46, 34.28 and 34.67%.

The ANN approach clearly outperforms the MTY method especially for small magnitude of shifts. For MTY method, as the number of variables increases, the correct classification percentage decreases very quickly as the result of [2]. But ANN approach showed a good performance for all cases.

3. CONCLUSION

Identifying the source of the out of control signal which responsible for the mean shift has become an considerable research area in multivariate process control and encouraging to continue developing effective methods for solve given problem. For traditional multivariate control charts, such as Hotelling T^2 charts, the design of the control limits is commonly based on the assumption that the quality characteristics follow a multivariate normal distribution. Importantly, ANNs do not require any a priori assumptions about the problem space, not even information about statistical distribution. On the other hand, MTY method require more extensive computations and elaborate decompositions, especially when the number of variables increases whereas ANNs require less computational effort for this case. In this research, we have designed ANN models for identifying the source of out-of-control signal which responsible for the mean shift in multivariate processes. A comparison of the MTY method and ANN approach, based on the correct classification percentages in terms of factors, shows that generally the ANN outperforms the MTY method especially small sample size and small magnitude of shifts. Moreover, ANN may be a substitute for Hotelling T^2 control chart.

REFERENCES

[1] Bersimis, S., Psarakis, S. and Panaretos, J. *Multivariate statistical process control charts: an overview*, Quality and Reliability Engineering International, (2007), 23 (5), 517-543.
[2] Aparisi, F. and José, S. *Interpreting the Out-of-Control Signals of Multivariate Control Charts Employing Neural Networks*, International Journal of Computer, Electrical, Automation, Control and Information Engineering, (2010), 4 (1), 24-28.
[3] Das, N. and Prakash, V. *Interpreting the out-of-control signal in multivariate control chart-a comparative study*, International Journal of Advanced Manufacturing Technology, (2008), 37 (9), 966-979.
[4] Mason, R. L., Tracy, N.D. and Young, J.C. *Decomposition of T^2 multivariate control chart interpretation*, Journal of Quality Technology, (1995), 27 (2), 99-108.
[5] Aparisi, F., Avendaño, G. and Sanz, J. *Interpreting T^2 Control Chart Signals: Effectiveness of MTY decomposition vs. a Neural Network*, IIE Transactions, (2006), 38 (8), 647-657.
[6] Cheng, H. P. and Cheng, C. S. *Denoising and feature extraction for control chart pattern recognition in auto-correlated processes*, International Journal Signal and Imaging Systems Engineering, (2008), 1 (2), 115–126.
[7] Wang, T. Y. and Chen, L. H. *Mean shifts detection and classification in multivariate process: A neural-fuzzy approach*, Journal of Intelligent Manufacturing, (2002), 13 (3), 211–221.
[8] Chen, L. H. and Wang, T. Y. *Artificial neural networks to classify mean shifts from multivariate T^2 chart signals*, Computers and Industrial Engineering, (2004), 47 (2–3), 195–205.
[9] El-Midany, T. T., El-Baz, M. A. and Abd-Elwahed, M. S. *A proposed framework for control chart pattern recognition in multivariate process using artificial neural Networks*, Expert Systems with Applications, (2010), 37 (2), 1035–1042.
[10] Noorossana, R., Farrokhi, M. and Saghaei, A. *Using neural networks to detect and classify out-of-control signals in auto correlated processes,* Quality and Reliability Engineering International, (2003), 19 (6), 493–504.
[11] Hwarng, H. B. *Detecting process mean shift in the presence of autocorrelation: A neural-network based monitoring scheme*, International Journal of Production Research, (2004), 42 (3), 573–595.
[12] Niaki, S. T. A. And Abbasi, B. *Fault diagnosis in multivariate control charts using artificial neural Networks*, Quality and Reliability Engineering International, (2005), 21 (8), 825–840.
[13] Atashgar, K. *Monitoring Multivariate Environments Using Artificial Neural Network Approach: An Overview*, Scientia Iranica, (2015), 22 (6), 2527–2547.

Diagnosing the Source of Variance Shifts in Multivariate Processes: An Artificial Neural Network Approach

Özkan Sarıkaya[a*] and M. Akif Bakır[b]

[a]*Department of Nursing, College of Health, Ahi Evran University, Kırşehir, Turkey*
[b]*Department of Statistics, Faculty of Science, Gazi University, Ankara, Turkey*

**e-mail corresponding author*: *ozkansrky@gmail.com*

Keywords: Multivariate Process, Artificial Neural Network, Out-of Control Signal, Variance shift

ABSTRACT

Statistical process control charts are important tools for monitoring process stability in various manufacturing industries. Most of the research in statistical process control has been focused on monitoring the process mean. However, it is also important to detect variance changes as well. Out-of-control signals in multivariate control charts may be caused by one or more variables, or a set of variables. In multivariate process control, the main problem of multivariate control charts is that they can detect an out of control event but do not directly determine which variable or group of variables has caused the out of control signal. So, we need to detect the process changes rapidly and accurately diagnose the source of those changes. This study approaches the diagnosis of out-of-control signals as a classification problem and proposes an artificial neural network model focused on variance shifts in multivariate processes. The correct detection percentages are calculated using both the traditional generalized variance chart and proposed artificial neural network model with various factors. Moreover, the correct classification percentages of the source of the variance shift are calculated using proposed artificial neural network model. Simulation results demonstrate the effectiveness of the proposed artificial neural network model in identifying the source of variance shift. The proposed method may facilitate the diagnosis of the out-of-control signal.
.

1. INTRODUCTION

In modern production process, it is prevalent to simultaneous control or monitor more than one quality variables, which are generally correlated with each other. Independently monitoring of these quality variables may be specious. Monitoring and control of these processes is named as multivariate statistical process control. The multivariate control charts are the most important assets of the multivariate process control. [1]. Multivariate process control techniques were firstly demonstrated by Hotelling. He acquainted the problem of correlation between the quality variables of a process and devised the admitted T^2 statistic to determine whether the entire process is out of control. However, the greatest disadvantage of the multivariate control charts is not providing information on the variable(s) that cause the out of control signal, even though they are able to determine the out of control situation in the process.

Most of researches in Multivariate Statistical Process Control have been focused on controlling of means but it is also desirable to monitoring process variability as well. In the multivariate process, variability is summarized by the *p x p covariance matrix* Σ, where *p* represents the number of process variables. The main diagonal elements of this matrix are the variances of the individual process variables, and the off-diagonal elements are the covariances. Alt [2] presented a useful method based on sample generalized variance, denoted by |S|. This statistic, which is the determinant of the sample covariance matrix, is a widely used measure of multivariate dispersion.

The probability distribution parameters for this statistic are as follows;

Mean of $|S|$,

$$E(|S|) = b_1|\sum| \tag{1.1}$$

Variance of $|S|$,

$$V(|S|) = b_2|\sum|^2. \tag{1.2}$$

The coefficients b_1 and b_2 in these equations are computed as,

$$b_1 = \frac{1}{(n-1)^2}\prod_{j=1}^{p}(n-j) \tag{1.3}$$

$$b_1 = \frac{1}{(n-1)^{2p}}\prod_{j=1}^{p}(n-j)\left[\prod_{j=1}^{p}(n-j+2) - \prod_{j=1}^{p}(n-j)\right] \tag{1.4}$$

.

Therefore, the parameters of the control chart for | **S** | would be

$$\begin{aligned} UCL &= E(|S|) + 3\sqrt{V(|S|)} \\ CL &= E(|S|) \\ LCL &= E(|S|) - 3\sqrt{V(|S|)}, \end{aligned} \tag{1.5}$$

Equations (1.1) and (1.2) are written in equation (1.5), then the parameters of the control chart for | **S** | would be

$$\begin{aligned} UCL &= b_1 + 3\sqrt{b_2|\sum|^2} \\ &= |\sum|\left(b_1 + 3\sqrt{b_2}\right) \\ CL &= b_1|\sum| \\ LCL &= b_1|\sum| - 3\sqrt{b_2|\sum|^2} \\ &= |\sum|\left(b_1 - 3\sqrt{b_2}\right). \end{aligned} \tag{1.6}$$

The lower control limit is replaced with zero if the calculated value is less than zero. Usually Σ will be estimated by a sample covariance matrix S, based on the analysis of preliminary samples. In this case, we should replace | Σ | by |S|/b1 [3].

Many researchers used artificial neural networks (ANNs) to control of process variability for the multivariate processes more effectively than the traditional methods and they purpose to diagnose of the variance shifts [4], [5], [6], [7]. However, there's not sufficient study in the control of the process variability for determining the variable(s) that cause out of control signal. In this study, in control of process variability for the multivariate processes; artificial neural network models, that are able to determine the out of control situation and the variable(s) which cause out of control signal, have been designed. Statistical learning methods, such as ANN, whose characteristics consist in that they include two phrases: First, training phrase, in which a classifier is learned from the training set; second, testing phrase, in which an instance is recognized using the classifier learned in the first phrase. The proposed ANNs were designed which calculated correct determination ratios which depends on the factors of: the sub-sample size, the magnitude of shift, the number of variables and type of shift.

In this study, two ANNs have been designed for diagnose the source of the variance shift when two and three variables are monitored simultaneously (p = 2 and 3). ANN will be responsible of detecting the out-of-control state and will classify the variables in the groups "no shift"/ "which variables responsible for the

shift". In the idea mentioned above, ANN is not only a substitute for sample generalized variance matrix $|S|$ control chart, but also a tool for diagnosing the source of variance shift.

In this section it is explained the procedure followed to simulate the cases employed to train the ANNs. We used a scaled conjugate gradient backpropagation training algorithm. There is no an exact procedure to choose the optimum number of hidden layers and neurons of these layers to design a neural network for optimize the solution. Several network configurations were tested in order to achieve the maximum correct determination ratios. The best results were obtained with the architecture 5-23-4 for the two variable cases. The configuration is a three-layer (one input-one hidden-one output) network in which all the neurons located between the layers are connected to one another. The first layer of the system requires a gaussian activation function and other layers use a sigmoid function. The input data for the network consist of raw sample means, variances and correlation among variables. The output consists of four neurons and an output of one for the first neuron indicates no-shift. An output of one for the second neuron indicates a shift in the first variable, an output of one for the third neuron indicates a shift in the second and an output of one for the third neuron indicates a shift in both variables. The type of neural network used for the three-variable case is a three-layer network (6-19-4), with six nodes in the input layer, nineteen nodes in the hidden layer, and four nodes in the output layer. The input data for the network consist of raw sample means and variances.

The performance of the ANNs, have been compared regarding the factors of: the number of variables, p, type of variance-shift, *only one variable-both two variable-both three variable*, the sub-sample size, m, and the magnitude of variance-shift, 1σ, $1{,}5\sigma$, 2σ, $2{,}5\sigma$ and 3σ. For analysis the ANN effectiveness in terms of the ratio of success in the determination of the variables that have actually shifted in the process, all results have been recalculated under same conditions using sample generalized variance matrix $|S|$ control chart which procedure has been widely referenced in literature.

2. RESULTS AND DISCUSSION

It is clear that the ANN approach had higher correct determination ratio than sample generalized variance matrix $|S|$ method in most situations. The ANN approach clearly outperforms the sample generalized variance matrix $|S|$ method especially for small sample sizes, small magnitude of shifts and only one variable shifted. On the other hand, the use of larger sample size (m=7 and 10), larger magnitude of shift ($2{,}5\sigma$, 3σ) and both two and three variables shifted situations, both methods shown similar performance. For the case of three variables ($P = 3$), the same procedure for two variables has been followed, and similar results were observed.

Moreover designed ANN models not only determination of variance shift but also can diagnose the source of variance shift. For example, with the sample size of m = 7, when small magnitude of shifts occurred ($1{,}5\sigma$) and only one variable shifted, correct determination of variance shift was %79,47 and the correct classification ratio of the source of variance shift was %61,25. Same conditions with both two variables shifted, correct determination of variance shift was %90,43 and the correct classification ratio of the source of variance shift was %55,25.

3. CONCLUSION

Diagnosing the source of the out of control signal which responsible for the variance shift has become an considerable research area in multivariate process control and encouraging researchers to continue developing effective methods for solve given problem. For traditional control charts, such as using sample generalized variance matrix $|S|$ control chart, the design of the control limits is commonly based on the assumption that the quality characteristics follow a multivariate normal distribution. Importantly, ANNs do not require any a priori assumptions about the problem space, not even information about statistical distribution. On the other hand, traditional control charts can determine the out of control situation in the multivariate process but not providing information on the variable(s) that cause the out of control signal.

Designed ANN models not only determine the out of control situation but also diagnose the source of out of control signals with high correct determination ratios.

REFERENCES

[1] Bersimis, S., Psarakis, S. and Panaretos, J. *Multivariate statistical process control charts: an overview*, Quality and Reliability Engineering International, (2007), 23 (5), 517-543.
[2] Alt, F. B., *Multivariate quality control*. In S. Kotz, N. L. Johnson, & C. R. Read (Eds.), The encyclopedia of statistical sciences, New York: Wiley, (1985), 110–122.
[3] D. C. Montgomery, *Introduction to Statistical Quality Control*, 6thed. New York, NY.; John Wiley Sons, (2009), 516-518.
[4] Salehi M, Kazemzadeh R. B., Salmasnia A.,*On line detection of mean and variance shift using neural networks and support vector machine in multivariate processes*, Applied Soft Computing, (2012), 12, 2973–2984.
[5] C. Low, C.M. Hsu, F.J. Yu, *Analysis of variations in a multi-variate process using neural networks*, International Journal of Advanced Manufacturing Technology, (2003), 22, 911–921.
[6] F. Zorriassatine, J.D.T. Tannock, C.O. Brien, *Using novelty detection to identify abnormalities caused by mean shifts in bivariate processes*, Computers and Industrial Engineering, (2003), 44, 385–408.
[7] C.-S. Cheng, H.-P. Cheng, *identifying the source of variance shifts in the multivariate process using neural networks and support vector machines*, Expert Systems with Applications, (2008), 35, 198–206.

Mathematical analysis of controlled slow release of poly-Ɛ-caprolactone microspheres encapsulated with doxycycline hyclate

Özlem Aydın

Department of Food Engineering, Faculty of Architecture and Engineering, Ahi Evran University, TR-40100 Kırşehir, Turkey

**ozlem.aydin@ahievran.edu.tr*

Keywords: mathematical analysis, slow release, poly-Ɛ-caprolactone, doxycycline hyclate

ABSTRACT

Microencapsulation is used to prolong a drug release and also reduce the adverse effects of drugs. For slow release formulations, many studies were based on biodegradable polymers such as poly(lactide) or poly(lactide-co-glycolide). Poly-Ɛ-caprolactone (PCL) is a very well-known synthetic, hydrophobic polyester for slow release formulations because it's degradation rate is slower than poly(lactide-co-glycolide). Doxycycline hyclate (DH) is reported to inhibit the activity of matrixmetalloproteinases (MMPs) in skin, synovial, cartilage, and corneal collagenase, neutrophil collagenase and gelatinase. It is a wide spectrum antibiotic for gram positive and negative bacteria, protozoa and anaerobs. PCL microspheres were prepared by the method of single emulsion-solvent evaporation technique. Briefly, PCL was dissolved in chloroform and DH was added into PCL solution. This phase was added drop-wise into surfactant and homogenized with ultraturrax (IKA). Then chloroform was removed by rotary evaporator. In vitro release profile of DH from PCL microspheres were determined by incubating the microspheres at 37°C in water bath. Release profile was compared with Fick's 2nd Law and modeled.

1. INTRODUCTION

Controlled release aims to supply bioactive agents within biocompatible carriers to the living system either by controlling the site and/or controlling the rate of drug released. Control on the application site can be achieved by drug targeting (passive or active) to the damaged region of the body. Microencapsulation is used to prolong a drug release and also reduce the adverse effects of drugs[1].

Tetracycline and its analogs have collagenase enzyme activity inhibition property as pointed out by many in vitro researches. Doxycycline hyclate (DH) is reported to inhibit the activity of matrix metalloproteinases (MMPs) in skin, synovial, cartilage, and corneal collagenase, neutrophil collagenase and gelatinase[2]. It is a wide spectrum antibiotic for gram positive and negative bacteria, protozoa and anaerobs. For slow release formulations, many studies were based on biodegradable polymers such as poly(lactide) or poly(lactide-co-glycolide). Poly-Ɛ-caprolactone (PCL) is a very well-known synthetic, hydrophobic polyester for slow release formulations because it's degradation rate is slower than poly(lactide-co-glycolide)[1].

PCL microspheres were prepared by the method of single emulsion-solvent evaporation technique. Firstly, PCL was dissolved in chloroform and doxycycline hyclate was added into PCL solution. This phase was added drop-wise into surfactant and homogenized with ultraturrax (IKA). Then chloroform was removed by rotary evaporator. In vitro release profile of DH from PCL microspheres were determined by incubating the microspheres at 37°C in water bath. To determine the morphology i.e. shape, size and diameter of microspheres scanning electron microscopy photography and particle size measurements were performed. The drug loading and encapsulation efficiency were calculated. Release profile was compared with Fick's 2nd Law and modeled. Diffusion Equation used in modelling is given in Equation 1[3]:

$$\frac{c_1}{c_{1\infty}} = 1 - \frac{6}{\pi^2}\sum_{n=1}^{\infty}\frac{1}{n^2}e^{-\frac{n^2\pi^2}{R^2}Dt} \qquad \text{(Eq. 1.)}$$

2. RESULTS AND DISCUSSION

According to SEM and particle size measurements, the microspheres were seen as spherically shaped. The diameter of the microspheres were measured as 46 μm. In vitro release percent of doxycycline loaded PCL microspheres were determined by using UV-VIS spectrophotometer. After 100 days 48 % of drug was released. In Figure 1, the release profile of the microspheres were seen. The drug loading and encapsulation efficiencies were 8.3 % and 25 %, respectively.

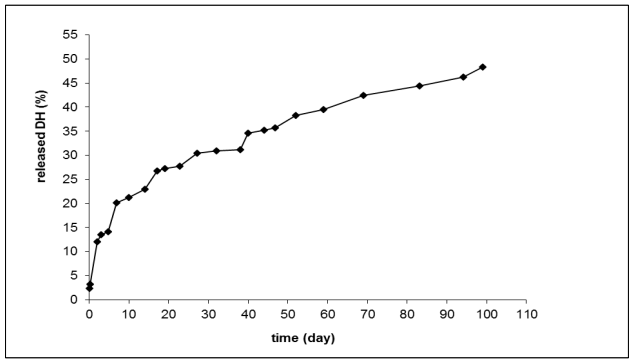

Figure 1. In vitro release percent of doxycycline from PCL microspheres after 100 days.

Diffusion equation (Eq. 1.) was used in mathematical analysis of release curve. In that reason, diffusion coefficient of the doxycycline loaded PCL microspheres were calculated by using following equation[3]:

$$C_1/C_\infty = 6.\sqrt{\left(D.t/\pi.R^2\right)} \qquad \text{(Eq. 2.)}$$

The diffusion coefficient was calculated as D= 4.0989x10^{-10} cm^2/s.

The calculated diffusion coefficient was used in Eq. 1 and the mathematical model graph was obtained (Figure 2). The in vitro release profile of doxycycline loaded PCL microspheres were compatible with diffusion model.

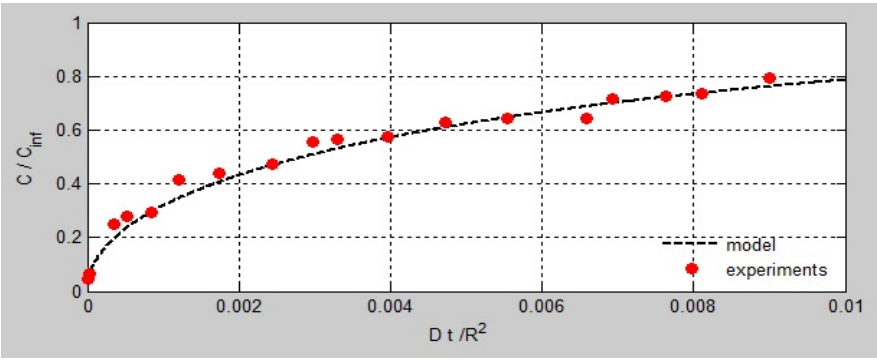

Figure 2. Mathematical analysis of release of doxycycline from PCL microspheres.

3. CONCLUSION

PCL microspheres showed Fickian diffusion and its release results were in good agreement with the diffusion model for the entire course of the experiments. PCL microspheres can be proposed as suitable for slow release doxycycline delivery systems. Yet, these outcomes should be investigated under in vivo conditions.

4. ACKNOWLEDGEMENTS

This work was supported by the Ahi Evran University Scientific Research Projects Coordination Unit. (Project Number: AEÜ- PYO-MÜH.4001.14.012).

REFERENCES

[1] J.P. Raval, D.R. Naik, K.A. Amin, P.S. Patel, Journal of Saudi Chemical S, **2014**, *18(5)*, 566-573.
[2] G.N. Smith, E.A. Mickler, K.A. Hasty, K.D. Brandt, Arth and Rheumatism, **1999**, *42(6),* 1140-1146.
[3] O. Aydin, B. Aydin, A. Tezcaner, D. Keskin, Journal of Applied Polymer Science, **2015**, *132*, 41768

Producing fibers containing dipyridine complexes via electrospinning for use in antibacterial textile industry

Ruken Esra Demirdöğen[a], Fatih Mehmet Emen[b], Zehra Gülten Altın[c]

aDepartment of Chemistry, Faculty of Science, Çankırı Karatekin University,TR-18100 Çankırı, Turkey
bDepartment of Chemistry, Faculty of Arts and Science, Mehmet Akif Ersoy University, TR-15100, Burdur, Turkey
cDepartment of Chemical Engineering, Faculty of Enginering, Çankırı Karatekin University, TR-18100 Çankırı, Turkey

**e-mail rukenesrademirdogen@yahoo.com*:

Keywords: dipyridine complexes, electrospinning, antibacterial textile.

ABSTRACT

Prevention of community origin infections made indiviuals become more aware of improtance of the goods and clothing they use in everyday life. For this purpose intense infection control programs have been launched . However, the incidence of diseases caused by bacteria has increased . For an effective struggle against these diseases new antibacterial agents and antibacterial textiles obtained by functionalization of textiles with these agents have gained importance regarding cost effectiveness and drug activity.
In this study antibacterial activity of the synthesized pyridine complexes, Ethyl Cellulose (EC) modified with pyridine metal complexes against bacteria such as E.coli were determined via modified disc-diffusion method (CLSI- M02-A11). Physical, chemical and mechanical characterization of the electrospun modified EC fibers were made. The average diameter of the electrospun fibers were determined by SEM images. Their structures were illucidated by FT-IR and XRD. The data regarding electrospun fibre bundles were obtained via CuKα between the 2 θ = 5o – 30o. Thermal properties of the electrospun fibers were determined via TG/TGA analysis. Antibacterial activities of the nanofiber were also determined via agar diffusion method as with the pure complexes.

1. INTRODUCTION

Medicinal inorganic chemistry is a developing research area that began in 1962 with the synthesis of cis-diamminedichloroplatinum (II), later known as cisplatin. Transition metal-containing inorganic compounds are also considered to be potential carcinogens and antimicrobial [1]. Pyridine is a heterocyclic organic compound with the chemical formula C5H5N.

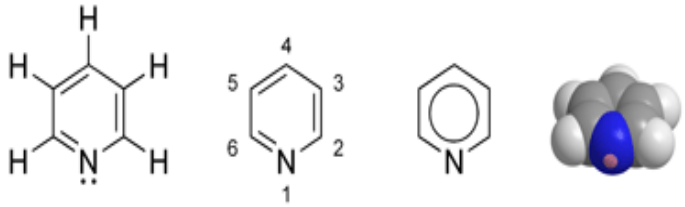

Figure 1. It is structurally related to benzene, with one CH group replaced by a nitrogen atom.

It is used as a precursor to agrochemicals and pharmaceuticals and is also an important solvent and reagent.1 Pyridine was first isolated and characterized by Anderson in 1846. The cyclic nature of pyridine was recognized by Korner and Dewar in 1869.2. It plays a key role catalyzing both biological and chemical systems. In many enzymes of living organisms it is the prosthetic pyridine nucleotide (NADP) that is involved in various oxidation–reduction processes. In the pharmaceutical industry, pyridine forms the

nucleus of over 7000 existing drugs. Pyridine ring system is very widely distributed in nature, especially in plants. Many important alkaloids atropine from Atropa belladonna, Deadly nightshade, contains saturated pyridine nucleus. A large number of compounds containing pyridine rings are associated with diverse pharmacological properties such as antimicrobial, anticancer, anticonvulsant, antiviral, anti-HlV, antifungal and antimycobacterial activities [2]. Metal halide complexes of pyridine derivatives such as 2-chloropyridine, 2-bromopyridine, 3-chloropyridine, 3-bromopyridine, 2-methoksipyridine, 2-(p-tolyl) pyridine, 2-methylpyridine, 3-methylpyridine, 3,4-dimethylpyridine, 4-benzoylpyridine, 3-hydroxypyridine, 4-ethylpyridine have been extensively studied [3,4].

2. RESULTS AND DISCUSSION

Synthesis of Complexes, Dichloro(3,4-dimethyl)dipyridinecopper(II) (CuCl2L12) and dichloro(3,5-dimethyl)dipyridinecopper(II) (CuCl2L22) synthesized via previously desribed method []. A solution of CuCl2 (0.025 mol) in ethyl alcohol (40 mL) was added dropwise to a stirred and heated (70°C) solution of 3,4-dimethylpyridine/3,5-dimethylpyridine (0.05 mol) in DMF(20 mL). The reaction mixture was refluxed for 2 h at a 70°C and then cooled to allow for the precipitation of the complex compound.

The complex that was obtained was filtered off, washed with ethyl alcohol and dried in a desiccator.

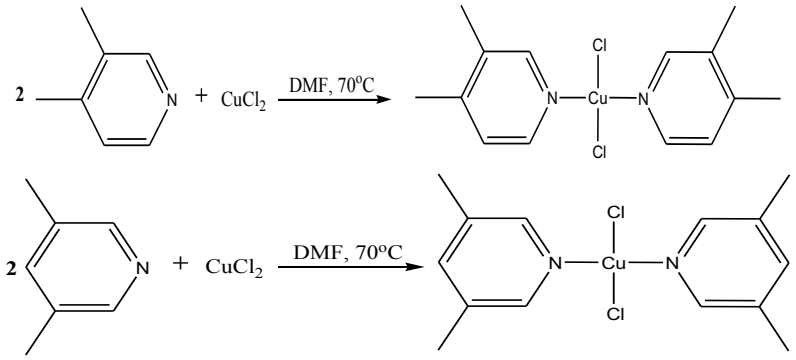

Figure 2. Pyridine synthesis reaction

2- Characterization of the phosphor, XRD, SEM, FTIR, DTA/TG, The crystal structure of the sample is refined by using the WinxPow software.

2- Characterization of the complexes, Infrared spectra were recorded in the range of 4000-400 cm-1 on a Mattson Satallite 5000 FT-IR spectrophotometer, equipped with Winfirst software(Mattson Instruments, Madison, WI, USA),using KBR pellets.

3- Preperation of the films containing complexes, In this study, cellulose acetate (CA) was used as host material for the synthesized phosphors since it is preferrable in biological and clinical analysis and sterility purposes. Two different molecular weight CA was used which were 50,000.

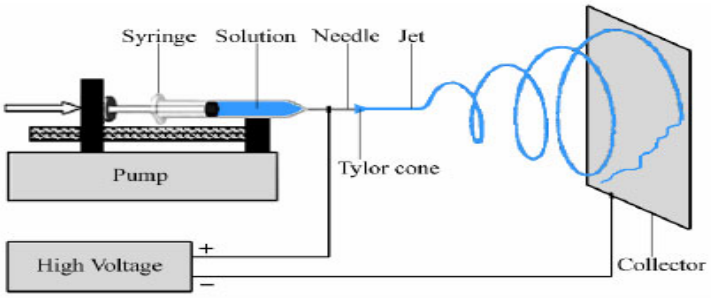

Figure 3. Process solution parameters, process conditions and external conditions were optimized

Solution parameters (concentration, viscosity.) Process conditions (distance from the collector to the nozzle, flow rate.) Voltage was optimized and the optimum voltage was found to be 14 kV.

Antibacterial studies of the film, clear text translation

Films were placed into a sterile cabinet. % NaCl Escherichia coli atcc 35150 strain over fresh 100 microliter 2 0.09 macfarland damlatild films to be dissolved. In the cabin were kept under a fluorescent lamp for 5 hours.

3. CONCLUSION

Elektroegirme primarily with bornitrur method using Nano fibres were obtained. Optimum experimental conditions were determined. FT-IR spectrum of Dichloro(3,4-dimethyl)dipyridinecopper(II) (CuCl2L12), and dichloro(3,5-dimethyl)dipyridinecopper(II) (CuCl2L22) and CA 50.000 were taken. By studying the antibacterial film, it was determined that had the desired characteristics of the product obtained. Work is currently ongoing.

4. ACKNOWLEDGEMENTS

This work is supported by Çankırı Karatekin University Scientific Research Projects Coordination Unit. (Project Number: FF060416B23)

REFERENCES

[1] Kismali G, Emen FM, Yesilkaynak T, Meral O, Demirkiran D, Sel T, Kulcu N., The cell death pathway induced by metal halide complexes of pyridine and derivative ligands in hepatocellular carcinoma cells - necrosis or apoptosis?, Eur Rev Med Pharmacol Sci. (2012), 16(8),1001-12.
[2] http//en.wikipedia.org/wiki/pyridine.
[3] Pandeya S.N.,'A text book of pharmaceutical organic chemistry (heterocyclic and biomolecules) vol. 2nd, 1st, (2003), 108-113.
[4]Patel, N.B.; Agravat, S.N.; Shaikh, F.M. Synthesis and antimicrobial activity of new pyridine derivatives-I. Med. Chem. Res.(2011), 20, 1033–1041.

Producing Boron Nitride containing fibers via electrospinning for use in cleaning waste water polluted with oil

Ruken Esra Demiröğen[a], Zehra Gülten Altın[b], Fatih Mehmet Emen[c]

aDepartment of Chemistry, Faculty of Science, Çankırı Karatekin University, TR-18100 Çankırı, Turkey
bDepartment of Chemical Engineering, Faculty of Enginering, Çankırı Karatekin University, TR-18100 Çankırı, Turkey
cDepartment of Chemistry, Faculty of Arts and Science, Mehmet Akif Ersoy University, TR-15100, Burdur, Turkey

**rukenesrademirdogen@yahoo.com*

Keywords: boron nitride, electrospinning, cleaning waste water

ABSTRACT

Global development, clean water and increasing environmental impact have brought about the necessity for utilizing membrane filtration choice for use in cleaning of waste water polluted with oil. It is known that membrane systems are the best solution which decreases cost while providing plant effectiveness and process facility. Membrane filtration method has been one of the most preferred method in water purification. Synthesis of membranes via eco-friendly methods have great importance.
In this study, membranes containing Boron Nitride are obtained via electrospraying. The physical, chemical and mechanical obtained membranes are characterized. Their structures were illucidated by FT-IR and XRD. The data regarding electrospun fibre bundles were obtained via Cu K α between the 2 θ = 5o – 30o. Thermal properties of the electrospun fibers were determined via TG/TGA analysis. The performance of the obtained BN modified membranes for removing mineral oil from oil/water mixture will be investigated. The BNNF Ethyl Cellulose membranes were placed in the oil/water mixture and were allowed to stay for a while. At the end of this period the membranes were removed from the solution and oil analysis were made in the solution. Sufficient performance was obtained in oil removal from waste waters.

1. INTRODUCTION

Oil spillage, organic solvents and dyes discharged by the textile, paper and tannery industries are primary pollutants of water sources [1].

Sorption is an efficient way to clean-up water but common absorbents, including activated carbon, zeolites, and natural fibers, suffer from low separation selectivity and low absorption capacity. A number of advanced materials have been developed and suggested to overcome these principal drawbacks, but they still show unsatisfactory regeneration and cycling ability.

Indeed, besides good absorbing properties in terms of capacity and kinetics, the desired absorbent materials should exhibit light weight for high gravimetric capacity, easy separation from cleaned water and easy cleaning for long-term cycling. Boron nitride (BN) nanosheets, so-called ‘white graphene’, consist of a few layers of hexagonal BN planes and have unique properties compared with graphene, including a wide energy band gap, electrical insulation, ultraviolet (UV) photoluminescence, high thermal conductivity and stability, and high resistance to oxidation and chemical inertness[2]. In addition, the polarity of BN bonds and the high surface area of h-BN-related nanostructures provide good adsorption properties of various substances ranging from organic pollutants to hydrogen [3].

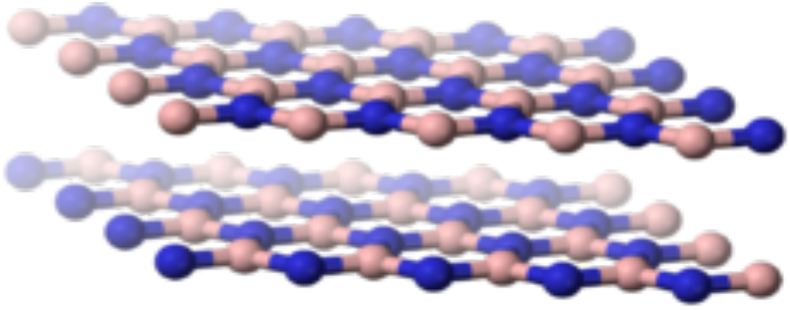

Figure1. Hexagonal form (h-BN) hexagonal analogous to graphite

As BN is composed of light elements, it promises absorbents of high uptake gravimetric capacity. Its high chemical and thermal stability also suggests that recycling could be easily achieved. Nanostructured BN is therefore an ideal candidate as an absorbent material [4]. In presen study, We aimed preparing polymeric fibers containing BN particules. Also we efforted to use for removal of mineral oil from water.

2. RESULTS AND DISCUSSION

BN nano powder was purchased from Nanografi 10g, molecular weight 5000 CA 7 g + 90 mlt was dissolved in acetone. Boron nitride was added to the prepared solution into g 0,1577. Then, the obtained solution with electrospinning method under high voltage (14 kV) was brought into the fiber. Oil testing machine for oil 3 ml + 100 ml water was added to the mixture containing 0.1 g to BN fibers. Oil was observed on the surface of the water of life absorpladig completely. Photographed the stages of fat absorption.

When I was treated with petroleum ether the oil fat absorption of the solvent of the dedicated fibers absorpladig history and the regeneration process has been successful.

Thus fibers can be regenerated and used repeatedly can be obtained. The study is ongoing.

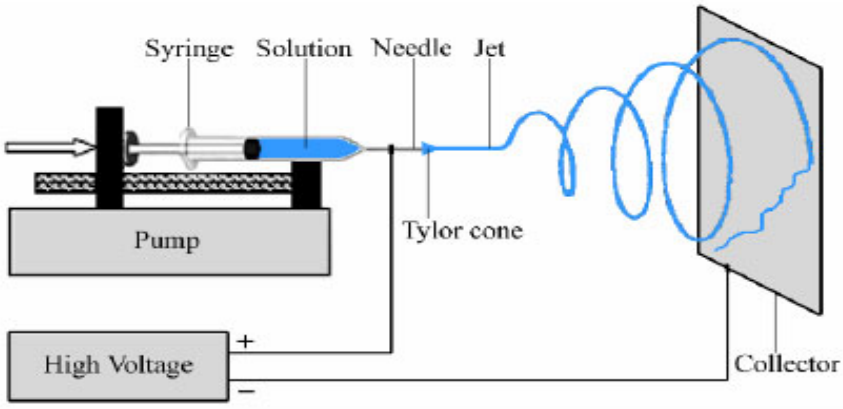

Figure 2. Insert the figure caption here

In this process solution parameters, process conditions and external conditions were optimized.
Solution parameters (concentration, viscosity.)
Process conditions (distance from the collector to the nozzle, flow rate.)
Voltage was optimized and the optimum voltage was found to be 14 kV.
Preperation of the fibers containing BN,
In this study, cellulose acetate (CA) was used as host material for the synthesized phosphors since it is preferrable in biological and clinical analysis and sterility purposes.
The molecular weight CA was used which were 50,000.

Oil testing machine for oil 3 ml + 100 ml water, was added to the mixture containing 0.1g to BN fibers. When I was treated with petroleum ether the oil fat absorption of the solvent of the dedicated fibers absorpladig history and the regeneration. Thus fibers can be regenerated and used repeatedly can be obtained. The study is ongoing.

3. CONCLUSION

Oil and organic solvent removal tests. The engine oil (%3) was used in this study. The absorption capacity values, W (wt/wt) %, were obtained by measuring the mass of fibers containing BN , and then the mass after oil absorption. Weight measurements were done rapidly to avoid evaporation of absorbed solvents or oils.

4. ACKNOWLEDGEMENTS

This work is supported by Çankırı Karatekin University Scientific Research Projects Coordination Unit. (Project Number: MF060416B22).

REFERENCES

[1] Dalton, T. & Jin, D. Extent and frequency of vessel oil spills in US marine protected areas. Mar. Pollut. Bull. (2010). 60, 1939–1945.
[2] Lee, C. G. et al. Frictional characteristics of atomically thin sheets. Science(2010). 328, 76–80.
[3] Zhang, X., Lian, G., Zhang, S. J., Cui, D. L. & Wang, Q. L. Boron nitride nanocarpets: controllable synthesis and their adsorption performance to organic pollutants. Cryst. Eng. Comm. (2012).14, 4670–4676.
[4] Vinu, A. et al. Synthesis of mesoporous BN and BCN exhibiting large surface areas via templating methods. Chem. Mater. (2005). 17, 5887–5890.

Phase transformation of HgSe at high pressure: An ab initio constant pressure study

Sebahaddin Alptekin

Department of Physics, Faculty of Science, Çankırı Karatekin University, TR-18100 Çankırı, Turkey

salptekin@karatekin.edu.tr

Keywords: High pressure, Ab initio calculation, Phase transition

ABSTRACT

A constant pressure ab initio MD technique and density functional theory with a generalized gradient approximation (GGA) were used to study the pressure-induced phase transition in zinc-blende HgSe. HgSe undergoes a structural first-order phase transition to (Fm-3m) structure in the constant pressure molecular dynamics simulation at 8 GPa. These phase transformations were also calculated using the enthalpy calculations. Our transition phases, lattice parameters and bulk properties are comparable with experimental and theoretical data.

1. INTRODUCTION

HgSe and HgTe appear to have similar behavior under compression. Their ambient-pressure (semimetallic) zinc-blende phases transform first into a semiconducting cinnabar-type structure at the very low high pressure of 1 GPa (Kafalas et al) into a NaCl phase at a pressure that has recently been located at about 20 GPa using high-resolution ADX techniques (Nelmes and McMahon, 1998).show rather similar sequences of structures under pressure. There have been, however, a number of experimental studies that indicate that the mercury chalcogenides [1–5]. In this study, we carry out a constant pressure ab initio MD technique to fully explain the microscopic nature of the pressure-induced phase transition of HgSe. .We show that ZB structure of HgSe undergoes a first order phase transition to I-4m2 and then to RS structure. (Fig.1)

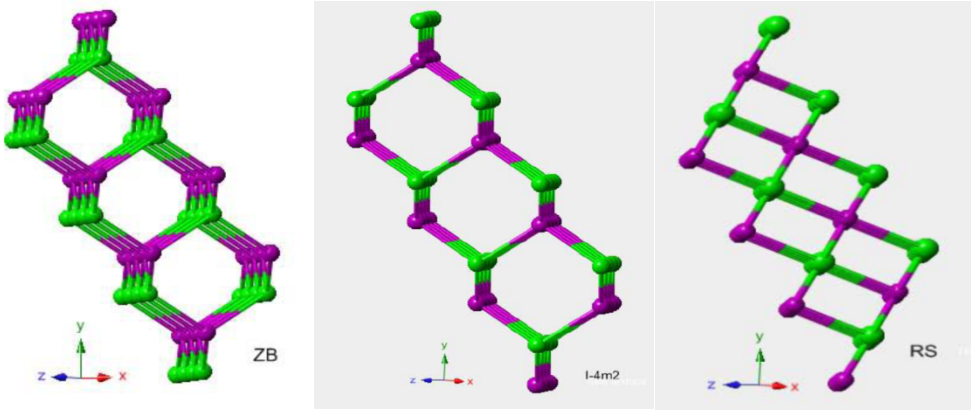

Figure1. Crystal structures of HgSe

Computational method

All calculations were carried out using the SIESTA code [6]. We used the density functional theory (DFT) with the generalized gradient approximation (GGA) of Perdew-Burke and Ernzerhof for the exchange-correlation energy. The norm-conservative Troullier-Martins Pseudopotentials were employed for core electrons, and valent electrons were described with a split-valence double-ξ basis sets expanded with polarized functions. A uniform mesh with a plane wave cut-off of 150 Ry was used to represent the electron

density, the local part of the pseudopotentials, and the Hartree and the exchange-correlation potential. The simulation cell consists of 64 atoms with periodic boundary conditions. We used Γ-point sampling for the supercell's Brillouin zone integration.

2. RESULTS AND DISCUSSION

.

In order to determine the ground states properties of HgSe, the total energies of ZB and RS phases are calculated for different volumes and fitted to the third order Birch Murnagam equation of state (EOS). The energy–volume data is given in Fig. 2. We obtain the lattice constants of the ZB and RS crystal as 6.422 Å and 5.764 Å respectively. These values are larger than the experimental results of 6.085 Å (for ZB) and 5.360 Å (for RS) [7]. The calculated equilibrium parameters of both phases are given in Table 1. In order to determine the transition pressure at T = 0 K, we calculate the enthalpy, H = E + PV. The stable structure at a given pressure is the state for which the enthalpy has its lowest value and the transition pressure is calculated at which the enthalpies for the two phases are equal. Our predicted transition pressure is 1 GPa, which is close to the experimental transition and theorical data. Enthalpy curves are given in Fig.3. We have observed in the MD simulation that phase transition of HgSe (ZB→ I-4m2 →RS) was produced at a transition pressure of about 8 GPa. Volume change as a function of hydrostatic pressure is given in Fig.4. We also investigated the electron density of state at 0 GPa and 8 GPa. The electron density of states (EDOS) of high pressure phases for HgSe are pictured in Fig.5

Table 1. The atomic fractional coordinates and equilibrium lattice parameters of the F-43m, I-4m2 and Fm-3m phases

Structure	a(Å)	a(Å)	a(Å)	x	y	z
ZB (F-43m)	6.4226	6.4226	6.4226	Hg:0.000	0.000	0.000
				Se:0.250	0.250	0.250
I-4m2	4.4927	4.4927	5.8493	Hg:0.000	0.000	0.000
				Se:0.000	0.500	0.250
Fm-3m	5.7643	5.7643	5.7643	Hg:0.000	0.000	0.000
				Se:0.500	0.500	0.500

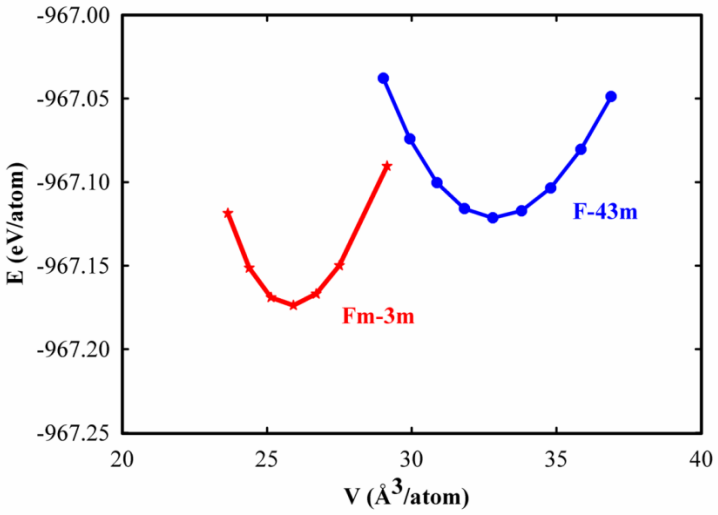

Figure 2. The computed energies of the ZB and RS phases of HgSe as a function of volume

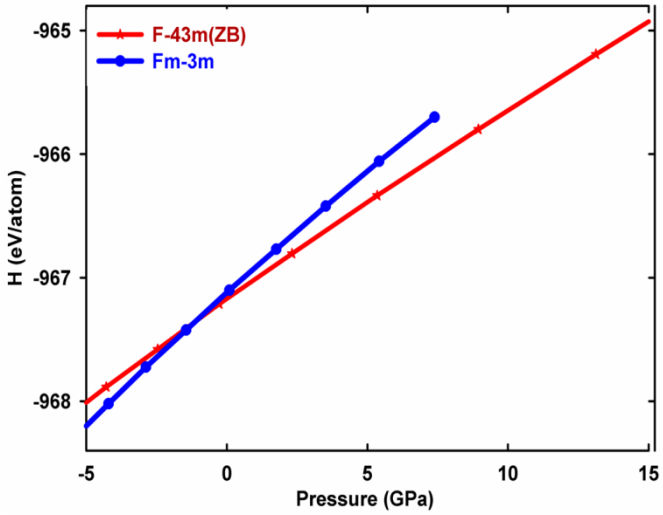

Figure 3. Enthalpy curves of the ZB and RS phases of HgSe as a function of pressure

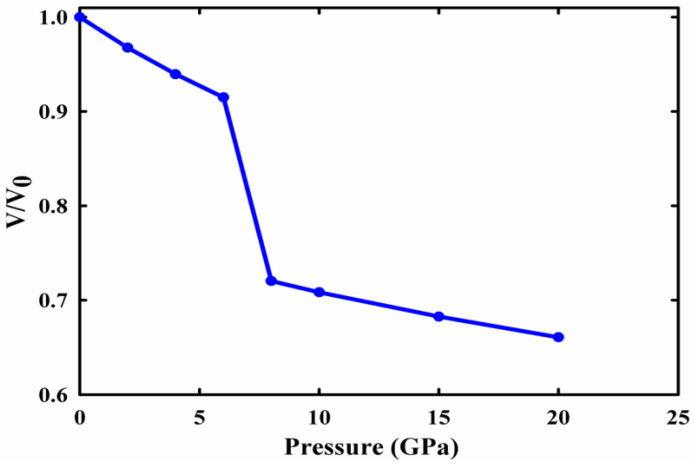

Figure 4. Volume change as a function of hydrostatic pressure

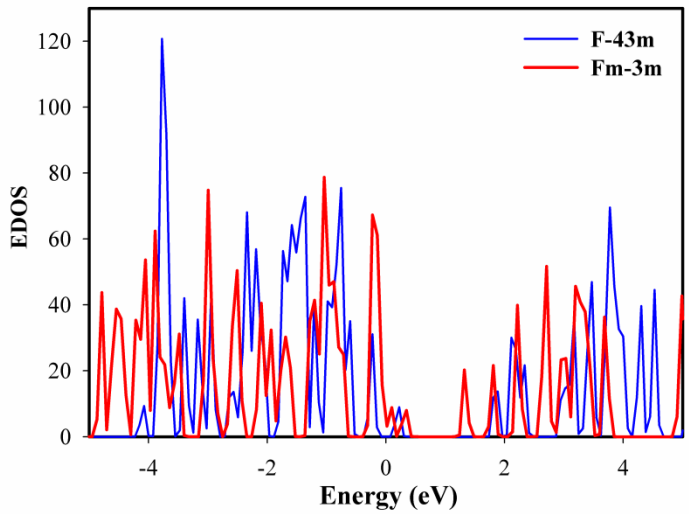

Figure 5. Calculated electronic density of states for HgSe at 0 GPa and 8 GPa

3. CONCLUSION

The pressure-induced phase transformation of HgSe was investigated using ab initio constant pressure molecular dynamics simulation. Our findings indicate that the ZB-to-RS phase transformation is a first-order phase change into I-4m2 and then to Fm-3m structure, which is successfully reproduced in the constant pressure simulation. This phase transformation is also studied from the total-energy calculations. Furthermore, the influence of pressure on the electronic structure of HgSe was investigated. Lattice parameters and bulk properties are comparable with experimental and previous theoretical data.

4. ACKNOWLEDGEMENTS

We are grateful to the SIESTA group for making their code publicly available.

REFERENCES

[1] Kafalas J.A, Gatos H.C, Levine M.C and Banus M. D J.Phys. Chem. Solids (1962), 23:1541
[2] Perdew JP, Burke K, M Ernzerhof, Phys Rev Lett. (1996),77,3865-3868
[3] Troullier N, Martins JM, Phys Rev B (1991),43,1993-2006
[4] Nelmes R.J and McMahon M.I, Semicond. Semimet. (1998), 54, 145
[5] Radescu S, Mujica A, and Lopez-Salcano, J. Phys Rev B (2011), 83,094107-14
[6] Ordejón P, Artacho E, Soler J.M, Phys. Rev. B (1996), 53, 10441.
Sánchez-Portal D, Ordejón P, Artacho E., Soler J.M, Int. J. Quantum Chem. (1997),65, 453
[7] Huang, T. and Ruoff, A.L, Phys. Rev.B (1983), 5, 27, 7811-7812 3.

Quality and Earthquake Risk of the Building in Urban Areas: A Case Study for Kırşehir, Turkey*

Seda Çellek[a], M. Mustafa Önal[b]

[a]*Department of Geological Engineering, Faculty of Engineering and Architecture, Ahi Evran University, TR-40100 Kırşehir, Turkey*
[b]*Department of Civil Engineering, Faculty of Engineering and Architecture, Ahi Evran University, TR-40100 Kırşehir, Turkey*

ABSTRACT

Kırşehir has been developing in relation with the development in population and building stock in the recent years; and the number of building storeys does increase according to the changing economical conditions. The inventory of the 5 building was taken in this study; the classification of the buildings, especially the ones built before 1988, were made according to their number of storeys, construction technique, and some other specifications. The performance analyses of those classified buildings were implemented regarding also local soil conditions and the building materials. Statistically significant numbers of buildings were evaluated; and the building quality of the building stock in Kirsehir and the probable earthquake risks of the buildings were determined. In Kirsehir province, like some other provinces, is among the regions where the earthquake region coefficient was changed and the quality of the building stock is rather unspecific. The damage ratio compared to the earthquake magnitude has been unfortunately very high as can be observed from the recent period earthquakes. A high ratio, of the investigated buildings is at risk as can be seen from the results of the investigations performed. Thus, reinforcement works should be initiated as soon as possible starting with the buildings at the high risk group.

1. INTRODUCTION

The purpose of this research is to determine the extent to which the 5 buildings selected in the provience of Kırsehir have been damaged by a severe earthquake with the EQ-Fast method. It was also aimed to measure the building quality of selected buildings within the scope of the research. The characteristics of selected buildings are given in Table 1.

Table 1. The characteristics of the five buildings

Building Name	Age of Building	Number of Floors	Class of Building	Load-Bearing System Control	Building/Soil Frequency Control	EDR (%) *
Gürdal	1990	4	D	Not Available	Available	41
Şahin	1997	5	D	Not Available	Available	41
Rahman	1993	6	D	Not Available	Available	41
Kaya	1986	5	C	Not Available	Available	36
Dinçer	1998	7	C	Not Available	Not Available	30

*EDR (%):Expected Damage Rate

EQ- Fast is called an expert system program used in this study a that allows to do an investigation on the building. The program determines the rate of damage in an earthquake vulnerability. Buildings are divided into four categories according on measurements (Table 2). Defects in the building are identified and there are 10 criteria for this.

Table 2. Class of Building in Earthquake Conditions

Class	Explain
A	It is expected a good attitude and building earthquake risk is low.
B	It is expected that no bad attitude and is an acceptable level of seismic risk of the building.
C	It is expected a poor attitude ve there is a high level of earthquake risk buildings.
D	It is expected a very inefficient attitude and seismic risk level of the building is very high.

According to do Table 2; B, C and D detailed examination and reinforcement is recommended.

Kırşehir is an area of high seismic risk. This means that, in this area, the return period of 475 years, the Modified Mercalli Intensity Scale (MMI) are based on the likelihood of an earthquake that 9 violence.
MMI=9 violence;
DR : Damage Ratio
MDR : Mean Damage Ratio
PL : Probable Loss
PML : Probable Maxsimum Loss

2. RESULTS AND DISCUSSION

We selected 5 building in Kırşehir and they were analyzed by EQ-Fast. The results are given in the following table.

Table 3. Shear Force Base and Overturning Account Control

TC97 (98)*	Gürdal	Şahin	Rahman	Kaya Apt.	Dinçer
A	10.3	9.53	8.5	9.58	9.33
B	0.4	0.4	0.4	0.4	0.4
C	4	4	4	4	4
D	14	19.6	22.5	14.6	19
E	11	13	15.8	13.7	19.65
F	1586.2	3035.305	4532.625	2395. 2395	6095.8721
G	1586.2	3035.305	4532.625	2395. 2395	6095.8721

* Shear Force Base and overturning Account Control, A: floor weight [kN/m^2], B: NEHRP peak acceleration coefficient, [g], C: NEHRP attitude factor, D: total length in the X direction Construction [m], E: The total length of the building in the Y direction [m], F: Shear Force calculated in X direction (kN), G: Shear Force calculated in Y direction (kN)

Table 4. Capable of transmitting torque (rigid bonded) floor in the framework of translational control

Drift Control *	Gürdal	**Şahin**	**Rahman**	**Kaya**	**Dinçer**
A	0.0014	0.0088	0.0114	0.00403	0.031
B	0.0034	0.00438	0.0043	0.0047	0.0045
C	4	3.9	4.3	4.6	5.6
D	4.4	5	4.4	3.5	3.9
E	24.300.000	25.000.000	25.000.000	243.000.000	253.000.000
F	8	9	12	15	20
G	10	15	25	10	12
H	4	4	4	4	4

* Capable of transmitting torque (rigid bonded) floor in the framework of translational control, A: X typical column moment of inertia in the direction (in y axes) (m^4), B: Y typical column moment of inertia in the direction (in x axes) (m^4), C: X direction of a typical gap length (m), D: Y direction of a typical gap length (m), E: Material elasticity modulus [kN/m^2], F: The number of horizontal load-bearing column in the X direction, G: Y direction, the number of horizontal load-bearing column, H: displacement amplification factor for NEHRP

Table 5. Shear Stress Control In Reinforced Concrete Frame Column

Stress Control *	Gürdal	Şahin	Rahman	Kaya	Dinçer
A	18	24	37	25	30
B	3	6	4	5	6
C	4	3	6	4	5
D	1.9	4.74	7.63	3.24	8.56

* Shear stress control in reinforced concrete frame column, A: Total number of columns, B: The total number of frames in the X direction, C: The total number of frames in the Y direction, D: The total horizontal cross-sectional area of the columns on the first floor (m^2)

Table 6. Frequency Control / Building and Ground Periods

Building Period	Gürdal	**Şahin**	**Rahman**	**Kaya**	**Dinçer**
X *	0.172	0.235	0.286	0.190	0.333
Y **	0.161	0.222	0.25	0.195	0.400

* 1 in the corresponding period of the vibration mode in the X Direction (sn)
** 1 in the corresponding period of the vibration mode in the Y Direction (sn)

Table 7. Level II: Final Results for the building, Earthquake building located in an area of high level (MMI=9)

Results	Gürdal	Şahin	Rahman	Kaya	Dinçer
A	Inappropriate!	Inappropriate!	Inappropriate!	Inappropriate!	Inappropriate!
B	Appropriate!	Appropriate!	Appropriate!	Appropriate!	Appropriate!
C	10	7	7	8	5
D	0.9	0.9	0.9	1.2	1.7
E	D	D	D	C	C
F	41	41	41	36	30
G	500	560	550	420	600

A: Control Delivery Systems, B: Building / Soil Frequency Control, C: Number of Structural Defects, D: Level II Note Results, E: Building Class, F: Damage Expected Rate MDR (%), G: Slip in Reinforced Concrete Columns Safety Strength (kN / m^2)

3. CONCLUSION

- ✓ Gürdal, Şahin, Rahman, Kaya and Dinçer buildings weren't appropriate for the carrier system evaluation! This result suggests that fulfill some of the issues mentioned in the building bylaws.
- ✓ These 5 buildings were appropriate in terms of vibration characteristics! These results, the vibration period of the building, away from where the period represents the seat can be raised on the ground.
- ✓ Defects structural system for buildings has been found. they must be corrected.

Table 8. Damage Per-expected rate

Earthquake Intensity MMI	Damage Per-expected rate MDR	% 90 Possibly the Maximum Loss PL_{90}	
6-7	5 %	10 %	**Gürdal Şahin Rahman**
8	16 %	27 %	
9	41 %	62 %	
6-7	4 %	8 %	**Kaya**
8	15 %	25 %	
9	36 %	55 %	
6-7	4 %	8 %	**Dinçer**
8	12 %	20 %	
9	30 %	45 %	

As a result;
For example, the cost of a building worth $ 1,000,000 $ 620,000 90% likely 'to be realized as equal to or less than that Gürdal, Şahin and Rahman building.
For example, the cost of a building worth $ 1,000,000 $ 520,000 90% likely 'to be realized as equal to or less than that Kaya Building
For example, the cost of a building worth $ 1,000,000 $ 450,000 90% likely 'to be realized as equal to or less than that Dinçer Building

REFERENCES

[1] Elnashai A.S., Engineering Structures. (2000), *22(1)*, 746-754.
[2] Güler K., Yüksel E. and Koçak A., Journal of Earthquake Engineering. (2008), *12(2)*, 140-150.

The current-voltage and interface States Properties of Ag/GO-PVA/p-Si structure

Şükrü Karataş

Kahramanmaras Sutcu Imam University, Faculty of Sciences and Arts, Department of Physics, Kahramanmaras 46100, Turkey

skaratas@ksu.edu.tr

Keywords: Electric properties; Interface state densities; Series resistance

ABSTRACT

In this study, the main electrical parameters of the Ag/nGO-PVA/*p*-Si hetero structure have been investigated by current–voltage (*I-V*) at room temperature. The interface state density (N_{SS}) as a function of energy distribution (E_{SS}-E_V) was extracted from the forward-bias *I–V* measurements by taking into account the bias dependence of the effective barrier height (Φ_b) and series resistance (R_S) for the Ag/nGO-PVA/*p*-Si heterojunction structure. Furthermore, the energy distribution of the interface state density is determined from the forward bias *I–V* characteristics by taking into account the bias dependence of the effective barrier height. The interface state density ranges from 4.52×10^{11} $cm^{-2}eV^{-1}$ in (E_{SS}–0.739) eV to 2.099×10^{12} $cm^{-2}eV^{-1}$ in (E_{SS}-*0.593*) eV, of the Ag/nGO-PVA/*p*-Si hetero structure.

1. INTRODUCTION

Semiconductor devices are the basic components of integrated circuits and are responsible for the startling rapid growth of electronics industry in the recent years. Due to the performance and stability of metal semiconductor structures which are of great importance to the electronic devices [1-3]. Because there is a continuing need for faster and more complex systems for the information age, existing semiconductor devices are being studied for improvement, and new ones are being invented [4-7]. Particularly, in the recent studies, it has been shown that graphene shapes a Schottky structure for conventional semiconductors such as GaAs, SiC, GaN and Si [8,9]. Graphene is a single sheet of carbon atoms tightly bound into a two-dimensional hexagonal network and is a basic building block for all other graphitic materials [10]. Thus, Graphene has become a valuable material in fundamental science and technology because of its excellent electronic, optical, thermal and mechanical properties [10-13]. However, although these devices have been studied extensively, satisfactory understanding in all details has still not been achieved.

In this study, the main electrical parameters of the Ag/nGO-PVA/*p*-Si hetero structure have been investigated by current–voltage measurements. Electrical properties of an Ag/nGO-PVA/*p*-Si hetero structure are characterized by its main electrical parameters such as ideality factor, barrier height, series resistance and interface states parameters.

2. RESULTS AND DISCUSSION

The forward bias current-voltage characteristics of the Ag/nGO-PVA/*p*-Si/Ag structure at room temperature (300 K) are given in Fig. 1. As can be seen in Fig. 1, the forward bias current-voltage characteristics are exponential at low bias voltages. However, at higher voltages a deviation in the current-voltage characteristic is observed due to series resistance and interfacial layer. The forward bias current–voltage characteristics of Ag/nGO-PVA/*p*-Si/Ag structure for with a series resistance and an interfacial layer is considered, according to the thermionic emission (TE) theory, the current across a device is expressed as [15,16];

$$I = I_o \exp\left(\frac{qV}{nkT}\right)\left[1 - \exp\left(-\frac{qV}{kT}\right)\right] \quad (1)$$

where *Io* is the saturation current derived from the straight line intercept of lnI at V=0 and is given by

$$I_o = AA^*T^2 \exp\left(-\frac{q\Phi_b}{kT}\right) \quad (2)$$

where q is the electron charge (1.6×10^{-19} C), V is the forward-bias voltage, A is the effective diode area, k is the Boltzmann constant (1.3806×10^{-23} J/K), T is the absolute temperature (300 K), A* is the effective Richardson constant for p-type Si (A*=32 $Acm^{-2}K^{-2}$) , Φ_b is the barrier height (BH) and n is the ideality factor. From Eq. (1) and (2) ideality factor (n) and barrier height (Φ_b) can be expressed as;

$$n = \frac{q}{kT}\left(\frac{dV}{d\ln I}\right) \quad (3)$$

and

$$\Phi_{bo} = \frac{kT}{q}\ln\left(\frac{AA^*T^2}{I_o}\right) \quad (4)$$

where n is ideality factor which is a measure of conformity of the diode to pure thermionic emission. For an ideal Schottky barrier diode n=1. However, n has usually a value greater than unity. This value indicates that the effect of the series resistance in the linear region is important. According to Eqs. (3) and (4), the values of the n and the barrier height Φ_b of the Ag/nGO-PVA/*p*-Si/Ag structure at room temperature were obtained as 2.46 and 0.762 eV, respectively. The current curve in forward bias region becomes dominated by series resistance from contact wires or bulk resistance of the semiconductor giving rise to the curvature at high current in the ln$I$ – V plot. As can be seen in Fig.1, ideality factor, n, has usually a value greater than unity, and this higher value of ideality factor of the Ag/nGO-PVA/*p*-Si/Ag structure is attributed to the interface states and series resistance effects which cause the non-ideal behaviour [4,6,17].

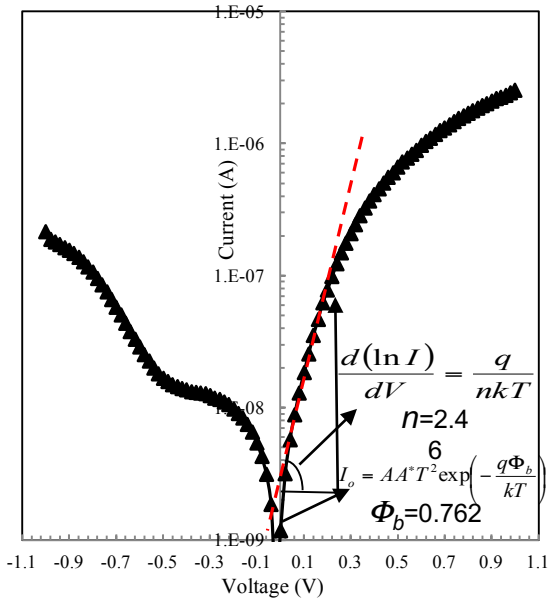

Figure 1. The *I-V* plot of the Ag/nGO-PVA/*p*-Si/Ag structure

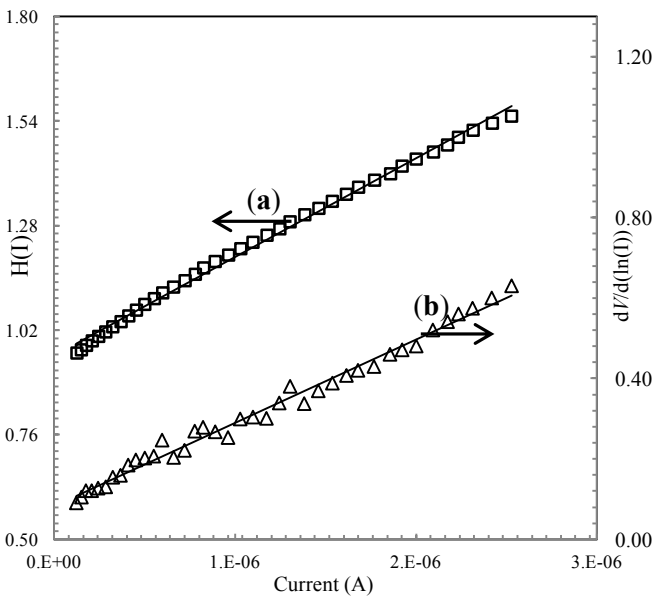

Figure 2. The experimental (a) H(I) vs. I and (b) dV/dln(I) vs. I plots

The barrier height value of 0.762 eV is remarkably higher than the conventional p-Si structure, where barrier height is 0.50 eV [18,19]. Thus, the series resistance effect cannot be ignored. The ideality factor

and the series resistance were evaluated using a method developed by Cheung et al.[20]. The Cheung's method defined by the following relations;

$$\frac{dV}{d(\ln I)} = R_s I + n\frac{kT}{q} \tag{5}$$

$$H(I) = V - n\left(\frac{kT}{q}\right)\ln\left(\frac{I}{AA^*T^2}\right) \tag{6}$$

$$H(I) = IR_S + n\Phi_{bo} \tag{7}$$

where barrier heights are the real barrier height extracted from the lower-voltage part of forward current voltage measurements. Fig. 2 represents H(I) (a) and dV/dln(I) (b) vice versa current, respectively. The values of ideality factor and series resistance from Eq. 5 were found as 3.16 and 207684 Ω, respectively. In the same way, the values of barrier height and series resistance from Eq.7 were found to be 0.31 eV and 245289 Ω. It is observed that the value of ideality factor obtained from the ln*I* – *V* plot is smaller than that of the dV/d(*lnI*) – *I* curves. This can be attributed to the effect of the series resistance and interface states and to the voltage drop across the interfacial layer [6,15,21,22]. Furthermore, the reason of this difference can be attributed to the existence of effects such as the series resistance and the bias dependence of the Ag/nGO-PVA/*p*-Si/Ag structure according to the voltage drop across the interfacial layer and change of the interface states with bias in this concave region of the ln*I*–*V* plot.

As addition to Cheung's functions, Norde proposed an alternative method to determine values of the series resistance and barrier height [23]. The following function has been defined in the modified Norde's method;

$$F(V) = \frac{V}{\gamma} - \frac{kT}{q}\ln\left(\frac{I(V)}{AA^*T^2}\right) \tag{8}$$

where γ is an arbitrary integer greater than ideality factor obtained from the *I*–*V* curve. The value of the barrier height of a diode can be determined as follows;

$$\Phi_b = F(V_0) + \frac{V_0}{\gamma} - \frac{kT}{q} \tag{9}$$

Figure 3 shows the F(*V*)-*V* characteristics of the Ag/nGO-PVA/*p*-Si/Ag structure. Once the minimum of the F(*V*) versus *V* plot is determined, the value of barrier height (Φ_b) can be obtained from Eq.(9). The value of the series resistance (RS) was obtained from Norde's method for Ag/nGO-PVA/*p*-Si/Ag structure. Also, Norde's functions seies resistance value is determined as

$$R_S = \frac{\gamma - n}{I} \quad \frac{kT}{q} \tag{10}$$

From the F(*V*)–*V* plot the values of barrier height and seies resistance of the structure have been determined as 0.441 eV and 271818 Ω, respectively, by using F(V_0)=0.400 V, V_0= 0.220 V values. It can be seen that there is a good agreement the values of series resistance obtained from the forward bias *lnI*–*V*, Cheung functions and Norde functions. The values of series resistance obtained from the Norde's method [23] are higher than that obtained from the Cheung's method. Because, the Cheung functions are only applied to the nonlinear region or high voltage region of the forward bias current-voltage characteristics, while Norde

’ s functions are applied to the full forward bias current-voltage characteristics of the junctions [19,24].

The interface states densities (N_{SS}) can be determined from the experimental data of the forward bias the current-voltage measuremets. The interface states densities as dependence to energy distribution (E_{SS}-E_V) of the Ag/nGO-PVA/*p*-Si/Ag structure structures is given in Fig. 4. The density of interface states of the Ag/nGO-PVA/*p*-Si/Ag structure can be calculated using the following equation [25];

$$N_{SS}(V) = \frac{1}{q}\left[\frac{\varepsilon_i}{\delta}(n(V)-1) - \frac{\varepsilon_s}{W_D}\right] \tag{11}$$

Also, the energy of the interface states with respect to the top of the valance band, EV, at the surface of the semiconductor is given by [6, 15].

$$E_{SS} - E_V = q\Phi_e - qV \tag{12}$$

where V is the applied voltage drop across the depletion layer and Φe is the effective barrier height. As seen in Fig. 4, the interface state density has an exponential drop with bias from the midgap towards the top of the valance conduction band for Ag/nGO-PVA/*p*-Si/Ag structure. This increase is probably due to the increase in the series resistance.

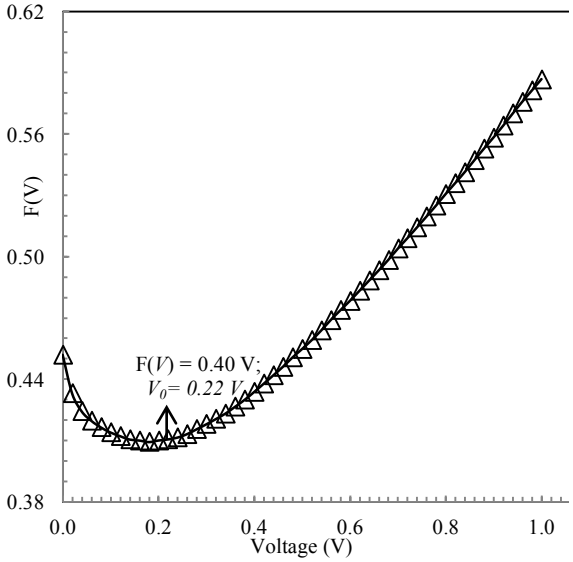

Fig. 3. F(V) vs.V plot of Ag/nGO-PVA/*p*-Si/Ag structure

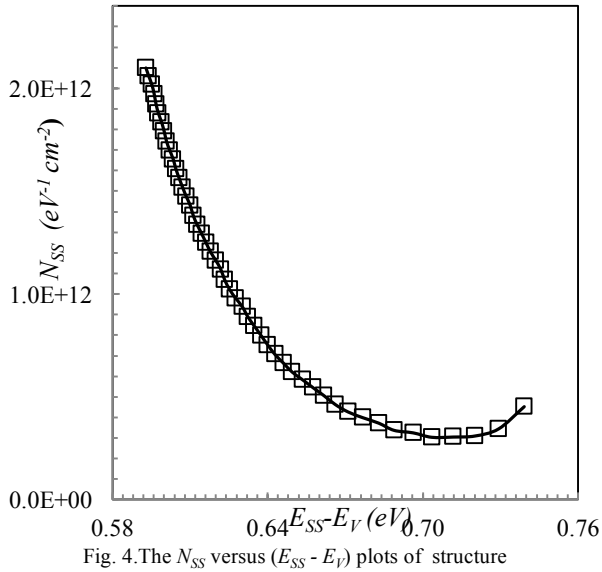

Fig. 4.The N_{SS} versus (E_{SS} - E_V) plots of structure

3. CONCLUSION

In this paper, electrical and interface state density distribution properties of Ag/nGO-PVA/p-Si/Ag structure have been investigated from current-voltage measurement at room temperature. The ideality factor and barrier height values calculated from Cheung functions and Norde' s functions. Furthermore, the interface states in equilibrium with the semiconductor were calculated from the downward curvature region caused by the presence of series resistance and interface states in the current – voltage plots. The interface state density obtained from the forward bias *I–V* ranges from $4.52x10^{11}$ $cm^{-2}eV^{-1}$ in (E_{SS}–0.739) eV to $2.099x10^{12}$ $cm^{-2}eV^{-1}$ in (E_{SS}-*0.593*) eV, of the Ag/nGO-PVA/*p*-Si hetero structure.

REFERENCES

[1] A. Hameed, V. Gombac, T. Montini, M. Graziani, P. Fornasiero, Chem. Phys. Lett. 472 (2009) 212.
[2] X. Miao, S. Tongay, M. K. Petterson, K. Berke, A. G. Rinzler, B. R.Appleton, and A. F. Hebard, Nano Lett. 12 (2012) 2745.
[3] S. Shivaraman, L. H. Herman, F. Rana, J. Park, and M. G. Spencer, Appl. Phys. Lett. 100 (2012) 183112.
[4] S. M. Sze, Physics of Semiconductor Structures, second ed., New York 1981 1-138
[5] P. W. Loscutoff, S. F. Bent, Annu. Rev. Phys. Chem. 2006 57 467.
[6] E.H. Rhoderick., R.H.Williams, Metal-Semiconductor Contacts, Second ed. Oxford, 1988.
[7] K.K. Kwok. , Complete Guide to Semiconductor Devices, New York: McGraw-Hill. 1995
[8] A. Hameed, V. Gombac, T. Montini, M. Graziani, P. Fornasiero, Chem. Phys. Lett. 472 (2009) 212.
[9] X. Miao, S. Tongay, M. K. Petterson, K. Berke, A. G. Rinzler, B. R.Appleton, and A. F. Hebard, Nano Lett. 12 (2012) 2745.
[10] A. K. Geim and K. S. Novoselov, Nat. Mater. 6 (2007)183
[11] İ.Karteri, Ş.Karataş, M. Çavaş, B. Arif, F.Yakuphanoğlu J. Nanoelect.Optoelect. 11 (2) (2016) 29.
[12] A. Kaya, E. Marıl, Ş. Altındal , İ. Uslu Microelect. Eng. 149 (2016) 166
[13] İ. Karteri, Ş. Karataş, F. Yakuphanoğlu, Appl. Surf. Sci.318, 74 (2014).
[14] Ş. Karataş, Ş. Altındal, A. Türüt, A. Özmen, Appl. Sur. Sci. 217 (2003) 250.
[15] S.M. Sze, Physics of Semiconductor Devices, second ed., Wiley, New York, 1981.
[16] Ş. Altındal, A. Tataroğlu, İ. Dökme, Sol. Energy Mater. Sol. Cells 85 (2005) 345.
[17] O. Gullu, A. Turut, Microelectronic Engineering 87 (2010) 2482–2487.
[18] R.K. Guptaa, Z. Serbetci, F. Yakuphanog˘lu, J. Alloys Compd. 515 (2012) 96.
[19] Ş. Karataş, F. Yakuphanoğlu J. Alloys Compd. 537 (2012) 6–11
[20] S.K. Cheung, N.W. Cheung, Appl. Phys. Lett. 49 (1986) 85.
[21] Ö. Gullu, T. Kilicoğlu, A. Türüt, J. Phys. Chem. Solids 71 (2010) 351.
[22] Ş. Karataş, Ş. Altındal, A. Türüt, M. Cakar, Physica B 392 (1–2) (2007) 43.
[23] H. Norde, J. Appl. Phys. 50 (1979) 5052.
[24] Ö. Güllü, Ş. Aydoğan, A. Türüt, Microelectron. Eng. 85 (2008) 1647.
[25] H.C. Card, E.H. Rhoderick, J. Phys. D 3 (1971) 1589.

Ab initio calculation of $AgXO_3$ (X: Nb, Ta) under pressure

Şevket Şimşek

Department of Material Science and Engineering, Hakkari University, TR-30000 Hakkari, Turkey

**e-mail corresponding author*: ssimsek_001@hotmail.com

Keywords: electronic structure, optical properties, DFT

ABSTRACT

The electronic band structure, density of state (DOS) and optical properties of $AgXO_3$ (X: Nb, Ta) compounds were investigated using the density functional theory within the local density approximation under pressure. The linear photon-energy dependent dielectric functions and some optical properties such as the energy-loss function, the effective number of valance electrons and the effective optical dielectric constant were also calculated under pressure. The results showed that the band gaps of $AgXO_3$ compounds increase with increasing pressure.

1. INTRODUCTION

The compounds in the form of ABO_3 belong to the perovskite family and form a subclass of transition metal oxides. Silver niobate ($AgNbO_3$) and silver tantalate ($AgTaO_3$) belong to the perovskite family. Because of recent developments in telecommunications, electro-optics and piezoelectric components perovskite niobates and tantalates have been placed on a short list of functional materials for future technologies [1]. Most of studies on $AgNbO_3$ and $AgTaO_3$ were focused on Raman scattering, structural phase transition and dielectric measurements. In this work, we have calculated the electronic band structure and optical properties of $AgXO_3$ using the density functional theory within the local density approximation under pressure in the cubic phase.

2. METHOD OF CALCULATION

The electronic and optical properties of $AgNbO_3$ and $AgTaO_3$ were theoretically studied by means of first principles calculations in the framework of density functional theory (DFT) and based on the local density approximation (LDA) [2] as implemented in the ABINIT code [3, 4]. The self–consistent norm-conserving pseudopotentials are generated using Troullier-Martins scheme [5] which is included in the Perdew-Wang [6] scheme as parameterized by Ceperly and Alder [7]. Pseudopotentials are generated using the following electronic configurations: For Ag, the $4d^{10}\,5s^{1}$, for Nb $4d^{4}\,5s^{1}$, for Ta $6s^{2}\,5d^{3}$, and for O $2s^{2}\,2p^{4}$ electron states are considered as the true valence. For calculations, the wave functions were expanded in plane waves up to a kinetic-energy cutoff of 40 Ha for $AgNbO_3$ and $AgTaO_3$. The Brillouin zone was sampled using a 8 x 8 x 8 the Monkhorst-Pack[8] mesh of special k points.

3. RESULTS AND DISCUSSION

3.1 Structural Properties

As a first step of our study, we determined structural parameters using experimental data for $AgNbO_3$ [9] and $AgTaO_3$ [10]. The theoretical lattice parameters were obtained by minimizing the ratio of the total energy of the crystal to its volume which are given in Table 1. Then, lattice constants were carried out as dependence pressure in the range from 0 to 15 GPa, and all calculations were performed using these theoretical lattice parameters. Our structural estimation in agreement with the available experimental and theoretical data.

3.2 Electronic Band Structure and Density of State

The electronic band structures of $AgXO_3$ have been calculated in high-symmetry directions in the first Brillouin zone. The band structures and total density of states (DOS) for cubic $AgNbO_3$ and $AgTaO_3$ are shown Figure 1. As seen in Fig. 1, the Fermi level (E_F) is set as zero of energy and specified by a horizontal dashed line. The calculated electronic band structures for both crystals are similar. In both crystals, the bottom band between about -18 eV and -16 eV exist three valance bands and originate from oxygen (O) 2s orbital. In calculated electronic band structures of $AgNbO_3$ and $AgTaO_3$ (see Fig. 1) between -6 eV and Fermi level (zero) exist fourteen valence bands. While Ag 4d orbitals between -6 and -5 eV localized, the top of the valence band between -5 and 0 eV mainly consist of the O 2p states hybridized with Nb 4d and Ta 5d states for $AgNbO_3$ and $AgTaO_3$, respectively. The top of valence band are mainly formed O 2p. In cubic phase for both crystals, the fourteen valence bands at Γ point are separated the four triply degenerate levels and one doubly degenerate level. These splittings are produced by the crystals field and the electrostatic interaction between O 2p orbitals.

Table 1. The calculated equilibrium lattice parameters and indirect band gaps together with the theoretical and experimental values for $AgXO_3$

Material	Reference	a (Å)	E_g (eV)	Space Group
$AgNbO_3$	Present (LDA-ABINIT)	3.9468	1.348	Pm3m (No:221)
	Theory (LDA-ABINIT)[10]	3.9584	1.533	
	Theory (GGA-CASTEP)[9]	3.9790	1.51	
	Theory (WC-GGA)[11]	3.951	1.64	
	Experimental[12]	3.9598		
$AgTaO_3$	Present (LDA- ABINIT)	3.9537	1.533	Pm3m (No:221)
	Theory (LDA-ABINIT)[10]	3.9545	1.537	
	Experimental[13]	3.9480		
	Theory (WC-GGA)[11]	3.9588	1.60	

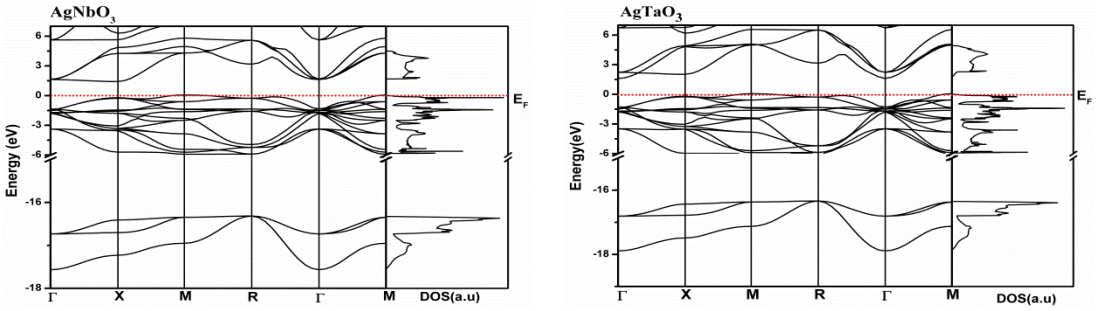

Figure 1. The calculated electronic band structures of $AgXO_3$.

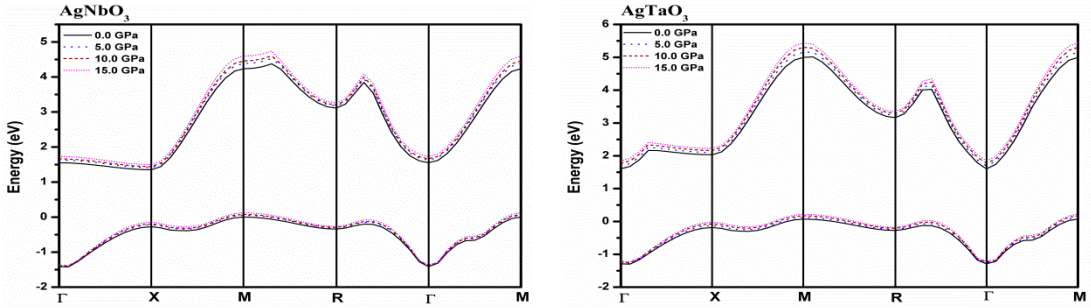

Figure 2. The change of band gaps of $AgXO_3$ under pressure.

It is clear for both crystals that the band gap appears between the top-most valence band at M-point and the bottom-most conduction band at X-point for $AgNbO_3$ and Γ-point for $AgTaO_3$. Accordingly both $AgNbO_3$ and $AgTaO_3$ have indirect band gap. The calculated indirect band gap values for $AgNbO_3$ and $AgTaO_3$ are

1.348 eV and 1.533 eV, respectively. Our calculated values are smaller than calculated values in Ref. [9, 10, 11]. These calculated values also may be smaller than experimental values, because ıt is well known that the band gap calculated by DFT is smaller than that obtained from experiments. DFT generally underestimates the band gap in semiconductors and insulators [14, 15]. The calculated equilibrium lattice parameters and band gaps together with the theoretical and experimental values for $AgNbO_3$ and $AgTaO_3$ are given in Table 1. We have also calculated the influence of external pressure on electronic band structures and band gaps of $AgNbO_3$ and $AgTaO_3$. The energy dispersions of the top valance band and the bottom conduction band in various pressures are calculated and given in Figure 2. It is well known that when pressure increases, value of band gap also increases. Our calculations showed that band gaps increase linearly as a function of pressure for both compounds.

3.3 Optical Properties

Because $AgNbO_3$ and $AgTaO_3$ have cubic crystal symmetry, the linear dielectric tensor of these crystals have one independent component which are diagonal elements of the linear dielectric tensor [16]. The calculated real and imaginary parts of the linear frequency dependent dielectric function are shown in Figure 3 for $AgNbO_3$ and $AgTaO_3$, respectively. The real part $\boldsymbol{\varepsilon_1}$ of dielectric function is equal to zero at about 9.46 eV, 14. 64 eV, 16.82 eV and 22. 74 eV for $AgNbO_3$. On the other hand, for $AgTaO_3$, function $\boldsymbol{\varepsilon_1}$ is equal to zero at about 10. 53 eV, 15.37 eV, 15.98 eV, 16.25 eV, 16.57 eV and 22.94 eV. The material shows dielectric properties where $\boldsymbol{\varepsilon_1}$ is greater than zero, the material behaves like a metal where it is less than zero. Also, the reflections decrease at the zero points of $\boldsymbol{\varepsilon_1}$. The imaginary part $\boldsymbol{\varepsilon_2}$ of dielectric function has peaks at A (3.25 eV), B (4.47 eV), C (5.20 eV), D (8.77 eV), E (9.37 eV), F (10.52 eV) and G (16.82 eV) points in $AgNbO_3$, whereas the function $\boldsymbol{\varepsilon_2}$ in $AgTaO_3$ shows peaks at A (3.08 eV), B (3.87 eV), C (5.93 eV), D (8.71 eV), E (10.58 eV), F (14.45 eV) and G (16.84 eV) points. The peaks of $\boldsymbol{\varepsilon_2}$ correspond to the transitions from the valence band to the conduction band.
The loss function L(ω) describes the energy loss of the fast electron traversing the material. The sharp maxima in the energy-loss function are associated with the existence of plasma oscillations. Using the dispersion of real and imaginary parts of dielectric functions, one can calculate energy loss spectrum coefficient, L(ω).

$$\boldsymbol{L(\omega) = \frac{\varepsilon_2(\omega)}{\varepsilon_1^2(\omega) + \varepsilon_1^2(\omega)}} \qquad (1)$$

The curve of energy loss function L(ω) in Fig. 3 has a maximum near 22.72 eV and 22.95 eV for $AgNbO_3$ and $AgTaO_3$, respectively. When the pressure increases, the maximum points of L(ω) shift to higher energy values for both compounds.

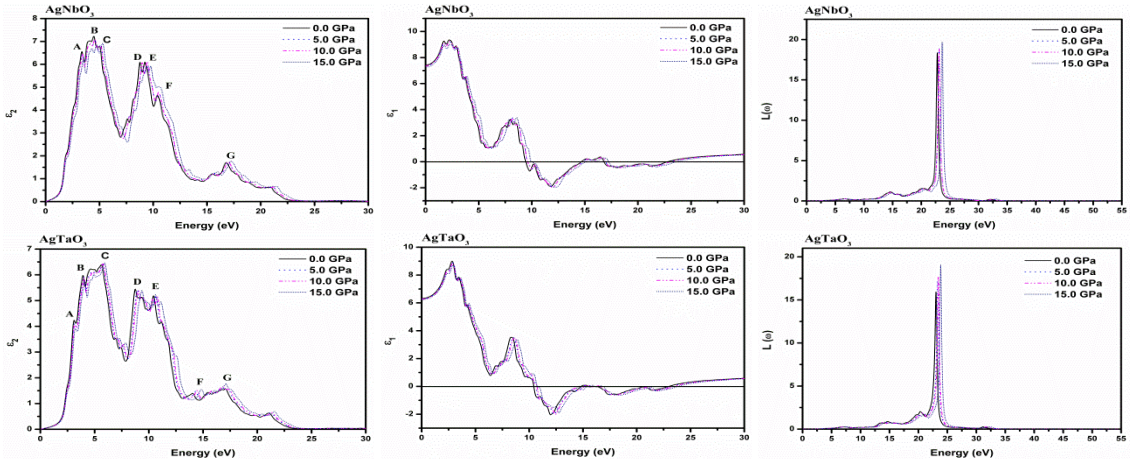

Figure 3. The real part and the imaginary part of dielectric function, the electron energy-loss spectrum of $AgXO_3$ under pressure.

The calculated effective number of valence electrons $\boldsymbol{N_{eff}}$ and effective dielectric constant $\boldsymbol{\varepsilon_{eff}}$ for both crystals are shown in Fig. 4. The effective number of valence electron up to about 2.25 eV is zero, then rises rapidly and reaches a saturation value at about energies of 22.5 eV for both crystals. This means that the deep-lying valence orbitals participate in the interband transition. As seen from Fig. 4, the effective

number of valence electron increases with pressure. Conversely, as can be seen in Fig. 4, the photon energy dependence of effective optical dielectric constant $\boldsymbol{\varepsilon_{eff}}$ can be separated into two regions. The first part of $\boldsymbol{\varepsilon_{eff}}$ is characterized by a rapid rise from 1.55 eV to 13.5 eV. The second part rises more smoothly and slowly after 13.5 eV, and tends to saturate at the energies about 23 eV. This means that the largest contribution to static dielectric constant is made by transitions corresponding to the bands between 1.55 eV and 13.5 eV. Conversely, it can be seen from Fig. 4 that $\boldsymbol{\varepsilon_{eff}}$ does not change much with pressure.

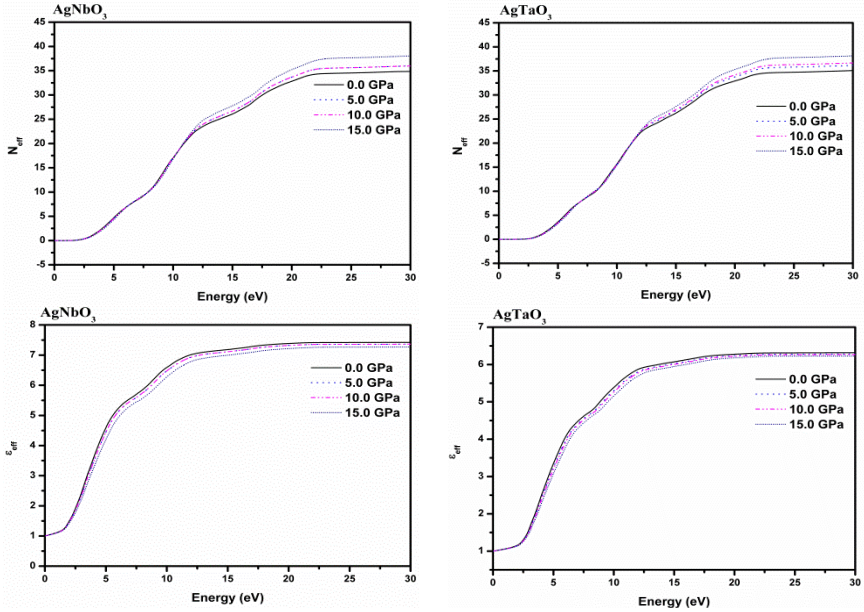

Figure 4. The effective number of valence electrons N_{eff} and the effective optical dielectric constant ε_{eff} of $AgXO_3$ under pressure.

4. CONCLUSIONS

We have calculated the electronic structure, DOS, linear optical properties of $AgNbO_3$ and $AgTaO_3$ using the density functional theory based on the ABINIT code. The electronic structure calculation showed that $AgNbO_3$ and $AgTaO_3$ have an indirect (M-X) band gap. The results show that the calculated band gaps under pressure of these compounds increase as dependence pressure.

5. ACKNOWLEDGEMENTS

This work was supported by the Hakkari University Scientific Research Projects Coordination Unit. (Project Number: MF2015BAP1).

REFERENCES

[1] Valant M., Axelsson A. K. And Alfold N., J. of the Eur. Cer.Soc. (2007), 27, 2549-2560.
[2] Cohen R., Krakauer H., Phys. Rev. B. (1990), 42, 6416-6423.
[3] Gonze X., Beuken J.-M. and et al., Comp. Mat. Sci. (2002), 25, 478-492.
[4] Fuch M., Scheffler M., Comput. Phys. Commun. (1999), 119, 67-98.
[5] Troullier N., Martins J. L., Phys. Rev. B. (1990), 43, 1993-2006.
[6] Perdew J.P., Wang Y., Phys. Rev.B. (1992), 45, 13244-13249.
[7] Ceperley D.M., Alder B.J., Phys. Rev. Lett. (1980), 45, 566-569.
[8] Monkhorst H.J., Pack J.D., Phys. Rev. B. (1976), 13, 5188-5192.
[9] Shigemi A., Wada T., Molecular Simulation. (2008), 34, 1105-1114.
[10] Cabuk S., Simsek S., Cent. Eur. J. Phys. (2008), 6, 730-736.
[11] Mahmood A ., Ramay S.M., and et al., Modern Physics Letters B. (2014), 28, 1450077-1450089.
[12] Sciau Ph., Kania A., Dkhil B., Suard E. and Ratuszna A., J.Phys.: Condens. Matter. (2004), 16, 2795-2810.
[13] Kugel G. E., Fontana M. D., Hafid M., Roledar K., Kania A. and Pawelczyk M., J. Phys. C: Solid State Phys. (1987), 20, 1217-1230.
[14] http://chem.ps.uci.edu/kieron/dft/book/
[15] Martin, R. M. Electronic Structure: Basic Theory and Practical Methods, Cambridge Uni. Press, Cambridge, 2004.
[16] Nye J. F., Physical Properties of Crystals (Oxford:Clarendon, 1957).

Preparation of a New Metal-Metal Oxide Electrolyte Diode

Zehra Gülten Altin[a] , Ruken Esra Demiröğen[b], Fatih Mehmet Emen[c], Derya Kilic[d]

a Department of Chemical Engineering, Faculty of Enginering, Çankırı Karatekin University, TR-18200 Çankırı, Turkey
bDepartment of Chemistry, Faculty of Science, Çankırı Karatekin University, TR-18200 Çankırı, Turkey
cDepartment of Chemistry, Faculty of Arts and Science, Mehmet Akif Ersoy University, TR-15100, Burdur, Turkey
dDepartment of Material Technology and Engineering, Faculty of Enginering, Mehmet Akif Ersoy University, TR-15100, Burdur, Turkey

**zaltin@karatekin.edu.tr*

Keywords: Zirconium, metal-metal electrolyte, electrolysis

ABSTRACT

In electrical and electronic circuits usually diodes are used to convert AC signal to DC signal [1]. First studies on this subject have started in 1822 when Berzelius prepared silicon (2). In 1847 Ferdinand Braun found that while pyrite and zenket, which are from the semi-conductors group, Show great resistance towards the current that would flow they Show very little resitance in the other direction. Thus crystal diodes came out and later it was used in detection of radio signs (electromagnetic wave). With respect to their basic structures semi conducting diodes can be classified in two groups: surface junction diodes and point contact diodes. At the beginning semi conducting diodes were used as point contact diodes. Later surface junction diodes took the place of point contact diodes. In the electrolysis made with alternative current zirconium metal was directly used as electrode. In XRD analysis it was determined the color change observed on zirconium surface indicates that the metal oxide (ZrO(1+x)) layer is formed and the electrode turned into a semi-conducting material.
Performances of pure zirconium and plated zirconium electrodes were compared via electrolysis of copper solution and water upon applying alternative current. It was observed that when pure zirconium was used the amount of current passing through the cell was higher. Therefore, in electrolysis of water via alternative current pure zirconium metal was directly used as electrode. Effect of electrolyte concentration, temperature and the rate, at which the electrolyte was stirred, on the performance of Zr/ZrO(1+x) electrode in electrolysis of water was investigated. The performance of the electrodes was determined via calculating the efficiency of electrolysis by using theoretical and experimental amount of hydrogen as equivalent grams. In experiments where strong acids and bases were used the highest results were obtained in 0,75 M KOH alkaline solution at 30°C and at a stirring speed of 240 min–1. It was observed that in the experiments made with weak acids and bases almost no current flowed through the cell.

1. INTRODUCTION

The direct current (DC) signal in the alternating current (AC) signal diodes are usually used to translate electrical and electronic circuits. The DC signal in the AC signal diodes are usually used to translate electrical and electronic circuits. The first studies on this subject begins with the preparation of silicon berzelius in 1822. From the group of Semiconductors for the first time in 1847 Ferdinand Braun prit survey and crystals, will in a direction against the current, the greater the resistance in the other direction it is found that show little resistance. Thus, the crystal diodes have emerged, and then Radio beacons of this invention (electromagnetic waves) have been used in the detection of. Winkler in 1886 during the effort to increase the sensitivity of the crystal detector germanyum if discovered, then began to exploit it properly. Strong

current in the field; the selenium rectifier as a diode in 1920, 1926, in copper oxide diode has been introduced. In 1906, Dr. Lee de forest lamp by the first electron has been implemented.
Between the years 1940-1948 in the United States, especially germanium and silicon rectifier issues. From 1942 on, the radar should have been used. [1, 2]. Semiconductor diodes, in terms of the basic structure of the surface, the Union (junction) diodes and point-contact diodes can be classified under two groups. Semiconductor diodes, the first point-contact diode in the case of the crystal has been introduced. Over time, these surface compounds has received the diodes [3, 4].

2. RESULTS AND DISCUSSION

When zirconium is used as the anode in the electrolysis system, although the system does not exceed the current from electrolysis continued. Although not Current, the electrolysis to continue in the hands of a semiconductor diode shows that there had been here. Metal oxide electrode during electrolysis on the surface of zirconium (ZrO(1+x)) comprises a layer of metal-metal oxide electrolyte Layer, and a semiconductor diode enables the electrode to have access to the task The obtained Zr/ZrO(1+x) electrode (semiconductor diode) the electrode in order to detect the performance of the electrolysis of cuso4 solution was carried out. At the end of the electrolysis of cuso4 solution, copper electrolysis, the amount of Zr/ZrO(1+x) were used in the evaluation of the performance of the electrode. Despite the use of alternating current in the electrolysis of cuso4 solution, electrolysis is the cause of the realization of p-type semiconductor behavior exhibit Zr/ZrO(1+x) electrode of the diode (rectifier), serves as

Zr/ZrO(1+x) electrode was obtained, mnso4 and H2SO4 on the concentration of the electrolysis performance of electrolysis the electrode and the work performed and the duration of the effect that temperature. At the end of the experiments; in 1.5 m H2SO4 solution with a concentration, a temperature of 35 ºC and at 30 V for 1.5 hours performed during the course of electrolysis obtained at the end of Zr/ZrO(1+x) showing the best performance of the electrodes. It was determined that the mnso4 concentration had a positive effect on the performance of the electrode. Zr/ZrO(1+x) used in the evaluation of the performance of the electrode with the increase of the concentration of the cuso4 solution in general, leads to an increase in the amount of electroplated copper.

Figure1. The results obtained in the experiments (85% yield).

Electrolytic	Concentration mol/lt	Temperature. oC	Mixing speed dk-1	Yield
KOH	0,75	30	240	94,95
H2SO4	1	35	360	93,19
H2SO4	1	35	120	90,23
NaOH	0,75	30	240	89,12
KOH	1,25	30	240	89,10
KOH	1,25	30	480	87,66
KOH	0,75	40	480	86,77
H2SO4	1,5	35	360	86,14
NaOH	1,25	30	480	86,14

In all experiments, the values of the temperature against time were determined. It is seen in Figure 2.

Figure 2. Temperature changes that occur in the electrolysis process in the cell.

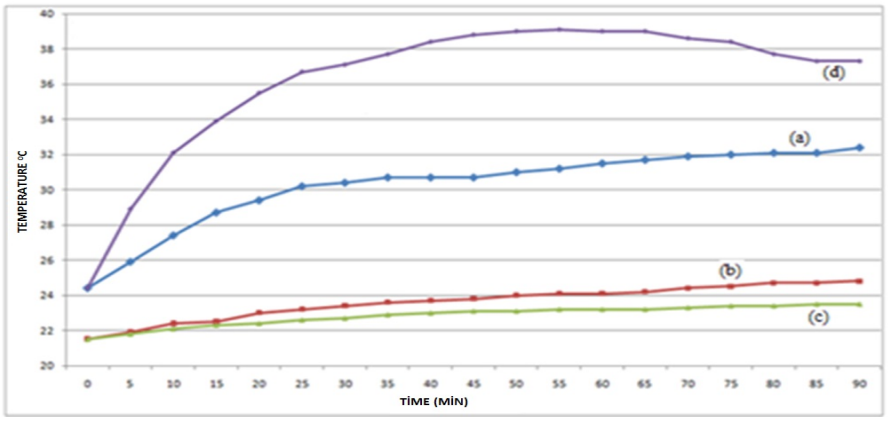

(a):11.5v , 1MH2SO4 , (b): 8 v, 1MH2SO4, (c) : 6v,1MH2SO4 , (d):11.5v ,1M KOH

3. CONCLUSION

Examination of parameters; For the parameters chosen, in order to examine the effects of electrolysis of water, response surface methodology was used. The results of these experiments the results obtained with H2SO4 and KOH are better because these electrolytes are used in cases where the parameters were evaluated.

REFERENCES

[1] Wang H, Tang Y, Khaligh A, Bridgeless Boost A. Rectifier for low-voltage energy harvesting applications. IEEE Trans Power Electron 2013;28:5206–14.
[2] Musavi F, Eberle W, Dunford WG, Phase-Shifted Gating A. Technique with simplified current sensing for the semi-bridgeless AC–DC converter. IEEE Trans Veh Technol 2013;62:1568–76.
[3]Hyde, F. J., Semiconductors, (1965), Macdonald, London.
[4] Tapia-Hernandez A, Ponce-Silva M, Olivares-Peregrino VH, Aguilar-Castillo C, Valdez-resendiz JE. Use of active diodes in autonomous sensorless three- phase boost-rectifier for energy harvesting applications. Energy Convers Congr Expo 2015:6642–7. http://dx.doi.org/10.1109/ECCE.2015.7310589.

Pasta ın a manufacturing plant L-tpye matrix and risk assessment study

Zehra Gülten Altın[a] , , Esra Ruken Demirdöğen[b] Fatih Mehmet Emen [c]

aCankırı Karatekin University Engineering Faculty, Chemical Engineering Department Uluyazı Campus TR-18200 Cankırı, Turkey
b Cankırı Karatekin University Faculty of Science Department of Chemistry, TR-18200 Cankırı, Turkey.
cMehmet Akif Ersoy University, Faculty Of Arts And Science, Department Of Chemistry, The independence Campus TR- 15030 Burdur, Turkey.

*zaltin@karatekin.edu.tr:

Keywords: pasta manufacture, risk assessment, L type matrix

ABSTRACT

An important era started for the workers and the business World upon adoption of the Law of Occupational Health and Safety with the issue 6331 (1). The law with the issue 6331 brought important arrangements regarding occupational health and safety and it exhibited a "preventive" approach rather than an "indemnifying" one. The concept of occupational health and security differs from Workers' Health and Occupational Security in that it includes work to be done for preventing the dangers and foreseeing, evaluating and eliminating or minimizing these risks (2).
In this study, risk evaluation was made in a pasta production facility via L type matrix. The facility producing pasta is in less dangerous category. Accident risk was investigated via L type matrix which is a risk evaluation method frequently used according to hazard classification. Estimating the dimension of the risk arising from the dangers is a method used for deciding whether the risk is acceptable or not upon taking into consideration the sufficiency of the existing controls.
The risks are evaluated, graded and a procedure is established for making the necessary control measurements. Acceptability of the risk levels are compared with the pre-determined criteria. Evaluation of multiplicity of the remaining risk, determining each necessary risk control measure, evaluation of risk control measures with respect to decreasing risk to acceptable level are made.

1. INTRODUCTION

Pasta from durum wheat semolina mixed with water and kneading the dough by drying after forming the shape is produced. Also in the mill during the milling of durum wheat flour Golden semolina % 10-12 is obtained. In the production of semolina pasta, the size of the particles is important in the production of semolina pasta. Pasta today to provide a uniform continuous flow in a production system, the production of pasta and best quality to achieve the development of a suitable paste pieces of dandruff, flour and black stain-free that are homogeneous in terms of massiveness on average 13% protein ın a medium size semolina are preferred.

The importance of water pasta, moderate toughness colorless odorless tasteless the quality of drinking

water in microbial quality of water should be used the amount of water the amount of semolina quality semolina pasta shape self-size, water temperature, the amount of water to be obtained vary depending on the type of dough. Step in the production of pasta, kneaded dough is obtained by using in the blender with enough water. Vacuuming, enough air comes into the bay, kneaded by dough pieces into the vacuum of the receipt of. Pasta, white-colored and yellow-colored become heterogeneous structure becomes homogeneous as a result of a product while vacuum. Dehydration, The most critical and difficult phase of the drying process in the production of pasta, it is known that. Press the pasta from a soft plastic structure and 30% moisture contains. Drying: the first pre-drying, pre-drying , final drying and smoothing as consists of four stages [1].

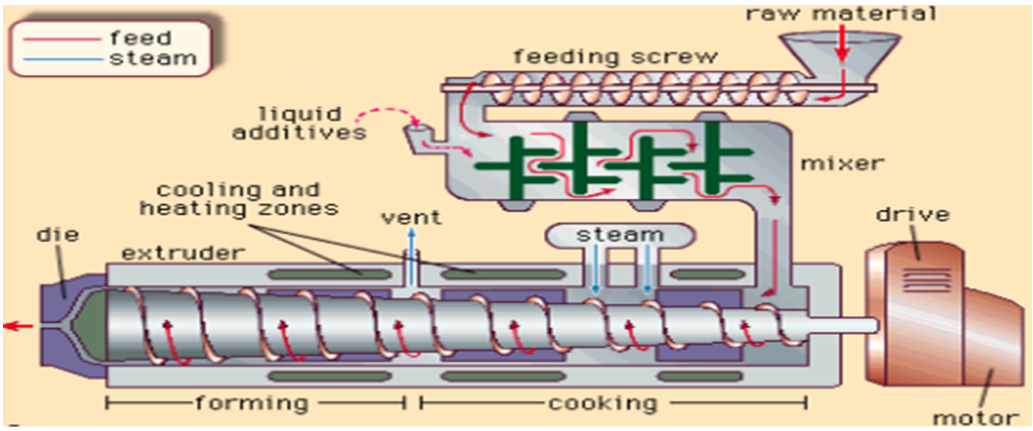

Figure 1. Pasta production process.

Danger, that may come from outside or present in the workplace, the workplace is the potential for loss or damage to employees or which may affect the environment. 3 is separated into hazard classes; Less dangerous workplaces, dangerous workplaces very dangerous workplaces.

What Is The Potential Danger? The possibility of realization, but unrealized is the case. Risk, A combination of likelihood of harm and the severity of a specified hazardous event occurring.

The Level of Acceptable Risk Legal obligations and workplace prevention policy in accordance with the risk level that will not cause injury or loss. Factors that affect the probability and severity of risk.

Risk= Probability X Violence

The Benefits Of Risk Assessment;

In Terms Of State, The state of the burden reduction, Ease of control, Continuous improvement, the study will contribute to the peace process, Reduction of losses Risk culture development

In Terms Of Employees; Determination of responsibilities, The ability to reach records, Coverage all employees, The rules determined in advance, A proactive approach and continuous improvement.

In Terms Of The Employer; To be able to foresee the hazard and risk, International respect, validation and positive image, Preparation for emergencies, Measures to reduction of losses, Responsibilities-tasks waist. Causal (cause-and-effect relationships in the determination of a method that is used. With this method, first, the results on the probability of an event and the occurrence of grading and measurement is performed. Risk value is calculated from the combination of probability and severity [2].

MACARONI (FOOD INDUSTRY)																			
EVALUATION CHART						RATING TABLE							REALIZATION STATUS BY PLANNED ACTIVITIES Y/N	PLANNED ACTIVITY RISK DOWNLOADABLE LEVEL? Y/N	PAGE NO	RESIDUAL RISK			
NUMBER	ACTIVITY AREA	ACTIVITY	EXPOSURE	DANGER	RISK	POSSIBILITY	VIOLENCE	RISK POINTS	PRIORITY SEQUENCE	PRECAUTIONS TO BE TAKEN	RESPONSIBLE	TERMİN			EXPLANATION	POSSIBILITY	VIOLENCE	RISK POINTS	PRIORITY SEQUENCE
22	GENERAL FACTORY AREA	QUALITY CONTROL ODAS	WORKING AREA IS NOT NOISE	INCOMPLETED WORKING ODAS	HEARING LOSS, HEALTH PROBLEMS	4	4	16	2	NOISE MEASUREMENT CONSTRUCTION ,KKD PROVIDING USE AND	EMPLOYER/ EMPLOYEE	1-30 DAY	Y	Y	OPTIMIZED	2	4	8	4
			NO AIR CONDITIONING SYSTEM	INCORPORATED WORK ENVIRONMENT	HEALTH PROBLEMS	4	4	16	2	APPROPRIATE AIR SYSTEMS MUST BE CREATED.	EMPLOYER/ EMPLOYEE	1-30 DAY	Y	Y	OPTIMIZED	2	4	8	4
			NOT FIRE EXTINGUISHING	NO FIRE INTERVENTION	MATERIAL LOSS, INJURY	4	4	16	2	SUPPLYING YOUR FIRE EXTINGUISHERS	EMPLOYER/ EMPLOYEE	1-30 DAY	Y	Y	OPTIMIZED	2	4	8	4
			CALIBRATION OF USED DEVICES	RESULTS OF FAULT ANALYSIS	NON QUALITY FOOD PRODUCTION, CUSTOMER DISSATISFACTION	4	4	16	2	PROVIDING THE TIME OF THE DEVICES 'CALIBRATIONS	EMPLOYER/ EMPLOYEE	1-30 DAY	Y	Y	OPTIMIZED	1	4	4	5
			NOT USED ELECTRICAL DEVICES GROUNDS	ELECTRIC SHOCK	INJURY, DEATH	4	5	20	2	ENSURING EQUIPMENT TO GROUND SYSTEM	EMPLOYER/ EMPLOYEE	1-30 DAY	Y	Y	OPTIMIZED	2	5	10	4

Figure 2. L - type (5x5) risk assessment matrix

2. RESULTS AND DISCUSSION

L-type matrix, because they are usually easy to apply, it is recommended to recruit new experts. L-type matrix used in the assessment of cause and effect relationships. Enterprises that are required to be taken immediately and the urgency of this method is used for the detection of hazards.

3. CONCLUSION

This property will perform risk assessment with a simulation study.

REFERENCES

[1] http://www.alomaliye.com/2016/01/11/6331-sayili-is-sagligi-ve-guvenligi-kanunu-idari-para-cezalari/.

[2] http://esertifika.anadolu.edu.tr/program/14/isveren-ve-isveren-vekili-icin-is-sagligi-ve-guvenligi.

Application of a New Catalyst in Synthesis of Biolubricant via Modification of Canola Oil

Zehra Gülten Altın[a], Mustafa Dağ[a] , Ruken Esra Demirdöğen[b] , Fatih Mehmet Emen[c], Derya Kılıç[c]

[a]*Cankırı Karatekin University Engineering Faculty, Chemical Engineering DepartmentUluyazı Campus TR-18200 Cankırı, Turkey*
[b] *Cankırı Karatekin University Faculty of Science Department of Chemistry, TR-18200 Cankırı, Turkey.*
[c]*Mehmet Akif Ersoy University, Faculty Of Arts And Science, Department Of Chemistry, The independence Campus TR- 15030 Burdur, Turkey.*
[c]*Mehmet Akif Ersoy University, Faculty Of Arts And Science, Department Of Chemistry, The independence Campus TR- 15030 Burdur, Turkey.*

**zaltin@karatekin.edu.tr*:

Keywords: New Catalyst, Biolubricant , Canola Oil

ABSTRACT

The lubricants named as mineral oils obtained from petroleum products. The lubricant property of the vegetable oils is superior to that of mineral oils and vegetable oils that do not contain additives offer better advantages than mineral oils with respect to their abrasion and friction, load carrying capacity and resistance properties. However, the thermal and oxidative stability of mineral oils were found to be superior to that of bio-lubricants.
In this study effort was devoted to overcome this problem via green means such as by using catalysts. Metal doped mesoporous structures have great importance in industrial catalysis and environmental applications. However, the number of studies on Lanthan doped mesoporous materials and their catalytic activity is very limited. In this study, catalyst was obtained by doping Eu3+ ions in mesoporous MCM-41 structure via hydrothermal method. Its structure is elucidated, pore size is determined and followingly it used as a heterogeneous catalyst in the hydrogenation reactions of canola oil. The modified products are obtained at Cankiri Karatekin University by reacting vegetable oils, the physical and chemical properties of which will be improved, with different amounts of the synthesized MCM-41:Eu3+ catalyst. The structures of the modified products were elucidated via Reometre.

1. INTRODUCTION

A vegetable oil is a triglyceride extracted from a plant Alfred Thomas [1] The term "vegetable oil" can be narrowly defined as referring only to plant oils that are liquid at room temperature,[2] or broadly defined without regard to a substance's state of matter at a given temperature.[3] For this reason, vegetable oils that are solid at room temperature are sometimes called vegetable fats. In contrast to these triglycerides, vegetable waxes lack glycerin in their structure. Although many plant parts may yield oil, in commercial practice, oil is extracted primarily from seeds. Lubricants derived from mineral oil are most commonly used despite they are non-biodegradable and contaminant [4]. Synthetic and solid lubricants and vegetable lubricants are the alternatives to the petroleum based lubricants , they are presentlybeing explored by the scientist and tribologists [5].
Vegetable oil based lubricants are attractive substitute to the petroleum based lubricants for these are friendly environmentally , renewable, non- toxic and biodegradable. Although vegetale oils based lubricants have some drawbacks such as poor oxidative and thermal stability. The oxidative stability of the vegetable oil based lubricants can be improved by polyunsaturated C=C double bonds of acid chain[6].

MCM-41 has a mesoporous silicate structure which was discovered in 1990s. A surfactant template is used to reach the MCM-41. The mesoporous material could be achieved by template removal from nanochannels as synthesized sample. MCM-41 has unique properties such as high surface area, narrow pore size

distribution, tunable and accessible pores. It has been a focus for several research areas like nanoscience, catalysis, environmental purification, adsorption and drug delivery [7,8].

MCM-41:Eu3+ mesoporous composite was prepared under hydrothermal condition using 27 % SiO2,14 % NaOH as silica and CTMABr as surfactant and Eu(NO3)3 as activator. XRD powder diffraction was used to structural characterization (Figure). PL spctrommetry was used to photolumineccent properties of MCM-41:Eu3+. The overall local environment of Eu3+ ion in the MCM-41 was investigated by Fourier-transform infrared. The Eu3+ ions were tetrahedrally or distorted tetrahedrally coordinated by oxygen ions. The catalytic activity of the sample was tested by the hydrogenation reactions.

2. RESULTS AND DISCUSSION

In this study, canola oil was modified with MCM-41Eu. Modified tests to be applied to oil. Acid value, kinematic viscosity, rheology, oxidative stability. The value of the ındex was the increase in acid. The value of the vıscosity was the increase modification at low temperature was happened a shorter period of modification the work in progress.

Table 1. Experimental study

MATERİALS	EXPERİMENTAL
Canola (mlt)	50
Temperature (°C)	30
MCM-41 Ln +3, Eu+3 (gr)	0,3
Sulfuric acid(molarite)	0,2
Reaction time (h)	3
The number of samples	5
Speed mixer(dev/dk)	150

A recipe for the experimental study of the above table it is seen Canola oil at low temperatures, in acidic environment , the modification was carried out with the catalyst in a short time. The FTIR spectra of modified canola were taken. Here, the unsaturated double bond of MCM-41, it is observed that it is becoming saturated with.

Table 2. Experimental results

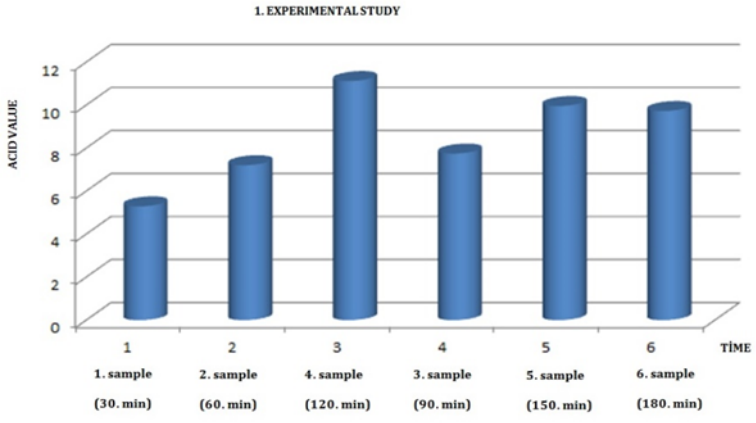

We showed that index values were increased after acid modification. This makes us suggest that fatty acids are free of (Table 2) .

Table 3. Experimental results viscosity

	Temperature (°C)	Dynamics viscosity (mPa. s)	Kinematic viscosity (mm^2/s)	Density (g/cm^3)
Raw Canola	26	0,0000671	59,487	0,886
1. sample	100	7,4578	8,6649	0,8605
2. sample	100	11,723	13,505	0,8679
3. sample	80	12,032	13,913	0,8646

The viscosity values of the samples increased after the experiments in Table 3 It is observed. By looking at these values it is said that the temperature changes of the viscosity of vegetable oils is the least of it. Vegetable oils are a very positive feature for this property.

3. CONCLUSION

As a result, plant oils, viscosity and viscosity index, acid value, base oil may be considered as an alternative to this in terms of features . As is well known, the oxidative stability of vegetable oils is the weakest of the features. In this study, for this feature continues to work. For this reason, vegetable oils, mineral oil as base oil in formulations tests to be done in order to reach a definitive judgment on the use of oxidation is a necessity. The lubricity properties of herbal oils in addition to other performance tests for understanding is a necessity. The first ten trials of canola oil, which is a newly developed material MCM-41:Eu3+.with modification yielded positive results. The value of the index was the increase in acid. The value of the viscosity was was the increase modification at low temperature was happened in a shorter period of modification.
The structures of the modified products were elucidated via FT-IR and rheology and oxidative stability, performance studies, DTA-TGA analysis.

4. ACKNOWLEDGEMENTS

This study Karatekin University project no= MF060515B21ile is supported by BAP.

REFERENCES

[1] Alfred Thomas, "Fats and Fatty Oils". Ullmann's Encyclopedia of Industrial Chemistry. (2002) Weinheim: Wiley-VCH. doi:10.1002/14356007.a10_173.

[2] Parwez Saroj, The Pearson Guide to the B.Sc. (Nursing) Entrance Examination. Pearson Education India. p. 109. ISBN 81-317-1338-5.

[3] Robin Dand , The International Cocoa Trade. (1999). Woodhead Publishing. p. 169. ISBN 1-85573-434-6.

[4] A. Adhvaryu, Z.S. Liu, S.Z. Erhan, Industrial Crops and Products 21 (2005) 113-119.

[5] Y.M.Shashidra, S.R. Jayaram, Tribology International 43 (2010) 1073-1081.

[6] L.E. Johanshon , S.T. Lundin, Journal of American Oil Chemists Society 56 (1979) , 974-980.

[7] C.T. Kresge, M.E. Leonowicz, W.J. Roth, J.C. Vartuli, J.S. Beck, Nature 359 (1992) 710.

[8] J.S. Beck, J.C. Vartuli, W.J. Roth, M.E. Leonowicz, C.T. Kresge, K.D. Schmitt, C.T. Chu, D.H. Olson, E.W. Sheppard, S.B. McCullen, J.B. Higgins, J.L. Schlenker, J. Am. Chem. Soc. 114 (1992) 10834.

Synthesis of two new metal halogen complexes; $Cd((2A1MB)_2)Cl_2$ and $Hg((2A1MB)_2)Cl_2$: Spectroscopic properties and antimicrobial activity

Zuhre Calisir[a], Fahriye Ercan[b], Elif Sevim[b], Nuri Ercan[c], Ali Sevim[b], Gozde Ciplak[a], Mustafa Kurt[a*]

[a]*Department of Physics, Faculty of Art and Sciences, Ahi Evran University, TR-40100 Kırşehir, Turkey*
[b]*Department of Genetic and Bioengineering, Faculty of Engineering and Architecture, Ahi Evran University, TR-40100 Kırşehir, Turkey*
[c]*Faculty of Agriculture, Ahi Evran University,TR-40100 Kırşehir, Turkey*

**e-mail corresponding author*: *mkurt@ahievran.edu.tr*

Keywords: benzimidazole, infrared, metal halogen complexes, antimicrobial activity, minimal inhibition concentration

ABSTRACT

In this study, the Fourier Transform Infrared spectra were reported for the metal(II)chloride2-Amino-1-MethylBenzimidazole (2A1MB) complexes with the following stoichiometries: Cd((2A1MB)2)Cl_2 and $Hg((2A1MB)_2)Cl_2$ were synthesized for the first time. FT-IR spectra of the title complexes in the solid phase were recorded in the region 4000-400cm^{-1}. The prepared samples and pure ligand (2A1MB) were analyzed for C, H and N. These complexes were tested in terms of antibacterial and antifungal activities. All test microorganisms were obtained from the Refik Saydam Hıfzısıhha Institute (Ankara, Turkey). The effect of complexes was determined by Agar Well Diffusion Method. According to the results of Agar Well Diffusion Method, these complexes were found to be effective against some microorganisms. The Cd((2A1MB)2)Cl_2 complex has a lethal effect against *Escherichia coli* ATCC 25922, *Bacillus subtilis* ATCC 6633, *Bacillus cereus* 709 ROMA, *Pseudomonas aeruginosa* ATCC 10145, *Enterobacter aerogenes* ATCC 13048, *Candida glabrata* ATCC 66032, *Candida tropicalis* ATCC 13803 and *Candida albicans* ATCC 60193. $Hg((2A1MB)_2)Cl_2$ complex has a lethal effect against *Escherichia coli* ATCC 25922, *Bacillus subtilis* ATCC 6633, *Bacillus cereus* 709 ROMA, *Enterococcus faecalis* ATCC 29212, *Klepsiella pnemoniae* ATCC 13883, *Staphylococcus aureus* ATCC 25923, *Enterobacter aerogenes* ATCC 13048, *Candida glabrata* ATCC 66032 and *Candida albicans* ATCC 60193. The minimal inhibition concentration of these complexes were detected.

1. INTRODUCTION

Benzimidazole, a heterocylic aromatic organic compound consisting of a fusion of benzene and imidazole, has been used as a ligand for transition metal complexes. They shows broad spectrum of pharmacological effects [1]. Benzimidazole moiety is structurally related to Purina bases, and is found in a variety of naturally occurring compounds with the different biological effects such as immunotropic, diuretic and antihistaminic [2,3]. Benzimidazole nucleus is a crucial pharmacophore in drug discovery. Pharmaceutical properties including antitumor [4], anti-HIV [5], anti-Parkinson [6], anti-microbial [7] and anti-HCV NS3/NS4Aserine protease [8] are unique characteristics known for benzimidazole derivatives. Halogenated benzimidazoles have raised special interest because of their diversified biological activity. Derivatives of imidazoles and benzimidazoles are known for their antibacterial, antiviral and fungicidal activities. These groups of compounds are wide of interest because of their diverse biological activity and clinical applications. Many different benzimidazoles have such activities as analgetics, anticarcinogens, antihistaminic, sedatives, etc. Various benzimidazoles are effective inhibitors of the growth of lactobacilli, vaccinia virus, influenza virus and HIV-virus [9].

2. RESULTS AND DISCUSSION

2.1. Vibrational Analysis of 2 Amino-1-methylbenzimidazole molecule (2A1MB)

The compound 2A1MB sample was purchased from Sigma-Aldrich Chemical Company with a stated purity 95% and it was used as no extra purification. The infrared spectrum for this investigation was collected on a Thermo Scientific Nicolet 6700 FT-IR Spectrometer. Molecular structure and atom numbering scheme for 2 Amino-1-methylbenzimidazole molecule was given Fig.1

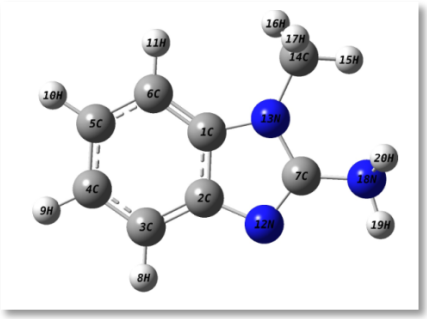

Fig 1. 2Amino-1-methylbenzimidazole molecule (2A1MB)

The aromatic C-H stretching vibrations are usually found between 3100-3000 cm^{-1}. We observed this band at 3022 cm^{-1} in FT-IR spectrum of free 2A1MB. The C-C stretching vibrational modes in the benzene ring generally occur in the region 1580-1620 cm^{-1}. In our study, this wave numbers were observed at 1612 cm^{-1} in FT-IR spectrum of Hg(2A1MB)2Cl2. The N-H stretching vibrations generally give bands in the range of 3500- 3300 cm^{-1}. In the present case, the band calculated at 3318 cm^{-1}, 3306 cm^{-1}, 3304 cm^{-1} in FT- IR spectrum of the Cd(2A1MB)2Cl2, Hg(2A1MB)2Cl2 and free 2A1MB molecules respectively (Fig. 2 and 3).

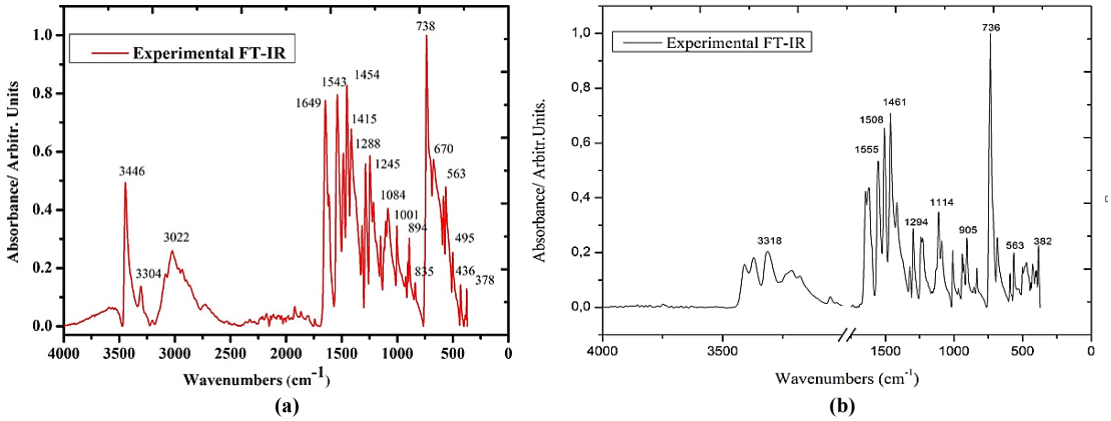

Fig 2. (a) The experimental FT-IR spectra of the 2A1MB. (b) The experimental FT-IR spectra of the Cd((2A1MB)$_2$Cl$_2$ molecule

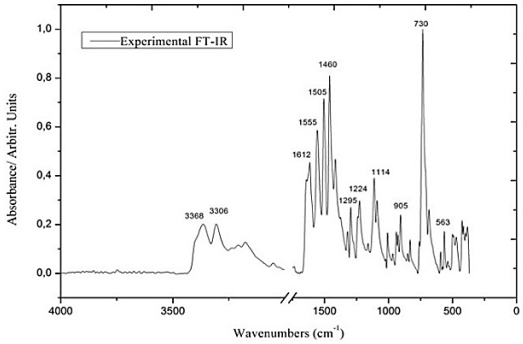

Fig 3. The experimental FT-IR spectra of the Hg((2A1MB)$_2$Cl$_2$ molecule

2.2. Antimicrobial activity of $Cd((2A1MB)_2)Cl_2$ and $Hg((2A1MB)_2)Cl_2$ complexes

The antibacterial and antifungal activities of Metal(II)chloride2-Amino-1-MethylBenzimidazole (2A1MB) complexes were determined by agar well diffusion method and minimal inhibition concentration [10, 11, 12]. All test microorganisms were obtained from the Refik Saydam Hıfzıssıhha Institute (Ankara, Turkey).

According to the results of Agar Well Diffusion Method, these complexes were found to be effective against some microorganisms. The $Cd((2A1MB)2)Cl_2$ complex has a lethal effect against *Escherichia coli* ATCC 25922, *Bacillus subtilis* ATCC 6633, *Bacillus cereus* 709 ROMA, *Pseudomonas aeruginosa* ATCC 10145, *Enterobacter aerogenes* ATCC 13048, *Candida glabrata* ATCC 66032, *Candida tropicalis* ATCC 13803 and *Candida albicans* ATCC 60193. $Hg((2A1MB)_2)Cl_2$ complex has a lethal effect against *Escherichia coli* ATCC 25922, *Bacillu ssubtilis* ATCC 6633, *Bacillus cereus* 709 ROMA, *Enterococcus faecalis* ATCC 29212, *Klepsiella pnemoniae* ATCC 13883, *Staphylococcus aureus* ATCC 25923, *Enterobacter aerogenes* ATCC 13048, *Candida glabrata* ATCC 66032 and *Candida albicans* ATCC 60193 (Table 1).

Table 1. The results of the agar well diffusion methods of metal(II)chloride 2-Amino-1-MethylBenzimidazole(2A1MB) complexes

	Microorganisms and inhibition zone (mm)*										
Complex names	*E.co*	*B.su*	*E.fa*	*B.ce*	*P.ae*	*K.pn*	*S.au*	*E.ae*	C.al	C.tr	C.gl
$Cd((2A1MB)2)Cl_2$	10	15	7	12	15	-	-	13	23	12	18
$Hg((2A1MB)_2)Cl_2$	13	16	10	14	-	20	17	16	25	12	12

*: E.co; *Escherichia coli* ATCC 25922, Bsu; *Bacillus subtilis* ATCC 6633, E.fa; *Enterococcus faecalis* ATCC 29212, B.ce; *Bacillus cereus* 709 ROMA, P.ae; *Pseudomonas aeruginosa* ATCC 10145, K.pn; *Klepsiella pnemoniae* ATCC 13883, E.ae; *Enterobacter aerogenes* ATCC 13048, C.al; *Candida albicans* ATCC 60193, C.tr; *Candida tropicalis* ATCC 13803, C.gl; *Candida glabrata* ATCC 66032.

The minimal inhibition concentrarion of these complexes were detected. $Cd((2A1MB)2)Cl_2$ complex and $Hg((2A1MB)_2)Cl_2$ complex were good activity against some bacteria and yeasts. MIC results of these complexes were given Table 2.

Table 2. Screening results for antimicrobial activity of metal(II)chloride2-Amino-1-MethylBenzimidazole (2A1MB) complexes

	MIC (µg/ml)										
Complex names	*E.co*	*B.su*	*E.fa*	*B.ce*	*P.ae*	*K.pn*	*S.au*	*E.ae*	C.al	C.tr	C.gl
$Cd((2A1MB)2)Cl_2$	125	60	1000	30	125	-	-	60	30	30	30
$Hg((2A1MB)_2)Cl_2$	125	10	1000	125	-	60	60	250	10	30	30

*: E.co; *Escherichia coli* ATCC 25922, Bsu; *Bacillus subtilis* ATCC 6633, E.fa; *Enterococcus faecalis* ATCC 29212, B.ce; *Bacillus cereus*709 ROMA, P.ae; *Pseudomonas aeruginosa* ATCC 10145, K.pn; *Klepsiella pnemoniae* ATCC 13883, E.ae; *Enterobacter aerogenes* ATCC 13048, C.al; *Candida albicans* ATCC 60193, C.tr; *Candida tropicalis* ATCC 13803, C.gl; *Candida glabrata* ATCC 66032.

Benzimidazoles are remarkably effective compounds with respect to their bacterial inhibitory activity and favorable selectivity ratio. Extensive biochemical and pharmacological studies have confirmed that these molecules are effective against various strains of microorganisms [13]. The antibacterial and antifungal activity of benzimidazoles and their metal complexes were determined in many studies [14, 15, 16, 17, 18]. In our study, we determined that Cd(II) and Hg(II) complexes were very effective against used all microorganism.

3. CONCLUSION

The chloride (II) complexes of 2-Amino-1-Methyl Benzimidazole molecule have been synthesized and spectrally characterized. The FT-IR spectra of the free ligand and the complexes exhibit various bands in the 400–4000 cm^{-1} region. According to the spectral analysis some shifts have been observed between free ligand and coordinated ligands due to the complex formation. The obtained $Cd((2A1MB)_2)Cl_2$ and $Hg((2A1MB)_2)Cl_2$ complexes showed good antimicrobial activity against some bacterial and fungal species.

4. ACKNOWLEDGEMENTS
This work was supported by the Ahi Evran University Scientific Research Projects Coordination Unit. Project Number: PYO-FEN.4001.16.015.

REFERENCES

[1] Unal A., Eren B., Spectrochimica Acta Part A: Mol. And Biomol. Spect. (2013), 114, 129-136.
[2] Nawrocka W., Zimecki M., Kuznicki T., Arch. Pharm. (1999), 332, 85-89.
[3] De Dios A.,Shih C.H., De Uralde B.L., J. Med. Chem. (2005), 48, 2270-2278.
[4] Rajendiran V., Murali M., Suresh E., Sinha S., Somasundaram K., Palaniandavar M., Dalton Trans. (2008), 148, 13-18.
[5] Camden JB., US Patent 6,077,862, 2002.
[6] Naithani P.K., Srivastava V.K., Saxena A.K., Barthwal J.P., Gupta T.K., Shanker K., Indian J. Exp. Biol. (1990), 28, 1145-1152.
[7] Goudgaon M.N., Dhondiba V., Vijayalaxmi A., Indian J. Heterocycl. Chem. (2004), 13, 271-279.
[8] Sperandio D., Gangloff A.R., Litvak J., Goldsmith R., Hataye J.M., Wang V.R., Shelton E.J., Elrod K., Janc J.W., Clark J.M., Rice K., Weinheimer S., Yeung K.S., Meanwell N.A., Hernandez D., Staab A.J., Venables B.L., Spencer J.R., Bioorg. Med. Chem. Lett. (2002), 12, 3129-3136.
[9] Podunavac-Sanja O.S., Markov S.L., Vojinovic L.S., APTEFF (2004), 35, 1-280.
[10] Gumrukcuoglu N., Serdar M., Celik E., Sevim A., Demirbas N. Turkish Journal of Chemistry (2007), 31, 335-348.
[11] Yaylı N., Sivrikaya S.O., Yasar A., Ucuncu O., Gulec C., Kolaylı S., Kucuk M., Celik E., Journal of Photochemistry and Photobiology A: Chemistry (2005), 175, 22-28.
[12] Demirbas N., DemirbasA., Alpay Karaoglu S., Sevim E., ARKIVOC(2005),1, 75-91.
[13] Sharma M.C., Drug Des. (2015), 4, 122-129.
[14] Singh N., Pandurangan A., Rana K., Anand P., Ahamad A., Tiwari A.K., Internal. Cur. Pharma. J. (2012), 1, 119-127.
[15] Podunavac-Kuzmanovic S.O., Cvetkovic D.M., J. Serb. Chem. Soc. (2007), 72, 459-466.
[16] Murthy Y.L.N., Durga G., Jha A., Med. Chem. Res. (2013), 22, 2266-2272.
[17] Apohan E., Yılmaz U., Yılmaz O., Serindag A., Kucukbay H., Yesilada O., Baran Y., Journal of Organometallic Chemistry (2017), 828, 52-58.
[18] Ashraf A., Siddiqui W.A., Akbar J., Mustafa G., Krautscheid H., Ullah N., Mirza B., Sher F., Hanif M., Hartinger C.G., Inorganica Chimica Acta (2016), 443, 179-185.

Microfungal diversity of Ihlara valley

Faruk Selçuk

Department of Biology, Faculty of Arts and Sciences, Ahi Evran University,
TR-40100 Kırşehir, Turkey
selcuk_faruk@yahoo.com

Abstract:

Forty tree species of microfungi were found in Ihlara valley's trees and shrubs, which carried out in Ihlara valley where important place according to historical and geographical side. These are belonging to 30 genera and 20 family. These species are spreaded according to Ascomycota and Basidiomycota divisio of Fungi kingdom like these: Ascomycota – 3 classes, 7 order, 18 families, 28 genera and 40 species; Basidiomycota – 2 classes, 2 order, 2 families, 2 genera and 3 species.

The microfungi in trees and shrubs which grow up research area were represented with the most of member's Ascomycota. Forty species of these have been found and these are 93 % of total microfungi. The Dothideomycetes class in Ascomycota appear itself from the point of view number and species (25 species), these members of this class have contained half more than Ascomycota. The rest of Ascomycota fungi are belong to Sordariomycetes class. Only one species have been found from Leotiomycetes.

Basidiomycota has the divisio contained the least species and Rust fungi influenced the situation of tree has important.

In the result of our investigation, *Cucurbitaria juglandis* Fuckel, *Mycosphaerella convexula* (Schwein.) F.V. Rand, *Phyllosticta destruens* Desm. and *Phoma juglandis* Sacc. species have been new recorded for our country.

Introduction:

Study area, Ihlara valley (Güzelyurt, Aksaray) is in "Ihlara Special Environmental Protection Area" (TKV, 2012) and it has very interesting geomorphological features as result of the volcanic activity of Hasan and Erciyes Mountains in Miocene and Pliocene age. Main rocks types are tuff, ignimbrite and volcanic ash in this region. There are widely depositing travertine masses around the Ihlara Valley. Main soil type of the valley is alluvial soils, the other colluvial brown soils. It's volcanic, hydrothermal activity, historical and cultural features make it unique and thus this area was declared Specially Protected Area in 21.11.1990 (Ören and Keçeli, 2014; Biler and Şahin, 2012; ÇOB, 2013; Sarı et al., 2005; Karabacak, 2007).

The area is located phytogeographically in the Irano-Turanian region. According to the grid square system adopted by Davis (1982) in the Flora of Turkey, Ihlara valley is located in the squares B5. While steppe vegetation is seen upper part of the valley, riparian vegetation is dominant along Melendiz Stream. Predominant trees and bushes species consist of *Celtis turnefortii*, *Colutea cilicica*, *Crataegus monogyna*, *Elaeagnus angustifolia*, *Juglans regia*, *Pistacia terebinthus*, *Populus alba*, *P. pyramidalis*, *Prunus spinosa*, *Pyrus elaeagnifolia*, *Quercus pubescens*, *Qu. robur*, *Salix alba*, *S. babylonica*, and *Ulmus glabra* etc. in Ihlara Valley (Ören and Keçeli, 2014; Biler and Şahin, 2012).

Material and Methods:

Material for this study collected in 2013 in different localities of Ihlara valley. Specimens of the host plants were identified using the "Flora of Turkey and East Aegean Island" (Davis, 1982). The microfungi were determined using relevant literature (Allescher, 1901, 1903; Arx Von, 1987; Barnett and Hunter, 1998; Braun 1995, 1998; Byzova et al., 1968, 1970; Carmichael et al., 1980; Ellis and Ellis, 1987; Grove, 1935 , 1937; Kiffer and Morelet, 2000; Mel'nik, 2000; Mel'nik et al., 1992; Nag Raj, 1993; Saccardo, 1882 – 1931, 1972; Smitskaya, 1991; Sutton, 1980; Şvartsman, 1973, 1975, 1971 and Tomilin, 1979 etc.) The author abbreviations of fungi checked using by Index fungorum. The collection materials

are deposited in the Mycology Laboratories of the Ahi Evran University, Sciences and Arts Faculty, Department of Biology in Kırşehir province of Turkey.

Results:

The species of fungi are given in alphabetic order. New records to Turkey are marked with an asterix (*). Abbreviations: m a.s.l. – altitude meters above sea level, FS – Faruk Selçuk, and specimen number.

List of the fungi species

Camarosporium elaeagnellum Vasyag. on dead branches of *Elaeagnus angustifolia*; Ihlara valley, around Belisırma, 38°15'965''N, 34°17'410''E, 1190 m a.s.l., 07.12.2013, FS 0957.

Camarosporium elaeagni Potebnia on dead branches of *Elaeagnus angustifolia*; Ihlara valley, around Belisırma, 38°15'965''N, 34°17'410''E, 1190 m a.s.l., 07.12.2013, FS 0957.

Camarosporium karstenii Sacc. & P. Syd. on dead branches of *Elaeagnus angustifolia*; Ihlara valley, around Belisırma, 38°15'985''N, 34°17'390''E, 1160 m a.s.l., 07.12.2013, FS 0961.

Coniochaeta pulveracea (Ehrh.) Munk on naked wood of *Pistacia terebinthus*; Ihlara valley, 38°15'389''N, 34°17'810''E, 1194 m a.s.l., 07.12.2013, FS 0972.

Coniothyrium pruni McAlpine on dead branches of *Prunus spinosa*; Ihlara valley, around Belisırma, 38°15'968''N, 34°17'408''E, 1190 m a.s.l., 07.12.2013, FS 0959.

Cucurbitaria celtidis Shear on bark of branches of *Celtis tournefortii*; Ihlara valley, around Belisırma, 38°15'886''N, 34°17'498''E, 1160 m a.s.l., 07.12.2013, FS 0966a.

****Cucurbitaria juglandis*** Fuckel on dead branches of *Juglans regia*; Ihlara valley, around Belisırma, 38°15'915''N, 34°17'487''E, 1160 m a.s.l., 07.12.2013, FS 0964.

Cucurbitaria obducens (Schumach.) Petr. on daed branches of *Populus alba*; Ihlara valley, around Belisırma, 38°15'966''N, 34°17'452''E, 1190 m a.s.l., 07.12.2013, FS 0960a.

Cytospora elaeagni Allesch. on dead branches of *Elaeagnus angustifolia*; Ihlara valley, around Belisırma, 38°15'985''N, 34°17'390''E, 1160 m a.s.l., 07.12.2013, FS 0961.

Cytospora salicis (Corda) Rabenh. on dead branches of *Salix alba*; Ihlara valley, around Belisırma, 38°15'970''N, 34°17'413''E, 1190 m a.s.l., 07.12.2013, FS 0956.

Cytospora terebinthi Bres. On dead twigs of *Pistacia terebinthus*; Ihlara valley, around Belisırma, 38°15'389''N, 34°17'810''E, 1194 m a.s.l., 07.12.2013, FS 0972a.

Dendrophoma cytisporoides Sacc. on branches of *Ulmus glabra*; Ihlara valley, around Belisırma, 38°15'492''N, 34°17'749''E, 1177 m a.s.l., 07.12.2013, FS 0971.

Diatrype disciformis (Hoffm.) Fr. on dead branches of *Elaeagnus angustifolia*; Ihlara valley, around Belisırma, 38°15'985''N, 34°17'390''E, 1160 m a.s.l., 07.12.2013, FS 0961.

Diatrypella pulvinata Nitschke on branches of *Quercus pubescens*; Ihlara valley, around Belisırma, 38°15'600''N, 34°17'781''E, 1180 m a.s.l., 07.12.2013, FS 0970b.

Dinemasporium pleurospora (Sacc.) Shkarupa on dead branches of *Pistacia terebinthus*; Ihlara valley, 38°15'389''N, 34°17'810''E, 1194 m a.s.l., 07.12.2013, FS 0972a.

Diplodia ulmi Fuckel on dead branches of *Ulmus glabra*; Ihlara valley, around Belisırma, 38°15'492''N, 34°17'749''E, 1177 m a.s.l., 07.12.2013, FS 0971.

Discula cytosporea (Pass.) Arx on leaves of *Populus alba*; Ihlara valley, around Belisırma, 38°15'900''N, 34°17'531''E, 1160 m a.s.l., 07.12.2013, FS 0965a.

Dothiorella crepinii (Speg. & Roum.) Grove on branches of *Populus alba*; Ihlara valley, around Belisırma, 38°15'900''N, 34°17'531''E, 1160 m a.s.l., 07.12.2013, FS 0965a.

Drepanopeziza populorum (Desm.) Höhn. on leaves of *Populus alba*; Ihlara valley, around Belisırma, 38°15'900''N, 34°17'531''E, 1160 m a.s.l., 07.12.2013, FS 0965a.

Gymnosporangium confusum Plowr. on leaves of *Crataegus monogyna*; Ihlara valley, around Belisırma, 38°15'648''N, 34°17'550''E, 1180 m a.s.l., 07.12.2013, FS 0969.

Gymnosporangium dobrozrakovae Mitrof. on leaves of *Pyrus elaeagnifolia*; Ihlara valley, around Belisırma, 38°15'920''N, 34°17'748''E, 1160 m a.s.l., 07.12.2013, FS 0963a.

Hendersonia celtidis-australis Scalia on bark of branches of *Celtis tournefortii*; Ihlara valley, around Belisırma, 38°15'886''N, 34°17'498''E, 1160 m a.s.l., 07.12.2013, FS 0966a.

Hendersonia sarmentorum Westend. on dead branches of *Colutea cilicica*; Ihlara valley, 38°15'389''N, 34°17'810''E, 1194 m a.s.l., 07.12.2013, FS 0973.

Hypoxylon glandiforme (Ellis & Everh.) P.M.D. Martin on bark of *Quercus pubescens*; Ihlara valley, around Belisırma, 38°15'600''N, 34°17'781''E, 1180 m a.s.l., 07.12.2013, FS 0970b.

Leucostoma persoonii (Nitschke) Höhn. on dead branches *Prunus domestica*; Ihlara valley, 38°15'389''N, 34°17'810''E, 1195 m a.s.l., 07.12.2013, FS 0974a.

Lophiostoma compressum (Pers.) Ces. & De Not. on wood of *Pistacia terebinthus*; Ihlara valley, around Belisırma, 38°15'389''N, 34°17'810''E, 1194 m a.s.l., 07.12.2013, FS 0972.

Melanomma pulvis-pyrius (Pers.) Fuckel on dead branches of *Elaeagnus angustifolia*; Ihlara valley, around Belisırma, 38°15'965''N, 34°17'410''E, 1190 m a.s.l., 07.12.2013, FS 0957.

Melanomma terebinthi Fabre on branches of *Pistacia terebinthus*; Ihlara valley, around Belisırma, 38°15'389''N, 34°17'810''E, 1194 m a.s.l., 07.12.2013, FS 0972.

Microdiplodia melaena Allesch. on bark of dead branches of *Ulmus glabra*; Ihlara valley, around Belisırma, 38°15'492''N, 34°17'749''E, 1177 m a.s.l., 07.12.2013, FS 0971.

Microdiplodia salicis Died. on dead branches of *Salix alba*; Ihlara valley, around Belisırma, 38°15'970''N, 34°17'413''E, 1190 m a.s.l., 07.12.2013, FS 0956.

Microstroma album (Desm.) Sacc. on leaves of *Quercus robur*; Ihlara valley, 38°15'399''N, 34°17'887''E, 1193 m a.s.l., 07.12.2013, FS 0953a.

****Mycosphaerella convexula*** (Schwein.) F.V. Rand on leaves of *Juglans regia*; Ihlara valley, around Belisırma, 38°15'886''N, 34°17'498''E, 1160 m a.s.l., 07.12.2013, FS 0967.

Mycosphaerella populi (Auersw.) J. Schröt. on leaves of *Populus piramidalis*; Ihlara valley, around Belisırma, 38°15'968''N, 34°17'408''E, 1190 m a.s.l., 07.12.2013, FS 0960.

Ophiobolus salicinus Rostr. On dead thin branches of *Salix alba*; Ihlara valley, around Belisırma, 38°15'970''N, 34°17'413''E, 1190 m a.s.l., 07.12.2013, FS 0956.

Paraconiothyrium fuckelii (Sacc.) Verkley & Gruyter on branches of *Pistacia terebinthus*; Ihlara valley, around Belisırma, 38°15'389''N, 34°17'810''E, 1194 m a.s.l., 07.12.2013, FS 0972.

Phyllosticta destruens Desm. on leaves of *Celtis australis*; Ihlara valley, around Belisırma, 38°15'886''N, 34°17'498''E, 1160 m a.s.l., 07.12.2013, FS 0966.

Phoma juglandis Sacc. on dead branches of *Juglans regia*; Ihlara valley, around Belisırma, 38°15'915''N, 34°17'487''E, 1160 m a.s.l., 07.12.2013, FS 0964.

Phoma pachytheca Vestergr. on dead branches of *Salix alba*; Ihlara valley, around Belisırma, 38°15'970''N, 34°17'413''E, 1190 m a.s.l., 07.12.2013, FS 0956.

Pyrenochaeta cava (Schulzer) Gruyter, Aveskamp & Verkley on dead branches of *Elaeagnus angustifolia*; Ihlara valley, around Belisırma, 38°15'965''N, 34°17'410''E, 1190 m a.s.l., 07.12.2013, FS 0957.

Rosellinia pistaciae Frolov on thin branches of *Pistacia terebinthus*; Ihlara valley, around Belisırma, 38°15'389''N, 34°17'810''E, 1194 m a.s.l., 07.12.2013, FS 0972.

Rosellinia salicum Fabre on thin branches of *Salix alba*; Ihlara valley, around Belisırma, 38°15'970''N, 34°17'413''E, 1190 m a.s.l., 07.12.2013, FS 0956.

Thyrostroma compactum (Sacc.) Höhn. on dead branches of *Ulmus glabra*; Ihlara valley, around Belisırma, 38°15'492''N, 34°17'749''E, 1177 m a.s.l., 07.12.2013, FS 0971.

Valsa sordida Nitschke on dead branches of *Salix alba*; Ihlara valley, around Belisırma, 38°15'970''N, 34°17'413''E, 1190 m a.s.l., 07.12.2013, FS 0956.

Fifty species were recorded previous study made by Hüseyin (2004), among them 25 species were new record for Turkish mycobiota. In this study, 43 species have been reported from Ihlara Valley, among them four species have been recorded from Turkey for the first time.

This study was supported by the Ahi Evran University Scientific Research Projects Coordination Unit. (Project Number: FBA – 1103)

References:

Allescher, A. 1901-1903. Fungi Imperfecti. In Rabenhorst's Kryptogamen-Flora von Deutschland, Osterreich und der Schweiz.

Arx Von, J.A. 1987. Plant Pathogenic Fungi. Nova Hedwigia, J. Cramer, Berlin Stuttgart.

Barnett, H.L.; Hunter, B.B. 1998. Illustrated Genera of Imperfect Fungi, Fourth Edition.

Biler, L., Şahin, M. 2012. Ihlara Özel Çevre Koruma Bölgesi Biyolojik Çeşitliliğinin Korunması Projesi, TC Çevre ve Şehircilik Bakanlığı Tabiat Varlıklarını Koruma Genel Müdürlüğü, Çınar mühendislik, Ankara.

Braun, U. A. 1995. Monograph of Cercosporella, Ramularia and Allied Genera (Phytopathogenic Hyphomycetes), IHW-Verlag, Eching.

Braun, U. A. 1998. Monograph of Cercosporella, Ramularia and Allied Genera (Phytopathogenic Hyphomycetes), IHW-Verlag.

Byzova, Z.M.; Vasyagina, M.P.; Deeva, N.G.; Kalımbetov, B.K.; Pisareva, N.F.; Şvartsman, S.R. 1968. Flora Sporovıkh Rasteniy Kazakistana. Tom 5, Nesoverşennıye gribı – Fungi imperfecti (Deuteromycetes), 2. Sferopsidnıye – Sphaeropsidales, Nauka, Alma-Ata.

Byzova, Z.M.; Vasyagina, M.P.; Deeva, N.G.; Kalımbetov, B.K.; Pisareva, N.F.; Şvartsman, S.R. 1970. Flora Sporovıkh Rasteniy Kazakistana. Tom 5, Nesoverşennıye gribı – Fungi imperfecti (Deuteromycetes), 3. Sferopsidnıye – Sphaeropsidales, Nauka, Alma-Ata.

Carmichael, J. W.; Kendrick, W. B.; Conners, I. L.; Singler, L. 1980. Genera of Hypomycetes, The Univ., Alberta Press.

ÇOB. 2013. Çevre ve Orman Bakanlığı, Özel Çevre Koruma Kurumu Başkanlığı, http://www2.ormansu.gov.tr/COB/Files/durum_rapor/ockkb/ockkb_ild.pdf.

Davis P.H. (ed.). 1982. Flora of Turkey and east Aegean Islands. Vol. 7. Edinburgh Univ. press., Edinburgh.

Ellis, M.B.; Ellis J.P. 1987. Microfungi on Land Plants. An Identification Handbooke, CROOM HELM, London-Sydney.

Grove, W.B. 1935. British Stem and Leaf Fungi (Coelomycetes), Sphaeropsidales, 1. Cambridge, At the University Pres, London.

Grove, W.B. 1937. British Stem and Leaf Fungi (Coelomycetes), Sphaeropsidales, 2. Cambridge, At the University Pres, London.

Hüseyin, E. 2004. Xylothrophic micromycetes of Ihlara Valley (Kapadokya, Turkey). Proceedings of The International Scientific Conference, September 20 – 24, Minsk.

Karabacak, V. 2007. Ihlara Vadisi (Orta Anadolu) Travertenlerinin Genel Özellikleri ve Kabuksal Deformasyon Açısından Önemleri. Eskişehir Osmangazi Üniversitesi Müh. Mim. Fak. Dergisi. 20 (2): 65-82.

Kiffer, R.; Morelet, M. 2000. The Deuteromycetes. Mitosporic Fungi, Classification and Generic Keys, Enfield.

Mel'nik, V.A. 2000. Definitorium Fungorum Rossiae. Classis Hyphomycetes, Fasc.1. Fam., Dematiaceae, Nauka, Petropoli.

Mel'nik, V.A.; Popushoj, İ.S. 1992. Nesoverşennıye Gribı Na Drevesnıkh i Kustasrnikovıkh Porodakh, Ştiintsa, Kişinev.

Nag Raj, T. R. 1993. Coelomycetes Anamorphs With Appendage-Bearing Conidia, Mycologue Publications, Waterloo, Ontario, Canada.

Ören, M., Keçeli T. 2014. The moss flora of Ihlara valley (Aksaray/Turkey). Bidicon. 7 (1): 88-93.

Saccardo, P. A. 1882 – 1931. Sylloge Fungorum Omnium Hucusque Cognitorum, 1-25, Pavia, Johnson Reprint Corporation, New York, London.

Sarı, M., Reis, S., Bayrak, T., Yılmaz, H.M. 2005. Ihlara Vadisindeki Doğal Ve Tarihi Yapının Korunmasına Yönelik Risk Haritasının Çıkarılması ve Vadi Bilgi Sisteminin Oluşturulması, 2. Mühendislik Ölçmeleri Sempozyumu 23-25 Kasım 2005, İTÜ – İstanbul, 604-614.

Smitskaya, M. F, 1991, Flora Fungorum RSS Ucrainicae. Ascomycetes, Hypocrealşes. "Naukova Dumka", Kiev.

Sutton, B. C. 1980. The Coelomycetes. Fungi Imperfecti With Pycnidia, Acervuli and Stromata, CABI Publishing.

Şvartsman, S. R.; Vasyagina, M. P.; Bızova, Z. M.; Filimonova, N. M. 1973. Flora Sporovıkh Rasteniy Kazakistana. Tom. VIII. Nesoverşennıye Gribı – Fungi Imperfecti (Deuteromycetes), 1. Monilial'nıye – Moniliales, Nauka, Alma-Ata.

Şvartsman, S. R.; Vasyagina, M. P.; Bızova, Z. M.; Filimonova, N. M. 1975. Flora Sporovıkh Rasteniy Kazakistana. Tom, VIII, Nesoverşennıye Gribı – Fungi Imperfecti (Deuteromycetes), 2. Monilial'nıye – Moniliales, Nauka, Alma-Ata.

Şvartsman, S. R.; Vasyagina, M. P.; Pisareva, N. F.; Bızova, Z. M. 1971. Flora Sporovıkh Rasteniy Kazakistana, Tom. VIII, Nesoverşennıye gribı – Fungi Imperfecti (Deuteromycetes). Melanconiales, Nauka, Alma-Ata.

Tomilin, B. A. 1979. Opredelitel' Gribov Roda Mycosphaerella Johans, Nauka, Leningrad.

Investigation of structural and electronic properties of Yttrium (III) Hydride under high hydrostatic pressure

Cihan Kürkçü[a,*], Ziya MERDAN[b], Hülya ÖZTÜRK[a]

[a] *Department of Physics, Faculty of Arts and Sciences, Ahi Evran University, TR-40100 Kırşehir, Turkey*
[b]*Department of Physics, Faculty of Sciences, Gazi University, TR-06500 Ankara, Turkey*

**e-mail corresponding author*:ckurkcu@ahievran.edu.tr

Keywords: Yttrium (III) Hydride, ab initio technique, phase transitions

ABSTRACT

We have investigated the pressure induced phase transition and electronic properties of Yttrium (III) hydride (YH_3) using density functional theory. YH_3 crystallizes under normal conditions in two modifications: hexagonal YH_3 (space group $P6_3/mmc$) and trigonal YH_3 (space group $P\bar{3}c1$). We studied $P\bar{3}c1$ phase of YH_3 under the hydrostatic pressure up to 180 GPa and obtained a phase transition from this phase to the hexagonal-type structure (space group $P6_3/mcm$). This phase transition is also studied by total energy and enthalpy calculations. According to these calculations, we obtained phase transition at about 18 GPa.

1. INTRODUCTION

The investigation of the structural and the electronic properties of metal hydride systems is important to understand technologically essential phenomena such as hydrogen desorption, catalysis, and storage. Once yttrium and most of the rare-earth metals are exposed to a hydrogen atmosphere, they form hydrides that may appear a reversible metal-insulator transition [1]. In this study we observed that YH_3 undergoes a phase transformation from the trigonal structure with space group $P\bar{3}c1$ to hexagonal structure with space group $P6_3/mcm$ at 90–100 GPa. Also we obtained the metallic property of YH_3 by calculating the electronic properties of both phases of this material.

2. METHOD OF COMPUTATION

The calculations in the present work were carried out with the *ab initio* program SIESTA [2] based on pseudopotentials and a localized basis set. The first-principles pseudopotential method within the density-functional theory (DFT) and the generalized gradient approximation (GGA) using the Perdew-Burke-Ernzerhof [3] functional was used for the exchange-correlation energy. A simulation cell chosen consists of 96 atoms with periodic boundary conditions. Conjugate-gradient method was used in order to apply pressure to the system. Firstly the system was equilibrated at zero pressure, and after that the pressure was gradually increased by a rise of 10.0 GPa. For each pressure value applied to the system, the structure was allowed to relax and find its equilibrium volume and lowest-energy by optimizing its lattice vectors and atomic positions. In order to find symmetries of the phases observed in the simulations, we used the RGS algorithm and the KPLOT program [4,5] that permit detailed data about a given structure such as space group, cell parameters and atomic positions.

3. RESULTS AND DISCUSSION

Initially, we relaxed 96 atoms of supercell at zero pressure to obtain the lattice parameters of the $P\bar{3}c1$ phase. The equilibrium unit cell lattice constants of YH_3 are obtained as $a = b = 6.3745$ Å, and $c = 6.9435$ Å.

The pressure-volume relation of YH_3 is investigated and presented in Fig. 1. The volume gives a sharp variation when the applied pressure is increased from 90 GPa to 100 GPa, indicating a first-order pressure-induced phase transition of this material.

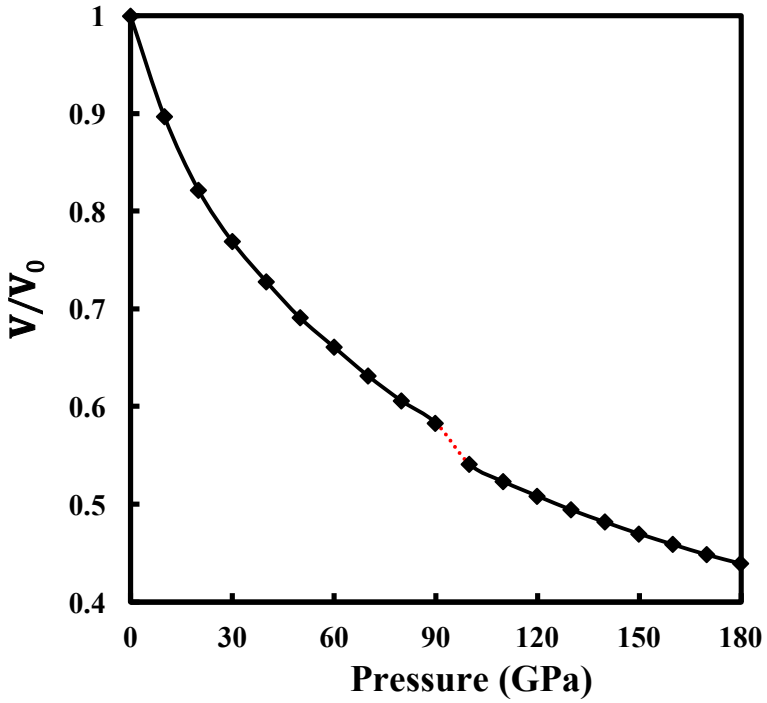

Figure 1. The volume change of the simulation cell as a function of pressure.

The structural analysis make known that the trigonal structure of YH_3 transforms to hexagonal structure at 100 GPa pressure as shown in Fig. 2. This result shows that the *ab initio* technique successfully produces the experimental observed high-pressure phase of YH_3 with an overvalued transition pressure.

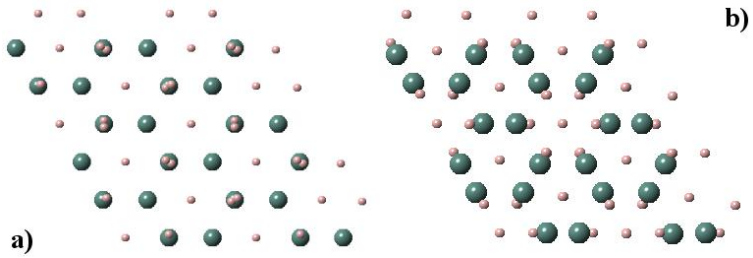

Figure 2. The crystal structures of YH_3:a) $P\bar{3}c1$ phase and b) $P6_3/mcm$ phase

Since the restricted conditions such as limited size of the simulation cell, the lack of any defect in simulated cell, etc. are considered, such an overvalued transition pressure is expected. Conversely, the thermodynamic theorem does not consider the probable presence of such an activation barrier separating the two structural phases. Thus, as a next step, we take the energy-volume computations into account to study the stability of high-pressure phases of YH_3. For these computations we used the unit cells for the $P\bar{3}c1$ and $P6_3/mcm$ high-pressure phases. The computed total energy as a function of volume is presented in Fig. 3.

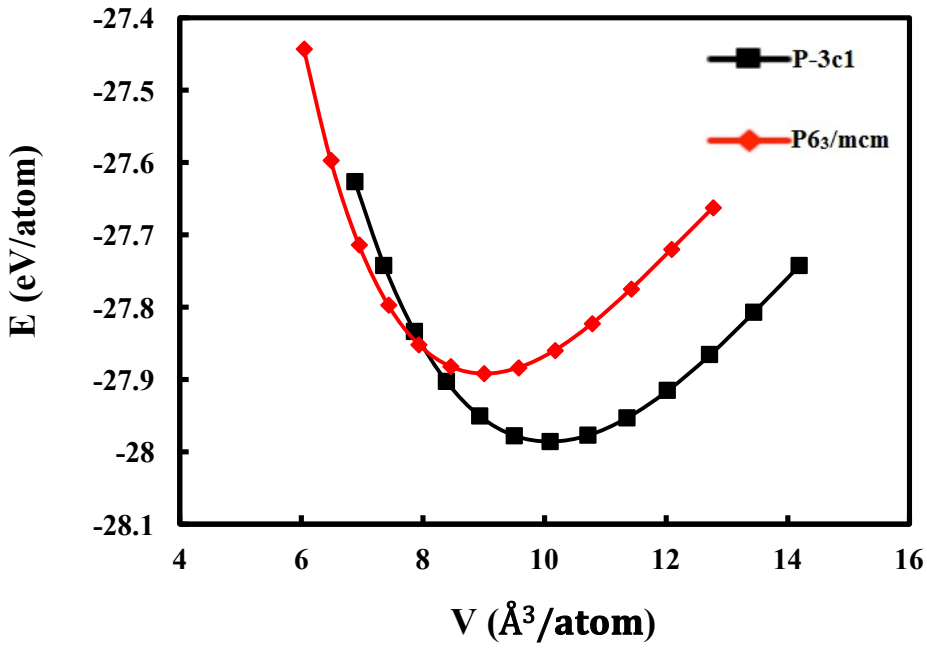

Figure 3. The energy-volume curves of structural phases of YH_3.

The transition pressure between the different phases of YH_3 is easily identified by a simple comparision of their static lattice enthalpy since the intersection of two enthalpy curves indicates a pressure-induced phase transition between these two phases. The computed enthalpy curves of the $P\bar{3}c1$ and $P6_3/mcm$ high-pressure phases are plotted as a function of pressure in Fig. 4. As seen from this figure the enthalpy curve of the $P\bar{3}c1$ phase crosses with that of the $P6_3/mcm$ phase at about 18 GPa, indicating a first-order phase transition between these phases.

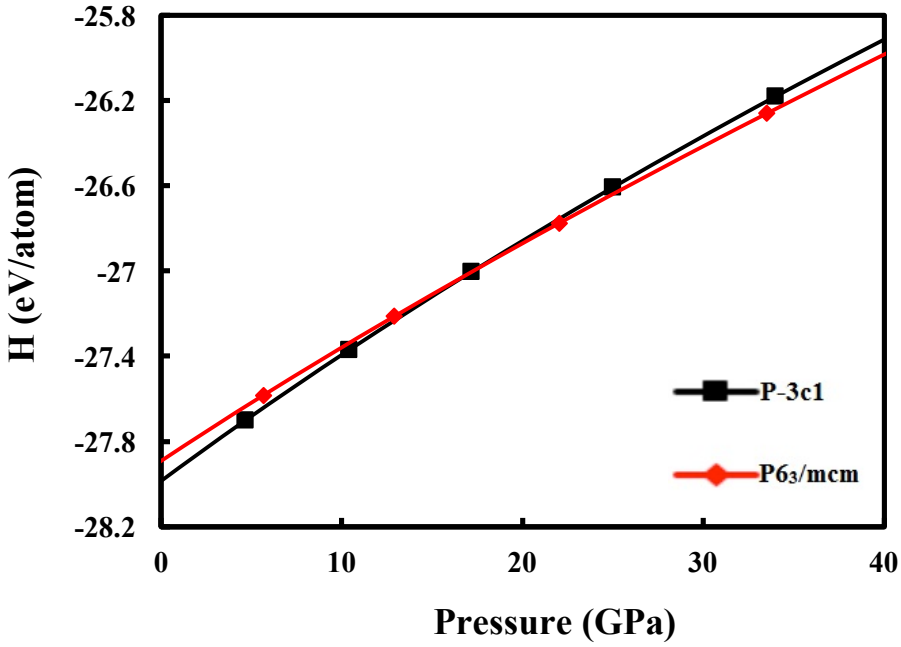

Figure 4. The enthalpy curves of structural phases of YH_3 as a function of pressure.

We calculated the electronic band structures for YH_3 along the high-symmetry directions and illustrated near the Fermi energy (E_F) level as a function of energy in Fig 5. Fermi level was set to be 0 eV. As seen

from electronic band structures of YH_3, the valance band is located below the E_F level, whereas the conduction band is located above it. There are no energy gaps (E_g) between the valance and conduction band in both phases of YH_3. This suggested that YH_3 indicates metallic behavior.

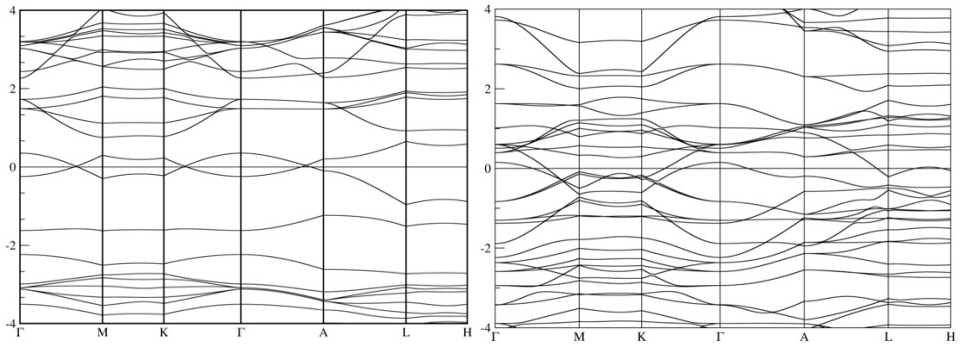

Figure 5. Band structures of YH_3 for $P\bar{3}c1$ (left) and $P6_3/mcm$ (right) phases

4. CONCLUSION

We have performed an *ab initio* constant pressure technique in order to study the pressure-induced phase transformation in the trigonal structured YH_3. We obtained a phase transition from this structure to hexagonal structure with space group $P6_3/mcm$. Furthermore, we study the trigonal structure to hexagonal structure phase transformation of YH_3 via the enthalpy calculations and find that the phase transformation should occurs from the trigonal structure to hexagonal structure around 18 GPa. In addition, we calculated the electronic band structure for $P\bar{3}c1$ and $P6_3/mcm$ phases of YH_3.

REFERENCES

[1] de Almeida J.S., Kim D.Y., Ortiz C., Klintenberg M. and Ahuja R., Appl. Phys. Lett. (2009), 94, 251913-1-3.
[2] Ordejón P., Artacho E. and Soler J.M., Physical Review B (1996), 53, R10441.
[3] Perdew J.P., Burke K. and Ernzerhof M., Physical Review Letters (1996), 77, 3865.
[4] Hannemann A., Hundt R., Schon J.C. and Jansen M., Journal of Applied Crystallography (1998), 31, 922.
[5] Hundt R., Schon J.C., Hannemann A. And Jansen M., Journal of Applied Crystallography (1999), 3, 413.

Restoration of motility to *Escherichia coli* YK4104 *fliA* mutant by the alternative sigma factor σ^{28} of *Geobacillus kaustophilus* and *Anoxybacillus flavithermus*

Ali Sevim[a], Elif Sevim[a*]

[a] *Department of Genetic and Bioengineering, Faculty of Engineering and Architecture, Ahi Evran University, TR-40100 Kırşehir, Turkey*

**e-mail corresponding author*: esevim@ahievran.edu.tr

Keywords: Sigma factor-28, flagella, motility, fliA gene, thermophilic bacteria

ABSTRACT

The enzyme of RNA polymerase is consisted of two subunits. One of these is core RNA polymerase consisting of five subunits (αI, αII, β, β' and, ω) which is responsible for catalytic activity. The second subunit is known as specific σ factor and it is responsible for recognizing promoters with specific DNA sequences. The sigma factor σ^{28} is responsible for expression of related genes in flagellar biosynthesis and chemotaxis in many bacteria such as *Escherichia coli*, *Pseudomonas aeruginosa* and, *Bacillus subtilis*. In this study, we cloned the sigma factor (*fliA*) of RNA polymerase from two thermophilic bacteria (*Geobacillus kaustophilus* and *Anoxybacillus flavithermus*) and, transformed into a *fliA* mutant of *E. coli* YK4104 under expression of T7 promoter included in pET-(28a) + plasmid vector. Interestingly, we showed that the *fliA* genes from *G. kaustophilus* and *A. flavithermus* restored the motility to the *E. coli* mutant which is a mesophilic bacterium. This indicates that *G. kaustophilus* and *A. flavithermus* σ^{28} protein is able to bind to the *E. coli* core RNA polymerase and, participate in the complex interactions to initiate the transcription of the flagellar units *in vivo*. These results suggest that the binding ability of thermofilic σ^{28} to the core RNA polymerase is not dependent on high temperature.

1. INTRODUCTION

Sigma factors (σ) are a class of proteins and, bacterial transcription initiation factors which facilitate specific binding of RNA polymerase to promoters [1]. Sigma factors which are an important element of transcription stage of gene expression were preserved in very tight throughout its evolution. These factors are able to determine related promoter regions where holoenzymes bind. In addition, sigma factors play an important role in the initiation of DNA softening stage which is necessary for the initiation of transcription [2]. Many bacteria synthesize different sigma factors binding promoters which have different conserved regions to form RNAP holoenzyme. This diversity among sigma factors provides both the provision of gene regulation and the maintaining of gene expression to response for specific environmental suppressor [3].

The filament region that is the third part of bacterial flagella is formed by the coming together of flagellin proteins consisting of single subunit. The expression of flagellin is controlled by the σ^D (σ^{28}) which is subunit of RNA polymerase. In this study, we aimed to amplify and sequence *sigD* gene region coding σ^D that is homolog of σ^{28} from two thermophilic bacterium (*Geobacillus kaustophilus* and *Anoxybacillus flavithermus*) and, to transform the *sigD* gene into *E. coli* YK4104 *fliA* mutant by pET-(28a) + plasmid vector. Therefore, it is intended to investigate the conservation of σ^D protein within the group of thermophilic bacteria as evolutionary.

2. RESULTS AND DISCUSSION

2.1. Amplification of *sig*D genes by PCR and their cloning into pET28a+ vector

In this study, two gram positive bacteria (*Geobacillus kaustophilus* and *Anoxybacillus flavithermus*) showing thermophilic reproduction characteristics were used. A few years ago the *Bacillus* group, the largest and most diverse group of bacteria, was divided into 9 genera and among this group, showing thermophilic character ones were separated as *Anoxybacillus* ve *Geobacillus* [4, 5]. The genus of *Geobacillus* is gram positive and obligatory thermophilic. The optimum growth temperatures of this group were 55-65 °C and approximately 19 species were identified within this genus [5, 6]. The genus of *Anoxybacillus* contains bacteria which are gram positive, spore forming and rod-shaped. The members of this genus are alkaliphilic or alkalitolerant, thermophilic, aerop or facultative anaerop and up to now, a total of 11 species were identified within this genus [7].

The *sig*D genes of *Geobacillus kaustophilus* and *Anoxybacillus flavithermus* bacteria were obtained from NCBI GenBank under the accession numbers of BA000043 and CP000922, respectively. These *sig*D genes were amplified by PCR using the primers designed to contain restriction endonuclease cleavage regions (Table 1).

Table1. Primers used in this study

Primer Name	Sequences(5'-3')[a]	T_m
Geo.ex Fwd	CATATGGGAAGCGCGCTAAAAGGAG	60
Geo.ex Rev	AAGCTTCATGGCTCTTTTTCAAAAAAGC	57
Anox.ex Fwd	GGATCCATGTGCTGGCAAAAGTGGATAG	61
Anox.ex Rev	CTCGAGTCATACTGCTTGCTCAATCAG	59

[a] underlined sequences indicate restriction enzyme site

After performing the PCR, the amplification products of 732 bp *sig*D gene of *Anoxybacillus flavithermus* and the 756 bp *sig*D gene of *Geobacillus kaustophilus* were separated on agarose gel and viewed under UV light (Figure 1). In order to clone *sig*D genes into pET28a+ vector, the amplified *sig*D genes and pET28a+ expression vectors were digested by appropriate restriction enzymes. After that, the digested *sig*D genes and pET28a+ vectors were ligated at 16 °C. The obtained recombinant plasmids were transformed into *E. coli* DH5α competent cells and the right clones were selected [8]. The pET28a+ vectors containing *Geobacillus kaustophilus* and *Anoxybacillus flavithermus sig*D genes were named as pES1 and pES2, respectively.

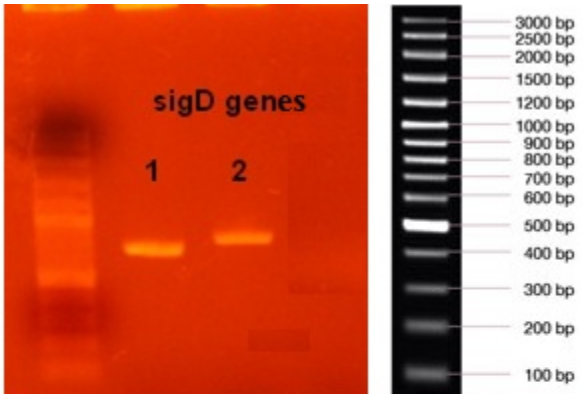

Figure 1. The amplified *sig*D genes. 1; *Anoxybacillus flavithermus sig*D gene, 2; *Geobacillus kaustophilus sig*D gene.

2.2. *in vivo* Complementation and the motility tests

The obtained recombinant pES1 and pES2 plasmids were transformed into *E. coli* YK410 wild type and *E. coli* YK4104 which is *flia*A mutant. The *fli*A gene coding σ^{28} protein was deleted from *E. coli*

YK4104 genome. In the family of Enterobacteriaceae and some other Gram negative organisms, the σ^D homolog is termed as σ^{28} [9]. *E. coli* YK4104 cells containing recombinant pES1 and pES2 plasmids were named as *E. coli* EE20 and *E. coli* EE21, respectively. For the motility tests, *E. coli* YK410, YK4104, EE20 and EE21 cells were inoculated on motility test medium by a sterile needle. At the same time, *E. coli* EE20 and EE21 cells were inoculated on motility test medium containing 100 mM IPTG by a sterile needle. As a result of the experiments, it was determined that wild type EE20 and EE21 cells gained the motility properties. Moreover, EE20 and EE21 cells growing on the motility test medium containing IPTG gained the motility more strongly (Figure 2).

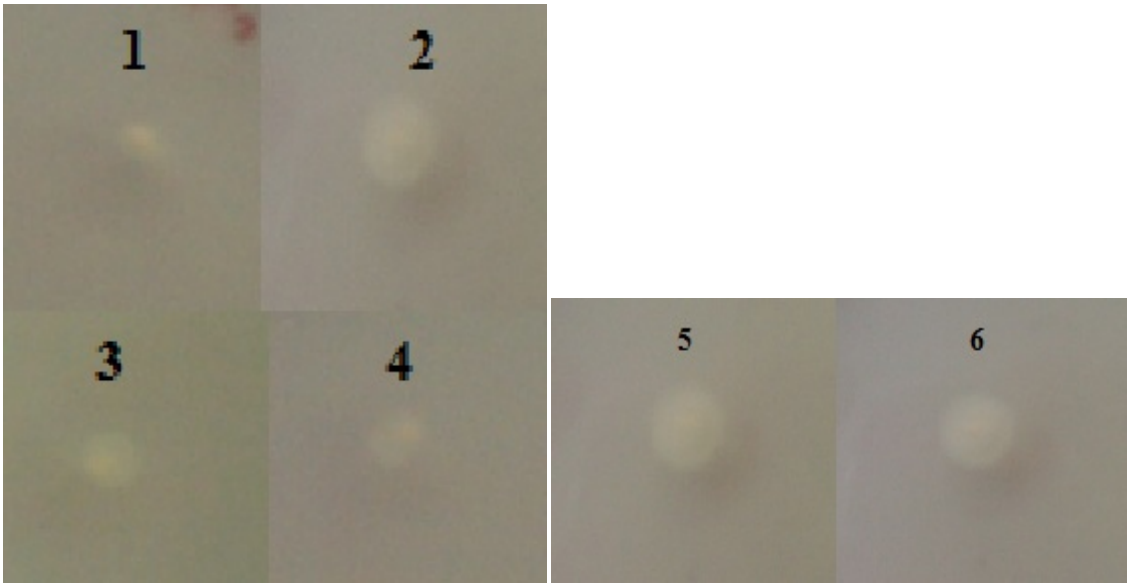

Figure 2. *in vivo* complementation and the motility tests. 1-4; the motility test medium (1, *E. coli* YK410, 2, *E. coli* YK4104, 3, *E. coli* EE20, 4, *E. coli* EE21). 5-6; the motility test medium containing IPTG (5, *E. coli* EE20 and 6, *E.coli* EE21).

The biological function of σ^D was determined by deleting *sig*D gene from the genome using genetic engineering techniques. It was determined that the mutant strains not including *sig*D gene were able to grow but not forming filamentous structure or flagella. Based on the Western blot analysis, it was shown that there was no flagellin polypeptide in the mutant strains. These results have been shown that σ^D is responsible for the controlling of flagellin gene transcription [10, 11]. Most of the genes controlled by σ^D don't include promoter regions that can be recognized by other σ-factors and these genes are completely dependent on σ^D for their expression. When promoter regions of genes whose expression is controlled by σ^D are examined, it is observed that the TAAA-N15-GCCGATAT motif is strongly conserved [12]. In this study, it was determined that the σ^D protein of *Geobacillus* and *Anoxybacillus* which are thermophilic bacteria can recognize the promoter region of *E. coli* flagellin gene in *in vivo* complementation test. Moreover, based on the motility tests, it was determined that the σ^D protein of *Geobacillus* and *Anoxybacillus* provides the motility to wild type cells. These all results showed that the flagellin gene of the mesophilic bacterium *E. coli* can be recognized by σ^D protein of *Geobacillus* and *Anoxybacillus* and the core RNA polymerae enyme of *E. coli* can form holoenyme formation with σ^D protein of *Geobacillus* and *Anoxybacillus*.

3. CONCLUSION

In conclusion, we determined that the *sig*D genes of *G. kaustophilus* and *A. flavithermus* could be expressed in *E. coli* cells and this expression restores motility to an immotile E. coli mutant strain. This indicates that the the σ^D proteins of *G. kaustophilus* and *A. flavithermus* can bind to the *E. coli* core RNA polymerase to initiate transcription.

REFERENCES

[1] Gruber T.M., Gross C.A., Annu. Rev. Microbiol. (2003), 57, 441-66.
[2] Helmann J.D., Encylopedia of Biological Chemistry (2004), 4, 41-44.
[3] Wosten M.M., FEMS Microbiol. Rev. (1998), 22, 127-50.
[4] Banat I.M., Marchant R. and Rahman T.J., Int. J. Syst. Evol. Microbiol. (2004), 54, 2197-2201.
[5] Nazina T.N., Tourova T.P., Poltaraus A.B., Novikova E.V., Grigoryan A.A., Ivanova A.E., Lysenko A.M., Petrunyaka V.V., Osipov G.A., Belyaev S.S. and Ivanov M.V., Int. J. Syst. Evol. Microbiol. (2001), 51, 433-46.
[6] Abd Rahman R.N., Leow T.C., Salleh A.B. and Basri M., BMC Microbiol. (2007), 7, 77-81.
[7] Pikuta E., Cleland D. and Tang J., Int. J. Syst. Evol. Microbiol. (*2003),* **53**, 1561–1562.
[8] Sambrook J., Fritsch E.F. and Maniatis T., Cold Spring Harbor Lab. Press (1990), NY.
[9] Helmann D.J. and Morgan P.C., ASM Press (2004), Washington.
[10] Helmann J.D., Marquez L.M. and Chamberlin M.J., J. Bacteriol. (1988), 170, 1568-74.
[11] Helmann J.D., Masiarz F.R. and Chamberlin M.J., J. Bacteriol (1988), 170, 1560-7.
[12] Helmann J.D., Mol. Microbiol. (1991), 5, 2875-82.

Ahi Evran University

10 year

Innovative University of Modern Turkey

WITAM-2016

2nd INTERNATIONAL CONGRESS ON THE WORLD OF TECHNOLOGY AND ADVANCED MATERIALS

28 SEPTEMBER - 02 OCTOBER 2016 KIRŞEHİR/TURKEY